Electrode Kinetics and Gas Conversion in Solid Oxide Cells

Njodzefon, Jean-Claude

Publication date:
2015

Document Version
Publisher's PDF, also known as Version of record

Electrode Kinetics and Gas Conversion in Solid Oxide Cells

Jean-Claude Njodzefon

Department of Energy Conversion and Storage—Applied Electrochemistry

Technical University of Denmark

jenjod@dtu.dk

Supervisors:

Johan Hjelm, PhD

Senior Scientist, Department of Energy Conversion and Storage—Applied Electrochemistry

Technical University of Denmark

johh@dtu.dk

Christopher Graves, PhD

Senior Scientist, Department of Energy Conversion and Storage—Applied Electrochemistry

Technical University of Denmark

cgra@dtu.dk

Dr.-Ing. Andre Weber

Senior Scientist and Group Leader, Institute for Applied Materials - Materials for Electrical and Electronics Engineering

Karlsruhe Institute of Technology

andre.weber@kit.edu

Technical University of Denmark

This manuscript is part of the requirements to achieve the degree of Doctor of Philosophy (PhD) at the Department of Energy Conversion and Storage, Technical University of Denmark

Roskilde, 2015

Release Date: 21.12.2015

Technical University of Denmark

Section for Applied Electrochemistry

Department of Energy Conversion and Storage

Frederiksborgvej 399

4000 Roskilde

Denmark

Technical University of Denmark

Abstract

The solid oxide fuel cell (SOFC) converts hydrogen, carbon monoxide and hydrocarbon fuels (directly) into electricity with very high efficiencies and has demonstrated almost comparable performance when operated in reverse mode as a solid oxide electrolysis cell (SOEC). In this case electrical (and thermal) energy is *stored* as chemical energy of reaction products. To this end, the cells are fed with steam (H_2O electrolysis), carbon dioxide (CO_2 electrolysis) or a mixture of both (H_2O/CO_2 co-electrolysis) and of course electrical (ΔG) and thermal ($T\Delta S$) energies for the splitting of reactant compounds. Hydrogen, carbon monoxide or both (synthesis gas) are produced at the fuel electrode meanwhile oxygen is produced at the oxygen electrode. In reversible or cyclic mode the solid oxide cell is operated alternatingly as fuel cell or electrolysis cell depending on the needs of the end user.

Upon polarization of the solid oxide cell (SOC) and independent of polarization mode (fuel cell mode or electrolysis mode), the current flowing through the cell is limited by processes such as adsorption and desorption of reactants or products, diffusion through the porous electrodes, activation or charge transfer at the reaction sites, gas conversion at the reaction sites and flow fields and ohmic drop across the electrolyte. These processes occur in both electrodes and often their characteristic frequencies overlap, rendering characterization of a given mechanism particularly challenging. To optimize the SOCs for operation in the different fuels, operation temperature and operation modes it is important to understand the kinetics of the SOC electrodes. This thesis was aimed at understanding the kinetics of the SOC under different operation conditions of temperature, polarization, and fuel mixture. For investigations on full cells, electrochemical impedance spectroscopy and distribution of relaxation times techniques were used to investigate kinetics of the Ni/YSZ fuel electrode in three fuel mixtures – hydrogen/steam and reformate fuels hydrogen/carbon-dioxide and hydrogen/methane/steam. It was found that the kinetics at the fuel electrode were exactly the same in both reformates. This means that chemical equilibrium reactions were much faster than the electrochemical reactions. The electrode displayed slightly faster kinetics in hydrogen/steam fuel than in the reformate fuels.

To minimize the influence of (i) joule heating effects as a result of current flow across the electrolyte, (ii) concentration-related effects like gas diffusion, and (iii) overlapping of the characteristic frequencies of processes, the investigations were extended from full cell geometries to a novel pseudo-three electrode cell geometry with working-electrode areas of ca. 1 mm^2 that enabled isolated investigation of the fuel and oxygen electrodes. In a 50/50 H_2/H_2O fuel mixture, the Ni/8 mol % yttria-stabilized zirconia (Ni/YSZ) fuel electrode showed slower reaction kinetics operating under cathodic polarization than anodic—the same finding had been reported in literature from investigations on full cells whereby together with the local pH_2O, substrate diffusion (specifically Knudsen diffusion) was identified as one of the causes of asymmetry between anodic and cathodic mode polarization. Obtained charge-transfer coefficients compared well with those reported in literature and their evolution with temperature was similar to that reported in literature based on porous Ni/YSZ fuel electrodes. From the two investigated oxygen electrodes, the higher performing $(La_{0.6}Sr_{0.4})_{0.99}CoO_3/Ce_{0.9}Gd_{0.1}O_{1.95}$ (LSC/CGO) oxygen electrode showed slower reaction kinetics under cathodic mode operation at 50 mV overvoltage than in anodic mode. The trend was opposite for the lower performing $La_{0.58}Sr_{0.4}Co_{0.2}Fe_{0.8}O_3$ (LSCF) oxygen electrode. However, with decreasing oxygen partial pressure both electrodes displayed increasing

asymmetry between anodic and cathodic modes. It could be shown that surface exchange kinetics were the major cause of the decreasing kinetics with decreasing pO_2 and that the cathodic mode kinetics were slowed down much more than the anodic branch kinetics thus increasing the asymmetry.

Independent of operation mode, commercialization of the SOC technology requires a guarantee of longevity as well as predictability of the SOC performance under desired operation conditions.

The performance is generally evaluated through the current/voltage (C/V) curve. As such, a deviation from the expected/predicted performance curve can serve to identify the presence of ageing or an ageing inducing process. A 0-D stationary model was previously developed at the *Institut für Angewandte Materialien - Werkstoffe der Elektrotechnik (IAM-WET)* in Germany to predict the C/V curve of a SOC for fuel cell operation mode. In this thesis, the applicability of this model was verified for electrolysis mode operation, the model was extended to accommodate temperature changes under polarization in fuel cell and electrolysis mode operation, and the model was further extended to cover operation in reformate fuels $H_2/H_2O/CO/CO_2$. The latter was accomplished by including a new concentration-related overpotential contribution in the model to account for the CO/CO_2 diffusion to the reaction sites as a result of the water gas shift equilibrium reactions.

The long-term stability of the system depends on whether the system is operated solely in fuel-, electrolysis-, reversible or dynamic mode. Optimization of the cells for high performance and/or durability in each of these operation modes requires a thorough understanding of the processes and mechanisms affecting the kinetics and ageing of the systems. In five tests with varying durations between 1000 h and 2500 h the long-term stability of the SOCs was investigated for constant electrolysis, cyclic and dynamic operation modes in a symmetric binary fuel of 50/50 H_2/H_2O at 800 °C and 700 °C. The SOCs investigated under constant electrolysis mode aged more than those investigated under cyclic mode with the fuel electrode dominating the ageing in constant electrolysis mode and the oxygen electrode dominating that in cyclic mode. During dynamic cycling, the SOCs aged less at 800 °C than at 700 °C. It was observed that for cycles with equal durations in SOEC and SOFC modes whereby the cycle lengths were less than or equal to 2 x 5 h the voltage ageing was almost symmetrical for both SOFC and SOEC modes. For longer cycle lengths SOEC mode voltage ageing was at least double the SOFC mode voltage ageing. This result is consistent with suggestions in literature that intermittent operation of SOCs in fuel cell mode slows down or even reverses SOC ageing that occurs during long-term electrolysis operation. Based on the finding that the fuel electrode dominated the ageing under constant electrolysis operation, it was speculated based on literature, to be caused by precipitation of nickel oxide that had diffused into the 8YSZ matrix of the fuel electrode during sintering. Constant electrolysis operation provided enhanced conditions for the precipitation of the nickel oxide as metallic nickel. Furthermore, Zr, Ni, Y, and O containing nano-particles were found on the Ni particles. In literature during electrolysis of H_2O/CO_2 under same conditions of temperature and current density nano particles were also found on Ni particles, identified as ZrO_2 and attributed the major cause of fuel electrode ageing. In cyclic operation these enhancing conditions were not maintained long-enough for severe nickel precipitation. It is known and was verified that the LSC/CGO electrode is better performing than the LSCF electrode. To compare the stability of these two state-of-the-art (s.t.a.) oxygen electrodes, 1000 h tests under non-polarized or open circuit voltage (OCV) conditions were carried out using symmetric cell geometry. Both electrodes displayed a two-step ageing trend with rapid initial ageing within the first 400 h followed by

relaxation to slower ageing rates. The LSCF electrode showed a larger increase in polarization resistance especially within the first 400 h in which it aged by factor 6 faster than the LSC/CGO electrode. The rapid ageing of the LSCF electrode within the first 300 – 400 h of operation has also been reported in literature.

Resumé (Danish Abstract)

Fastoxid brændselsceller (SOFC) omdanner brint, kulmonoxid og kulbrinteholdige brændstoffer (direkte) til elektricitet med meget høje virkningsgrader og har demonstreret næsten tilsvarende resultater, når de drives i omvendt tilstand, som en fast oxid elektrolysecelle (SOEC). I dette tilfælde lagres elektrisk (og termiske) energi som kemisk energi i reaktionsprodukterne. Til dette formål tilsættes cellerne med damp (H_2O elektrolyse), kuldioxid (CO_2 elektrolyse) eller en blanding af begge dele (H_2O / CO_2 co-elektrolyse) og selvfølgelig elektrisk (ΔG) og termiske (TΔS) energier for opdelingen af reaktantforbindelserne. Brint, kulmonoxid eller begge (syntesegas) produceres på brændselselektroden imens ilt produceres på oxygen elektroden. I reversibel eller cyklisk tilstand drives fastoxid cellen skiftevis som brændselscelle eller elektrolysecelle afhængigt af behovene hos slutbrugeren.

Ved polarisering af fastoxid celler (SOC) og uafhængig af polariserings tilstanden (brændselscelle- eller elektrolysetilstand), er den strøm, der løber gennem cellen begrænset ved processer, såsom adsorption og desorption af reaktanter eller produkter, diffusion gennem de porøse elektroder, aktivering eller ladningsoverførslen ved reaktionsbetingelserne steder, gasomddannelse ved reaktionsbetingelserne tilstede og flow felter og Ohmske spændingsfald på tværs af elektrolytten. Disse processer forekommer i begge elektroder og ofte overlapper deres karakteristiske frekvenser hinanden, hvilket gør karakterisering af en given mekanisme specielt udfordrende. For at optimere SOC'ne til drift i forskellige brændsler, drift temperaturer og driftstilstande, er det vigtigt at forstå kinetikken af SOC elektroderne. Denne afhandling fokuserer på at forstå kinetikken af SOC under forskellige driftsforhold som temperatur, polarisering og brændstofblanding. Ved undersøgelserne på helceller er elektrokemisk impedans spektroskopi og distribution af relaksationstid, teknikker som blev brugt til at undersøge kinetikken af Ni/YSZ brændstofelektroden i tre brændstofblandinger - brint / damp og reformatbrændselssammensætningerne brint/kuldioxid og brint/metan/damp. Det konstateredes, at kinetikken ved brændselselektroden var helt ens i begge reformatbrændselssammensætniger. Dette betyder at de kemiske ligevægtsreaktioner var meget hurtigere end de elektrokemiske reaktioner. Elektroden viste en smule hurtigere kinetik ved brint/damp som brændsel end i reformatetbrændselssammensætningerne.

For at minimere indflydelsen af (i) Joule-opvarmnings effekten som følge af strøm på tværs af elektrolytten, (ii) koncentrationsrelaterede effekter som gasdiffusion, og (iii) overlapning af de karakteristiske frekvenser af processer, blev undersøgelserne udvidet fra helcelle geometrier til en ny pseudo-treelektrode cellegeometri med aktive elektrodearealer på ca. 1 mm^2 der gjorde det muligt at isolere undersøgelserne af brændsels og ilt elektroderne. I en 50/50 H_2/H_2O brændselsblanding, blev på en Ni/8 mol% yttriumstabiliseret zirconia (Ni/YSZ) brændselselektrode påvist langsommere reaktionskinetik under katodisk polarisering end anodisk polarisering-samme fund er tidligere blevet rapporteret i litteraturen fra undersøgelser på helceller hvorved sammen med den lokale pH_2O, substratdiffusion (specifikt Knudsen diffusion) blev identificeret som en af årsagerne til asymmetrien mellem anodisk og katodisk polarisering. De opnåede aktivitetskoefficienter for ladningsoverførslen er i overensstemmelse med hvad der tidligere er rapporteret i litteraturen, og deres ændring i forhold til temperaturen var ligeledes den samme som rapporteret i litteraturen for porøse Ni / YSZ brændselselektroder. Ud fra de to undersøgte iltelektroder, blev det fundet at den bedst ydende

$(La_{0.6}Sr_{0.4})_{0.99}CoO_3/Ce_{0.9}Gd_{0.1}O_{1.95}$ (LSC / CGO) oxygen elektrode udviste langsommere reaktionskinetik under katodisk påvirkning ved 50 mV end i anodisk tilstand. Denne trend var modsat for $La_{0.58}Sr_{0.4}Co_{0.2}Fe_{0.8}O_3$ (LSCF) iltelektroden. Ved faldende oxygenpartialtryk udviste begge elektroder stigende asymmetri mellem anodiske og katodiske påvirkning. Det kunne påvises, at overfladens udvekslingskinetik var den væsentligste forskel til den mindskede kinetik med faldende pO_2, og at kinetikken ved katodisk strømpåvirkning blev sænket væsentligt mere end ved anodisk strømpåvirkning, og dermed øgede asymmetrien.

Uanset af driftsmåden, kræver kommercialiseringen af SOC teknologien en garanti for lang levetid samt forudsigelighed for cellernes ydeevne under de ønskede driftsbetingelser.

Ydeevnen bestemmes normalt gennem strøm/spændingskurver (C/V). Som sådan kan en afvigelse fra den forventede ydeevnekurve bruges til at identificere tilstedeværelsen af ældning eller en ældningsproces. En 0-D stationær model er tidligere blevet udviklet på *Institut für Angewandte Materialien - Werkstoffe der Elektrotechnik* (IAM-WET) i Tyskland til at forudsige C/V kurven for en SOC i brændselscelle tilstand. I denne afhandling blev anvendeligheden af denne model undersøgt ved SOC i elektrolyse tilstand, Modellen blev udvidet til at rumme temperaturændringer under polarisering i brændselscelle- og elektrolysetilstand, samt yderligere udvidet til at omfatte reformatbrændsler H_2/H_2O: CO: CO_2. Sidstnævnte blev udført ved at indføre et nyt koncentrationsafhængigt overspændingsbidrag i modellen, for at tage højde for CO/CO_2 diffusion til reaktionsstederne som følge af vand-gas-skift-ligevægtsreaktionen.

Stabiliteten af cellerne på længere sigt afhænger af om systemet udelukkende drives i brændselscelle-, elektrolyse-, reversibel eller dynamisk tilstand. Optimering af celler for at øge ydeevnen og/eller holdbarhed i hver af disse driftstilstande kræver en grundig forståelse af de processer og mekanismer der påvirker kinetikken og ældningsprocessen specifikt under hver af disse driftstilstande. I fem forsøg af varigheder mellem 1000 og 2500 timer, blev den langsigtede stabilitet af SOC'ne undersøgt under konstant elektrolyse, cyklisk og dynamiske driftstilstand i et symmetrisk binært brændsel, 50/50 H_2/H_2O, ved 800 og 700 °C. SOC'ne der blev testet under konstant elektrolysetilstand ældedes hurtigere end dem undersøgt under cyklisk driftstilstand, hvor brændselselektroden dominerede ældningen ved konstant elektrolysetilstand og iltelektroden dominerede ældningen i cyklisk driftstilstand. Ved dynamisk cykling ældedes SOC'ne mindre ved 800 °C end ved 700 °C. Det blev observeret at, ved cykler med ens varighed i SOEC og SOFC tilstand, hvor cykluslængderne var mindre end eller lig med 2 x 5 timer, blev spændingsældningen næsten symmetrisk ved både SOFC og SOEC tilstandene. Ved længere cykluslængder i SOEC tilstand ældedes spændingen mindst dobbelt så meget som i SOFC tilstanden. Dette resultat er i overensstemmelse med litteraturen, at periodisk drift af SOCs i brændselscelletilstand bremser eller endda modvirker SOC ældningen, der opstår under langvarig elektrolyse drift. Da det blev vist at brændselselektroden dominerer ældningen under konstant elektrolysetilstand, blev det på baggrund af litteratur spekuleret på om det kunne være forårsaget af udfældning af nikkeloxid, der kunne være diffunderet ind i 8YSZ matrix af brændselselektroden under sinteringsprocessen. Tests under konstant elektrolysedrift øgede betingelserne for udfældning af nikkeloxid som metallisk nikkel. Endvidere blev Zr, Ni, Y, og O nanopartikler fundet på Ni partiklerne. I litteraturen, blev der ved elektrolyse af H_2O/CO_2 under samme temperatur og strømtæthed også fundet nanopartikler på Ni-partikler, der er identificeret som ZrO_2 og tilskrevet den væsentligste årsag til brændselselektrodens ældning. Ved cyklisk driftstilstand opretholdes disse forhold ikke

længe nok til væsentligt at øge nikkeludfældningen. Det er kendt, og blev bekræftet, at LSC/CGO elektroden er bedre end den LSCF elektroden. For at sammenligne stabiliteten af disse to topmoderne iltelektroder, blev der udført test i 1000 timer under ikke-polariseret eller tomgangsspændings (OCV) betingelser ved hjælp af celler i symmetrisk celle geometri. Begge elektroder påviste en to-trins ældningstendens; med en hurtig opstartsældning inden for de første 400 timer, efterfulgt af en langsommere ældningshastighed. LSCF elektroden påviste en større stigning i polarisationsmodstanden inden for de første 400 timer, hvor ældningen var en faktor 6 gange hurtigere end for LSC/CGO elektroden. Den hurtige ældning af LSCF elektrode inden for de første 300-400 timers drift er også rapporteret i litteraturen.

Preface

This thesis is submitted to the Technical University of Denmark (DTU) in partial fulfillment for the requirements of the PhD degree. The work presented in this thesis is a product of four years and three months of research work on solid oxide cells. Two years and four months of the work was carried out at the Karlsruhe Institute of Technology (KIT) at the *Institut für Angewandte Materialien-Werkstoffe der Elektrotechnik (IAM-WET)* formerly *Institut für Werkstoffe der Electrotechnik (IWE)*. The remaining two years were carried out at the Department of Energy Conversion and Storage (DTU Energy) at DTU.

The investigations at KIT were in close collaboration with Forschungszentrum Jülich (FZJ) that generously provided the investigated SOFC single cells and is gratefully acknowledged. The cells investigated at DTU were in-house developed. The cell development team, technical and laboratory staff is gratefully acknowledged.

Financial support from Energinet.dk through the ForskEL programmes “Solid Oxide Fuel Cells for the Renewable Energy Transition” contract no 2014-1-12231 and “Towards Smart Grid Ready SOFC" contract no 2012-1-10747 is gratefully acknowledged.

Jean-Claude Njodzefon

Roskilde, 21st December 2015

Acknowledgement

This thesis is a result of research activities on the one hand at the *Institut für Angewandte Materialien-Werkstoffe der Elektrotechnik* (IAM-WET) of the Karlsruhe Institute of Technology (KIT) in Germany and on the other hand at the Applied Electrochemistry (AEC) section of the Department of Energy Conversion and Storage (DTU Energy) of the Technical University of Denmark (DTU). I wish to express my utmost gratitude to the head of IAM-WET Prof. Dr.-Ing. Ellen Ivers-Tiffée and head of AEC Prof. Dr. rer. nat. Anke Hagen for offering me the possibility to carry out the research work at their respective research institutions and above all for overseeing and guiding my development as a researcher within the framework of my PhD.

To my supervisor Johan Hjelm, PhD and co-supervisor Chris Graves, PhD I would like to express my gratitude for taking up supervision of my thesis at DTU. While I enjoyed the admiration of fellow PhD colleagues for having the two best supervisors possible, I enjoyed our work together even more. Thank you Chris and Johan for giving me everything I needed to express myself and for patiently walking me across the line.

Dr.-Ing. André Weber has walked every mile of my PhD thesis with me guiding my every step and with Chris, co-supervised my thesis. It has been an unbelievable experience to learn from you every day of my PhD program. Like my numerous questions, you dwarfed the most challenging moments of my PhD to routine challenges. Thank you André!

I would also like to express huge gratitude towards Dr.-Ing. Andre Leonide not only for guiding and mentoring me before and at the beginning of my thesis but above all for the friends we have become.

I would like to thank all of my former colleagues for the interesting discussions, amazing moments at and after work, the very interesting and crazy moments during our conference travels. While I certainly am not doing justice to all the great colleagues I had in these past years, I would like to specially acknowledge Prof. Mogens Mogensen, Prof. Peter Vang, Jimmi Nielsen, Anne Hauch, Søren Højgaard Jensen, Dino Klotz, Heidi Adler Berggren, Martin Nielsen, Andrea Schäfer, Bhaskar Reddy Sudireddy, Annika Utz, Sune Velzé, Christian Gabi, Henrik Henriksen for those very many moments when I felt you were God-sent!. Even here, I would like to acknowledge Sune V. once more for translating the abstract of this thesis to Danish.

To my former students who in their respective theses helped me tackle some of the tasks in this thesis; Julianne Stahl, Carolina Ksellmann, Bernhard Schwarz, Mina Krompic and Alexandra Lenis, it was an honor to grow together in this field. I enjoyed every moment of our work together.

My friends Johannes Fink, Stefan Nelles, Florian Winger, Mathieu Bescond, Roberto Scipioni, Anar Salenge, Regina Bulatova, Rasmus Mosbæk, Gregory Johnson, Wulliam Tchoumy, Terence Afube, Valery Nkemngu, Jochen Joos, Simona Ovtar, Julia Sinner, Keneth Muabeze, Jörg Illig, Tesfaye Tadesse, Daniel Manka and those I have left out, thank you for being the great friends you are.

I would also like to acknowledge my secondary and high school teachers and mentors, with particular thanks to Mr. Njie Tecku, Mr. Ajong, Mr. Nwanakang and Mr. El Ngokwe for laying the very solid foundations on which I have stood to come this far.

Finally I would like to thank my beloved family for all your prayers and encouragements. You all ached when I ached and smiled when I was smiling. You are all the reason I have made it. Jytte, and Christian, I would not be in Europe were it not for you. Christian, you made sure I kept on going to the end. Larry, I had to hear your voice to keep keeping on. Granny I know you have prayed for me every single day and Esther, I know I have been in your prayers throughout. To my little ones, Roberto, Kila, Eli, Junior, Berence, Mildred, Louis, Kerka, Kinyuy; thanks for making me the poorest PhD student alive. Ngeng Marxcel you are more than a brother, thanks for the motivation. To my better half Stella, I say, you are a gift from heaven and a big thank you to your parents and family for the prayers. I was lucky to have you around during the trickiest times of this project. Finally, to my beloved mom; thank you for everything I am and the person I have become mom. Let me take care of you now. And to my late grandfathers, Pa Langai Vincent and Tata wo Kikai; May your souls rest in peace. It is a shame time has not let you see me finish this whole school business! You know I wanted to take you both to “my white man´s country” to see for yourselves. May your souls rest in peace.

Table of Contents

Chapter 1 Introduction

The solid oxide fuel cell[1] (SOFC) that generally converts hydrogen, hydrocarbons as well as reformate fuels directly into electricity with very high efficiencies can potentially be, and is increasingly being operated in reverse mode as a solid oxide electrolysis cell (SOEC). In this case electrical (and thermal) energy is "stored" as chemical energy of reaction products. To this end, the cells are fed with steam (steam electrolysis), carbon dioxide (Carbon dioxide electrolysis) or a mixture of both (H_2O/CO_2 co-electrolysis) and of course electrical (ΔG) and thermal ($T\Delta S$) energies for the splitting of reactant compounds. Hydrogen, Carbon monoxide or both (Synthesis gas) are released as products at the fuel electrode respectively meanwhile oxygen is released at the oxygen electrode. In reversible or cyclic mode the solid oxide cell is operated interchangeably as fuel cell or electrolysis cell depending on the needs of the end user. By varying the durations of the different modes in cyclic operation the systems are operated in dynamic mode.

Thus the robustness and longevity of the system depends on whether the system is operated solely in fuel cell mode, electrolysis mode or in reversible mode. Optimization of the system for each of these operation modes demands a thorough understanding of the processes and mechanisms affecting the kinetics and ageing of the systems. Independent of operation mode, eventual commercialization of the technology requires not only a guarantee of longevity but also predictability of the SOC performance under given operation conditions. Deviation from the expected/predicted performance curve can thus serve to identify the presence of ageing or an ageing enhancing process.

1.1 Goals

This thesis was aimed at understanding the kinetics of the SOC under different operation conditions of temperature and fuel mixture. To that end cells with different geometries including full cells, symmetric cells and pseudo-three electrode cells with surface areas from 16 cm^2 down to ca. 1 mm^2 respectively will be investigated.

The performance of the SOC is generally evaluated through the current/voltage (C/V) curve. A 0-D stationary model has been developed[2–4] at the *Institut für Angewandte Materialien - Werkstoffe der Elektrotechnik (IAM-WET)* at KIT in Germany with which the C/V curve of a SOC can be predicted for fuel cell operation mode. It was aimed in this work to verify the applicability of this model for electrolysis mode operation. Furthermore, the model was extended to cover operation in reformate fuels or H_2O/CO_2 co-electrolysis operation.

Finally, in tests with varying durations between 1000 h and 2500 h the longevity or long-term stability of the SOCs will be investigated for OCV, constant electrolysis, cyclic and dynamic operation modes.

1.2 Outline

Chapter 2 will describe the fundamentals related to the solid oxide cell, employed electrochemical techniques and analysis required to understand the manuscript.

In Chapter 3 AC and DC techniques will be applied to investigate the electrochemical reaction kinetics of SOCs and the porous SOC electrodes on different cell geometries. The main tools will involve electrochemical impedance spectroscopy, DRT and CNLS fit analysis.

In Chapter 4 the 0-D stationary model predicting the current / voltage (C/V) characteristic of a SOC in both SOFC and SOEC modes will be discussed. This will include operation in H_2/H_2O, CO/CO_2 and H_2O/CO_2 co-electrolysis modes.

Chapter 5 will discuss the long-term stability of the solid oxide cell under constant electrolysis, cyclic, dynamic and open circuit operation modes.

Finally, a summary of findings and conclusions will be given in Chapter 6.

A list of published articles, conference contributions and supervised student theses within the framework of and during the period of this thesis are given towards the end of the manuscript.

Chapter 2 Fundamentals of the Solid Oxide Cell Technology

2.1 Introduction

In this section the working principle of the solid oxide cell (SOC) will be explained. A brief summary of the major electrochemical techniques employed in this thesis will be given. These include the current/voltage (C/V) characteristic and electrochemical impedance spectroscopy (EIS).

Further analysis of recorded impedance spectra involved the use of distribution of relaxation times[5,6] (DRT) to identify/pre-identify dynamic processes and their evolutions with varying operation conditions. The DRT also facilitated the determination of starting values for complex non-linear least squares (CNLS) fits with equivalent circuit models (ECM). Prior to these fits the quality of recorded spectra was investigated by checking the compliance with Kramers Kronig (KK) transforms. The basics of DRT and KK-transforms will also be discussed in this section.

2.2 Solid Oxide Cell Component Materials

The solid oxide cell is composed of three major components; two porous electrodes—the fuel and oxygen electrodes separated by an oxygen ion conducting and gas-tight electrolyte.

The electrolyte is required to (i) be gas-tight so that oxidant gas and fuel do not mix as this will reduce the cell voltage (ii) have a high oxygen ion conductivity to facilitate transport of oxygen ions between the electrodes (iii) have a low but non zero electronic conductivity—a high electronic conductivity will internally short-circuit the SOC and the non-zero electronic conductivity protects the electrolyte (and thus the cell)[7,8] from damage (reduction) during high SOEC currents (generally unintentional) with insufficient reducible gas e.g. H_2O or CO_2, (iv) be chemically stable both in the oxidizing atmosphere of the oxygen electrode gas chamber but also stable in the reducing conditions present in the fuel electrode gas compartment and (v) be mechanically stable especially in electrolyte supported SOCs. The standard SOC electrolyte material is 8 mol % yttria-stabilized zirconia (Y_2O_3 - ZrO_2), 8YSZ. However 6 – 11 mol % scandia-stabilized zirconia (Sc_2O_3 - ZrO_2)[9,10] have also been used e.g. 10ScYSZ.

The fuel electrode is required to have a high catalytic activity for the oxidation of the fuel. In SOEC mode a high catalytic activity for the reduction of steam or CO_2 is also required. A high electronic conductivity is required to supply electrons to and from the reactions sites. A high ionic conductivity is also required to extend the electrochemical reactions sites from the electrolyte / electrode interface towards and into the fuel electrode i.e. increase the penetration depth of the electrochemical reactions and thus the performance. The fuel electrode material should be porous enough so that the fuel can get to the reaction sites. It´s thermal expansion coefficient

(TEC) should match that of the electrolyte. Finally, the fuel electrode should be stable in the very reducing atmosphere under fuel cell mode operation but also during the increased oxidizing atmosphere during electrolysis operation mode. The common fuel electrode of state-of-the-art SOCs is a composite between metallic nickel (Ni) and oxygen ion conducting YSZ (i.e. Ni/YSZ) or 10ScYSZ (i.e. Ni/10ScYSZ). This composite is generally called cermet, i.e. ceramic metal. However CGO or Nb- doped $SrTiO_3$ infiltrated with CGO nanoparticle are gaining importance for SOCs operated in CO/CO_2 mixtures[11]

Similar requirements with respect to porosity, electronic and ionic conductivities and TEC match to electrolyte are valid for the oxygen electrode as well. It is required to have a high catalytic activity for the redox reactions occurring there. Stability under the predominantly oxidizing atmosphere is prerequisite. However, it should also be stable under the increasingly reducing atmosphere present during SOEC operation. The oxygen[i] electrodes generally are made of single phase mixed ionic and electronic conducting (MIEC) materials such as strontium-doped lanthanum manganite (LSM) e.g. $La_{0.75}Sr_{0.2}MnO_3$, lanthanum strontium cobaltite ferrite (LSCF) e.g. $La_{0.58}Sr_{0.4}Co_{0.2}Fe_{0.8}O_3$, strontium-doped lanthanum cobaltite (LSC) e.g. $(La_{0.6}Sr_{0.4})_{0.99}CoO_3$, two phase composites strontium-doped lanthanum cobaltite / gadolinia-doped ceria (LSC/CGO) e.g. $(La_{0.6}Sr_{0.4})_{0.99}CoO_3/Ce_{0.9}Gd_{0.1}O_{1.95}$ and LSM/YSZ. Due to the comparably low ionic conductivities of LSM and LSC the inclusion of better ionic conducting YSZ or CGO improves the ionic conductivity of the electrode and like the fuel electrode composite these composites increase the electrochemically active surface area and increase the penetration depth of the electrochemical reactions.

2.3 Working Principle of a Solid Oxide Cell

The working principle of the SOC is illustrated for operation with H_2 (or H_2O) as fuel and oxygen as oxidant gas at the oxygen electrode.

When operating in fuel cell mode (SOFC mode), oxygen is reduced at the oxygen electrode to produce O^{2-} ions which are then incorporated into the electrolyte according to the forward half reaction in reaction (2-1).

$$\frac{1}{2}O_2(g) + 2e^-(oxygen\ electrode) \leftrightarrow O^{2-}(electrolyte) \qquad (2\text{-}1)$$

[i] The oxygen electrode is generally supplied with either pure oxygen or air. As such in this work, ”air electrode” and ”oxygen electrode ” will be interchangeably used.

At the fuel electrode the fuel, H_2 is oxidized to steam according to the forward half reaction (2-2) releasing two electrons per molecule of H_2O formed.

$$O^{2-}(electrolyte) + H_2(g) \leftrightarrow H_2O(g) + 2e^- \ (fuel\ electrode) \qquad (2\text{-}2)$$

The overall reaction is given by reaction (2-3)

$$\frac{1}{2}O_2(g) + H_2(g) \leftrightarrow H_2O(g) \qquad (2\text{-}3)$$

When the SOC is operated in electrolysis mode (SOEC mode), the backward half reactions occur at the electrode whereby oxide ions are oxidized at the oxygen electrode and steam is reduced at the fuel electrode. These reactions have been illustrated in Figure 2.3-1 for both SOFC and SOEC modes (black and red arrows respectively) for a SOC with single phase LSCF oxygen electrode, Ni/YSZ cermet fuel electrode and 8YSZ electrolyte.

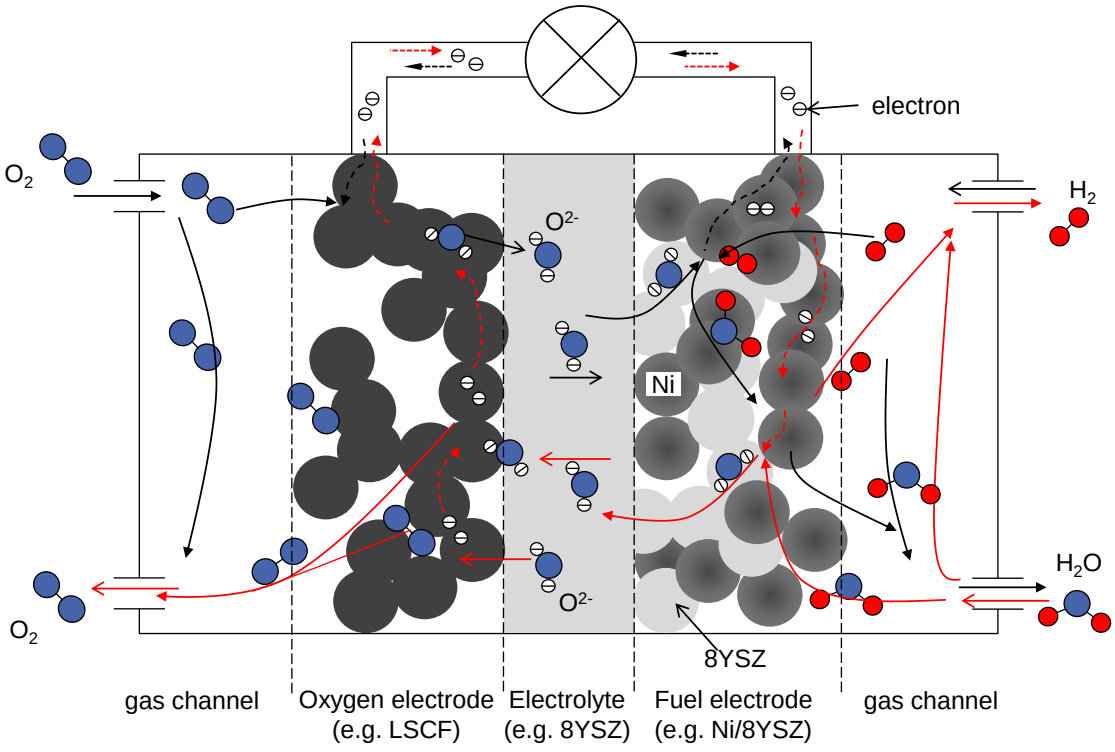

Figure 2.3-1: Working principle of the solid oxide cell illustrated for fuel cell operation (black arrows) and electrolysis mode operation (red arrows)

2.4 Basic Electrochemical Characterization Techniques

From the large pool of electrochemical techniques available in literature with which the SOC can be characterized only those employed in this thesis will be briefly discussed.

2.4.1 Current / Voltage Characteristic

Under OCV conditions, and assuming no internal electronic or gas leaks across the electrolyte the cell voltage (theoretical) is given by the oxygen partial pressures at the electrodes through the Nernst equation (1)

$$U_N(T) = \frac{RT}{nF} \ln \left(\frac{\sqrt{pO_{2,\,oxygen\ electrode}}}{\sqrt{pO_{2,\,fuel\ electrode}}} \right) \tag{1}$$

but can also be calculated[2,12] through the Gibbs free energy of reaction $\Delta G(T)$ (cf. equation (2))

$$U_N(T) = \frac{\Delta G(T)}{nF} \tag{2}$$

through which temperature and fuel electrode gas partial pressures $p\mathrm{H_2}$ and $p\mathrm{H_2O}$ can be accommodated according to equation (3).

$$\Delta G(T) = \Delta G_0(T) - RTln \left(\frac{pH_2O_{fuel\ electrode}}{\sqrt{pO_{2,\,oxygen\ electrode}}\, pH_{2,\,fuel\ electrode}} \right) \tag{3}$$

Equation (2) is thus becomes:

$$U_N(T) = \frac{\Delta G_0(T)}{nF} - \frac{RT}{nF} ln\left(\frac{pH_2O_{fuel\ electrode}}{\sqrt{pO_{2,\ oxygen\ electrode}}\ pH_{2,\ fuel\ electrode}}\right) \quad (4)$$

In equations (1) - (4) R, T, n and F represent the universal gas constant, the absolute temperature, number of electrons involved and Faraday constant respectively. pX_i represents the partial pressure of gas X at electrode i and ΔG_0 is the temperature dependent standard free energy of reaction.

In real systems though, the measured cell voltage under OCV conditions is lower than the ideal theoretical $U_N(T)$ because[12]: (i) the electrolyte may not be totally gas tight allowing the gas components of both electrode to mix and react (ii) a non-zero electronic conductivity of the electrolyte allowing flow of electrodes through the electrolyte (iii) products and educts of electrode half reactions are not in thermodynamic equilibrium because of low catalytic activities at the electrode—leads to slow buildup of the voltage (iv) the internal -resistance of the measurement equipment is in the same order of magnitude as that of the cell.

Polarization of a SOC such that the oxygen electrode is more negative than it is at OCV and the fuel electrode more positive than it is at OCV changes the equilibrium of the gases at the electrodes such that the forward reaction of reaction (2-1) occurs at the oxygen electrode and the forward reaction of (2-2) occurs at the fuel electrode. Thereby oxygen molecules are reduced at the oxygen electrode and hydrogen molecules oxidized at the fuel electrode. As current flows, the cell voltage drops from the OCV value due to activation and mass transport losses at the electrodes and ohmic/joule losses mainly across the electrolyte. The SOC is operating in fuel cell mode or being *discharged*. The evolution of the cell voltage under load and the involved performance limiting processes are discussed in detail in sections 3.3.1.4 and 4.2.1.

If the SOC is so polarized such that the fuel electrode is more negative than at OCV, steam will be reduced at the fuel electrode. The formed oxide ions will be transported across the electrolyte where their electrons will be accepted by the oxygen electrode that due to polarization is more positive than at OCV, thus releasing oxygen. The backward reaction in reactions (2-1) and (2-2) are taking place. Similar to the fuel electrode mass transport and electrochemical losses as well as those due to electron and oxide ion transport will occur. Thus to drive the required electrolysis current through the cell, the required cell voltage must be large enough to cover the voltage losses associated with these loss mechanisms as well. The SOC is thereby operated in electrolysis or reverse mode and is being *charged*.

A C/V curve of a SOC is displayed[13] in Figure 2.4-1 showing the evolution of the cell voltage with current density for both SOEC and SOFC operation modes. Along with the curve a schematic of the cross-section of the SOC

displaying the distribution of the oxygen and electrical activities[ii] across the cell under SOEC, OCV and SOFC operation modes is also given.

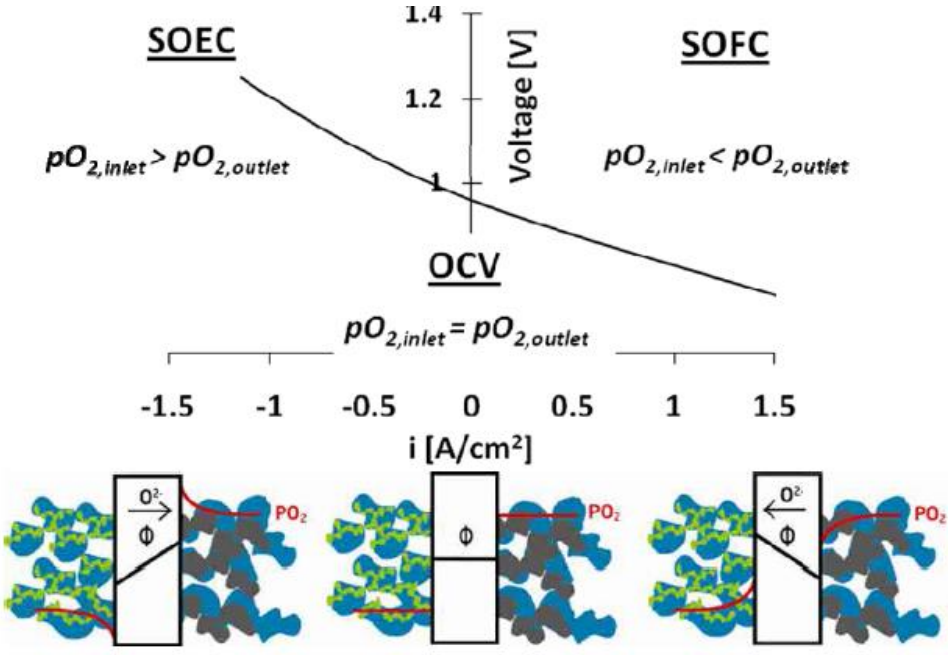

Figure 2.4-1: C / V and SOC cross-section schematic showing the electrical and oxygen activity gradients in SOEC, OCV and SOFC modes. The oxygen electrode oxygen partial pressures at the inlet and outlet are also indicated. The C/V curve is recorded at 850 °C in a 50/50 H_2/H_2O as fuel and air as oxidant supplied to the oxygen electrode[14]. In the cross-section schematics the fuel electrode is on the left and the oxygen electrode on the right of the electrolyte (center)

2.4.2 Electrochemical Impedance Spectroscopy

2.4.2.1 Concept

The concept of electrochemical impedance spectroscopy (EIS) is simple and straightforward; a direct current bias (I_{load}) through the sample or system under investigation is superimposed with a sinusoidal signal $i(t) = i_0 \sin(\omega t)$ of small (and adequate) amplitude i_0, the corresponding sinusoidal voltage response $u(t) = u_0(\omega)\sin(\omega t + \varphi(\omega))$ is recorded and the complex impedance $\underline{Z}(\omega)$ calculated as ratio of both complex signals[2] (cf. equation (5)). A simple experimental set-up for EIS measurement is displayed in Figure

[ii] The chemical and electrical activity gradients represent the oxygen partial pressure and electrical potential. These sum up to give the electrochemical potential.

2.4-2 (a) and the corresponding C/V curve in Figure 2.4-2 (b). EIS recorded in this manner whereby the excitation signal is the current and the measured/recorded response is voltage is called *galvanostatic* EIS or current controlled EIS and is more suited for investigating samples with very small impedances[15]. The excitation signal or perturbation can also be the voltage and the measured response is the current. In this case the impedance is *potentiostatic* in nature (or voltage controlled) and is more suitable for samples with high resistances as unsuitably high currents are avoided at high impedances[15,16]. In either case, the application of a small amplitude signal to the system at equilibrium or non-equilibrium steady state causes a perturbation of the system without disturbing the equilibrium or steady state[17].

$$\underline{Z}(\omega) = \frac{\underline{u}(t)}{\underline{i}(t)} = \frac{u_0(\omega)}{i_0} e^{j\varphi(\omega)} = \left|\underline{Z}(\omega)\right| e^{j\varphi(\omega)} = Re\{\underline{Z}(\omega)\} + jIm\{\underline{Z}(\omega)\} \qquad (5)$$

In equation (5) $\omega = 2\pi f\ [s^{-1}]$ is the angular frequency and $\varphi(\omega)$ is the frequency dependent phase shift between voltage and current.

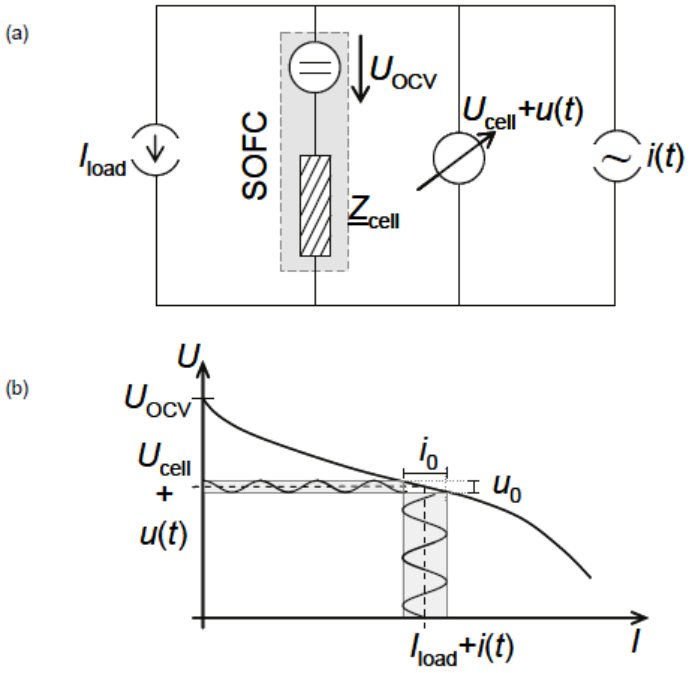

Figure 2.4-2: (a) Basic experimental set-up for the impedance measurement of a real SOFC with internal resistance $\underline{Z}_{cell}$ and (b) corresponding U / I (or C / V) curve.[2]

Since dynamic processes in an electrochemical system have different characteristic or relaxation times, the recording of an impedance *spectrum* is commonly done for discrete number of frequencies in a frequency range e.g. 1 MHz – 100 mHz for an SOC. The processes with very short relaxation times will thereby be triggered at high frequencies while slower processes with longer relaxation or characteristic times are triggered at low frequencies. The results are displayed in a *Nyquist-plot* in the complex plane (cf. Figure 2.4-3 (a)).

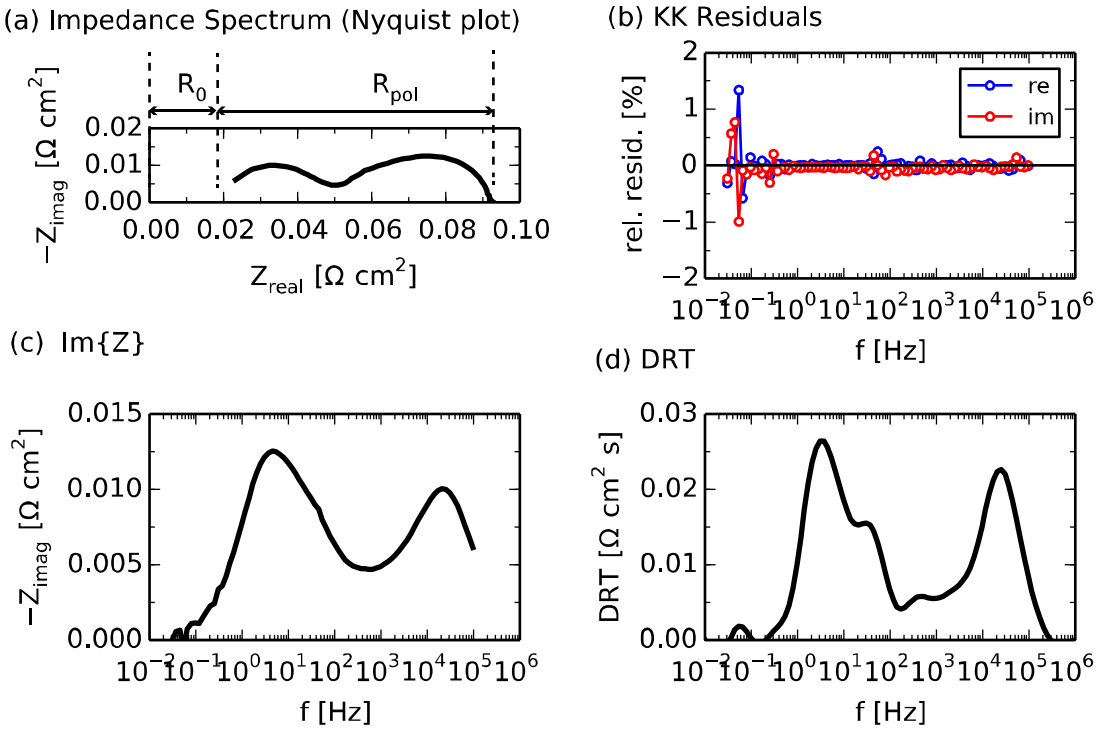

Figure 2.4-3: (a) Impedance Spectrum displayed in a Nyquist plot (b) KK-test residuals of the EIS spectrum (c) Imaginary part of the EIS spectrum (d) DRT of EIS Spectrum

For an impedance spectrum of a system to be valid the investigated system has to satisfy the conditions of linearity, time invariance, causality and finiteness[16]. The linearity condition requires that the system is linear within the excitation amplitude or measured in a linear regime. The causality condition requires that the measured response is exclusively caused by the excitation. Time invariance means system does not change its electrochemical properties during the period the spectrum is being recorded. Finiteness means the impedance must have finite values for $\omega \rightarrow 0$ and $\omega \rightarrow \infty$. These conditions have been further discussed in reference [16,18] meanwhile reference [16] is also recommended for discussion on how to choose the adequate excitation amplitude.

2.4.2.2 Data Quality Control

The quality of the recorded spectrum can be verified by checking the compliance with Kramers-Kronig (KK) transforms[19,20]. They allow one to calculate the real part of a complex function from the imaginary part and the imaginary part from the real part only[18]. To satisfy the KK-relations the cell (or system) has to fulfill the four criteria cited in section 2.4.2.1 above (i.e. linearity, causality, time invariance and finiteness).

Thus by using one of the two component parts of the spectrum (e.g. the real part component, $Re\{\underline{Z}\}_{measured}$), the other component ($Im\{\underline{Z}\}_{KK-calculated}$) can be calculated and then compared with its measured equivalent ($Im\{\underline{Z}\}_{measured}$). The data is of good quality if the error or residuals are small e.g. less than 0.5 %. In Figure 2.4-3 (b) the quality of an impedance spectrum (cf. Figure 2.4-3 a) has been verified for KK-transforms compliance. As can be seen, the data is of good quality for $f > 0.1$ Hz as both real and imaginary part residuals lie well within $\pm$ 0.25 % in the investigated frequency range. Furthermore, the residuals are randomly distributed around the zero line. A systematic distribution would indicate (i) a serious violation of the criteria for the KK-relations or (ii) that the number or RC-circuit elements n chosen was too small[16].

2.4.2.3 Distribution of Relaxation Times (DRT)

The DRT[5] is a non-parametric technique employed for further evaluation of recorded impedance spectra. It is adequate for system screening since no *a priori* knowledge of the system is required and no a priori assumptions about the system in terms of equivalent circuit models (cf. section 2.4.2.4) are made[5]. It offers a better deconvolution of dynamic processes than the Nyquist plot or its imaginary part representation by revealing the characteristic frequencies of dynamic processes (cf. Figure 2.4-3 (a) and (c) vs. (d)).

The concept of DRT is based on the fact that every impedance function that obeys the Kramers-Kronig relations can be represented as a differential sum of infinitesimal small RC-elements[2,5] in series. These elements have relaxation times ranging continuously from 0 to ∞[2]. In the following paragraphs the major steps and assumptions employed in calculating the DRT taken from references [2,5,16] are given.

The recorded spectrum $\underline{Z}(\omega)$ can be written according to equation (6) where R_0 is frequency-independent series resistance or ohmic part of the spectrum and $\underline{Z}_{pol}(\omega)$ the frequency dependent (polarization) part of the spectrum.

$$\underline{Z}(\omega) = R_0 + \underline{Z}_{pol}(\omega) = R_0 + Re\left\{\underline{Z}_{pol}(\omega)\right\} + jIm\left\{\underline{Z}_{pol}(\omega)\right\} \quad (6)$$

Considering a serial connection of RC-elements (cf. Figure 2.4-4), with $R_{pol,n} = \gamma_n \cdot R_{pol}$ the real part resistance and τ_n the relaxation time of the n^{th} RC-element and R_{pol} the total polarization resistance of the circuit equation (7) holds:

$$\underline{Z}_{pol}(\omega) = \sum_{n=1}^{N} \frac{R_{pol,n}}{1 + j\omega\tau_n} = R_{pol} \sum_{n=1}^{N} \frac{\gamma_n}{1 + j\omega\tau_n} \quad (7)$$

with

$$\sum_{n=1}^{N} \gamma_n = 1 \quad (8)$$

Whereby $\omega = 2\pi f$ represents the angular frequency, N the number of RC-elements, j the imaginary unit and γ_n weighing the contribution of the n^{th} dynamic process to the total polarization resistance[2].

Assuming an infinite number of RC-elements equation (7) becomes:

$$\underline{Z}_{pol}(\omega) = R_{pol} \int_0^{\infty} \frac{\gamma(\tau)}{1 + j\omega\tau} d\tau \quad (9)$$

and equation (8) becomes

$$\int_0^{\infty} \gamma(\tau) d\tau = 1 \quad (10)$$

In equations (9) and (10) $\gamma(\tau)$ is the required distribution function and the expression $\frac{\gamma(\tau)}{1+j\omega\tau}$ the fraction of the overall polarization resistance with relaxation times between τ and $\tau + d\tau$. As such the area beneath every DRT peak corresponds to the total polarization resistance contribution of the corresponding dynamic process[2,5,16].

To obtain $\gamma(\tau)$ from $\underline{Z}_{pol}(\omega)$ the compliance with KK-transform is then exploited so that only the imaginary part of $\underline{Z}_{pol}(\omega)$ will be further considered.

However, as a reminder at this juncture, the impedance of an RC-element (e.g. Process 1 or parallel combination of R_1 and C_1 in Figure 2.4-4) is given by:

$$\frac{1}{\underline{Z}_{RC}(\omega)} = \frac{1}{R} + \frac{1}{\frac{1}{j\omega C}} = \frac{1 + j\omega RC}{R} \tag{11}$$

$$\underline{Z}_{RC}(\omega) = \frac{R}{1 + j\omega RC} \cdot \frac{1 - j\omega RC}{1 - j\omega RC} \tag{12}$$

$$\underline{Z}_{RC}(\omega) = \frac{R}{1 + (\omega RC)^2} - j\frac{\omega R^2 C}{1 + (\omega RC)^2} \tag{13}$$

With the time constant $\tau = RC$ equation (13) becomes

$$\underline{Z}_{RC}(\omega) = \frac{R}{1 + (\omega\tau)^2} - jR\frac{\omega\tau}{1 + (\omega\tau)^2} = Re\left\{\underline{Z}_{RC}(\omega)\right\} - jIm\left\{\underline{Z}_{RC}(\omega)\right\} \tag{14}$$

Thus considering only the imaginary part of $\underline{Z}_{pol}(\omega)$

$$Im\{\underline{Z}_{pol}(\omega)\} = Z^{"}(\omega) = -R_{pol}\int_0^{\infty}\frac{\omega\tau}{1+(\omega\tau)^2}\gamma(\tau)d\tau \quad (15)$$

Due to the logarithmic sampling of the impedance data the frequency variables are then substituted as follows[5]:

$$y = \ln(\omega\tau) \quad (16)$$

From which

$$d\tau = \tau dy \quad (17)$$

Is obtained and equation (15) becomes

$$Z^{"}(\omega) = -R_{pol}\int_0^{\infty}\frac{e^y}{1+e^{2y}}\gamma(\tau)\tau dy \quad (18)$$

However

$$\mathrm{sech}(y) = \frac{2}{e^y + e^{-y}} = 2\frac{e^y}{1+e^{2y}} \quad (19)$$

leading to the expression:

$$Z^{"}(\omega) = -\frac{R_{pol}}{2}\int_0^{\infty}\mathrm{sech}(y)\gamma(\tau)\tau dy \quad (20)$$

So that with the substitutions

$$x = \ln \frac{\omega}{\omega_0} \tag{21}$$

and

$$\hat{g}(y - x) = \gamma(\tau)\tau \tag{22}$$

equation (15) is recognizable as the convolution product

$$\begin{aligned} Z^{"}(\omega) &= -\frac{R_{pol}}{2} \int_{-\infty}^{\infty} \operatorname{sech}(y)\, \hat{g}(y - x) dy \\ &= -\frac{R_{pol}}{2} \operatorname{sech}(x) * \hat{g}(x) \end{aligned} \tag{23}$$

and with $g(x) = R_{pol} \cdot \hat{g}(x)$

$$Z^{"}(\omega) = -\frac{1}{2} \operatorname{sech}(x) * g(x) \tag{24}$$

A possibility to obtain the required distribution function $g(x)$ is to convert the convolution product to an algebraic expression through Fourier transformation, calculate the Fourier transformed equivalent and then inverse Fourier transform it. In the Fourier space though, numerical error amplification occurs, such that inverse Fourier transformation of the whole data does not give useful results[5] and thus requires digital filtering with an appropriate filter e.g. Hanning filter prior to the inverse Fourier transform. This method of solving the inversion problem has been employed in the DRT calculations in the RAVDAV softeware[21] used in this work. For a detailed description of the procedure reference [5] is recommended.

Leonide[2] on the other hand has solved the inversion problem by identifying the convolution product in equation (23) as a Fredholm integral equation of first kind as described by equation (25) whereby $g(y)$ represents the unknown solution and K the kernel of the given function $z(x)$. The inverse problem (termed ill-posed problem) is then solved using the Tikhonov regularization method, Fast TIKhonov REGularization FTIKREG[6].

$$\int_a^b \mathrm{K}(x,y)\, g(y)dy = z(x) \tag{25}$$

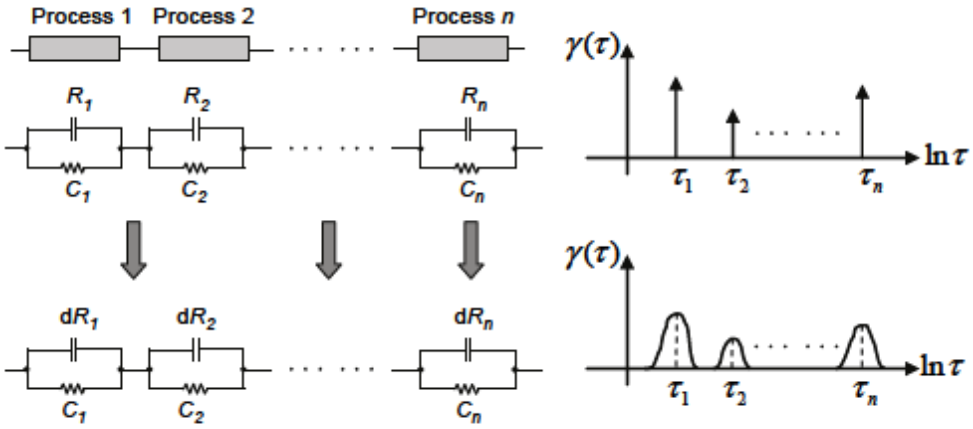

Figure 2.4-4: Interpretation of EIS data in terms of equivalent circuit models and distribution of relaxation times[2].

Further details on the DRT and the mathematical steps involved in obtaining the distribution function $\gamma(\tau)$ from the recorded impedance spectrum $\underline{Z}(\omega)$ can be obtained from references [2,5,6,16,22]. While awaiting the public release of RAVDAV software, the free Matlab-based DRT tool of Wan *et al.* [22] can be used to evaluate DRTs of recorded impedance spectra.

2.4.2.4 Equivalent Circuit Modeling and CNLS Fit

Unlike the non-parametric approach for analyzing electrochemical impedance spectra, the Complex Non-linear Least Squares (CNLS) fit modelling can either be based on well understood physics of the system or be phenomenological in nature[23]. This type of modelling is not adequate for system screening except the system is very simple and its impedance response can be well and wholly described with equivalent circuit elements.

Irrespective of the model approach, CNLS fit of electrochemical impedance spectra more often than not involves the three basic elements resistor (R), capacitor (C) and inductance (L) describing ohmic, capacitive and inductive behaviors or the system respectively. Other elements commonly found in CNLS fits of electrochemical systems include the RC-, RQ-, Warburg- and Gerischer elements. With the exception of the ideal capacitor C, the RC-element and the inductor that in this work was always removed through a KK-procedure (cf. section 3.2.3) these

equivalent circuit model (ECM) elements have all been used in this thesis. Their Nyquist plot representations have been exemplarily simulated and displayed in Figure 2.4-5. For details of the impedance expressions, derivations and differences of between these elements references [2,15,16,18] are recommended.

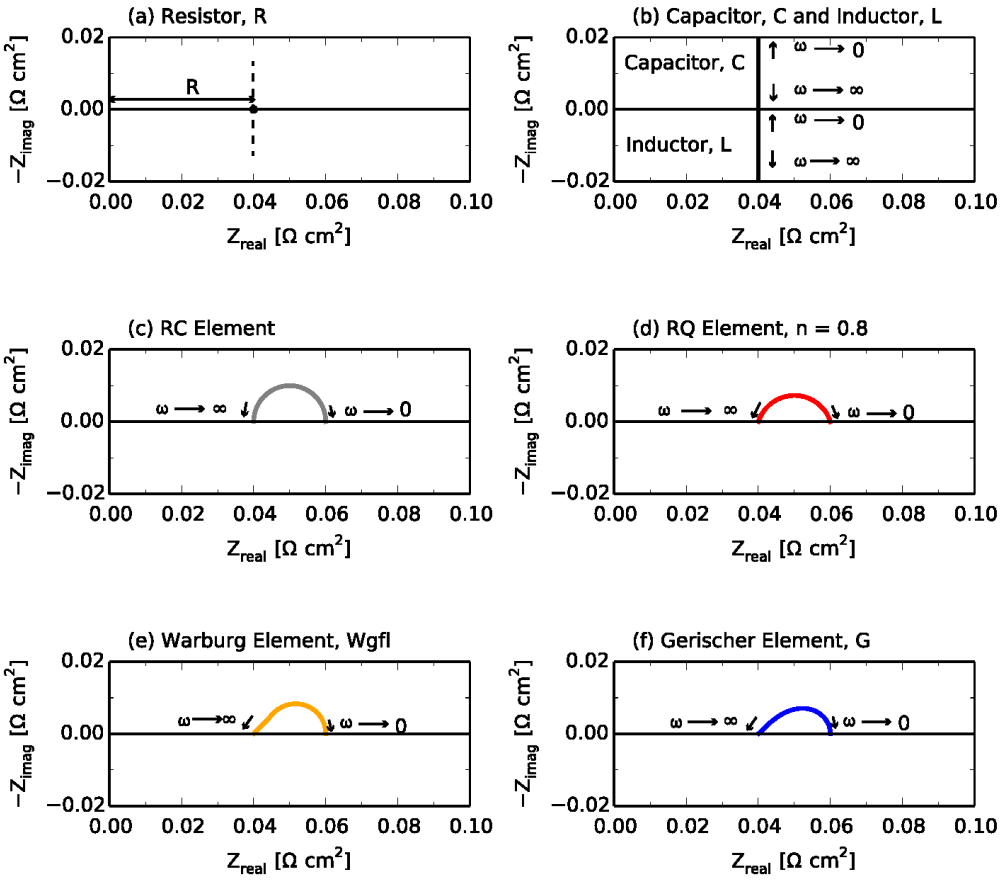

Figure 2.4-5: Simulated CNLS fit elements displayed in Nyquist plots. (a) Resistor (b) Capacitor (top half) and Inductor (bottom half) (c) RC element (d) RQ element with exponent n = 0.8 (e) Warburg element (generalized finite length) (f) Gerischer element. The elements in subplots b to f are in series with a series resistance of 0.04 Ωcm²

Chapter 3 Kinetic Investigations on Solid Oxide Cells

3.1 Introduction

The investigation of SOC kinetics requires a clear definition of the depth at which the investigations will be done. The degree of detail depends on the goal of the investigation and as such different techniques and instrumentation come into play. To a fundamental electrochemist, investigating SOC kinetics would not be complete without detailed elementary kinetics. This entails, distinguishing between the possible reaction mechanisms, the corresponding thermodynamic data (enthalpy and entropies of activation), surface coverage of solid phases, adsorption and desorption enthalpies, sticking coefficients of reactants, etc. On the other hand details such as porosity, tortuosity, diffusion coefficients, partial pressure dependences, and overall activation energies would interest an application oriented electrochemist more.

In this chapter AC and DC techniques will be applied to investigate electrochemical reaction kinetics of SOCs and the porous SOC electrodes on different cell geometries. The main tools involve Electrochemical Impedance Spectroscopy (EIS), Distribution of Relaxation Times (DRT) and Complex Non-linear Least Squares (CNLS) fit analysis. Detailed elementary kinetics is out of the scope of the thesis. Firstly, the kinetics of the full cells will be investigated. This will be done with SOCs from DTU as well as cells from Forchungszentrum Jülich (FZJ). Since the impedance response of a SOC contains contributions from both fuel and oxygen electrodes, symmetric cell geometries will be applied to isolate and investigate different electrodes separately. To obtain DC kinetics of the electrodes with minimal concentration, heating or cooling effects a specially designed and novel[11] pseudo-3-electrode cell geometry will be used.

3.2 Experimental

3.2.1 Investigated Cell Types, Geometries and Cell Manufacture

An overview of the investigated cell geometries is given in Table 3.2-1 in Figure 3.2-1a - e.

Table 3.2-1: Investigated cell geometries

Cell type	Full Cell			Symmetric Cell	SmallWE
	Type I	Type II	Type III	Type IV	Type V
	Standard DTU Risø Cell	Masked DTU Risø Cell	Standard FZJ (KIT) Cell		
Top View	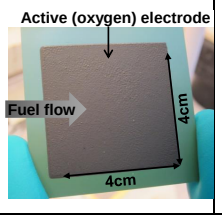	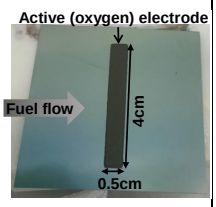	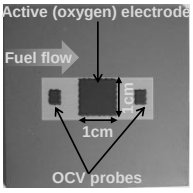	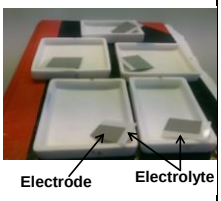	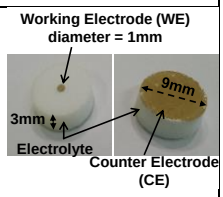
Substrate	3YSZ (300 µm)		8 YSZ (0.5 – 1mm)	-	-
Fuel/working electrode	Ni/YSZ (10 µm)		Ni/YSZ (7 µm)	Varying	Varying
Electrolyte	8YSZ (5 µm)		8YSZ (10 µm)	8YSZ (CGO for ox. electrodes)	8YSZ (CGO for ox. electrodes)
Buffer layer	CGO (2 µm)		CGO (2 µm)	-	-
Oxygen/counter electrode	LSC/CGO (40 µm)		LSCF (45 µm)	Varying	Varying
Current collection	LSC (30 µm)		-	Varying	Varying
Active electrode area	16 cm^2	2 cm^2	1 cm^2	0.2 – 0.4 cm^2	1 mm^2
	(a)	(b)	(c)	(d)	(e)

Figure 3.2-1: Investigated cell geometries (a) standard DTU Energy (Risø) 4 x 4 cm^2 cell (b) newer generation of DTU Energy cells with reduced active electrode areas (4 x 0.5 cm^2) (c) standard FZJ 1 x 1 cm^2 cells with inlet OCV probes before and after cell (d) freshly screen-printed symmetric cells (Ni/YSZ) about to be sintered and from which smaller adequate-sized cells (ca. 0.3 cm^2) will be laser-cut (or hand-broken) (e) *Small working electrode* (SmallWE) pseudo-symmetric cells with working electrode areas of maximum 1 mm^2 and counter electrodes with 9 mm diameter.

3.2.1.1 Full Cells

The Ni/YSZ fuel electrode supported state-of-the-art (s.t.a.) full cells investigated in the sections of this work that were carried out at the Karlsruhe Institute of Technology (KIT) were obtained from Forschungszentrum Jülich[24–26] (FZJ) and manufacturing details are given elsewhere[27,28]. The full cells investigated at the Technical University of Denmark (DTU) were s.t.a. and in-house developed at the Department of Energy Conversion and Storage (DTU Energy) and manufacturing details are as well found elsewhere[29].

The FZJ cells (cf. Figure 3.2-2 and labelled Type III cells in Table 3.2-1) are composed of a 1000 µm Ni/YSZ substrate, a *ca*. 7 µm thick Ni/YSZ fuel electrode functional layer and a 10 µm thick 8YSZ electrolyte co-fired under oxidizing atmosphere at 1400 °C. Onto the electrolyte, a GDC interlayer ($Ce_{0.8}Gd_{0.2}O_{2-\delta}$) with a thickness of 7 µm is screen-printed and fired at 1250 °C. This GDC interlayer prevents chemical reaction between the electrolyte material 8YSZ and the air electrode material LSCF ($La_{0.58}Sr_{0.4}Co_{0.2}Fe_{0.8}O_{3-\delta}$) of thickness 45 µm, screen-printed on top of the fired GDC layer and fired at 1080 °C. The active surface area of the air electrode, and thus the active cross-sectional area of the cell, is 1 cm^2 (10 mm × 10 mm). To monitor the open circuit voltage, an OCV probe is screen-printed before and after the working oxygen electrode in the direction of the gas flow[2].

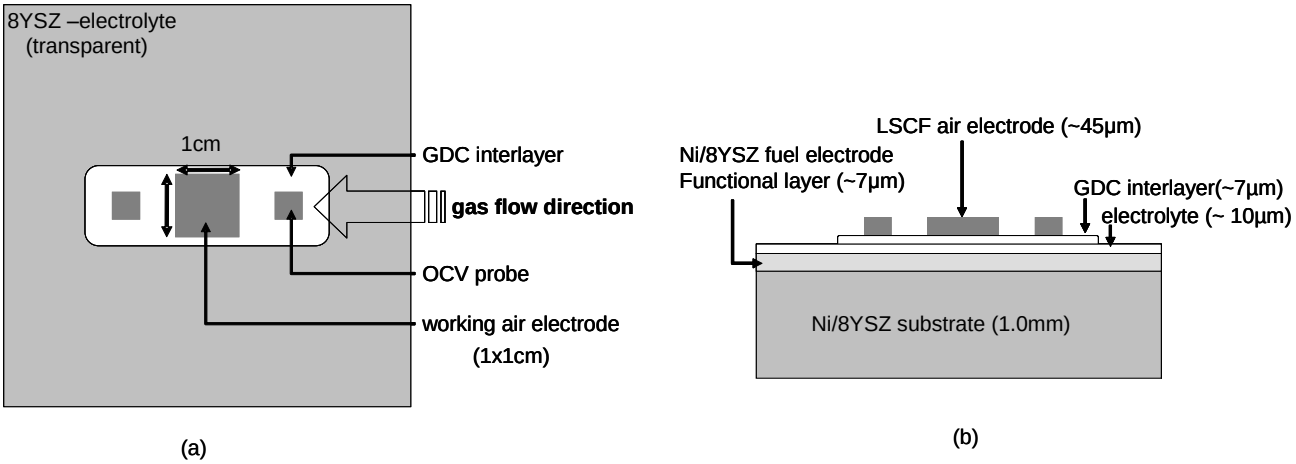

Figure 3.2-2: Schematic of FZJ 1cm² cell (a) top view (b) cross section view[2]

The investigated DTU Energy single cells were composed of porous Ni/3YSZ substrates (ca. 0.3 mm), porous Ni/YSZ fuel electrodes (ca. 10 µm), dense 8YSZ electrolytes (ca. 5 µm), dense $Ce_{0.9}Gd_{0.1}O_{2-\delta}$ buffer layers (ca. 1 µm) and porous $La_{0.6}Sr_{0.4}CoO_{3-\delta}/Ce_{0.9}Gd_{0.1}O_{2-\delta}$ oxygen electrodes (ca. 30 µm). The cell system is completed by a ca. 30 µm LSC current collection layer. Investigated cells were of two types of geometries. Type I cells (cf. Table 3.2-1) had a 4 x 4 cm^2 active electrode area. The top view and schematic of the corresponding cross-section are displayed in Figure 3.2-3 (i) and (ii) respectively. Type II cells had a 4 x 0.5 cm^2 strip of oxygen electrode material screen-printed at the center resulting in an active electrode area of 2 cm^2. Cell mounting of the cells was such that at the fuel electrode the fuel flowed across the 4 cm edge parallel to the 0.5 cm edge. The top view of a Type II cell and the corresponding schematic of the cross-section are displayed in Figure 3.2-3 (ii) and (iv) respectively.

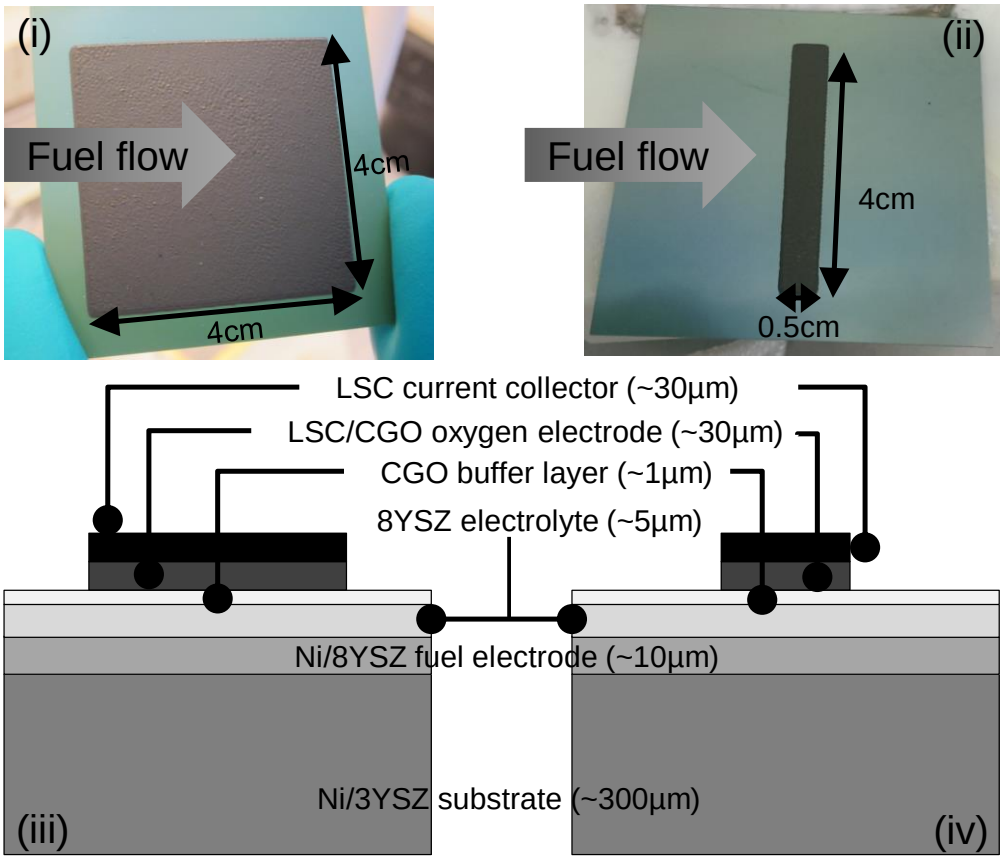

Figure 3.2-3: Cell Geometry: (i) top view of a typical DTU Energy cell (Type I), (ii) top view of DTU Energy strip cell (Type II), (iii) schematic of cross-sections of Type I cell and (iv) schematic of cross-section of Type II cell.

3.2.1.2 Symmetric Cells

The investigated Ni/YSZ fuel electrode symmetric cells were manufactured by screen-printing the electrode ink on either side of a 5 x 5 cm^2 and ca. 200 µm thick 8YSZ electrolytes and sintering for 4 h in air between 1200 – 1350 °C. The LSC/CGO or LSCF oxygen electrodes were screen-printed on a similarly thick CGO electrolyte and sintered for 24 h at 930 °C in air. The sintered electrodes were then laser cut to required dimensions or broken by hand and the areas determined using an optical microscope. Symmetric cells have been labeled Type IV cells in Table 3.2-1 and Figure 3.2-1 (d) shows Ni/YSZ symmetric cells screen-printed on broken 8YSZ pieces in crucibles prior to sintering at different temperatures.

3.2.1.3 SmallWE Pseudo-Symmetric Cells

The geometry and manufacturing steps of the *SmallWE* (Type V cell in Table 3.2-1) are displayed in Figure 3.2-4. The geometry consists of 0.8 – 1 mm^2 working electrode (WE) on one side and a counter electrode of same material and of a radius of 4.5 mm on the other side of a specially fabricated electrolyte pellet. The cell manufacturing included the following steps displayed in Figure 3.2-4. (i) The electrolyte pellet was fabricated using 8YSZ or CGO (TOSOH, Japan or Rhodia, France respectively) powder. Initially a cylindrical bar of 10 mm diameter was uniaxially pressed at 50 - 100 MPa followed by isostatic pressing at 250 MPa. The cylinder was then sintered at 1500 °C – 1600 °C for 10 h to obtain a dense pellet. (ii) The pellet was machined to the required dimensions. (iii) A ca. 200 µm thin 8YSZ tape (CGO tape for CGO pellets) was then pressed onto the machined knob to mask the surface of the electrolyte pellet but not the tip of the knob. (iv) The counter electrode was screen-printed on one side of the sample, placed in drying chamber heated to ca. 90 °C – 150 °C for ca. 20 minutes. (v) The working electrode was then screen-printed and dried in a similar manner. (vi) Finally, the masking tape was carefully lifted off to remove the excess material, and the cells were sintered between 1200 °C – 1350 °C for 4 h in air for fuel electrodes and 24 h at 930 °C for oxygen electrodes.

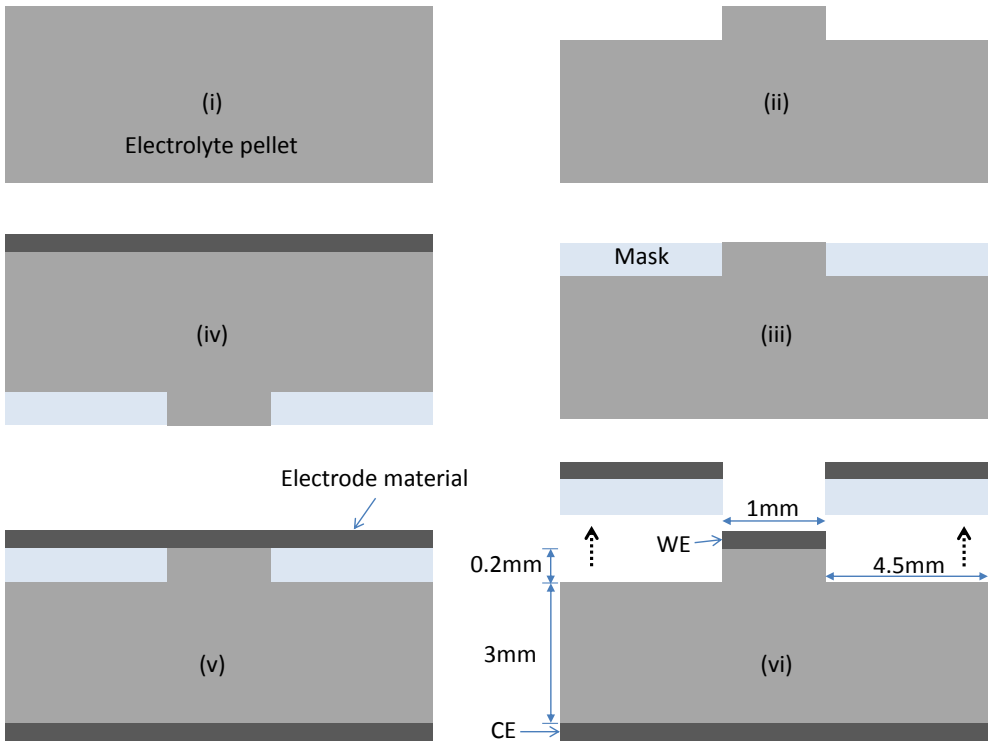

Figure 3.2-4: Illustration of dimensions and manufacturing steps of the *SmallWE* electrode geometry also displayed in Table 3.2-1 Figure 3.2-1(e)

3.2.2 Measurement Set-ups (Test-rigs)

Characterization of full SOCs in the investigations carried out at KIT was done using the test set-up shown in Figure 3.2-5[2] and for those at DTU Energy laboratories using the set-up shown in Figure 3.2-6. In both rigs the required amounts of component fuel gases - controlled by digital mass flow controllers - were allowed to mix in a combustion chamber before reaching the cell. Appropriate amounts of H_2 would for instance react with the right amount of O_2 in the combustion chamber to produce the desired steam content in the fuel stream. Gold seals were employed in all tests. Further details on the electrical contacting can be found elsewhere[30].

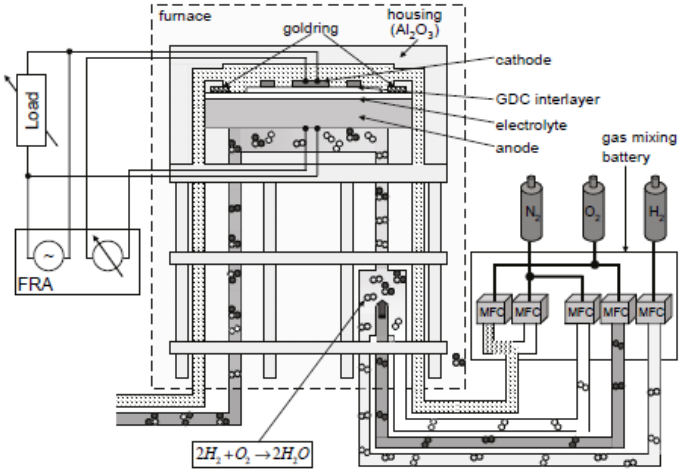

Figure 3.2-5: Full cell measurement set-up at IAM-WET Karlsruhe[2]

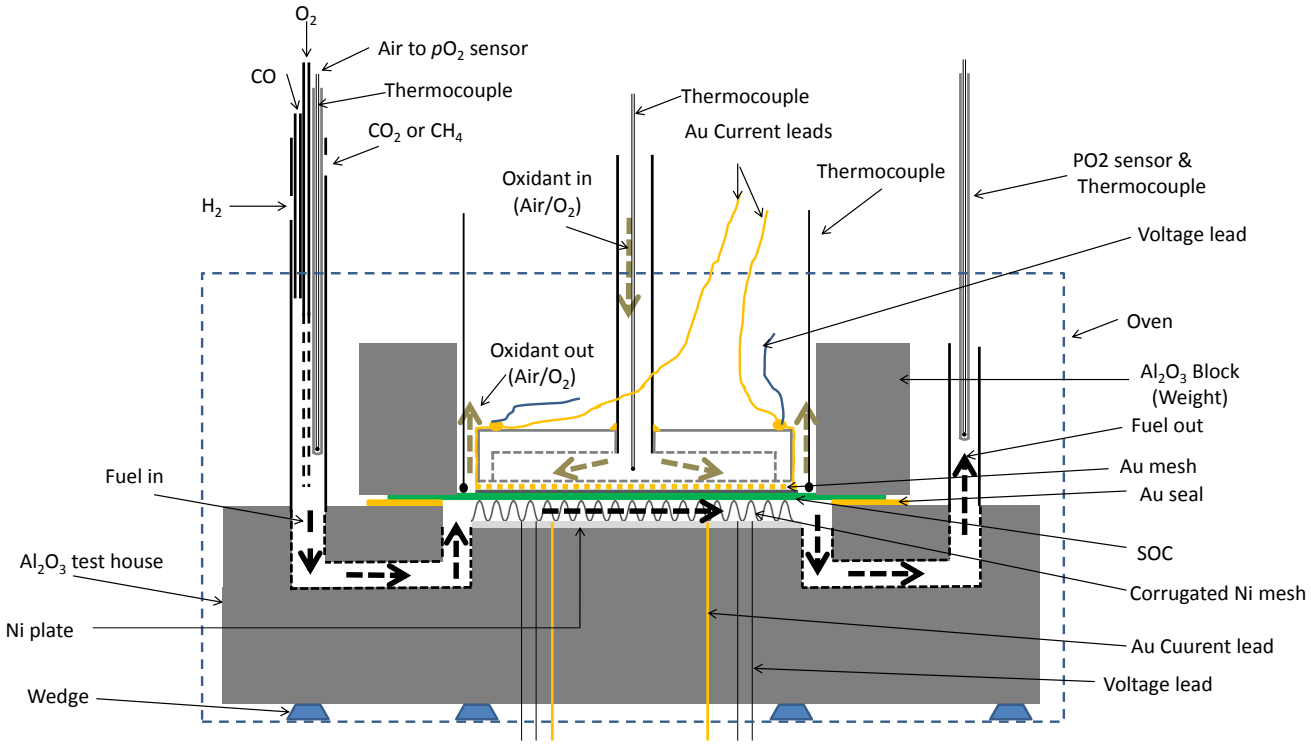

Figure 3.2-6: Full cell measurement set-up at DTU Energy showing gas supply to and from cell

All symmetric and *SmallWE* cells were characterized at DTU Energy laboratories using test rigs of the type displayed in Figure 3.2-7. Although for clarity only a single sample holder is displayed, the rigs have four sample holders enabling characterization of four separate cells in the same test. The characterization e.g. recording of impedance spectra is done serially from one channel to the next. Furthermore, the rig is of single gas atmosphere type (both sides of the sample are exposed to the same atmosphere) with a maximum flow rate of 6 l/h and as such had to be allowed enough time (min. 90 mins) to equilibrate after temperature or gas mixture change. The alumina tube has a capacity of 1.7 L. Further details on the set-up can be obtained elsewhere[31].

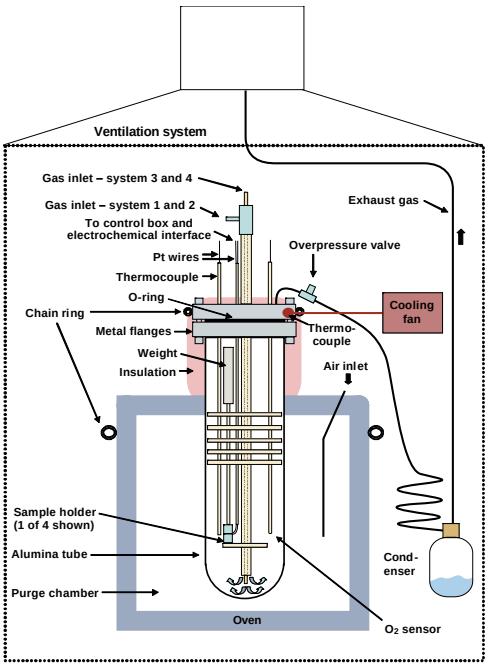

Figure 3.2-7: Symmetric cell test rig at DTU Energy with one of four sample holders (channels) shown[31]. The rig Alumina tube has a capacity of 1.7 L

3.2.3 Electrochemical Characterization

The cells were characterized by electrochemical impedance spectroscopy (EIS) under open circuit conditions or under current load in both SOFC and SOEC modes. The measurements were carried out with a Solartron 1260 FRA. For measurements done at KIT, the spectra were recorded in the frequency range 1 MHz - 100 mHz meanwhile for measurements in DTU Energy laboratories spectra were recorded in the frequency range 96.850 kHz to 30 mHz. Characterization of *SmallWE* cells was carried out with a Gamry Reference 600™ potentiostat in the frequency range 1 MHz to 30 mHz. The same equipment was used for recording of *SmallWE* current/voltage characteristics at a potential scan rate of 1 mV/s.

To exclude contributions from the test set-up, spectra recorded at DTU Energy were corrected with a short-circuit measurement and lead inductance was removed through a procedure utilizing the Kramers-Kronig relations[19,20]. This procedure involves comparing the imaginary impedance generated from the measured real impedance, with the measured imaginary impedance, and the difference between these is used to determine the inductance. On the other hand the inductances from KIT laboratory test-set up were very small and undetectable in the investigated frequency range.

For data recorded in DTU Energy laboratories, all CNLS fits, DRT- and KK-transforms as well as simulations were done using the software RAVDAV[21], whereas the commercial software Zview®[32] was used for CNLS fits of KIT spectra.

3.3 Full Cell Investigations and Gas Conversion

In this section results from investigations of the electrochemical reaction kinetics at the electrodes of SOCs at 700 °C for a binary H_2/H_2O fuel and two model reformate fuels—a CO/CO_2-based reformate and a CH_4 – based reformate, will be presented. The influence of microstructure on kinetics was evaluated by comparing two cells with the same geometry but with one cell having a finer functional layer microstructure. Furthermore the influence of fuel utilization was investigated by comparing the cell with finer microstructure with a third cell of same microstructure but having a reduced active electrode area. Gas conversion and other concentration-related processes will be discussed for H_2/H_2O and reformate-based fuels. Finally results from investigations of H_2/H_2O reaction kinetics on an FZJ cell will be presented as well.

3.3.1 Experimental

3.3.1.1 Cell Systems and Geometries

An overview of the investigated cells is given in Table 3.3-1. Cells A and B had an active electrode area of 16 cm^2 against Cell C with 2 cm^2. Furthermore, cells B and C differed from Cell A in that they had a finer microstructure than Cell A. The geometries have been displayed in Figure 3.2-3 whereby cells A and B are of Type I and Cell C of Type II. The cell system and component dimensions have been summarized in Figure 3.2-1 meanwhile cell and manufacturing details are described in literature[29,33].

Table 3.3-1: Investigated Cells

Cell ID	Active Electrode Area [cm^2]	Fuel Electrode Microstructure
A	16	Reference
B	16	Finer
C	2	Finer

3.3.1.2 Operation Conditions

The majority of the investigations were carried out at 700 °C in three fuel mixtures – *Fuel I*, *Fuel II* and *Fuel III*. *Fuel I* was composed solely of hydrogen and steam in an 80/20 ratio at the inlet. At 700 °C this corresponded to an open circuit voltage (OCV) of 1030 mV. The second fuel, *Fuel II* had hydrogen and carbon dioxide in the ratio 81:19 % at the inlet. The third fuel, *Fuel III* was a methane-based reformate fuel with hydrogen, methane and steam with mole fractions of 10 %, 30 % and 60 % respectively.

The choice of the component mole fractions, aided by thermodynamic calculations, was such that the equilibrium composition of the reformates (Fuel II and Fuel III) was the same — 64 % H_2, 16 % H_2O, 5 % CO_2, 13 % CO and 2 % CH_4. It was further ensured that at equilibrium, the OCV of the reformate fuels was also 1030 mV at 700 °C. The required steam content was obtained by allowing appropriate amounts of oxygen and hydrogen to react in a combustion chamber close to the cell inlet. A summary of the inlet compositions of the fuels is given in Table 3.3-2.

Table 3.3-2: Inlet compositions of investigated fuel mixtures as well as equilibrium concentrations of the reformate fuels at 700 °C.

Gas [atm]	Inlet			
		Reformate		
	Fuel I	***Fuel II***	***Fuel III***	**Equil. Compositiion**
H_2	0.8	0.81	0.1	0.64
H_2O	0.2	-	0.6	0.16
CO_2	-	0.19	-	0.05
CO	-	-	-	0.13
CH_4	-	-	0.3	0.02

Fuel I was obtained by flowing 7 l/h of hydrogen and 0.7 l/h of oxygen. To obtain *Fuel II* 5.6 l/h of hydrogen and 1.3 l/h of carbon dioxide were supplied to the cell. *Fuel III* was obtained by supplying 3.0 l/h of hydrogen, 1.29 l/h of oxygen and 1.29 l/h of methane. With these flows, the fuel utilization at the investigated maximum current density of 0.5 A/cm² was 60 % for the 16 cm² cells (A, B) and 7.5% for the 2 cm² cell (C). The fuel utilization and current density range were chosen to emulate practical conditions. In all cases, the oxygen electrode was supplied with 40 l/h of air. All flow rates are reported with respect to a temperature of 273.15 K and a pressure of 1 atmosphere.

3.3.1.3 Characterization and Equivalent Circuit Modeling

Once the appropriate fuel composition was set 30 minutes were allowed for the system to attain a steady state and then an impedance spectrum was recorded. The current density was increased stepwise from OCV to the maximum current density of 0.5 A/cm^2 and impedance spectra recorded at each step. From 0.5 A/cm^2 the system was brought to OCV a control spectrum recorded and a C/V curve recorded for validation of calculations. (cf. section 3.3.1.4)

To isolate and quantify the area specific resistance (ASR) contributions of the involved processes, an adequate equivalent circuit model (ECM) was fitted to the recorded impedance spectra using complex non-linear least squares (CNLS) minimization. A model M0 for anode supported SOFCs[34] was used to quantify spectra recorded in H_2/H_2O fuel. This model was extended with an RQ-element to accommodate *gas conversion*[35], which was negligibly small (and thus not considered) in the system in reference [34]. Also, gas phase diffusion at the oxygen electrode was neglected. For spectra recorded under reformate operation the model M1 was used, obtained by extending M0 with another RQ-element to describe the extra low frequency process present in reformate fuel spectra[36–38]. The employed ECM (cf. Figure 3.3-1) thus comprised an ohmic resistance to model the ohmic losses across the cell (predominantly caused by ionic transport across the electrolyte), two RQ-elements to quantify the fuel electrode electrochemical oxidation and ionic transport as well as diffusion in the functional layer in the fuel electrode, a Gerischer element to model surface exchange and oxygen ion bulk diffusion in the oxygen electrode, a Warburg element for gas phase diffusion in the substrate, an RQ-element for fuel electrode gas conversion and finally an RQ-element for the extra low frequency process in reformate fuels.

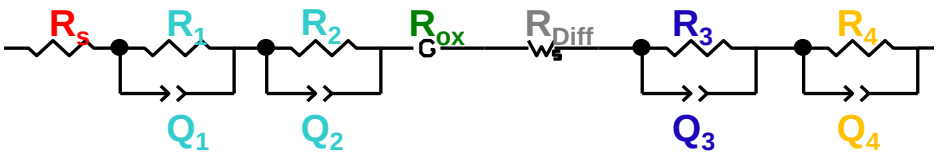

Figure 3.3-1: Equivalent electric circuit model used to quantify the ASRs for EIS spectra in reformate operation. R_s quantifies the ohmic losses. The two RQ-elements comprising the elements R_1, Q_1, R_2, and Q_2 correspond to the fuel electrode processes RQ1_FE_1 and RQ2_FE_2 in Figure 3.3-2 meanwhile the elements labeled with R_{ox} and R_{Diff} correspond to G_ox and Wgfl_RDiff respectively. The RQ element composed of R_3 and Q_3 models the gas conversion process RQ3_GC and the RQ element composed of R_4 and Q_4 model the reformate process RQ4_Ref in Figure 3.3-2.

Pre-identification of the processes prior to the CNLS fitting as well as fit quality validation by simulation of fitted processes was done by calculating the distribution of relaxation times (DRT)[5]. Prior to the fitting and calculation of DRTs, adequate data quality was assured by checking the compliance of the data with Kramers-Kronig (KK) transforms[19,20] and the fit residuals and goodness of fit values were also carefully considered. As can be seen

from Figure 3.3-2 the data and fit quality are very good with residuals well within the ± 0.5 % range. The evenly fluctuating distribution of the residuals about the zero-line further stresses the absence of systematic errors.

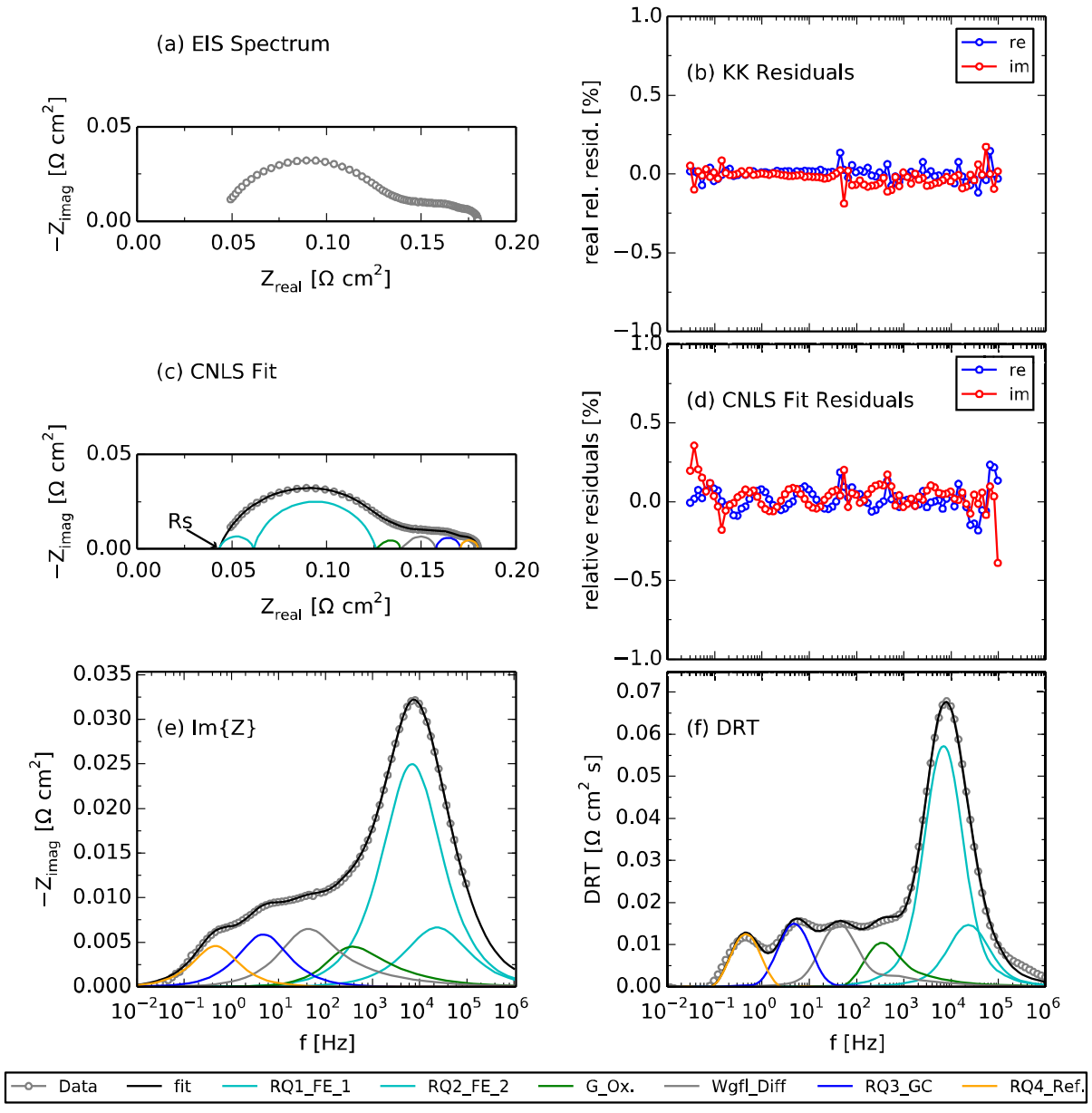

Figure 3.3-2: (a) Impedance spectrum of Cell C at 700 °C at a current density +0.5 A/cm2 in reformate fuel Fuel II, (b) the corresponding KK-test residuals, (c) the CNLS fit, with Boukamp goodness of fit χ^2 = 1.4·10^{-4}, (d) corresponding CNLS fit residuals, (e) imaginary part of spectrum and fits, (f) DRT of spectrum and simulation of fit process

The imaginary part representation of the spectrum together with a simulation of the dynamic processes is given in Figure 3.3-2 (e). However as would be expected the DRT representation in Figure 3.3-2 (f) gives a better overview of the characteristic/peak frequencies of the dynamic processes. Thereby, the fuel electrode electrochemical processes (RQ1_FE_1 and RQ2_FE_2) are located in the frequency region f > 1 kHz, the oxygen electrode electrochemical process (G_ox.) at 100 Hz < f < 1kHz, substrate diffusion (Wgfl_Diff) at 10 Hz < f < 100 Hz, gas conversion (RQ3_GC) at 1 Hz < f < 10 Hz and the reformate process (RQ4_Ref.) at 100 mHz < 1 Hz.

3.3.1.4 Current Density vs. Overpotential Curves—Concept and Methodology

The total measured impedance at each current corresponds to the slope of the current-voltage curve at each individual current. Thus, by integration of the curve defined by the determined slopes it is possible to reconstruct the current-voltage curve.

Through integration of the ASRs obtained from the CNLS fit (cf. Figure 3.3-3 b) of impedance spectra measured at various current densities (cf. Figure 3.3-3 a) the overpotential contributions of the individual processes could be determined (cf. Figure 3.3-3 c). A cumulative deduction of the obtained overpotentials from the OCV results in a simulation of the C/V- characteristic. This can be compared with the measured characteristic to validate the procedure and as displayed in Figure 3.3-3 d the simulated curve perfectly overlays the measured curve, thereby validating the procedure.

Besides determining the overpotential contributions of individual loss mechanisms, an important benefit of the described procedure is that it can be applied to define a safe operation window for the cell (electrode) at the chosen operation point. This is shown in Figure 3.3-3 d where the oxidation potential of Ni to NiO is marked and can be compared to the fuel electrode potential at all current densities. This curve is obtained by cumulative subtraction of contributions of the fuel electrode processes (gas conversion, substrate diffusion and the ASR of electrochemical oxidation and ionic transport in the fuel electrode) from OCV. As can be read from the curve, the fuel electrode potential at + 0.5 A/cm^2 is - 900 mV vs air and oxidation of Ni does not start until ca. - 764 mV vs. air at 700 °C.

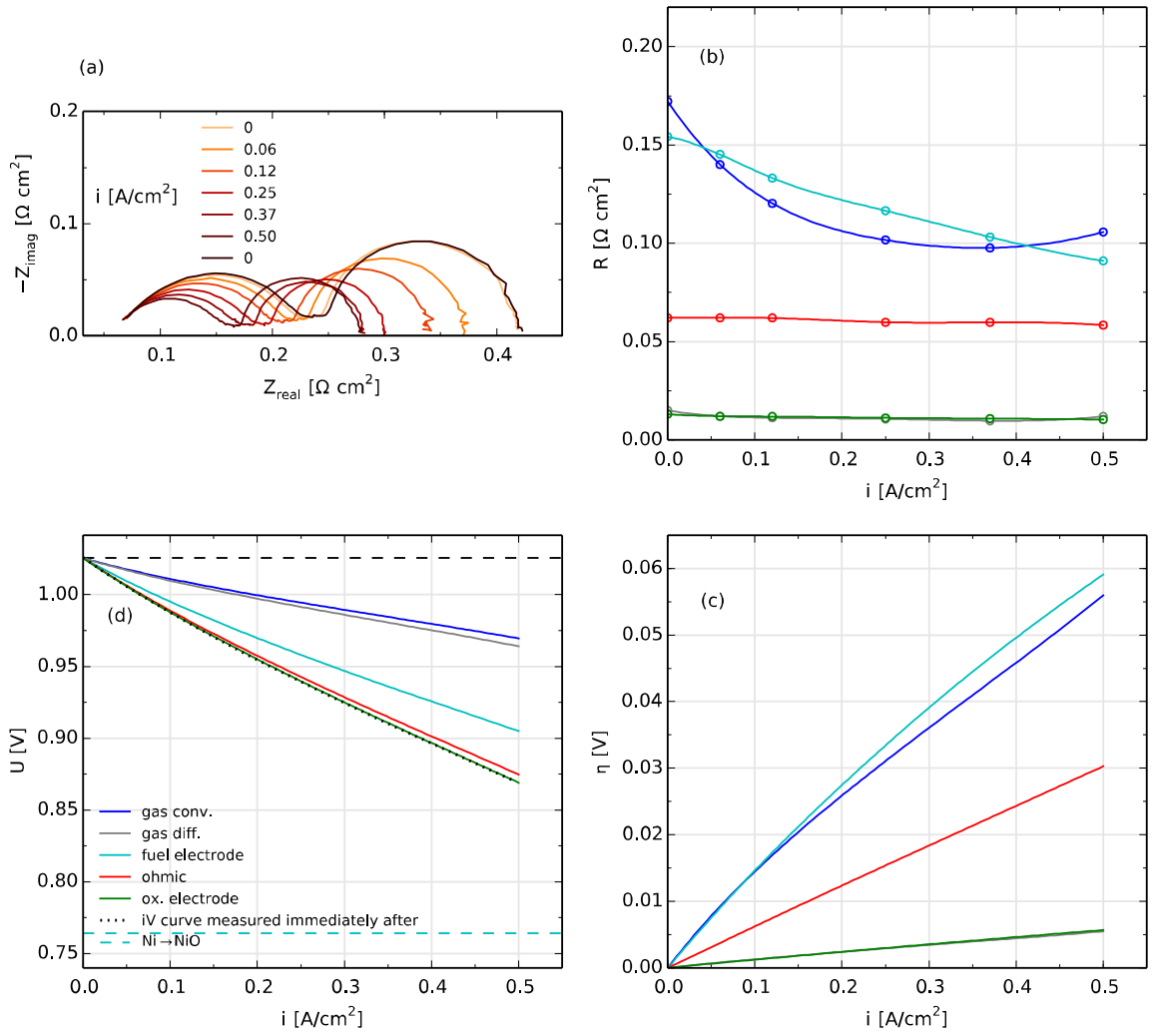

Figure 3.3-3: Impedance Spectra of Cell A recorded at 700 °C in Fuel I (80/20 H_2/H_2O) in the current density range 0 to +0.5 A/cm², (b) ASR contributions of individual processes, (c) corresponding overpotential contributions obtained through integration, (d) validation of procedure by cumulative subtraction of overpotentials from OCV and comparison with C/V characteristic recorded after return to OCV and OCV control spectrum.

3.3.2 Results and Discussion

3.3.2.1 Process Evolution under Load

By calculating DRTs from impedance spectra recorded at all current densities a qualitative appreciation of the evolution of individual processes under current load could be obtained. These are displayed in Figure 3.3-4 for cells A, B and C and the investigated fuel mixtures, *Fuel I*, *Fuel II* and *Fuel III.*

The area enclosed by a DRT peak corresponds to the ASR of the dynamic process[5,34,39] and based on the frequencies of the involved dynamic processes as displaced in Figure 3.3-2 f the following observations can be made from Figure 3.3-4:

i. The polarization resistance related to gas conversion (ca. f = 1 Hz) does not depend on the microstructure of the fuel electrode (cf. (a_i) vs. (b_i)) but only on the active electrode geometric area (cf. (a_i) and (b_i) vs. (c_i)). This is consistent since a reduced active electrode area (at constant unchanged fuel flow rate) results in reduced fuel utilization leading to a decrease in the associated conversion ASR.

ii. The gas conversion ASR decreases with increasing current density to a minimum value then starts increasing at around 0.5 A/cm^2. With an inlet average pH_2O of 20 %, the steam partial pressure increases with increasing current density and as such the gas conversion ASR is expected to decrease going through a minimum at 50 % average pH_2O over the cell[40]. This coincides with a current density between 0.4 and 0.5 A/cm^2 in Figure 3.3-4 (a_i) and (b_i).

iii. The gas conversion peak in *Fuel I* splits into two low frequency peaks in reformate fuels (cf. (a_i) vs (a_ii) or (b_i) vs. (b_ii) and (b_iii)).

iv. The two low frequency processes in the reformate fuels are very similar in magnitude and display similar current density behavior (cf. (b_ii) vs (b_iii) for f < 10 Hz).

v. Gas phase diffusion in the substrate (cf. 10 Hz < f < 100 Hz in (a_i)) decreases with increasing current density in the investigated range.

vi. The ASR related to the surface exchange and bulk ion transport at the oxygen electrode is very small and overlaps with the fuel electrode process rendering accurate deconvolution difficult.

vii. The ASR related to electrochemical oxidation and ionic transport at the fuel electrode (cf. f >1 kHz) decreases with increasing current density. Unlike the gas conversion peak (cf. f <10 Hz in a_i or b_i) that maintain the peak frequency, the electrochemical reaction peaks are drifting towards higher frequencies with increasing current density.

viii. A finer fuel electrode microstructure decreases the ASR related to electrochemical oxidation and ionic transport in the fuel electrode (cf. Cell A vs. Cell B for f >1 kHz and all fuel mixtures)

ix. Active electrode area has negligible impact on electrochemical oxidation and ionic transport at the fuel electrode. (cf. Cell B vs. Cell C for f >1 kHz and all fuel mixtures)

The above listed points will be discussed in greater detail together with the current density vs. overpotential curves in the next sections.

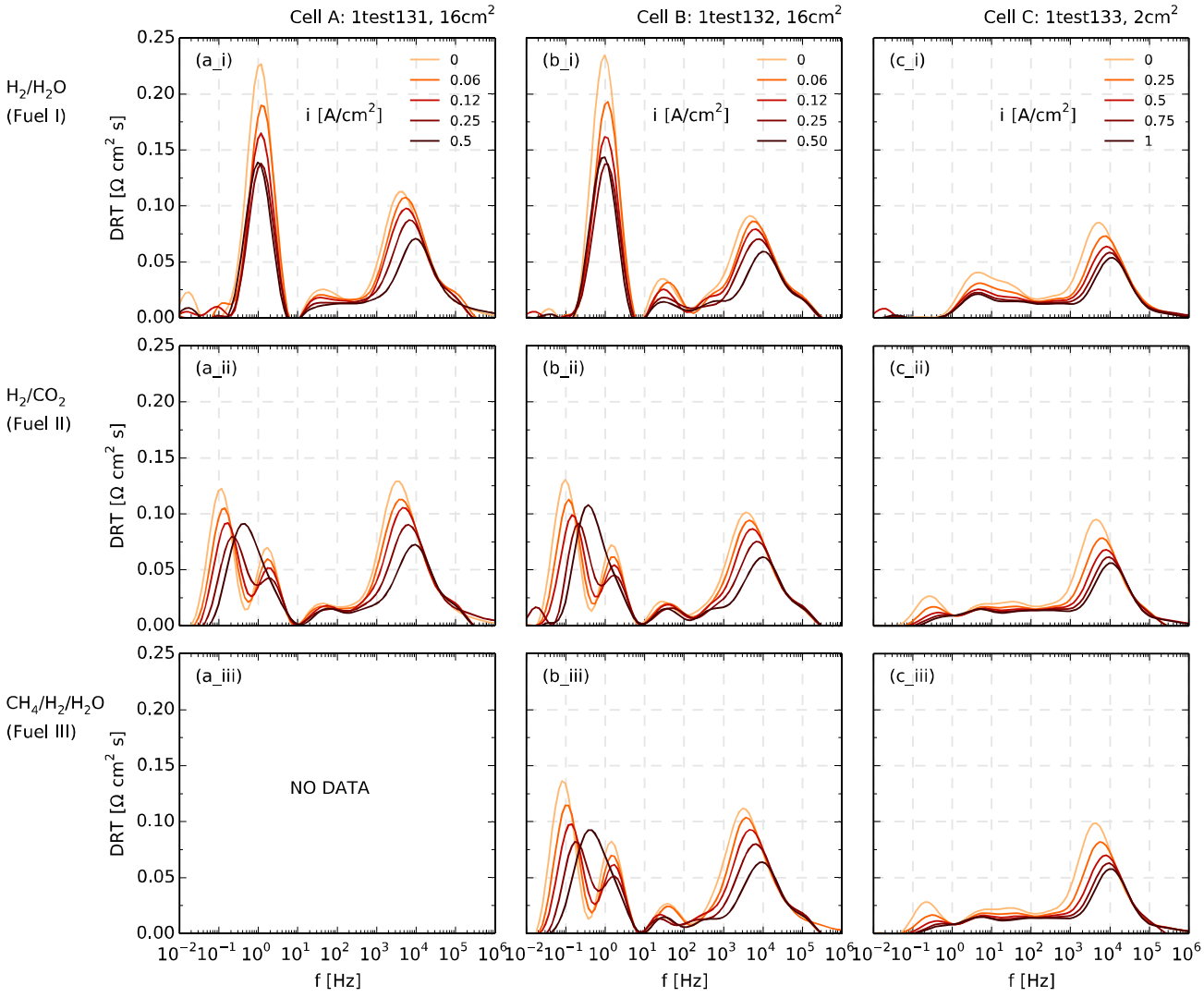

Figure 3.3-4: DRTs of cells A, B and C calculated from impedance spectra recorded during operation with the three fuels Fuel I, Fuel II and Fuel III at 700 °C showing the evolution of ASRs of individual processes from OCV to + 0.5 A/cm². No data is available for subplot a_iii however, based on tests on a sister cell (not reported) as well as subplots b_ii vs. b_iii, the expected DRT trends are expected to be similar to those in subplot a_ii.

3.3.2.2 Current Density vs. Overpotential Relations of Individual Processes

Based on the concept description in section 3.3.1.4, overpotential contributions of the different dynamic processes were calculated from the recorded spectra (cf. DRTs in Figure 3.3-4). These overpotential contributions have been displayed in Figure 3.3-5 for cells A, B and C in the three investigated fuels. Thereby "Ref.", "gas conv.", "gas diff.", "fuel electrode", "ohmic" and "ox. electrode" correspond to contributions from the low frequency reformate process, gas conversion at the fuel electrode, gas diffusion at the substrate, fuel electrode electrochemical processes, ohmic contributions and oxygen electrode electrochemical processes respectively.

It is important however to note that each overpotential value is the average overpotential of the component, e.g. along the flow channel, the overpotential might be less than and greater than this value at the inlet and outlet respectively, depending on the gas composition, temperature changes due to reactions, etc. These gradients will be larger at higher fuel utilization, as is the case in the 16 cm^2 data compared with the 2 cm^2 data.

3.3.2.2.1 Reference Case

If Cell A, fuel mixture *Fuel I* i.e. Figure 3.3-5 (a_i) and current density 0.4 A/cm^2 (if not otherwise stated) are considered the reference then the following claims can be made about the investigated cell system at 700 °C:

- The fuel electrode electrochemical reactions (charge transfer, ionic transport and diffusion in the functional layer) make the largest overpotential contributions (ca. 39 % of total overpotential drop). This implies that engineering efforts to optimize cell performance should focus on the fuel electrode.
- Gas conversion resistance has the second largest overpotential contribution. (ca. 35 %)
- The voltage drop due to ohmic losses across the electrolyte accounts for 20 % of the total voltage drop and thus half as much as in the fuel electrode.
- The oxygen electrode accounts for the smallest share of the total potential drop. (ca. 4 % of the total overpotential drop).
- Gas phase diffusion equally contributes the least (ca. 4%) to the voltage drop.

From a global perspective it can be deduced from Figure 3.3-5 (a_i) that in the current density range 0 to 0.5 A/cm^2 gas diffusion displays a linear relationship between current density and overpotential[40]. This suggests that the change of gas diffusion ASR in the investigated range is negligible[41]—this will be addressed in more detail in section 3.3.2.3. The voltage drop across the electrolyte displays a linear relationship between current density and overpotential. This suggests that the impact of joule heating (for $j < 0.5$ A/cm^2 ca. < 2 °C increase of temperature[42]) in the investigated current density range is not enough to visibly curb the overpotential trend of

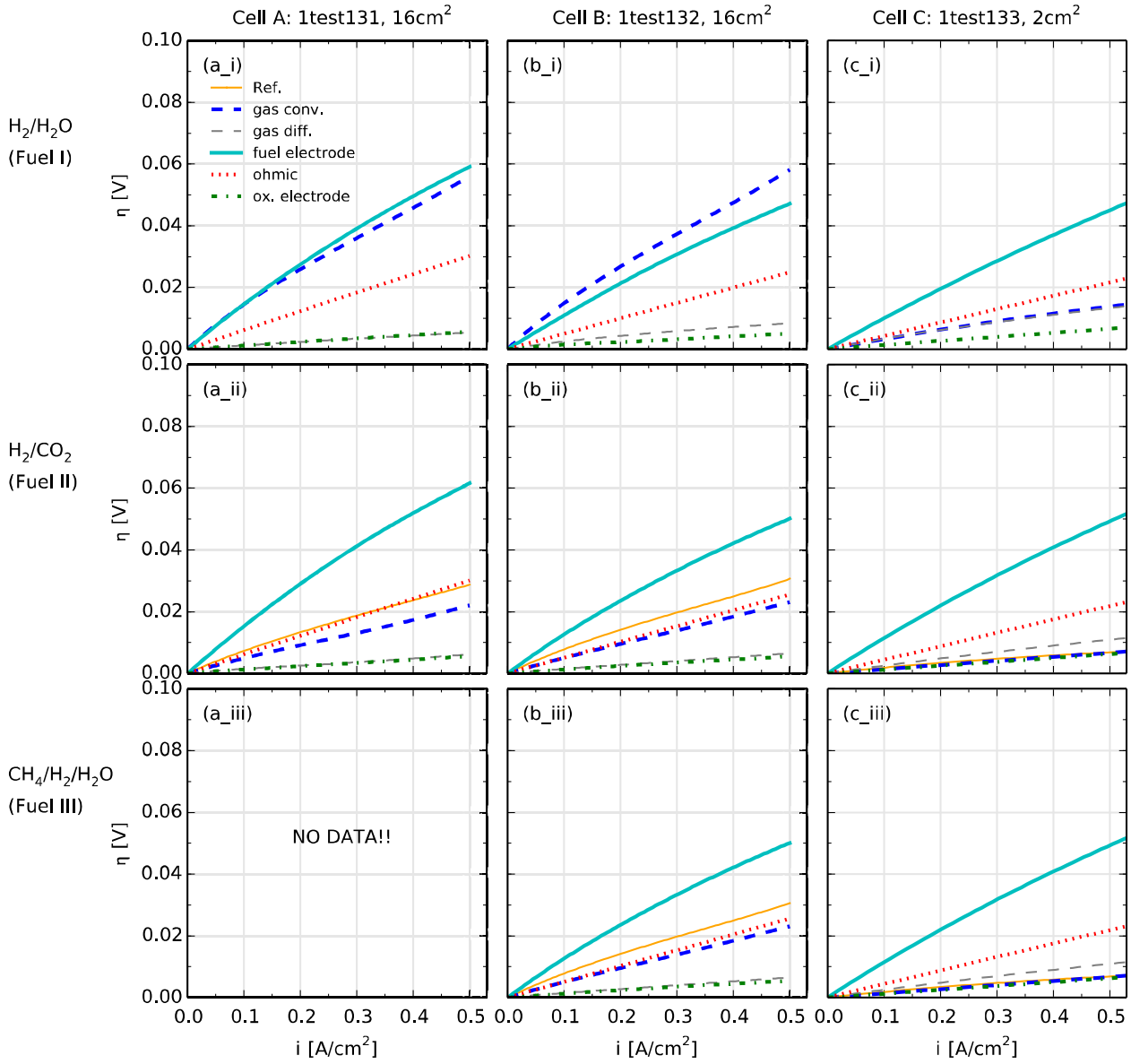

Figure 3.3-5: Current density, i vs. overpotential η relations for all processes for cells A, B and C in the three fuels Fuel I, Fuel II and Fuel III at 700 °C. No data is available for subplot a_iii however, based on tests on a sister cell (not reported) as well as subplots b_ii vs. b_iii, the expected overpotential trends are expected to be similar to those in subplot a_ii.

the electrolyte resistance. The electrochemical reactions at the fuel electrode on the other hand shows non-linear current density vs. overpotential relations[42] at 700 °C [iii]. The nonlinearity is such that the overpotential deviates towards "smaller" values with increasing current density (decrease in slope). Independent of the nature of the pure kinetically defined course, the curbing away from linearity may partly be attributed to:

a. Increasing temperature under current load as a result of joule heating across the electrolyte

b. Increasing temperature due to the exothermic hydrogen oxidation at the fuel electrode.

c. At the fuel electrode, the increasing steam content at the triple phase boundaries (TPB) with increasing current densities results in increased electrochemical reaction rate[3,42] and thus reduced ASR.

d. Butler-Volmer type kinetics

At the oxygen electrode the overall temperature effect related to the electrochemical reactions is exothermic in nature due to dissociation and ionization enthalpies of oxygen molecules and atoms respectively. However major oxygen electrode processes such as surface exchange and bulk ion transport are thermally activated with activation energies for K^{δ} and D^{δ} of 1.05 eV and 1.26 eV respectively[2]. As such the slightly decreasing slope at higher current densities suggests that the heat from electrochemical reaction and joule heating are influencing the kinetics. The effect is much lower than at the fuel electrode if considered that the oxygen electrode is heating up less (an order of magnitude thinner) and that the air is supplied at 40 l/h against 7 l/h for fuel.

It is also important to note at this junction that in SOFC or SOEC modes the change in entropy at the electrode, where an oxygen molecule "disappears" or is "created" respectively, is much larger than that at the fuel electrode where 1 molecule of H_2 is converted to 1 molecule of H_2O. This means that if all external influences that would retain or generate thermal energy in the system (non-ideal diffusion, finite heat exchange rate, finite electrolyte ion conductivity) are eliminated and ideal heat conduction of component materials is assumed, and only the reaction heat balances are considered then the heat produced or consumed at the oxygen electrode determines the overall heat evolution of the cell.

This can be elucidated for example by calculating the involved thermal components $T\Delta S$ of the half reactions involved during SOFC mode operation at 800 °C in which 1 mol of H_2O is produced from 1 mol of H_2 and half a mol of O_2. These are reactions (2-1) for the oxygen electrode and reaction (2-2) for the fuel electrode. Using specific heat capacities from the VDI Wärmeatlas[43] the calculated $T\Delta S$ for O_2, H_2 and H_2O are – 264 kJ/mol, - 184 kJ/mol and + 253 kJ/mol. However at the oxygen electrode, only half of the oxygen is involved in the oxygen electrode half reaction. This means that total $T\Delta S$ at the oxygen electrode is **– 134 kJ/mol** (= 0.5 · - 264 kJ/mol) and **+ 69 kJ/mol** (= - 184 kJ/mol + 253 kJ/mol) at the fuel electrode. Clearly, the thermal contribution of the exygen electrode is double that at the fuel electrode. The overall thermal contribution is then – 134 kJ/mol + 69 kJ/mol = - 65 kJ/mol. This corresponds to the heat evolved during SOFC mode as a result of the

[iii] The trend of the oxygen electrode cannot be unambiguously discussed due to the very small resistance contribution from this electrode

electrochemical reactions alone. The same amount of thermal energy is also consumed in the reverse mode, i.e. in SOEC operation. In a similar manner consistent overall reaction enthalpy, ΔH and Gibbs free energy ΔG of - 251 kJ/mol and - 187 kJ/mol respectively were calculated for 800 °C.

3.3.2.2.2 Influence of Electrode Microstructure

A comparison of the reference—Cell A, with Cell B that had a finer fuel electrode microstructure at 0.4 A/cm^2 reveals a decrease in the overpotential due to electrochemical reactions from 49.7 mV to 39.2 mV (i.e. from 39 % to 33 %). This is more visible by comparing Figure 3.3-5 (a_i) vs. (b_i). The result is anticipated since a finer microstructure is translated into an increase in the amount of electrochemically active TPBs and an effective decrease in ASR or overpotential. The trend is consistent with the DRTs shown in Figure 3.3-4.

On the contrary, the gas conversion and gas diffusion overpotentials increase slightly from 46- to 48 mV and from 4- to 8 mV (i.e. 36- to 40 % and 3- to 6 %) respectively. These are small and within error margin. The oxygen electrode overpotential as expected is not affected by the change in microstructure of the fuel electrode.

The polarization related to ohmic losses decreases from 24- to 20 mV (i.e. from 19- to 17 % of total polarization). This decrease is not significant and on the contrary indicates good reproducibility of the electrode manufacturing, and characterization procedure at DTU Energy.

3.3.2.2.3 Influence of Fuel Mixture

By comparing operation in *Fuel I* and *Fuel II* i.e.Figure 3.3-5 (a_i) vs. (a_ii) or (b_i) vs. (b_ii) a drastic reduction in the gas conversion related overpotential can be observed. At 0.4 A/cm^2 the change in Cell A is from 46 mV in *Fuel I* to 17 mV in *Fuel* II (i.e. from 35- to 14 % of total potential drop) and in Cell B from 48 mV in *Fuel I* to 19 mV in *Fuel II* (i.e. from 40 to 16 %).

In the reformate fuel *Fuel II,* for Cell A the extra process at ca. 0.1 Hz in Figure 3.3-4 (a_ii) appears and accounts for 24 mV (19 %) of the total voltage drop. For Cell B the process accounts for 24 mV (21 %) in both *Fuel II* and *Fuel III*.

As would be expected, no significant change is observed in the overpotential contribution of the oxygen electrode or electrolyte as a result of change in fuel mixture from H_2/H_2O to either of the reformate fuels. The change of fuel also does not impact the fuel electrode electrochemical reaction rate significantly. A slight increase in the overpotential curve of the fuel electrode can be observed when comparing *Fuel I* and *Fuel II* of Cell A. At 0.4 A/cm^2 the change is from 50- to 52 mV (i.e. from 39 % to 41 % of total overpotential). In Cell B, the change is from 39- to 42 mV (i.e. from 33- to 36 %) in both reformate fuels. These findings are consistent with expectation

considering that H_2 is preferentially[44] oxidized (activation energy, 1.1 eV)[3] compared with CO (activation energy, 1.23 eV)[4] which is partly converted through the fast water gas shift reaction[38].

3.3.2.2.4 Comparison of Fuel Electrode Kinetics

The principal objective of this work was to investigate the kinetics of the fuel electrode in three different fuels consisting of two model reformate fuels and a reference binary hydrogen/steam fuel. Furthermore, it was aimed at investigating the extent to which the microstructure influenced kinetics in these fuels. This information already contained in Figure 3.3-5 has been extracted and compared separately in Figure 3.3-6 for the cells Cell A and Cell B. Both figures show that under the investigated conditions, the Ni/YSZ fuel electrodes of the investigated cells display comparable kinetics in the reformate fuels and slightly better performance in hydrogen/steam fuel. A significant improvement in the kinetics is also observed for the cell with a finer microstructure.

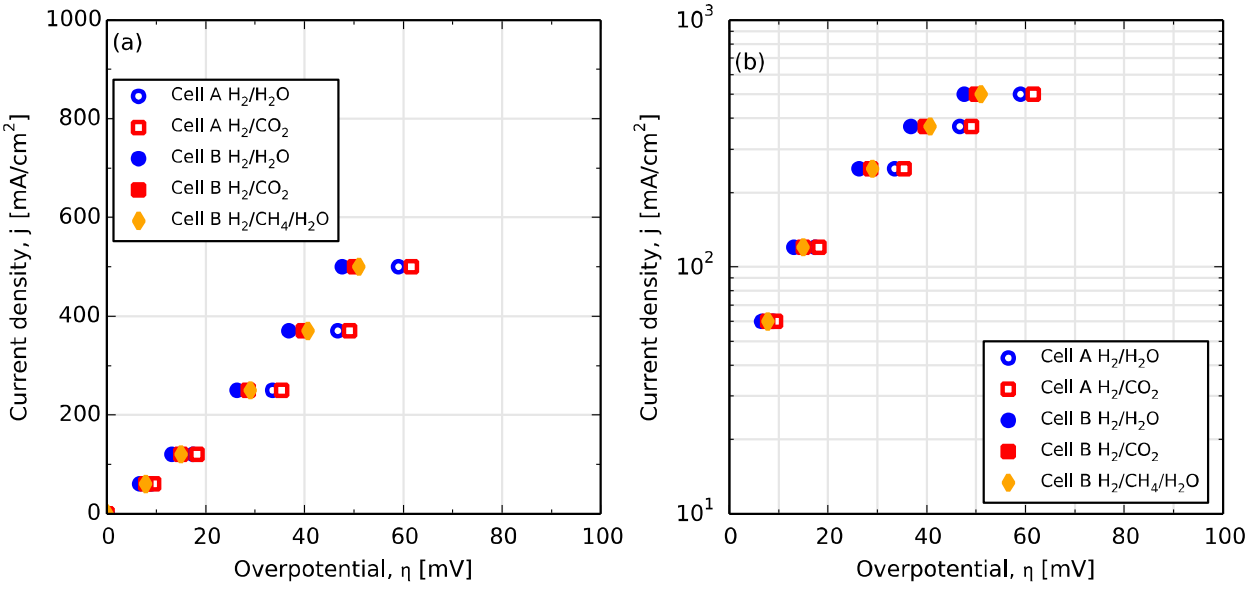

Figure 3.3-6: Current density vs. overpotential relations for the three fuels H_2/H_2O (*Fuel I*), H_2/CO_2 (*Fuel II*) and $H_2/CH_4/H_2O$ (*Fuel III*) at 700 °C for Cell A (reference cell) compared with Cell B (a finer fuel electrode microstructure). Data in the methane-based reformate could not be recorded for Cell A. The OCV in all three fuels was 1030 mV and the fuel utilization at 0.5 A/cm² was 60 %. Linear representation in (a) and logarithmic scale representation in (b)

As mentioned in section 3.3.2.2.1 the curves in Figure 3.3-6 are intrinsically accompanied by increase in temperature and steam content with increasing current density. These influences introduce a non-linearity and need to be isolated in an appropriate cell geometry in a bid to obtain an analytical description of pure Ni/YSZ

kinetics. This will be done in section 3.4.1.3. The KIT test set-up minimizes steam content increase by minimizing gas conversion through very high flow rates and by having cells of only 1 cm^2 active electrode area.

3.3.2.2.5 Influence of Fuel Utilization

The fuel utilization at a given operation point and current density reveals the amount of the inlet fuel that is actually converted to release the measured electric current. For SOC operation, it would be of economic sense to convert as much of the inlet fuel as possible since unconverted fuel must be either wasted or recycled—partially or fully depending on the system. However, for long-term stability of the cell, it is equally important to know how the different processes are affected by high fuel utilization. A decrease in fuel utilization leads to an increased cell performance, as fuel conversion and diffusion losses are diminished[45].

The fuel utilization can be varied by changing the active electrode area (at constant gas flow) or by changing the fuel flow rate across the electrode. At much higher flow rates the fuel does not dwell long enough over the electrode for most of it to be electrochemically converted; meanwhile a smaller active electrode area leads to the same result as the fuel mixture crosses the electrode faster than the fuel can be converted enough. In both cases, the resistance associated with fuel conversion would be reduced.

Cell C differed from Cell B in that it had an active electrode area of 2 cm^2 instead of 16 cm^2 (cf. Figure 3.2-1). In Figure 3.3-5 therefore, the observed differences between overpotential trends of the individual processes of Cell B against those of C can be attributed to the change in fuel utilization.

Comparing the trends of both cells in Figure 3.3-5 the first important observation is that the total overpotential (not plotted) across the cells drops from Cell B (ca. 118.5 mV in *Fuel I* at 0.4 A/cm^2) to Cell C (ca. 82.8 mV in *Fuel I* at 0.4 A/cm^2).

Secondly, the course of the overpotential related to the fuel electrode electrochemical reactions is quantitatively similar for both cells in all fuels. The implication is that in larger cell systems like those in commercial stacks the overpotential related to electrochemical reactions at the fuel electrode will be less determining, than for instance the polarization related to gas conversion (e.g. cf. Fig. 2.59 in Ref. [15]).

Indeed, there is a major difference in the overpotential contributions related to gas conversion in all fuels. At 0.4 A/cm^2 in *Fuel I* the process is accounting for 47.6 mV (40 %) of total overpotential in Cell B but in cell C its contribution is only 11.8 mV (14 %). In reformates the drop is from 18.4- to 5.4 mV (16- to 6 %). However, the relative drop in gas conversion overpotential contribution (not normed with the total overpotential drop) from Cell B to Cell C is 75 % in *Fuel I* and 71 % in both reformates.

For an H_2/H_2O binary fuel composition, the fuel utilization f_u at a given current density can be calculated based on Faraday´s law as displayed in equation (26).

$$f_u = \frac{jblRT_0}{zFP_0\varphi_{H_2} \cdot 1000 \cdot 3600} \quad (26)$$

In equation (26) j is the current density in A/m^2, b and l are width and length of the cell in meters perpendicular to and along the flow direction respectively. R and F are the gas and Faraday constants in J / mol /K and As / mol respectively, T_0 the reference flow temperature (= 273.15 K), P_0 the reference flow pressure (101325 Pa), φ_{H_2} the hydrogen flow rate[iv] in liter per hour and z the number of electrons per hydrogen molecule (2).

With reference to equation (26) and the fact that although Cell B and Cell C have the same width (b = 0.04 m) they have different lengths (l = 0.04 m for Cell B and 0.005 m for Cell C) it is evident that a smaller fuel utilization for Cell C for a given fuel flow rate φ_{H_2} and current density j explains the difference observed in the according overpotentials in Figure 3.3-5. Furthermore, for given H_2 and H_2O inlet mole fractions x_{i,H_2} and x_{i,H_2O} the average corresponding equivalents under load can be calculated through equations (27) and (28).

$$x_{H_2,average} = \left(1 - f_{u,eff}\right) \cdot x_{i,H_2} \quad (27)$$

$$x_{H_2O,average} = \left(1 - x_{H_2,average}\right) \quad (28)$$

In equations (27) and (28) $f_{u,eff}$ is the effective utilization ($= f_u/2$) upon assumption of uniform and linear utilization along the cell. Further, equation (28) is based on the fact that in the binary H_2/H_2O fuel mixture, the sum of the component mole fractions amounts to unity. The fuel utilization as well as the average hydrogen and steam mole fractions $x_{H_2,average}$ and $x_{H_2O,average}$ respectively under current have been calculated for Cell B and Cell C and displayed in Figure 3.3-7 (a) and (b) respectively. From the figures, at 0.5 A/cm^2 the fuel utilization in Cell B is 60 % against 7.5 % for Cell C and corresponding average steam mole fractions are 44- and 23 % respectively.

[iv] For corresponding φ_{H_2} in reformates; If the appropriate inlet O_2 flux to produce the required H_2O is $\varphi_{O_{2,in}}$ then twice as much H_2 will be converted to produce H_2O. In the CO_2–based reformate therefore, $\varphi_{H_2} = \varphi_{H_{2,in}} - 2 \cdot \varphi_{O_{2,in}}$. In the CH_4 – based reformate, 1 mol of CH_4 through steam reforming and shift reaction (and 2 mol of H_2O) is converted to 4 mol of H_2 so that in CH_4 –based reformate $\varphi_{H_2} = \varphi_{H_{2,in}} - 2 \cdot \varphi_{O_{2,in}} + 4 \cdot \varphi_{CH_{4,in}}$

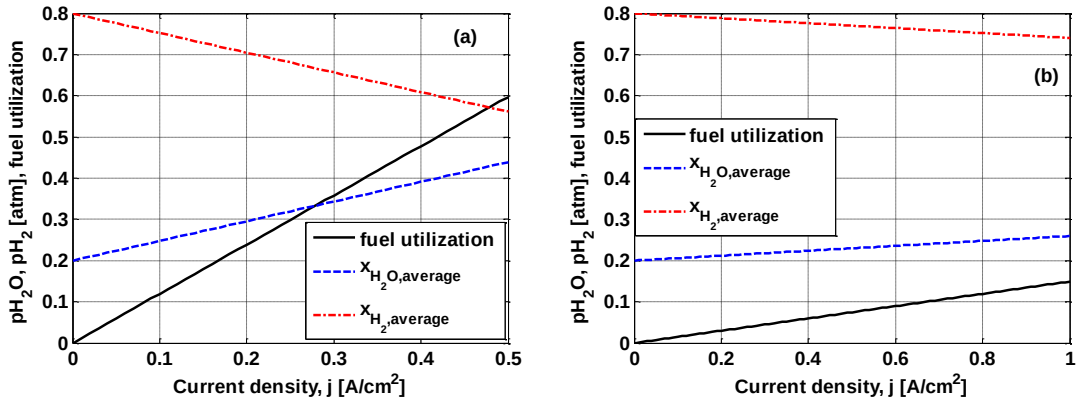

Figure 3.3-7: Evolution of fuel utilization and the average steam and hydrogen mole fractions under load for (a) Cell B and (b) Cell C

The above discussions have shown that at a given current density and flow rate the difference in active electrode area results in a different fuel utilization, which in turn results in differences in average mole fractions of component gases, corresponding gas conversion and diffusion ASRs or overpotentials.

In a first approximation the consistency of the herein observed gas conversion and substrate diffusion ASRs (in the herein used test set-up) with theoretical predictions will be further elucidated in section 3.3.2.3.

3.3.2.3 Gas Conversion and Concentration-Related Processes

3.3.2.3.1 H_2/H_2O Binary Fuel

Gas Conversion

The AC gas conversion ASR has been described for H_2/H_2O (or CO/CO_2) fuel mixtures in a continuously stirred tank reactor (CSTR)[35] type set-up at OCV as well as under load for a plug flow reactor (PFR)[46] set-up. The ASRs for both cases are described by equation (29), whereby m is 4 for the AC CSTR and 8 for the PFR flow type. This means that the gas conversion ASR based on the PFR model is expected to be half of that based on the CSTR model.

$$R_g = \frac{RT}{mF^2 J_i}\left(\frac{1}{x_{i,H_2}} + \frac{1}{x_{i,H_2O}}\right) \quad (29)$$

In equation (29) R_g represents the gas conversion ASR, R, T and F the gas constant in J / mol /K, absolute temperature in K and Faraday constant in As / mol respectively. The area specific inlet flow rate J_i is in mol /s /m^2 and x_{i,H_2} and x_{i,H_2O} are inlet mole fractions of gases H_2 and H_2O respectively.

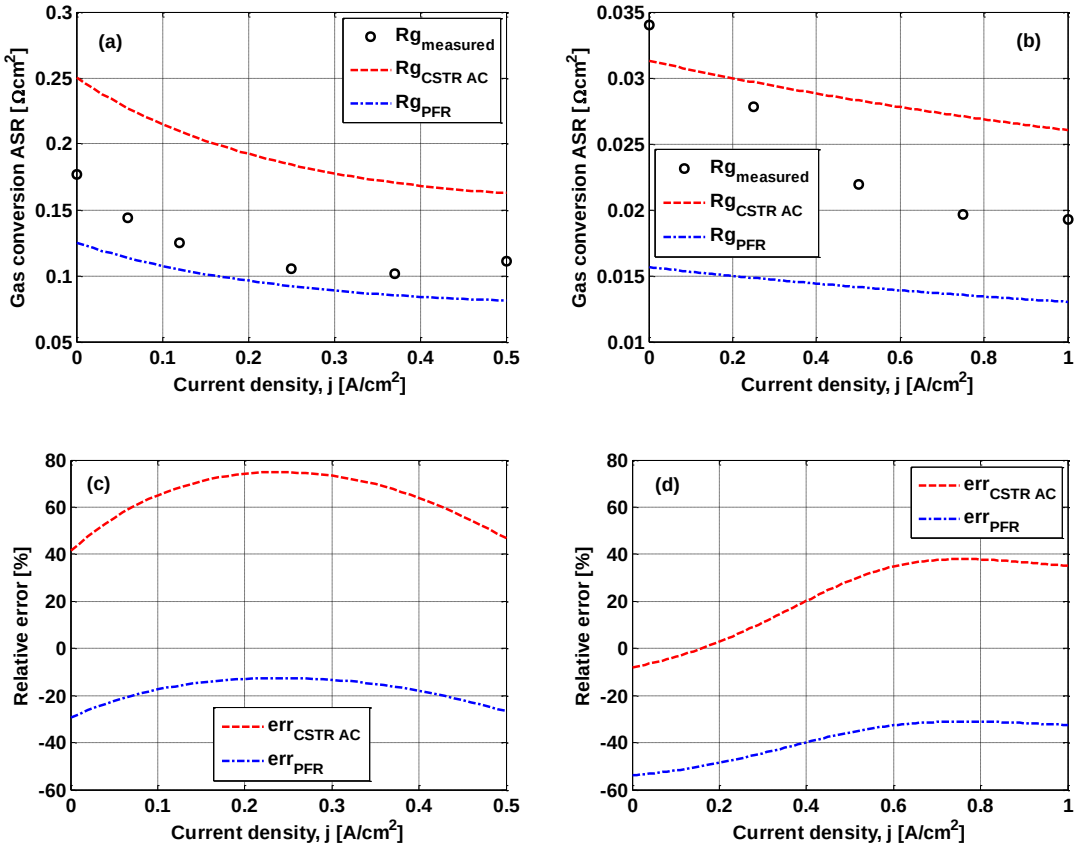

Figure 3.3-8: (a) Gas conversion ASR in the 80/20 H_2/H_2O fuel mixture at 700 °C compared with ASR predictions from the plug flow and CSTR AC models for the 16 cm² Cell B and (b) the 2 cm² Cell C. (c) Relative errors between model prediction of the gas conversion ASR and measurement for Cell B and (d) Cell C

The gas conversion ASR $R_{g_{measured}}$ in a 20/80 H_2O/H_2 fuel obtained from the CNLS fits at different current densities, and which has been integrated with current density to obtain the corresponding overpotential curves in Figure 3.3-5 has been compared with the above described two models for the 16 cm^2 Cell B and the 2 cm^2 Cell C and results displayed in Figure 3.3-8 (a) and (b) respectively.

In the calculations, the average hydrogen and steam mole fractions calculated using equations (27) and (28) respectively and displayed in Figure 3.3-7 (a) and (b) for Cell B and Cell C respectively have been used. The corresponding relative errors are displayed in Figure 3.3-8 (c) and (d). From these the CSTR AC model shows its best approximation of the measured gas conversion ASR for both cells at OCV. However, Cell B is approximated

with a relative error of 40 % against -8 % for Cell C. Further, whereas the CSTR AC model approximates Cell C data in the current density range 0 A/cm^2 – 1 A/cm^2 with a maximum error of 38 % at 0.76 A/cm^2 Cell B is approximated with a maximum error of 75 % at 0.24 A/cm^2.

Thus the geometry of Cell C under the investigated conditions of temperature, fuel mixture, flow rate and AC signal amplitude of 85 mA best approaches that necessary for the assumption of CSTR model. Furthermore, the OCV error of Cell B is negative, i.e. the AC CSTR model underestimates the measured data somewhat, but only by a factor 1.1.

On the other hand the plug flow model[46] gives a much better approximation of Cell B data with a maximum error of - 29 % at OCV meanwhile Cell C is approximated to a lesser degree, with a maximum error of - 54 % at OCV. Consistent with reported results from measurements done on similar cells and similar test set-ups, the Cell B data lie between the CSTR and plug flow model predictions[41].

A question which arises from the error curves of both cells in Figure 3.3-8 (c) and (d) is why the plug flow reactor model predicts Cell C data with a greater error than Cell B. Assuming all of the 85 mA excitation is converted, then the corresponding current densities would be 5.3- and 42.5 mA/cm^2 for Cell B and Cell C respectively. With these the corresponding average fuel component change Δx is 5.1·10^{-3}, a value which under load fulfills the condition $\Delta x \ll x_i$ better in Cell B than in Cell C (cf. Figure 3.3-7 (a) and (b)).

Gas Phase Diffusion

Contrary to gas conversion, gas diffusion overpotential contributions in Figure 3.3-5 increase slightly from Cell B to Cell C in all fuels. Since both gas conversion and gas diffusion are concentration-related processes this observation suggests a strong relation between both processes. As demonstrated by Jacobsen *et al*.[47] for these two processes, a Warburg diffusion impedance is found at higher frequencies, meanwhile the dimensions of the gas volume relative to the support (substrate) determines if the low frequency part tends towards the real axis as a Nernstian diffusion impedance or semicircle.

The relationship in equation (30) has been suggested[40] to calculate the ASR of a finite diffusion limitation found around 10 Hz – 100 Hz—the frequency range at which the diffusion impedance in this work lies (cf. DRTs in Figure 3.3-2). In this work, the height of the corrugated nickel current collection mesh at the fuel electrode is 850 µm against a substrate thickness of ca. 300 µm and the flow rate is 7 l/h in the H_2/H_2O fuel. Primdahl *et al*.[40] could demonstrate that the measured diffusion resistance was that of the stagnant layer above the cell; that is not necessarily the case in this work. Primdahl´s fuel electrode thickness was 40 µm – 50 µm thick with 1 to 3 layers of Ni felt above the cell and a total flow rate of 6 l/h.

$$R_D = \left(\frac{RT}{2F}\right)^2 \frac{l}{PD_{eff}} \left(\frac{1}{x_{H_2,B}} + \frac{1}{x_{H_2O,B}}\right) \quad (30)$$

In equation (30) R_D is the diffusion resistance, D_{eff} the effective diffusion coefficient, P the pressure, $x_{i,B}$ the molar fraction of species i in the bulk gas, l the bulk height. R, T and F have their usual meanings. Through a binary[v] gas variation of H_2 and H_2O in the pH_2O range 10 % – 40 % at 800 °C in Cell B, the measured diffusion resistances obtained through CNLS fit on the ECM in Figure 3.3-1 (without the last RQ-element for the reformate process) were fitted with equation (30) to obtain the ratio $\frac{l}{D_{eff}}$. From the fits the value of 31.3 m/(m²/s) was obtained. Due to the negligible temperature dependence of the diffusion ASR, this ratio will be assumed to be the same at 700 °C. Furthermore Primdahl *et al.*[40] have suggested that the peak frequency f_s of the Warburg impedance can be approximated by:

$$f_s \approx \frac{2.53 D_{eff}}{2\pi l^2}. \quad (31)$$

From the DRTs in Figure 3.3-4, the diffusion peak frequency f_s is located at ca. 40 Hz for both cells B and C. With the two values and equation (31) an effective diffusion coefficient D_{eff} of $1.027 \cdot 10^{-5}$ m²/s is obtained—a value in the same order of magnitude as the effective diffusion coefficients of H_2 and H_2O in the Ni/YSZ substrate[42].

With the obtained D_{eff} and the ratio $\frac{l}{D_{eff}}$ of 31 m/(m²/s) a bulk thickness l of 321 µm is obtained—this matches perfectly with the substrate thickness of both cells B and C of ca. 300 µm.

A comparison between measured and calculated diffusion ASRs for Cell B and Cell C is displayed in Figure 3.3-9 (a) and the corresponding errors in Figure 3.3-9 (b). A major consistency is that the calculated values for Cell C under load are larger than those of Cell B in accordance with the lower average steam partial pressure under load for Cell C. The next consistency involves the better accuracy in both cells at OCV, with less than 20 % error since a linear dependence between steam partial pressure and current density is only valid for low current densities [40]. Finally, Cell C data is approximated with a lower error than Cell B in the whole investigated current density range suggesting that in the used set-up and under the investigated conditions, the geometry of Cell C results in a better approximation of perfect one-dimensional diffusion through the 300 µm thick porous Ni/YSZ substrate. Although decreased in size, the shift to higher frequencies of the gas conversion peak and increased overlap with the diffusion peak increases the possibility of overestimating the diffusion ASR in the CNLS fit. The increasing

[v] Variation of pH_2O without balancing, so that sum pH_2O + pH_2 is always unity

relative error with increasing current density for both cells stresses the inadequacy of the used model for estimating diffusion ASR under load.

To achieve a better approximation of the gas diffusion ASR under load, microstructural information such as average pore radius of the substrate is required. With this, the Knudsen diffusion coefficient can be determined and together with the bulk diffusion coefficient the molecular diffusion coefficients of H_2 and H_2O calculated. With the known bulk height of ca. 300 µm the structural parameter ψ can be determined from a binary H_2/H_2O variation. The diffusion ASR can then be calculated with equation (30) whereby instead of D_{eff} weighting the last term, ψ does and the individual gas components inside the last term are weighted by the corresponding calculated molecular diffusion coefficients. Details are given in literature[3,42]. The calculation of the substrate diffusion overpotential through the Nernst equation and accounting for bulk and Knudsen diffusions is described in section 4.2.4.

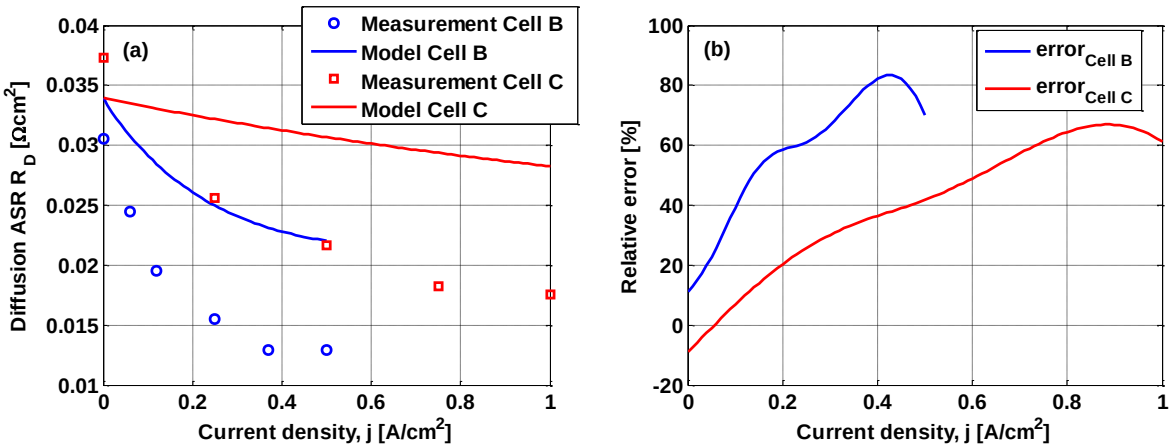

Figure 3.3-9: Diffusion ASR in the 80/20 H_2/H_2O fuel mixture, Fuel I at 700 °C compared with ASR predictions from equation (30)

For a more detailed investigation of the OCV situation, the modeling work of Jacobsen *et al.*[47] for binary systems like the H_2/H_2O fuel investigated herein was employed. They presented two model approaches for the SOCs having diffusion in the substrate and fuel conversion in the gas volume outside the substrate (support). The model approaches, composed of a CSTR on the one hand and a plug flow on the other hand, qualitatively produced the same result, whereby a Warburg diffusion impedance is seen at high frequencies and depending on the dimensions of the gas volume relative to the support layer tends towards the real axis as Nernstian diffusion impedance or semicircle dominating the low frequency region.

From Figure 3.3-8 (b) it was shown that the CSTR model best described the conversion ASR of Cell C especially at OCV. Furthermore the diffusion ASR of Cell C has been shown to be reproduced best at OCV (cf. Figure 3.3-9 (b)) by equation (30) also derived for a CSTR type flow.

To verify the modeling predictions of Jacobsen *et al*. [47] the gas "volume above the substrate" was systematically varied, by varying the inlet fuel flow rate of Cell C at 800 °C for pH_2O ratios of 0.2- and 0.6 atm. The results are displayed in Figure 3.3-10 (a) for the pH_2O = 0.2 atm and (b) for pH_2O = 0.6.

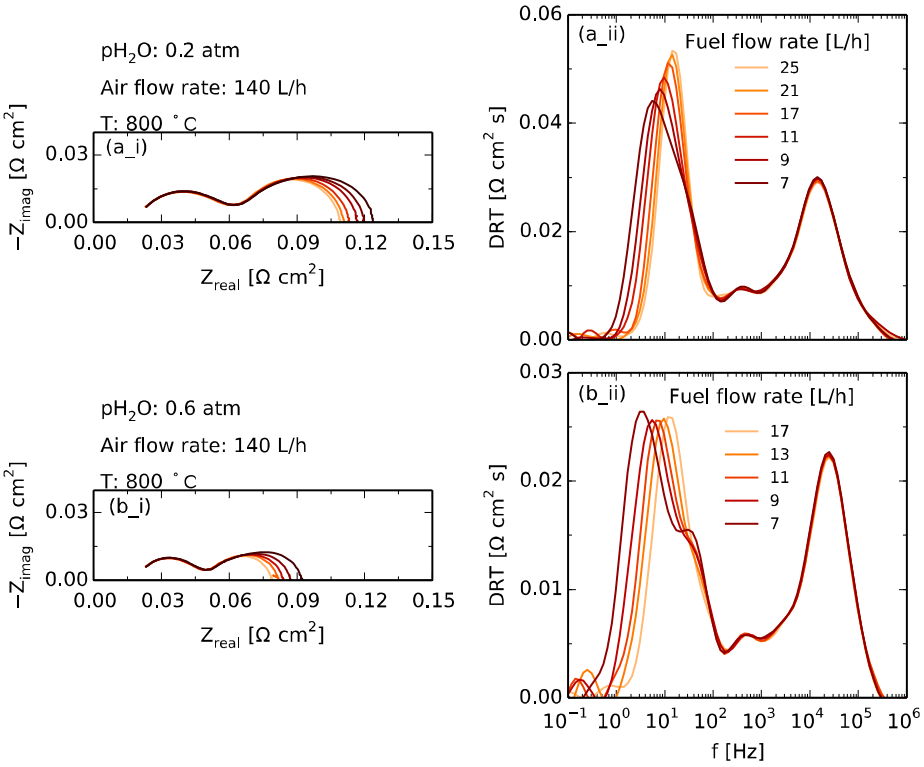

Figure 3.3-10: Variation of fuel flow rate across Cell C at 800 °C for at constant fuel compositions of (a) pH_2/pH_2O of 80/20 and (b) 40/60. The Nyquist representation of the EIS spectra are displayed in subplots x_i, x = a or b and the corresponding DRTs are displayed in subplots x_ii, x = a or b.

From the Nyquist plots of both cases, an outgrowth is observed at low frequencies and DRTs display a drift towards lower frequencies. However, from Figure 3.3-10 (a_ii) a decrease in the peak height of the process at 11 Hz may at first sight be perceived as a decrease in ASR. This is not correct as in reality, the decrease is a result of the characteristic frequencies of both processes overlapping less due to the drift to lower frequencies of the gas conversion process.

The increasing gas conversion ASR and drift to lower frequencies are better resolved in the fuel with higher pH_2O of 0.6 atm (cf. Figure 3.3-10 (b_ii)). Still, the diffusion process in this figure seems to increase with decreasing

flow rate. Based on the Jacobsen model the diffusion process should not be affected. The increase is thus the overlap at higher frequencies of the increasing conversion peak with the constant diffusion peak.

In earlier comments it was mentioned that at high flow rates, the gas flows across the small area of Cell C faster than enough of it can be converted. In light of, and consistent with the Jacobsen article, it can be concluded that at higher flow rates, the AC signal (at low frequencies) going beyond the substrate into the gas volume "sees the same fuel composition", i.e. no gas is converted.

3.3.2.3.2 Reformate Fuels

To further understand the low frequency concentration-related processes in Figure 3.3-4, impedance measurements were recorded at OCV for the three fuels in Table 3.3-2 for cells B and C in the temperature range 900 °C - 700 °C. Further measurements were conducted at higher fuel flow rate in all three fuel compositions as displayed in Figure 3.3-11.

Temperature Dependency

The main focus of this section will be the course of the low frequency processes i.e. f < 100 Hz in Figure 3.3-11. The frequency range f > 100 Hz contains the well-studied LSC/CGO composite oxygen electrode[48,49] in the range 100 Hz <f < 1 kHz with an activation energy of 123 kJ/mol[49] and the well investigated[34,39,50] Ni/YSZ fuel electrode (f > 1 kHz) with an activation energy of 105 kJ/mol[3].

Considering Cell B alone, Figure 3.3-11 (b_i) displays the known[35,51] negative thermal activation for the gas conversion process (peak frequency at 1 Hz at 900 °C). It is important to note the drift of the process to *higher* frequencies with *decreasing* temperature. In reformate fuels *Fuel II* and *Fuel III* the equivalent process (peak frequency at 2 Hz at 700 °C in both reformates) shows a different thermal behavior displaying a weak positive thermal activation with consistent drift to lower frequencies.

Based on this observation it is evident that the process in the reformate fuels is not a pure gas conversion process like the one in H_2/H_2O fuel. This process by virtue of the used cell geometry and higher flow rates was absent in reference [38] and will be termed *pseudo-gas conversion* in this work. Substrate gas diffusion in all three fuels 10 Hz <f < 100 Hz shows no (or very small) temperature dependence. This is expected since only a very weak negative thermal activation of - 0.024 eV is reported in literature[40].

The low frequency process at 0.1 Hz <f < 1 Hz in reformates displays a *pronounced* negative thermal activation in Cell B. However, contrary to the gas conversion peak in the H_2/H_2O fuel mixture (cf. Figure 3.3-11 (a_i)), the peak drifts to *lower* frequencies with *decreasing* temperatures. Furthermore, the process displays a different activation energy from 750 °C towards lower temperatures. The drift to lower frequencies is consistent with

literature[38]. However the pronounced negative thermal activation digresses from Kromp's results which were based on investigations done on 1 cm^2 SOCs and no thermal activation of the process detected[38].

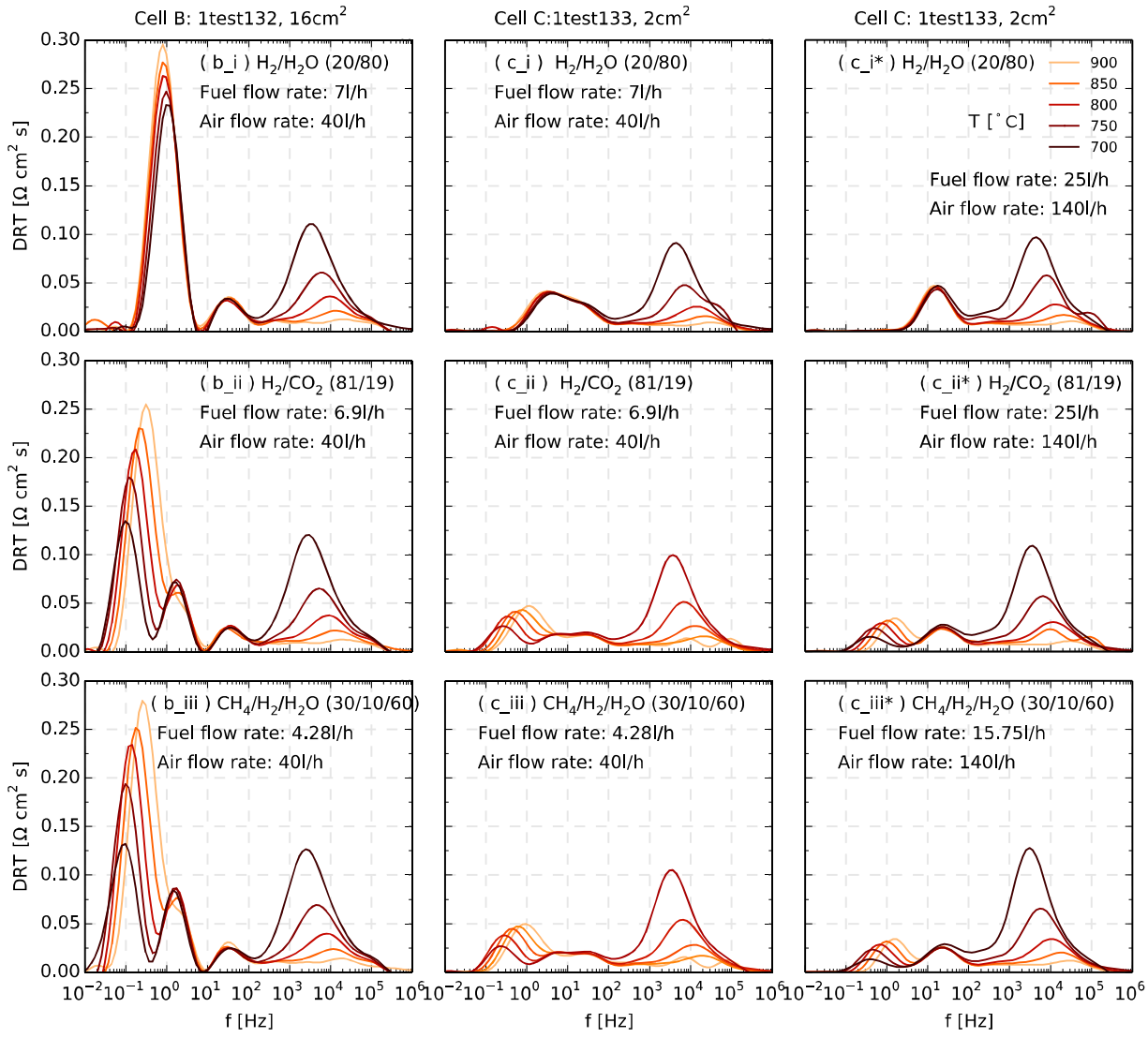

Figure 3.3-11: DRTs of cells B and C calculated from OCV impedance spectra in the three fuels H_2/H_2O (*Fuel I*), H_2/CO_2 (*Fuel II*) and $H_2/CH_4/H_2O$ (*Fuel III*) in the temperature range 900 °C- 700°C. The curves (c_x*, x = i, ii, iii) show tests on Cell C with much higher fuel flow rates than the corresponding (c_x, x = i, ii, and iii) curves

It is important to note that in reference [38] the total fuel flow rate of 250 sccm flowing over an active electrode area of 1 cm^2 corresponds to an effective flow rate of 15 l/h per cm^2. However the reformates *Fuel II* and *Fuel III* in Cell B have area specific flow rates of only 0.43 l/h per cm^2 (= 6.9 l/h/16 cm^2) and 0.27 l/h per cm^2 (= 4.28 l/h/16 cm^2) respectively.

Extrapolating on the conclusions of Kromp *et al*. [38] and bearing in mind that the water gas shift reaction is mildly exothermic[52] it can be hypothesized that the *negative* activation energy is related to the overlapping of the reformate process (catalytic conversion + CO/CO_2 diffusion in the substrate) and the *gas conversion* process in the gas channels. As such: (i) by virtue of its exothermic nature the catalytic conversion of CO to CO_2 via the shift reaction is favored at lower temperatures (decreasing ASR/DRT peak size) but the reaction rate is decreasing (drift to lower frequencies). This reduces the overlap of the reformate process with the conversion processes.

Furthermore with decreasing temperature, the *favored* catalytic conversion is associated with increasing *conversion* ASR with decreasing temperature as observed for the pseudo-gas conversion process at ca. 2 Hz in both reformates for Cell B. (cf. Figure 3.3-11 (b_ii) and (b_iii) at 2 Hz).

For Cell C, with 2 cm^2 active electrode area instead of 16 cm^2, a drastic reduction in all processes below 10 Hz (i.e. the gas concentration related impedance contributions) was observed in all three fuel mixtures as displayed in Figure 3.3-11 (c_i), (c_ii) and (c_iii). In a similar manner as done above, the flow rates for Cell C per active electrode area in the reformates *Fuel II* and *Fuel III* are 3.45 l/h per cm^2 (= 6.9 l/h/2 cm^2) and 2.14 l/h per cm^2 (= 4.28 l/h/2 cm^2) respective (cf. 0.43- and 0.27 l/h/2 cm^2 respectively for Cell B). Furthermore, all processes in Cell B with 16 cm^2 active electrode area were present and could be identified in the EIS measurements in Cell C despite the drastic reduction in peak sizes.

<u>Fuel flow rate Dependency</u>

The flow rates of the three fuels for Cell C were increased from 7-, 6.9- and 4.28 l/h[vi] in the fuels *Fuel I*, *Fuel II* and *Fuel III* respectively to 25, 25 and 15.75 l/h respectively (cf. Figure 3.3-11 (c_x) to (c_x*), x = i - iii). It was thereby ensured that the cell voltage as well as equilibrium concentration of the reformate fuels remained unchanged.

By considering the flow rates per unit active electrode area, the reformates *Fuel II* and *Fuel III* have 12.5 l/h per cm^2 and 7.88 l/h per cm^2 respectively against 15 l/h per cm^2 in reference [38]. From Figure 3.3-11 (c_i*) it can be seen that the gas conversion peak in *Fuel I* appears to *vanish.* This is consistent with expectation[47] since according to equation (29) the gas conversion ASR decreases with increasing flow rate J_i and given that the peak frequency of an RQ-element is given by $f_S = \frac{1}{2\pi \sqrt[n]{RY_0}}$,[40] the decreasing ASR translates to a drift to higher frequencies. Consequently, the much diminished ASR either vanishes beneath or overlaps the diffusion peak. A slight increase in the size of the gas diffusion peak was also observed, reflecting the decreased average H_2O content of the fuel at high flow rates, as well as a probably diminished conversion contribution.

[vi] Due to internal reforming and shift reactions that produce more H_2 the comparably low flow rate of *Fuel III* actually becomes a ”faster” flow comparable to that of *Fuel II* and I. (cf. footnote in section 3.3.2.2.5)

Of particular interest is the behavior in the reformate fuels of the *pseudo-gas conversion* peak which is drastically diminished and drifted to higher frequencies such that its DRT peak overlaps with the diffusion peak. This means that the two processes are not separable through DRT under such operation conditions.

The reformate peak at f < 10 Hz is reduced but clearly does not disappear (cf. Figure 3.3-11 (c_ii*) and (c_iii*)). Its temperature dependence is similar to that observed by Kromp *et al.* [38] in 1 cm^2 cells. However, Kromp describes the process as not exhibiting thermal activation behavior and relates it to a coupling of shift reaction and gas phase transport within the substrate.

3.3.2.4 Activation Overvoltage

Whereas ohmic losses occur predominantly across the electrolyte, gas diffusion and gas conversion processes take place in the gas phase in the porous structures and flow fields, activation polarization/overpotential describes the electrochemical loss mechanisms taking place mainly in the vicinity of the electrode/electrolyte interface or three-phase boundary (TPB) where ionic-conducting, electronic-conducting and gas phases meet. The corresponding electrode activation overpotential contributions have been modelled with the widely discussed Butler-Volmer-type equation (32) [4,34,42,53–60].

In this section, the activation polarization of SOC electrodes will be approximated with equation **(32)** for FZJ cells (cf. Type III in Table 3.2-1) at 800 °C in a 50/50 pH_2/pH_2O fuel mixture. For comparison, the activation polarization of the Ni/YSZ fuel electrodes of the DTU Energy cells investigated in herein (cf. Figure 3.3-6) will as well be evaluated with the Butler-Volmer (BV) type equation:

$$j = j_{0,el}\left[\exp\left(\alpha_{el}\frac{n_e F \eta_{act,el}}{RT}\right) - \exp\left(-\left(1-\alpha_{el}\right)\frac{n_e F \eta_{act,el}}{RT}\right)\right]. \qquad (32)$$

In equation (32), $j_{0,el}$ is the partial pressure and temperature dependent exchange current density of the fuel or air electrode, n_e the number of exchanged electrons, which in this case $n_e = 2$, α_{el} the apparent charge transfer coefficient, and $\eta_{act,el}$ the activation overpotential of the according electrode. The exchange current density and activation polarization ASR R_p have be shown[3,4] to be related by equation (33) for the OCV case.

$$j_0 = \frac{1}{R_p} \cdot \frac{RT}{2F} \tag{33}$$

To enable the investigations, impedance spectra were recorded at different current densities in SOFC mode in a stepwise manner from OCV to 1.2 A/cm². Thereby at least 30 minutes were allowed for relaxation before recording. The same evaluation was then repeated in SOEC mode. The spectra for both modes and corresponding DRTs are displayed in Figure 3.3-12. The labels in the figure are based on Ref. [34] whereby through extensive analysis of impedance spectra recorded under OCV conditions for diverse operation conditions 5 individual electrochemical processes were identified. These are related to gas diffusion in the fuel electrode substrate (P_{1A}), coupled charge transfer reaction, ionic and gas phase transport in the fuel electrode (P_{2A}, P_{3A}), gas diffusion in the oxygen/air electrode (P_{1C}, this process is not considered here as the resistance is below 5 mΩ·cm² in air, cf. total polarization, R_p of ca. 90 mΩcm² in the OCV spectra of Figure 3.3-2) and oxygen surface exchange coupled with O^{2-}-diffusion in the LSCF oxygen electrode material (P_{2C}). Because the model is based on spectra recorded under OCV conditions, the model is valid for the SOFC as well as the SOEC-mode.

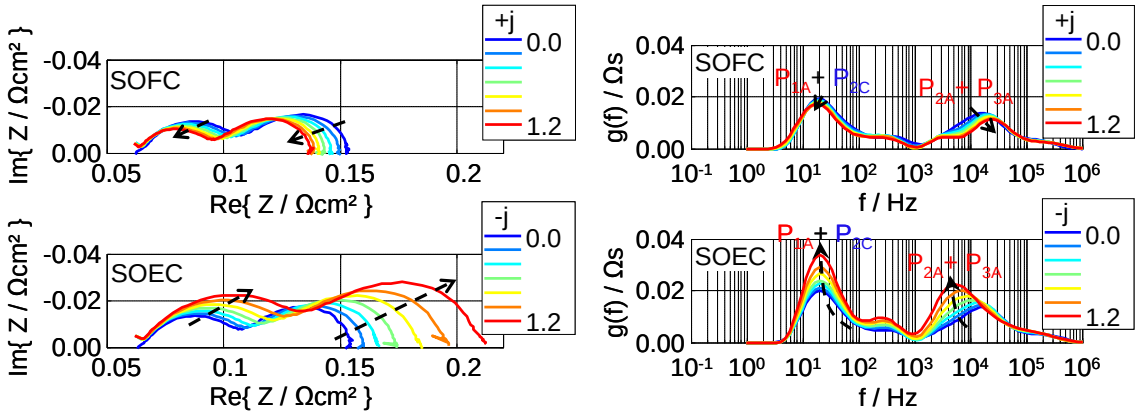

Figure 3.3-12: Impedance spectra of FZJ cells recorded for FZJ cells in the current density range 0 – 1.2 A/cm² in fuel cell or SOFC mode (top left) and in electrolysis or SOEC mode (bottom left). The corresponding DRTs are displayed to the right with SOFC mode DRTs at top right and SOEC DRTs bottom right.

Qualitative analysis of the DRTs in Figure 3.3-12 reveals the following:

i. In SOFC mode the peaks P_{2A} + P_{3A} are decreasing but increasing (to a greater degree) in SOEC mode. This means that the ASR of the fuel electrode electrochemistry or activation polarization is decreasing in SOFC and increasing in SOEC modes.

ii. It can also be seen that whereas peaks P_{1A} and P_{2C} are decreasing slightly in SOFC mode, these peaks are increasing greatly in SOEC mode. This suggests that the ASRs of the air electrode activation (P_{2C}) and fuel electrode diffusion P_{1A} are increasing to a larger extent in SOEC mode than they are decreasing in SOFC mode.

These observations suggest that cell operation in SOEC mode is faced with greater activation and diffusion resistance than SOFC operation. This also means, that fuel electrode diffusion ASR is more likely to influence the value of the charge transfer coefficient determined in SOEC than SOFC mode.

3.3.2.4.1 Parameter Determination

To obtain the current density vs. overpotential relations for the electrodes, the procedure detailed in ref. [3] was literally followed i.e. carrying out a CNLS fit of the spectra with the appropriate[3] EEC model to obtain the ASRs related to activation mechanisms at corresponding current densities, fitting these to a second-order polynomial to obtain an analytical expression relating ASR and current density j, integrating the expression to obtain the corresponding expression for the activation polarization $\eta_{el}(j)$ and by simply inserting the adjusted current densities into the expression, the corresponding overpotentials could be determined. The obtained overpotentials were then fit to equation (32) whereby the exchange current density j_0 was obtained from the OCV spectrum ASR through equation (33).

3.3.2.4.2 Results and Discussion

A plot of the determined current density vs. overpotential curves including the BV fits for both Ni/YSZ electrode and the LSCF oxygen/air electrode are displayed in Figure 3.3-13 for operation in SOFC as well as SOEC modes.

The fitted curves are annotated with the fitted out transfer coefficients α_{el}. These parameters together with the employed corresponding exchange current densities determined through equation (33) are summarized in Table 3.3-3 and for comparison α_{el} values determined[3] from FZJ cells with the same electrode materials solely in fuel cell mode are displayed.

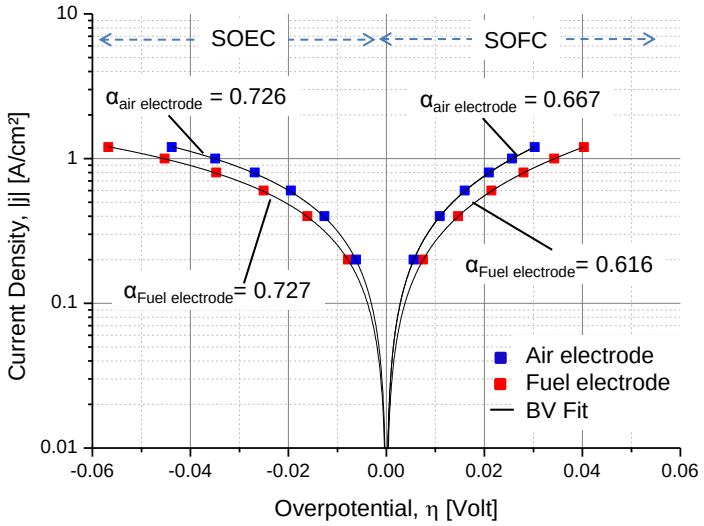

Figure 3.3-13: Current density j as a function of electrode overpotential η with corresponding fits to the BV-type equation (32) of an FZJ SOC at 800 °C in a 50/50 pH$_2$/pH$_2$O fuel and air at the oxygen electrode

Table 3.3-3: Exchange Current densities, $j_{0,el}$ and charge transfer coefficients α_{el} of an FZJ SOC at 800 °C in a 50/50 pH$_2$/pH$_2$O fuel and air at the oxygen electrode obtained from OCV spectra using equation (33) and BV-fit to equation (32) respectively.

Operation Mode	Electrode	$j_{0,el}$ [A/cm^2]	α_{el}	α_{el} [3]	Rel. deviation from values in Ref. [3] [%]
SOFC	Fuel	1.21	0.616	0.590	4.4
	Air	1.62	0.667	0.650	2.6
SOEC	Fuel	1.22	0.727	-	23.2
	Air	1.53	0.726		11.7

The results summarized in Table 3.3-3 suggest the following statements about the investigated cell at 800 °C and pH$_2$/pH$_2$O ratio of 50/50, with air supplied to the oxygen/air electrode:

i. The LSCF air electrode displays larger exchange current densities than the fuel electrode. This means that further optimization of the cell could be directed towards the fuel electrode.

ii. For both electrodes transfer coefficients determined from SOEC mode impedance spectra are higher than those determined from SOFC mode spectra.

iii. In SOFC mode, approximately the same α_{el} is obtained for the air electrode as in Ref. [3] with a 2.6 % deviation. With the same LSCF air electrode and same conditions of temperature and oxygen partial pressure at the air electrode, similar values are to be expected, so that the 2.6 % deviation is attributed to CNLS fit inaccuracies.

iv. For the fuel electrode, a similar value to that in Ref. [3] with a 4 % deviation is obtained. This deviation can partly be attributed to the different generations of cells fabricated with different technologies; the cells investigated herein differ from the ones in Ref. [3] in thickness (0.5 vs. 1 mm) and fabrication method (tape casting vs. warm pressing) of the substrate and fuel electrode functional layer (screen printing vs. vacuum slip casting). All other components of the cell are nominally identical.

v. In SOEC mode the relative deviation of 11 % and 23 % for the air electrode and fuel electrode values respectively to those in Ref. [3] are considerably large. These differences in charge transfer coefficients determined from EIS-measurements in the SOFC and the SOEC mode are contradictory to the BV-theory. There should be only one single value for both operating modes.

Whereas the small deviations discussed in points i to iv are straightforward, an explanation for the strong deviation between SOFC and SOEC mode in point v has to be found. In the described procedure to determine the charge transfer coefficient, constant operating conditions of the electrodes (i.e. a constant operating temperature and a constant gas composition) have been used. This assumption is not fulfilled, as it can be exemplarily seen in Figure 3.3-7 for the fuel electrode whereby H_2 and H_2O vary under current. Due to the gas diffusion processes in the substrate and the electrodes the gas composition in the active part of the electrodes close to the electrode / electrolyte interface is differing from the gas composition of the feed gas. Furthermore the diffusion is neither symmetrical for both SOFC and SOEC modes[42] nor is the temperature constant under load[42,61]. These influences need to be isolated for such analysis.

Despite the above discussed influences and the fact that the procedure does not claim to depict Butler-Volmer kinetics, the procedure was used to evaluate the kinetics of cells B and C in the three fuels in SOFC mode at 700 °C. The results are summarized in Table 3.3-4, from which the following comments can be made:

i. The same transfer coefficient of 0.63 is obtained for both cells in the H_2/H_2O fuel (Fuel I)

ii. In reformate fuels Cell A displays a transfer coefficient 3.3 % smaller than that in Fuel I whereas in Cell B, the transfer coefficients in Fuel II and Fuel III are 11.3- and 11.9 % larger than those in Fuel I.

iii. The exchange current densities of Cell B are smaller in the reformate fuels Fuel II and Fuel III than those in Fuel I by 14.1- and 16.6 % respectively.

iv. Cell B that had a finer microstructure displays (consistently) higher current densities in all fuels than Cell A.

Whereas the trends of the exchange current density are consistent in all aspects, the trends of the transfer coefficient will not be speculated upon at this point. However, it was the aim of these analysis to determine these values for the investigated DTU Energy cells and compare with those of FZJ discussed above as well as the values obtained in Ref. [3].

Comparing thus the transfer coefficients of the Ni/YSZ fuel electrode operated in H_2/H_2O and determined from fuel cell mode impedance spectra 0.63 is obtained for both DTU Energy cells against 0.62 for the herein investigated FZJ cells (cf. Table 3.3-4 vs. Table 3.3-3) and 0.59 for the cells investigated in Ref. [3].

Based on these results, the reproducibility of the Ni/YSZ transfer coefficient can be confirmed for cells from both producers. It has to be further stressed that the parameters for the FZJ cells reported in this work were determined at 800 °C in the current density range 0 A/cm^2 – 1.2 A/cm^2, the values from Ref. [3] at 800 °C and in the range 0 A/cm^2 – 2.2 A/cm^2, meanwhile the parameters for DTU Energy cells were determined at 700 °C and in a much smaller current density range of 0 A/cm^2 – 0.5 A/cm^2. Furthermore, the investigations on FZJ cells in this work and in Ref. [3] were carried out in a 50/50 H_2/H_2O fuel against 80/20 H_2/H_2O ratio for DTU Energy cells. This stresses an irrelevance of the H_2/H_2O ratio (at least within the range of these ratios employed)[vii] and temperature when determining the transfer coefficient with the procedure used herein.

Table 3.3-4: Exchange Current densities, $j_{0,el}$ and charge transfer coefficients α_{el} of the fuel electrodes of investigated DTU Energy SOCs at 700 °C the investigated fuels Fuel I, Fuel II and Fuel III. The $j_{0,el}$ is obtained from OCV impedance spectra using equation (33) and α_{el} from the BV-fit to equation (32).

Cell	Parameter	Fuel		
		Fuel I (H_2/H_2O)	Fuel II (H_2/CO_2)	Fuel III (CH_4 / H_2/H_2O)
A	$j_{0,el}$ [A/cm^2]	0.272	0.263	-
	α_{el}	**0.633**	**0.612**	-
B	$j_{0,el}$ [A/cm^2]	0.362	0.311	0.302
	α_{el}	**0.629**	**0.700**	**0.704**

3.3.2.4.3 Discussion on the Butler-Volmer Model

The BV equation in its original form (Eq. (32) with $n_e = 1$) is defined for a single electron transfer in a one-step (rate determining step) process from an ion in solution to a metal or vice versa [62]. Thereby the charge transfer coefficient is replaced by the symmetry factor $0 < \beta_{el} < 1$ that reflects the symmetry of the activation barrier.

It´s use in SOFC or SOECs with porous electrodes, in which multiple electrons are transferred in a number of consecutive diffusive transport processes and reaction steps[63,64] is thus controversial on the one hand because of the unrealistic probability of transferring two electrons in a single rate determining step.

More so contrary to the metal and liquid electrolyte case in which most of the change in potential occurs across a double layer that is approximately 1–2 nm thick, the length scale in the complex case of SOCs is in the order of 1 µm [65] so that the rate determining step is not easy to determine. Notwithstanding, and for good reasons[3,4,61,66] the use of the full BV equation is widely used in literature. Thereby the transfer coefficient is essentially a

[vii] The situation could be different in a much dryer fuel e.g. 97/3 H_2/H_2O due to Nernst effects, as the exponential part of the Nernst is over at ratios around 80/20 H_2/H_2O.

reflection of all steps needed for the charge transfer reaction to take place and embraces both the fundamental symmetry factor and stoichiometric properties of an overall electrode reaction involving more than one step[62].

Another criticism to the BV-type equation of the form displayed in equation (32) is having the transfer coefficient of the backward reaction expression as 1 - α_{el}. This means that the sum of transfer coefficients for the forward and backward reactions is unity—a condition that is valid for the symmetry factor but does not necessarily have to hold for the transfer coefficient[62]. The general form of the BV-equation[67] displayed in equation (34) solves the problem.

$$j = j_0 \left[exp\left(\alpha_1 \frac{n_e F \eta_{act,el}}{RT}\right) - exp\left(-\alpha_2 \frac{n_e F \eta_{act,el}}{RT}\right)\right] \quad (34)$$

To verify the difference between equations (34) and (32) the current density vs overpotential curves for DTU Energy cells Cell A and B were fit to equation (34) for comparison. Thereby unlike in equation (32) the exchange current density j_0 was not held constant but fitted out with the transfer coefficients α_1 and α_2 of the forward and backward reactions respectively however using corresponding j_0 values from Table 3.3-4 as starting guess values. For both transfer coefficients 0.5 was employed as starting guesses. The results are displayed in Table 3.3-5.

For both cells, in H_2/H_2O fuel, slightly higher exchange current densities are obtained than the ones obtained through equation (33) and held constant in the fits with equation (32).

On the other hand, slightly smaller transfer coefficients α_1 for the forward reaction (cf. 0.549 vs. 0.633 and 0.602 vs 0.629 for the transfer coefficients of Cell A and Cell B respectively) were fitted out with the general BV equation (34). The transfer coefficients for the backward reaction according to equation (32) i.e. as 1 - α_{el} would be 0.367 and 0.371 for Cell A and Cell B respectively in H_2/H_2O fuel. The equivalent values corresponding to α_2 in equation (34) are 0.237 and 0.371. Thus Cell B with the finer microstructure has the same value meanwhile a slightly smaller transfer coefficient for the backward reaction is obtained with the general equation (34) for Cell A.

Based on and limited to the values in H_2/H_2O fuel[viii], it can be concluded that the transfer coefficients α_i obtained through the general BV are more appropriate for Ni/YSZ electrodes, since unlike the symmetry factor β they have not been limited to sum up to unity, and the reactions are expected to be consisting of multiple steps whereby the rate determining one is not always clearly known, especially to be the charge transfer step.

[viii] Considering the complexity of the fuel system in reformate fuels with four components at equilibrium, the reformate parameters will not be further discussed and since no work is available in literature on these systems the determined values will be left for future validation, criticism or explanation.

Table 3.3-5: Exchange Current densities, $j_{0,el}$ and charge transfer coefficients α of the Ni/YSZ fuel electrodes of investigated DTU Energy SOCs at 700 °C in the investigated fuels Fuel I, Fuel II and Fuel III. The $j_{0,el}$ is fitted out along α_1 and α_2 from the general BV equation (34)

Cell	Parameter	Fuel					
		Fuel I (H_2/H_2O)		Fuel II (H_2/CO_2)		Fuel III (CH_4 / H_2/H_2O)	
		Equation					
		(32)	(34)	(32)	(34)	(32)	(34)
A	$j_{0,el}$ [A/cm^2]	0.272	0.345	0.263	0.220	-	
	α_{el}	0.633		0.612			
	α_1		**0.549**		**0.687**		
	α_2		**0.237**		**0.51**		
B	$j_{0,el}$ [A/cm^2]	0.362	0.378	0.311	0.420	0.302	0.226
	α_{el}	0.629		0.700		0.704	
	α_1		**0.602**		**0.592**		**0.813**
	α_2		**0.371**		**0.147**		**0.607**

3.4 Fuel Electrodes

The impedance response obtained during characterization of a full cell through impedance spectroscopy involves contributions from both fuel and oxygen electrodes. Symmetric cell geometries enable investigation of only a single electrode material through impedance spectroscopy. In this section results of investigations on the standard porous Ni/YSZ cermet fuel electrode will be presented. The test setup used in the investigations is shown in Figure 3.2-7 and details are described elsewhere[31].

3.4.1 Ni/YSZ

Current s.t.a. solid oxide cells are manufactured with a composite Ni/YSZ fuel electrode. Symmetric cells were manufactured by screen-printing Ni/YSZ inks on both sides of a 200 µm thick 8YSZ electrolyte and sintered at three different temperatures; 1250 °C, 1300 °C and 1350 °C. The purpose of this study was to investigate the influence of sintering temperature on the performance of the electrodes and above all to identify the optimal sintering temperature for these electrodes.

3.4.1.1 AC Analysis on Symmetric Cells

3.4.1.1.1 Nitrogen Mole Fraction Dependency

To identify the concentration-related processes, the mole fraction of N_2 was varied while keeping the $pH_2O/(pH_2O+pH_2)$ ratio constant[39] at 9 %. A summary of the mole fractions of the gases in the fuel gas mixture used in this investigation is displayed in Table 3.4-1.

Table 3.4-1: Mole fractions of the components in the fuel gas during N_2 partial pressure variation

pH_2	pH_2O	pN_2	$pH_2O/(pH_2+pH_2O)$
0.91	0.09	0.00	0.09
0.77	0.08	0.15	0.09
0.67	0.07	0.27	0.09
0.59	0.06	0.35	0.09
0.53	0.05	0.42	0.09

The impedance spectra recorded during the variation are displayed in Figure 3.4-1 a_i, b_i and c_i for cells sintered at 1250-, 1300- and 1350 °C respectively and tested at the same time due to the many channels in the test rig displayed in Figure 3.2-7. The corresponding DRTs are displayed in subplots a_ii, b_ii and c_ii respectively. The observed trends were reproducible in other tested cells. The DRTs reveal four peaks—P1 - P4. Peaks P1 at 10 < f < 100 Hz and the much smaller peak P2 at 100 < f < 1 kHz are concentration related peaks as they display a dependence on pN_2 change. Sonn et al.[39] attributed P1 to diffusive transport in flow channels of the flow field and P2 to gas phase diffusion in the volume of the contact meshes. In Sonn's study the cell was mounted in a fixture where the fuel gas was passed over the electrodes at a flow rate of 0.4 L / min. However it has been shown that in the used rig (in which the atmosphere is more stagnant, as it is a large volume container of 1.7 l/h, see Figure 3.2-7 in which the gaseous atmosphere is replaced ca. 4 times per hour) there is a gas concentration related contribution from the stagnant layer outside and above the cells[11,40,68,69] in the frequency region 10 to 100 Hz[40]. This would be P1 in Figure 3.4-1. The less pronounced P2 which was equally less pronounced in literature[39] can as well be attributed to diffusion in the volume of the contact meshes. Processes P3 and P4 in the frequency range f > 1 kHz are well known to belong to the Ni/YSZ electrochemical processes[3,34,39,50,51] and as would be expected[70] their ASR or area beneath their DRT peaks[39] decreases/improves with sintering temperature[70]. In the same taken, the independence of processes P1 and P2 on sintering temperature suggest the processes are *outside* the electrode structure.

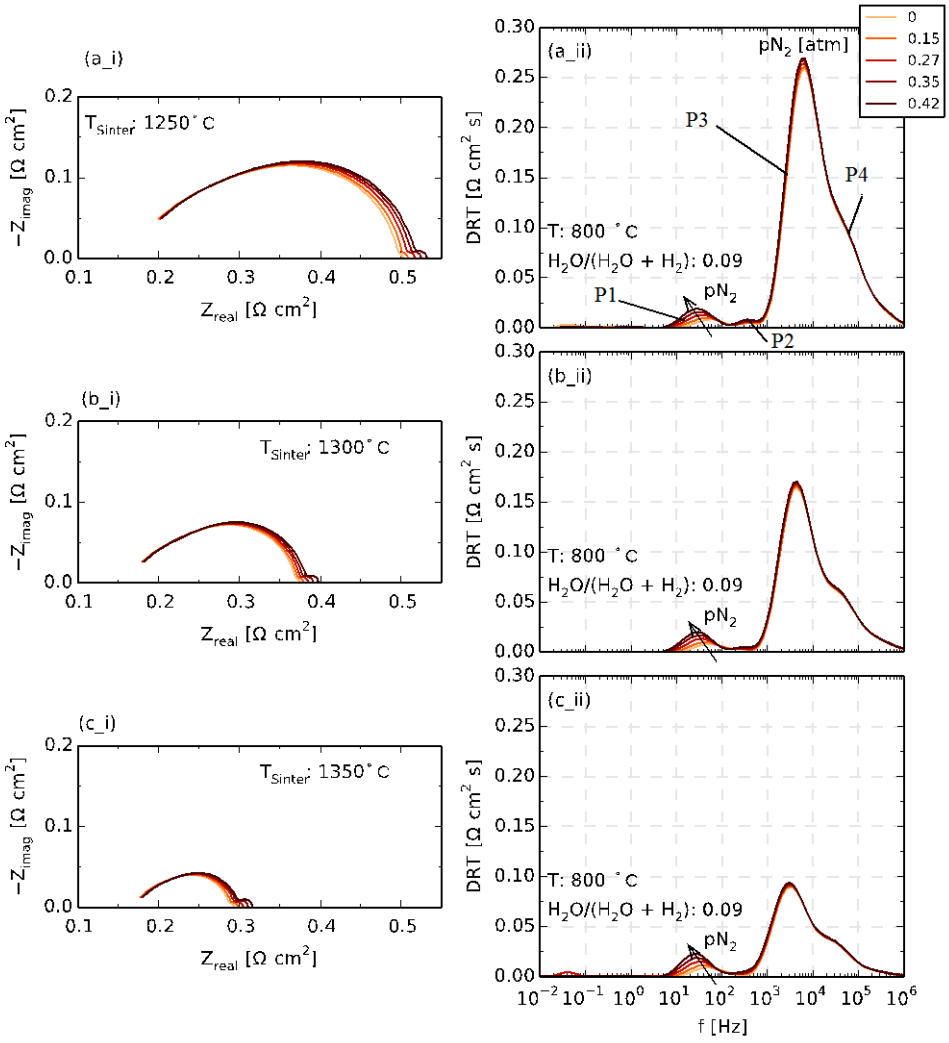

Figure 3.4-1: (a_i) – (c_i) Electrochemical impedance spectra and (a_ii) – (c_ii) corresponding DRTSs for three cells sintered at 1250 °C, 1300 °C and 1350°C respectively 800 °C in a pN_2 variation.

3.4.1.1.2 Temperature Dependency

A temperature variation was carried out in all three cells in the range 850 °C to 650 °C as displayed Figure 3.4-2 from which the following observations can be made: (i) for all three sintering temperatures, the DRTs reveal the expected decrease in polarization resistance with increasing operation temperature. This is because the thermally activated[51] processes of charge transfer and ionic transport are facilitated at higher temperatures. (ii) A decrease in overall polarization resistance with increasing sintering temperature as explained already in section 3.4.1.1.1 is observed (iii) Finally a drift of peak frequencies of the electrochemical reactions towards lower values with increasing sinter temperature can be observed (cf. compare DRT peak frequencies of P3 for the 650 °C

spectra for all three sintering temperatures). This means that although the ASR is decreasing, the interfacial capacitance mainly resulting from the Ni-YSZ contact points is increasing more with higher sintering temperatures. The resulting time constant ($\tau = RY_0$) is increasing and its reciprocal, the characteristic/peak frequency is decreasing ($f_s = \frac{1}{2\pi\sqrt[n]{RY_0}}$, for an RQ-element[40]).

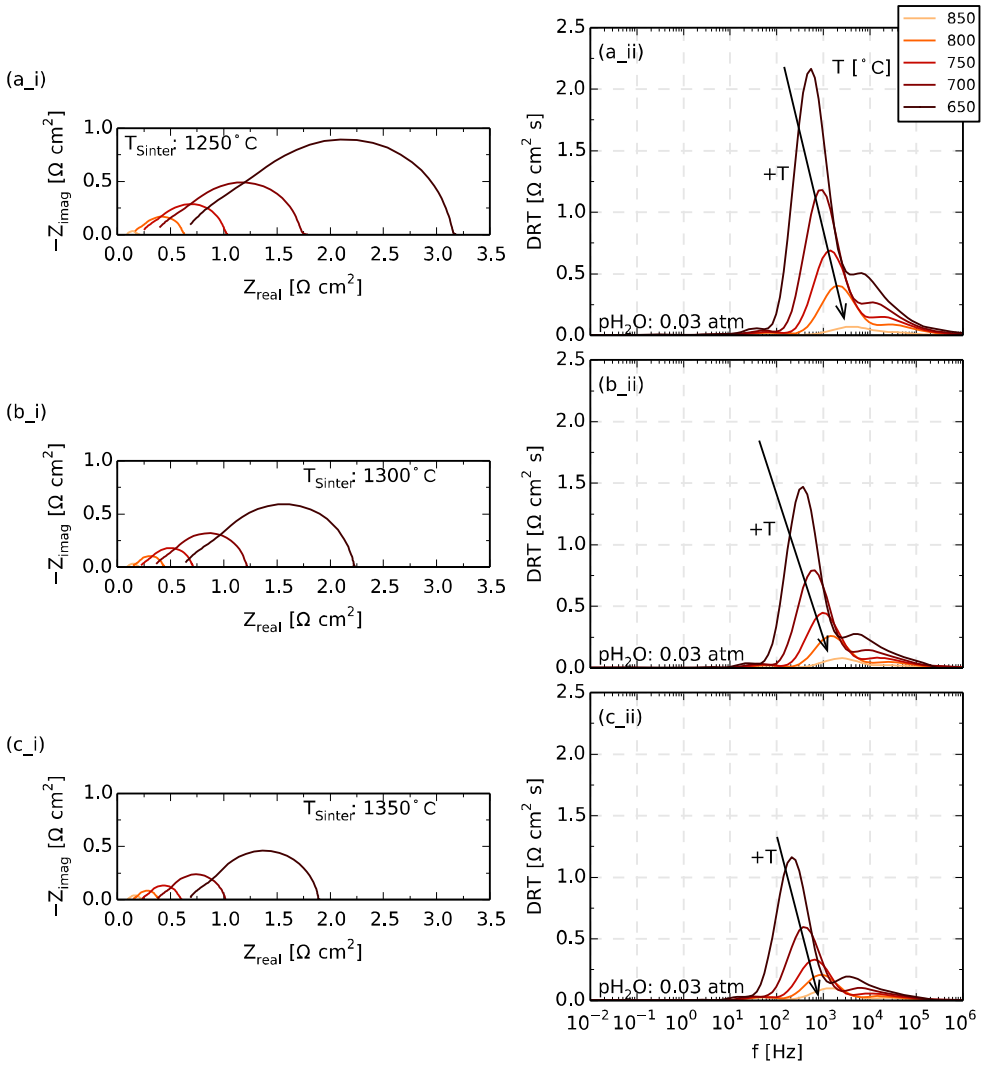

Figure 3.4-2: Electrochemical Impedance Spectra and corresponding DRTSs for three cells sintered at 1250 °C , 1300 °C and 1350 °C in the temperature range 850 °C to 650°C in a 3% *p*H$_2$O atmosphere.

Quantitative Analysis through CNLS FIT

The spectra of cells sintered at 1250 °C and 1350 °C were fit using two model approaches:

i. M1: A series resistance (R) for the electrolyte ASR, two RQ-elements for the electrochemical reactions[3,34] (i.e. f > 1 kHz) and a finite length Warburg element (Wgfl) for gas concentration impedance[40] (p1). The two RQ elements account for the coupled processes of charge transfer, ionic transport and diffusion in the electrode functional layer[2,3].

ii. M2: A series resistance (R), transmission line (TL) model[39,71,72] and a Finite length Warburg element (Wgfl). The TL model displayed in Figure 3.4-3 accounts for ionic transport in the 8YSZ matrix/rail (χ_1), electronic transport in the percolating Ni phase (χ_2) and the interfacial impedance (ζ) between the two phases. In a similar manner as done by Sonn et al.[39] the electronic rail contribution has by virtue of the high conductivity of nickel (χ_1 >> χ_2) been neglected.

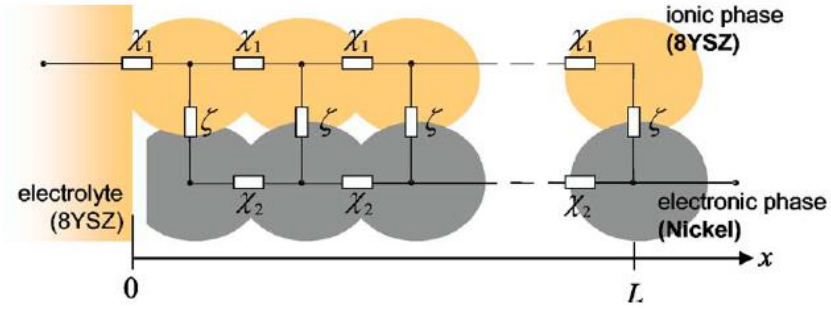

Figure 3.4-3: Transmission line model for a porous two-phase composite electrode[39]

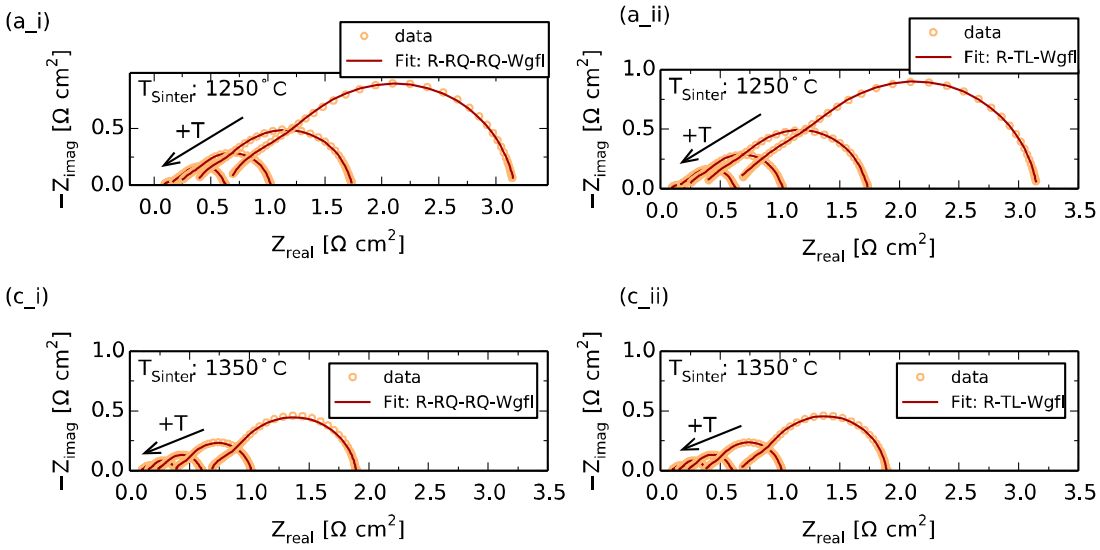

Figure 3.4-4: CNLS fits of cells sintered at 1250 °C (a_i) and 1350 °C (c_i) with R-RQ-RQ-Wgfl model. The same spectra are fitted with a transmission line model (TL) instead of two RQ-elements and displayed in subplot (a_ii) and (c_ii) for cells sintered at 1250 °C and 1350 °C respectively

Excellent fits were obtained from both models as displayed in the comparison between fit and measurement in Figure 3.4-4. The series (or ohmic or electrolyte) resistance from both models as well as the resistance of the ionic rail of the TL model were evaluated assuming thermally activated ionic conduction using equation (35) meanwhile the ASR obtained as sum of the two RQ elements of model M1 as well as the resistance of the interfacial exchange (charge transfer) from model M2 have been evaluated with equation (36). The obtained activation energies $E_{act,ohm}$ and E_a as well as the pre-exponential factors B_{ohm} and B are displayed in Table 3.4-2.

$$R_{\text{ohm}}(T) = \frac{T}{B_{\text{ohm}}} \exp\left(\frac{E_{\text{act,ohm}}}{RT}\right) \tag{35}$$

$$R_{el.}(T) = B \cdot \exp\left(\frac{E_a}{RT}\right) \tag{36}$$

Table 3.4-2: Kinetic parameters from CNLS fit with models M1 (R-RQ-RQ-Wgfl) and M2 (R-TL-Wgfl) of spectra recorded in a temperature variation for cells sintered at 1250 °C and 1350 °C.

Sinter [°C]	M1: R-RQ-RQ-Wgfl				M2: R-TL-Wgfl					
	Rs		Gas diffusion coupled with charge transfer and ionic transport (AFL)[34,39,73]		Rs		Charge transfer		Ionic transport	
	B [SK]	Ea [kJ/mol]	B [Ω]	Ea [kJ/mol]	B [SK/m^2]	Ea [kJ/mol]	B [Ωcm]	Ea [kJ/mol]	B [SK/cm]	Ea [kJ/mol]
1250	$7.2\cdot10^{7}$	**93.17**	$2.6\cdot10^{-5}$	98.31	$2.7\cdot10^{13}$	**92.93**	$9.0\cdot10^{-9}$	**107.0**	$3.63\cdot10^{4}$	**94.47**
		0.97eV		1.02eV		0.96eV		1.11eV		0.98eV
1350	$8.9\cdot10^{7}$	**94.29**	$1.0\cdot10^{-5}$	98.78	$2.9\cdot10^{12}$	**94.4**	$4.4\cdot10^{-9}$	**105.1**	$1.98\cdot10^{5}$	**100.3**
		0.98eV		1.02eV		0.98eV		1.09eV		1.04eV

The activation energies of the 8YSZ electrolyte determined from both models lie within the range 92.9 – 94.4 kJ/mol (0.96 - 0.98 eV) and are consistent with literature. Leonide et al.[3] reported 90 kJ/mol, Ried *et al*.[74], 96 – 99 kJ/mol, Gibson et al.[75] reported 0.92 eV for temperatures from 600 °C – 800 °C.

The activation energy related to the electrochemical reactions of the Ni/YSZ fuel electrode obtained from model M1 is independent of sintering temperature of the cell and has a value of 1.02 eV. The value is only 5 % smaller than the 1.09 eV obtained by Leonide[3] from a full cell also using two RQ-elements. Primdahl et al.[51] using a single RQ-element obtained an even smaller value of 0.8 eV. However the here obtained values lie well within the 0.8 – 1.8 eV reported by Brown et al[50]. For cermets with finer microstructure Brown had a single arc and for coarser microstructures two arcs whose activation energies were evaluated separately. This approach was followed by Leonide et al.[34] obtaining 1.3 eV and 0.35 eV (900 °C – 750 °C) and 2.05 eV (750 °C – 700 °C) for the higher and lower frequency arcs respectively, until they could demonstrate later[73], that the two processes (arcs) together with the often neglected and overlapped diffusion in the functional layer[2,40,76] were coupled and had to be considered together.

From the transmission line model fit data for both cells, interfacial charge transfer displays a higher activation energy than that of ionic transport with 1.11 eV > 0.98 eV and 1.09 eV > 1.04 eV for cells sintered at 1250 °C and 1350 °C respectively. The trend is consistent with Sonn et al.[39] whose activation energy for charge transfer of 1.35 eV was larger than that of ionic conductivity of 0.902 eV. However the charge transfer activation energies are smaller than those reported by Sonn[39] meanwhile the ionic transport activation energies are larger than Sonn´s. This means that in the cells reported in this work, charge transfer is *easier* than in Sonn´s cells whereas ionic transport in the 8YSZ matrix is *more difficult* than in Sonn´s cells. The difference can be attributed to material and processing differences e.g. Sonn sintered his cells at 1350 °C for 5 h against 4 h for the cells reported here.

Ramos et al.[68] although investigating Ni/ScYSZ cermets reported charge transfer activation energies in the range 110.5 – 122.7 kJ/mol (1.14 – 1.27 eV) which are smaller than Sonn´s values for Ni/YSZ. Furthermore for ionic transport Ramos obtained activation energies in the range 113 – 117 kJ/mol (1.17 – 1.2 eV)—values which are larger than Sonn´s 0.904 eV for Ni/YSZ samples or the 73 - 87 kJ/mol (0.76 – 0.9) for transport within ScYSZ[10]. With the results the authors suggested composition and processing routes as possible causes for the discrepancy. This is important as it stresses the fact that activation energies are very dependent on processing steps such as sintering temperature as this determines the microstructure. This in turn calls for care when comparing literature values. Activation energy is not an absolute value for a given electrode chemistry.

From Table 3.4-2 it is also evident that the interfacial charge transfer activation energy for cells sintered at 1350 °C (105 kJ/mol) is smaller than that of cells sintered at 1250 °C. This suggests that cells sintered at 1250 °C may have more isolated or non-percolating TPBs against those sintered at a 1350 °C which may have an overall less TPB density, but more percolating. This hypothesis is confirmed by comparing (qualitative) the microstructure of samples sintered at 1250 °C against those sintered at 1350 °C in Figure 3.4-5. From Figure 3.4-5 (a_iii) and (c_iii) it is evident that the 8YSZ network of the cells sintered at 1350 °C is more percolating than

that of the cells sintered at 1250 °C. This results in greater TPB length and a correspondingly lower charge transfer activation energy for cells sintered at 1350 °C.

On the other hand and still from Table 3.4-2 the activation energy for ionic transport for the cell sintered at 1350 °C is with 1.04 eV larger than the 0.98 eV of the cell sintered at 1250 °C. This could misleadingly suggest that as a consequence ionic transport is more facile in cells sintered at 1250 °C. However the pre-exponential factor B of the 1350 °C cell is with $1.98 \cdot 10^5$ SK/cm (i.e. a conductivity) an order of magnitude larger than the $3.63 \cdot 10^4$ SK/cm for the cell sintered at 1250 °C. These values are consistent with the denser and more sintered solid phases of the cell sintered 1350 °C. These results point out the relevance of taking into account not only the activation energies but also the pre-exponential factor that contains microstructural information—which in turn stresses the relevance of considering processing details when comparing results with literature values.

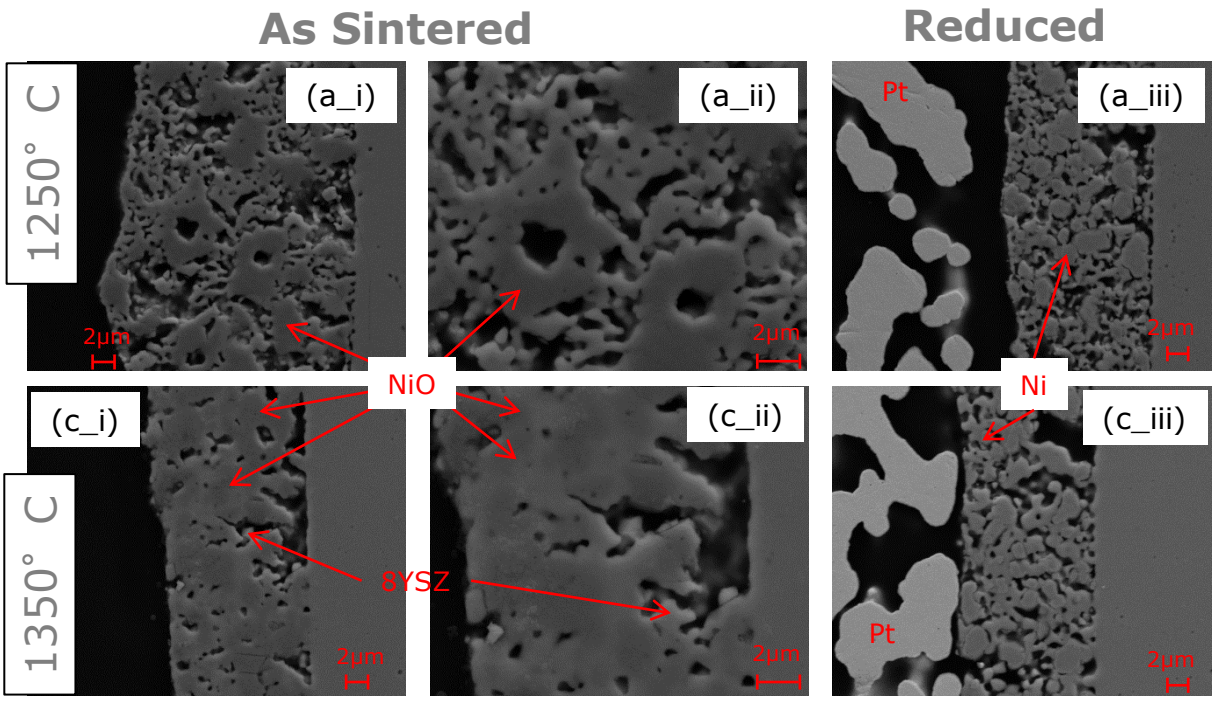

Figure 3.4-5: SEM micrographs of Ni/YSZ samples sintered at 1250 °C (a-i) and (a_ii) *as sintered* and (a_iii) in reduced form. Corresponding micrographs for cells sintered at 1350 °C are displayed in (c_i), (c_ii) and (c_iii). The displayed samples are from tests (not reported) in which platinum paste was used for current collection. Coarse Ni/YSZ was used in the results discussed in this work.

3.4.1.2 AC Analysis on Small Working Electrodes

Ni/YSZ *SmallWE* electrodes were manufactured as described in Figure 3.2-4 and based on the findings from the Ni/YSZ symmetric cell investigations in section 3.4.1.1 above the electrodes were sintered at 1350 °C (for 4 h). Characterization and instrumentation was done as described in section 3.2.3

3.4.1.2.1 Nitrogen Mole Fraction Dependency

As done with symmetric cells in section 3.4.1.1.1 to check for the presence of concentration-related contributions in the impedance response, the nitrogen mole fraction was varied from 0- to 0.42 atm while holding the ratio of steam to sum of steam and hydrogen partial pressures ($pH_2O/(pH_2O+pH_2)$) constant at 0.09. The Nyquist plot of the recorded spectra is displayed in Figure 3.4-6 (a) and the corresponding DRTs in subplot (b).

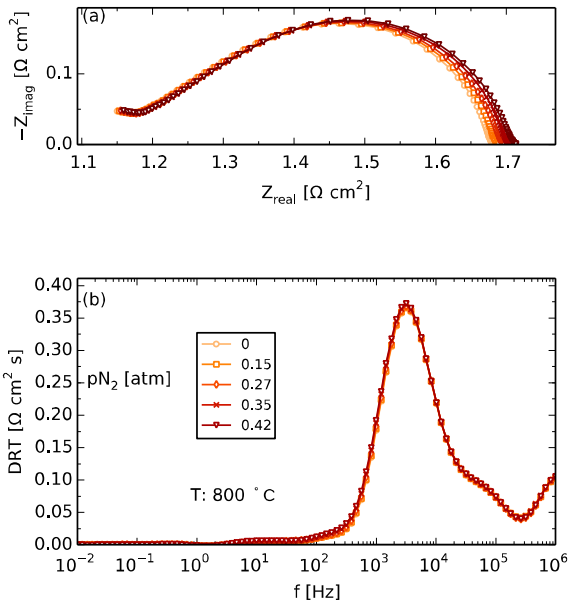

Figure 3.4-6: EIS and DRT of Ni/YSZ SmallWE cells under stepwise variation of partial pressure of nitrogen pN_2 at 800 °C

From Figure 3.4-6 no concentration related process grows or emerges with increasing pN_2, even though spectra were recorded down to 30 mHz. The slight increase at low frequencies in the Nyquist plot is insignificant as can be seen from the DRT plot, showcasing the huge benefit of and motivation for the used cell geometry as the resistances associated with concentration-related processes are effectively reduced to insignificant values.

3.4.1.2.2 Equivalent Circuit Model, CNLS Fit and Data Quality

Quantitative analysis of recorded impedance spectra was realized with an EEC comprising a series resistance and three RQ-elements in series. Data and fit quality were controlled as described in section 2.4.2. Results of these analyses for a *SmallWE* cell operated at 650 °C are displayed in Figure 3.4-7 from which can be seen that data and fit quality are very good with residuals well within the ± 0.5 % range and fluctuating about the zero-line.

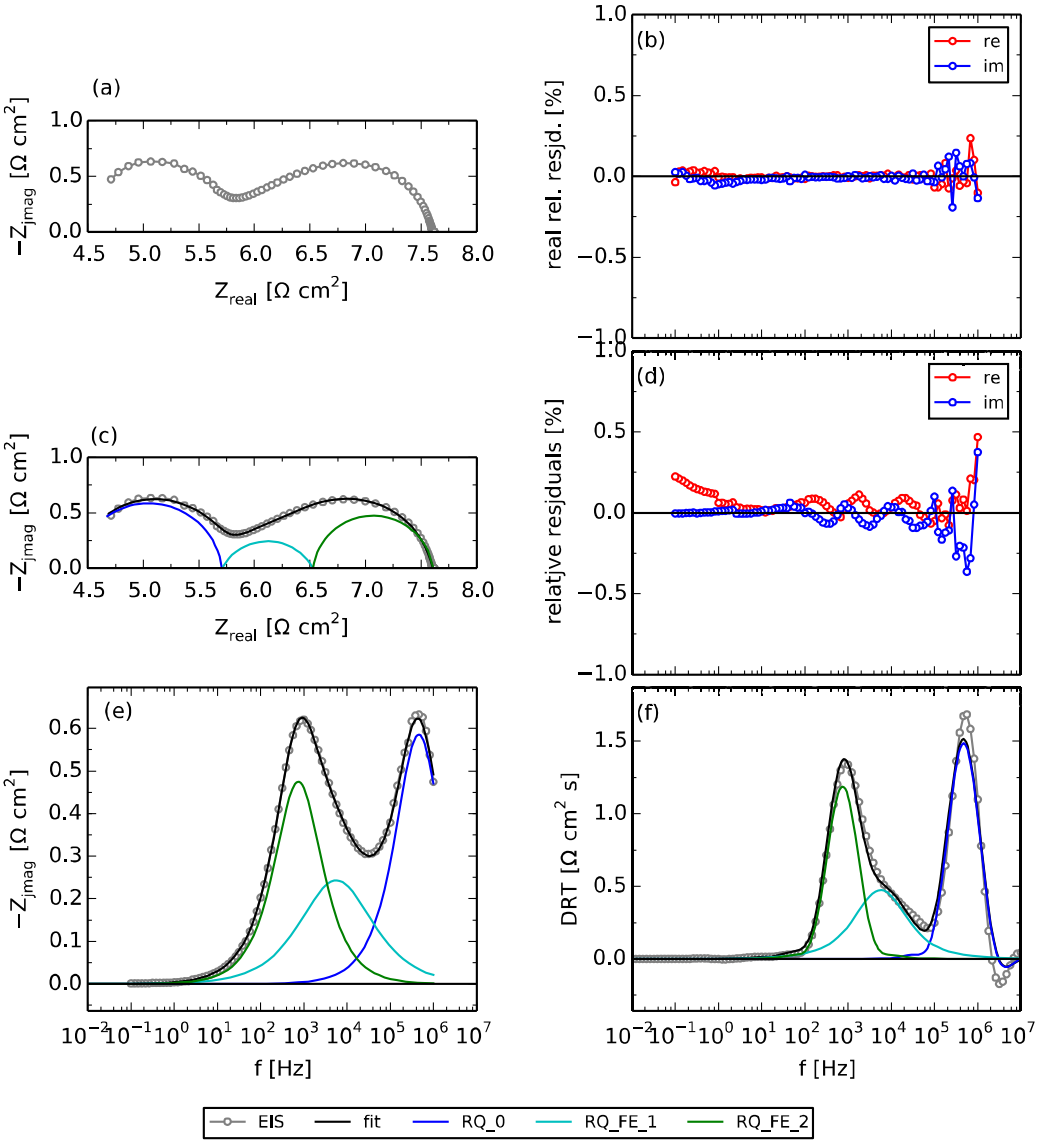

Figure 3.4-7: (a) Impedance spectrum of a SmallWE cell recorded at 650 °C (b) the corresponding KK-test residuals, (c) the CNLS fit, with Boukamp goodness of fit χ^2 = 1.4·10^{-4}, (d) corresponding CNLS fit residuals, (e) imaginary part of spectrum and fit, (f) DRT of spectrum and simulation of fit processes

3.4.1.2.3 Temperature Dependency

The operation temperature was varied from 850- down to 650 °C at constant fuel composition of 0.5 atm pH_2O and 0.5 atm pH_2 and EIS spectra recorded. The spectra and corresponding DRTs are displayed in Figure 3.4-8. It can be seen that coupled to the well-known temperature dependence of the Ni/YSZ fuel electrode, an extra process at ca. f > 10^5 Hz emerges at decreasing temperatures. This process is attributed to the 8YSZ electrolyte e.g. grain boundary resistance. As shall be seen in section 3.4.1.2.4, this process shows no dependence on fuel composition.

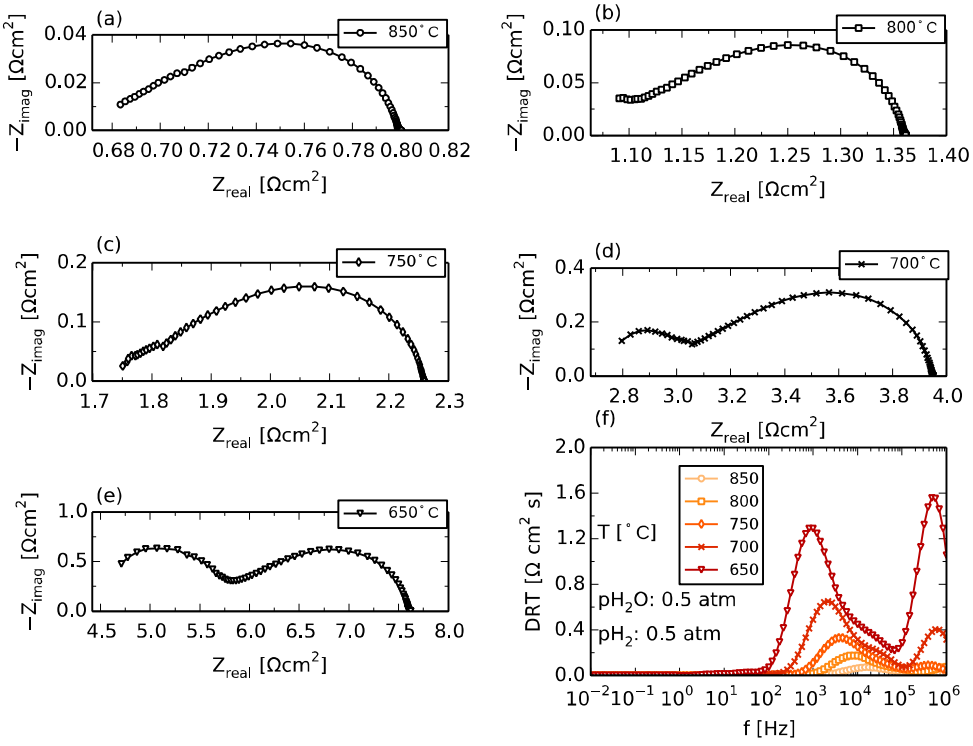

Figure 3.4-8: EIS and DRT of Ni/YSZ SmallWE cells under a stepwise variation of operation temperature from 850 °C to 650 °C in a 50/50 H_2/H_2O fuel mixture.

Combining the ASRs of the two RQ-elements for the Ni/YSZ electrode (cf. model M1 in section 3.4.1.1.2) a consistent activation energy E_a of 1.13 eV and a pre-exponential factor B of 1.28·10^{-6} Ωcm^2 were obtained using equation (36). 1.02 eV and 1.0·10^{-5} Ω (= ca. 1.0·10^{-5} x 0.36 cm^2 = 3·10^{-6} Ωcm^2) was obtained from symmetric cell analysis in section 3.4.1.2.3 and these values were also compared to literature values in that section. For the series resistance and the high frequency arc 0.88- and 2.1 eV were obtained using equations (35) and (36) respectively. Whereas the 2.1 eV is much larger than the grain boundary activation energies found in literature[77]

the 0.88 eV for the series resistance is in the adequate range (cf. section 3.4.1.1.2). Furthermore, combining the two ASRs as 8YSZ electrolyte resistance, 1.04 eV is obtained which is in the appropriate range.

3.4.1.2.4 Steam- and Hydrogen Partial Pressure Dependencies

Hydrogen and steam partial pressure dependencies a and b have been demonstrated[2,3] to be related to the exchange current density j_0 of the Ni/YSZ electrode as shown in equation (37) and that the electrode ASR, R_p and j_0 are further linked by equation (33). Thus by varying the $p\mathrm{H_2}$ at a given temperature while ensuring that $p\mathrm{H_2O}$ is constant e.g. by balancing with an inert gas like nitrogen, and recording impedance spectra the corresponding exponent a describing the $p\mathrm{H_2}$ dependency of the exchange current density can be determined through equations (33) and (37). The $p\mathrm{H_2O}$ dependency can be determined in a similar procedure at constant $p\mathrm{H_2}$.

$$j_0 = \gamma_{el}\left(\frac{pH_2}{P}\right)^a\left(\frac{pH_2O}{P}\right)^b \exp\left(-\frac{E_a}{RT}\right) \qquad (37)$$

Hydrogen Partial Pressure Dependency, a

A $p\mathrm{H_2}$ variation was carried out at 800 °C for the *SmallWE* cells in the range 0.15 – 0.8 atm while maintaining the $p\mathrm{H_2O}$ constant at 0.2 atm and balancing with N_2 and then recording impedance spectra. These are displayed in Figure 3.4-9 (a) and the corresponding DRTs in subplot (b). The spectra were fit with the EEC model M1 described in section 3.4.1.1.2 and as displayed in Figure 3.4-9 (c) very good fits were obtained. The results are displayed in a double logarithmic plot in subplot (d) which also displays a slope of 0.07 from the linear fit resulting in a $p\mathrm{H_2}$ dependency a of - 0.07 of the exchange current density. Investigating structured Ni/YSZ fuel electrodes Utz *et al*.[66] obtained - 0.07 from line specific resistances (LSR) meanwhile Leonide *et al*.[3] obtained a slightly stronger dependency of - 0.1 from FZJ cells.

Steam Partial Pressure Dependency, b

In a similar manner as done above for $p\mathrm{H_2}$ variation, the steam partial pressure was varied at 800 °C thereby maintaining $p\mathrm{H_2}$ constant at 0.3 atm and balancing with N_2. The recorded spectra were fit with the same EEC model as well. The results are displayed in Figure 3.4-10 from which a $p\mathrm{H_2O}$ dependency of the R_p of - 0.22 has been obtained. Consequently the exchange current density dependency b of the cells investigated herein is 0.22 at 800 °C against 0.33 reported for FZJ cells[3] or 0.32 – 0.88 obtained from LSRs of patterned Ni/YSZ[66,78].

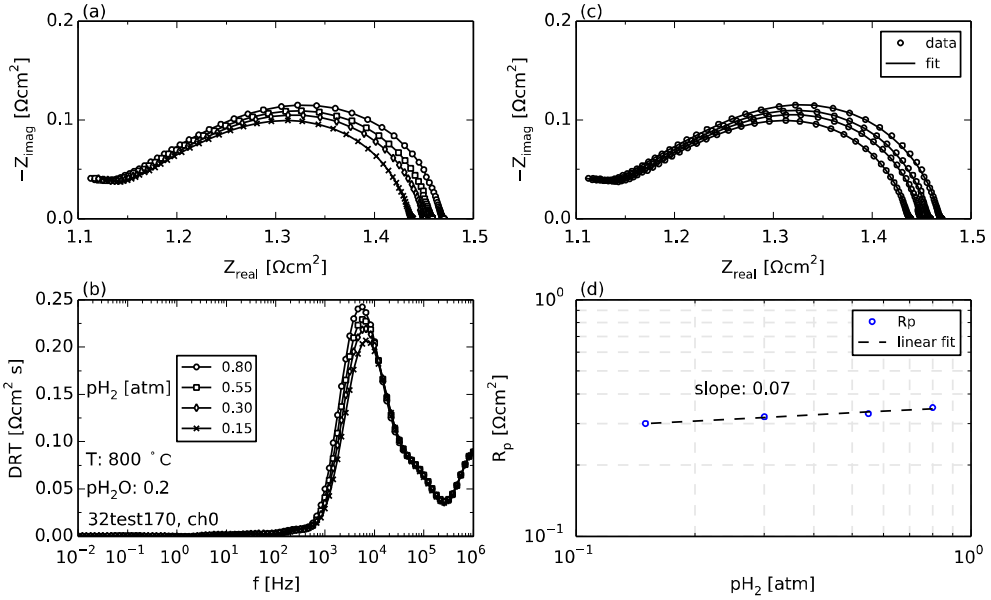

Figure 3.4-9: (a) Nyquist plots of EIS spectra recorded at 800 °C in a pH_2 variation at constant pH_2O of 0.2 atm and N_2 balance. (b) DRTs of spectra in (a), (c) CNLS fits of spectra in (a). (d) pH_2 dependency of the ASR, Rp

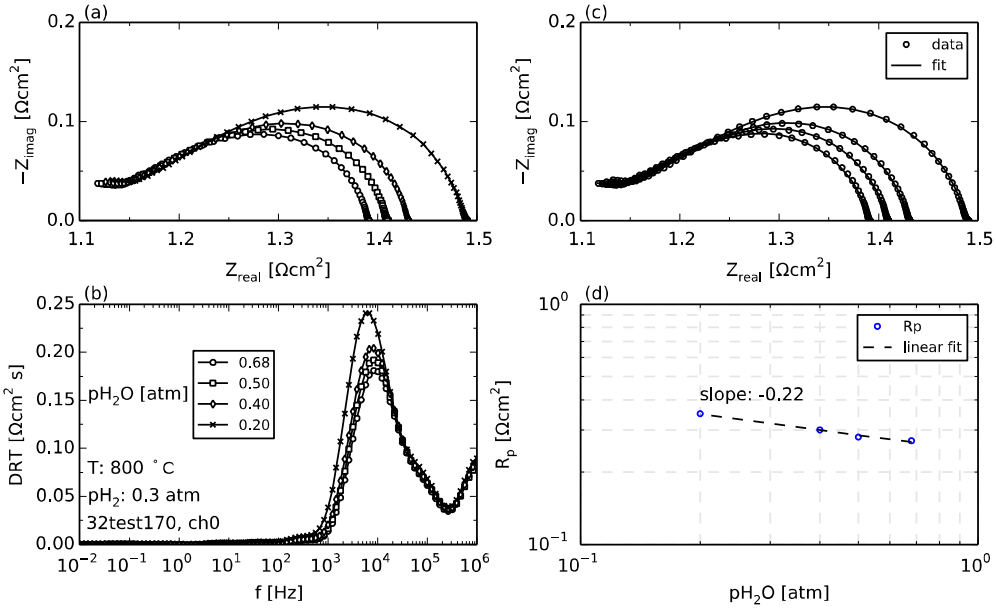

Figure 3.4-10: (a) Nyquist plots of EIS spectra recorded at 800 °C in a pH2O variation at constant pH_2 of 0.3 atm and N_2 balance. (b) DRTs of spectra in (a), (c) CNLS fits of spectra in (a). (d) pH_2O dependency of the ASR, Rp

Exchange Current Density Pre-factor, γ_{el}

From equations (36), (37) and (33) the determined parameters a, b and B *as well as* hydrogen and steam partial pressures $p\mathrm{H_2}$ and $p\mathrm{H_2O}$ of 0.5- and 0.5 atm, the parameter $\gamma_{an}(T)$ in equation (37) of $37 \cdot T$ A/cm^2 or $3.7 \cdot 10^5 \cdot T$ A/m^2 is obtained as a function of temperature as done by Leonide *et al.*[3]. This value is one order of magnitude smaller than the $1.83 \cdot 10^6 \cdot T$ in the Ni/YSZ electrodes characterized by Leonide et al[3], reflecting as much difference in the corresponding exchange current densities or electrode performance. A comparison of the absolute ASR values R_p of the cells investigated herein (screen-printed electrodes with a non-optimized ink) with the s.t.a. cells investigated by Leonide et al.[3] does indeed differ by one order of magnitude. At 800 °C and 40 % $p\mathrm{H_2O}$ for instance, R_p in this work is 0.3 Ωcm^2 against ca. 0.041 Ωcm^2 under similar conditions in literature[3]. Furthermore, using all the parameters determined so far for these electrodes, an exchange current density of 35 mA/cm^2 is calculated for these electrodes at 700 °C in an 80/20 $\mathrm{H_2/H_2O}$ fuel using equation (59). For Ni/YSZ electrodes of the DTU Energy full cells investigated at 700 °C in the same fuel mixture in section 3.3.2.4.2 an exchange current density of 270 mA/cm^2 was obtained for the standard cell, Cell A and 360 mA/cm^2 was obtained for Cell B with the finer electrode microstructure—values one order of magnitude larger than the screen-printed electrodes investigated in this section.

3.4.1.3 DC Analysis on Small Working Electrodes

In this section current density vs. overpotential (C/V) characteristics of *SmallWE* were investigated for varying conditions of temperature and fuel mixture. The C/V curves[ix] were recorded at a rate of 1 mV/s employing the same instrument as in AC characterization (Gamry Reference 600™ potentiostat) as well as the single gas atmosphere test-rig with maximum flow rate of 6 l/h displayed in Figure 3.2-7. A minimum of 90 minutes was allowed for thorough change of gas or temperature prior to the current/voltage curve recording.

3.4.1.3.1 Temperature Dependency

Current density vs. overpotential curves were recorded at 50 K intervals (except at 700 °C) in a symmetrical 50/50 $\mathrm{H_2/H_2O}$ fuel mixture immediately after recording the impedance spectra discussed above. The choice of 50/50 $\mathrm{H_2/H_2O}$ fuel composition was to exclude any contributions to asymmetry from the fuel mixture. From the CNLS fits of the spectra in Figure 3.4-8 the sum of the series resistance and the ASR of the process for f > 100 kHz were used to i-R correct the overpotential curves so that the resulting current density vs. overpotential curves could

[ix] The right notation here should be j/η or C/η curves since they are current density vs overpotential and not current density vs. voltage curves but C/V curves will be used throughout this work and depending on context the "V" will be "Voltage" or "Overpotential".

solely be attributed to the electrochemical reactions of the Ni/YSZ electrode and any minor contribution from gas diffusion. These are displayed in Figure 3.4-11 (a).

Figure 3.4-11 (a) displays an asymmetry of the cathodic and anodic branches at all investigated temperatures and overpotentials. Holtappels *et al*.[79] also observed this asymmetry although in a fuel mixture composed of 0.48 bar pH_2 and 0.05 bar pH_2O. They concluded that the asymmetry was an indication of different reaction kinetics for the hydrogen oxidation reaction and water reduction reactions. In ref. [42] activation polarization of the fuel electrode was identified alongside substrate diffusion as being the major contributors to the asymmetry between SOFC and SOEC operation modes. It was pointed out that alongside the intrinsic endothermic and exothermic nature of steam reduction and hydrogen oxidation respectively[x], the reaction rate depends on pH_2O. Since this was *consume*d in SOEC mode (cathodic branch) the reaction site was depleted of H_2O resulting in lower reaction rates than in SOFC mode where the exact opposite was happening. With the cell geometry used in this work designed to minimize ohmic heating and gas concentration related losses (cf. absence of diffusion or gas conversion peaks in Figure 3.4-6 (b), the observed asymmetry of current density vs. overpotential curves observed in Figure 3.4-11 (a) can be narrowed down to:

i. pH_2O dependency of reaction rates at reaction sites and
ii. exothermic and endothermic nature of H_2 oxidation and H_2O reduction respectively.

A comparison of the current densities a $\pm$ 50 mV reveals that the asymmetry increases with increasing temperature from 11.4 mA/cm^2 at 650 °C to 268 mA/cm^2 at 850 °C. This finding is counter intuitive since it would be expected that the endothermic of the two reactions dominate at higher temperatures while the exothermic one dominates at decreasing temperatures. This finding suggests that at least at 50 mV overvoltage the dominant contributor to the asymmetry is not the intrinsic endothermic or exothermic nature of the reactions but the H_2O content of the reaction sites. A validation of this hypothesis would necessitate a plug-flow set-up in which the replenishing and removal of reactants and products respectively is much faster than at the herein used rather continuously stirred-tank reactor type of set-up.

Current densities at – 50 mV, – 100 mV and – 140 mV SOEC overpotentials as well as at + 50 mV from the anodic branch were read off at the different temperatures and the corresponding Arrhenius plots displayed in Figure 3.4-11 c and d respectively. Activation energies of 1.17, 1.17 and 1.16 eV were obtained at - 50, - 100 and - 140 mV overpotentials in the cathodic branch, depicting an independence of activation energy on overpotential of the cathodic branch in the investigated temperature range of 850 °C – 650 °C. From the anodic branch data at 50 mV overpotential, a slightly larger activation energy of 1.25 eV was obtained.

[x] It has been shown in section 3.3.2.2.1 that effectively the larger change in entropy at the oxygen electrode actually determines the overall heating/cooling behavior under load if all external impacts such diffusion and heat transport from active sites were ideal.

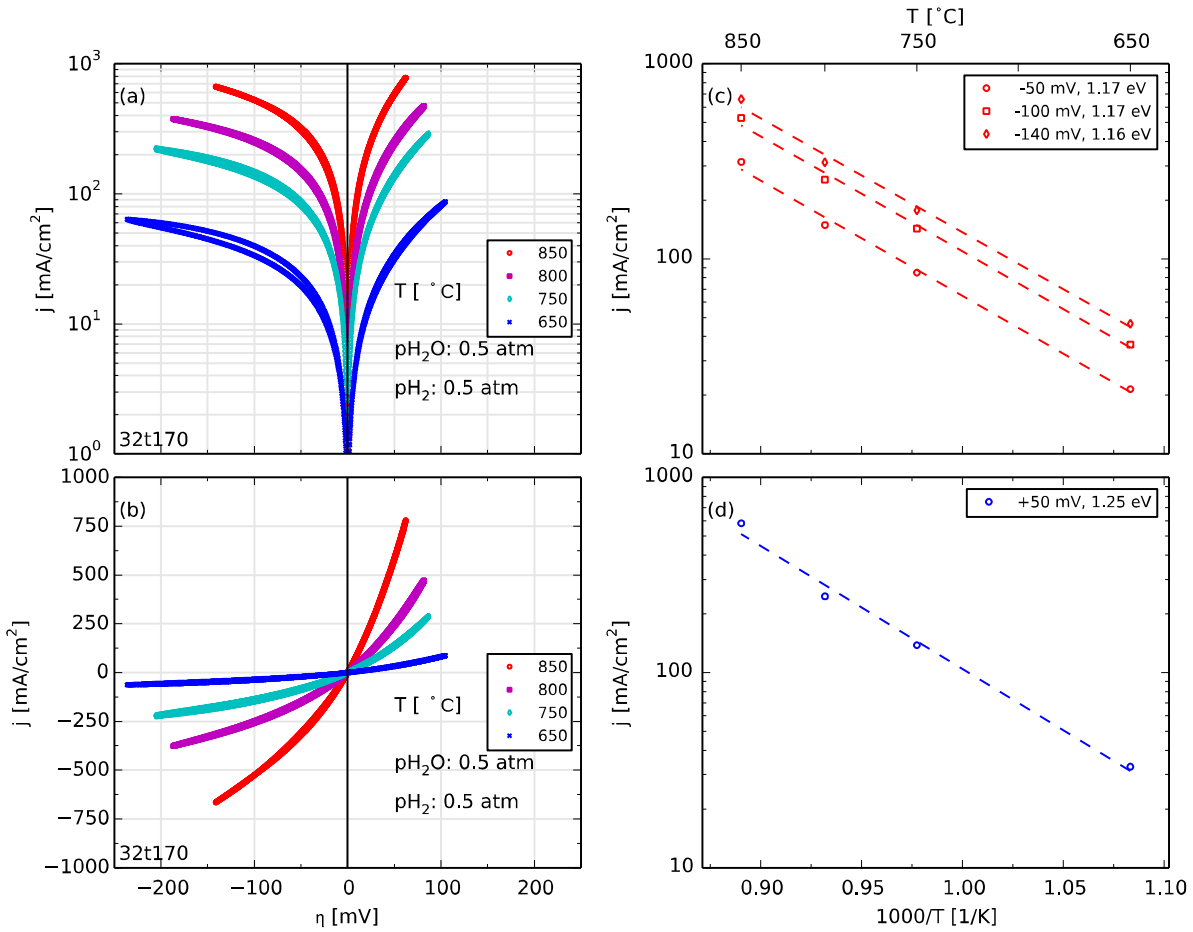

Figure 3.4-11: (a) Current density – overpotential curves in a 50/50 H_2/H_2O atmosphere recorded between 650 °C– 800 °C. (b) Linear scale representation of curves in (a), (c) Arrhenius plot of current densities at - 50-, - 100- and – 140 mV read off from (a), (d) Arrhenius plot of current density at + 50 mV in (a).

Holtappels et al.[79] similarly demonstrated an independence of activation energy on overpotential for the cathodic branch in a similar temperature range of 725 °C – 845 °C although with a slightly lower value of ca. 88 kJ/mol (0.91 eV). For the anodic branch Holtappels et al.[79] obtained 135 kJ/mol (1.4 eV) at 100 mV overpotential, decreasing almost linearly with increasing overpotential at a rate of - 0.7 eV/V. Bearing in mind the dependence of activation energies on microstructure, materials or fabrication details[80] that would account for the difference in magnitude of literature values with those in this work, a major consistency of the results obtained in this work for both branches with literature[79] lies in the fact that the activation energy for the anodic branch is larger than that of the cathodic branch at all overpotential values. As such, if the activation energy were the sole factor influencing the reaction rate, under polarization in the investigated overpotential range H_2O reduction would take place more readily than H_2 oxidation.

3.4.1.3.2 Determination of Charge Transfer Coefficient from C/V-Curves

The charge transfer coefficient has been determined indirectly from impedance spectra of s.t.a. full SOCs recorded under load[3] (cf. section 3.3.2.4 also). In a similar procedure used to investigate patterned Ni/YSZ anodes, Utz et al.[66] also determined the charge transfer coefficient from impedance spectra under load with the added value that their values were void of possible concentration, counter electrode (oxygen electrode in a full cell) or ionic transport contributions.

With the *SmallWE* geometry, current density vs. polarization curves of the investigated (porous) working electrode are determined almost completely free of (i) joule heating of the electrolyte (ii) concentration-related contributions and (iii) counter electrode contributions. As such with the exception of processing-related tailoring of microstructural characteristics, the curves obtained from these cells are expected to provide the purest electrode chemistry-specific kinetics for porous electrodes.

By fitting[81] the BV-type equation (32) to the anodic branches of the C/V-curves displayed in Figure 3.4-11 (a) the charge transfer coefficients of the here investigated Ni/YSZ porous electrodes could be determined for the temperatures 650 °C, 750 °C, 800 °C and 850 °C in a fuel mixture of 50/50 H_2/H_2O. The measured curves, fits and obtained charge transfer coefficients α for the anodic branch are displayed in Figure 3.4-12 (a). The exchange current densities j_0 (i.e. α and j_0 were free parameters or fit results) also obtained from the fits are displayed in Figure 3.4-12 (b).

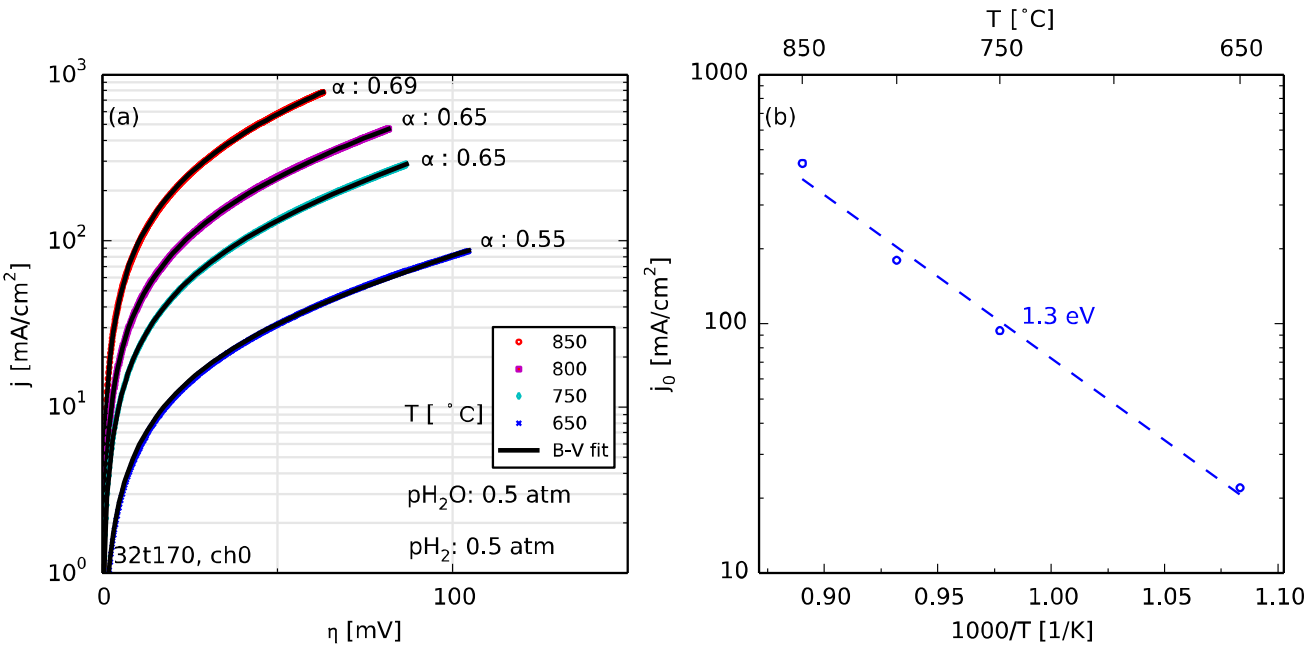

Figure 3.4-12: (a) Anodic current density – overpotential curves in a 50/50 H_2/H_2O atmosphere recorded between 650 – 800 °C and corresponding BV fits. (b) Arrhenius plot of exchange current density from the BV fits in (a).

From the above anodic branch fits (apparent)[79] charge transfer coefficients α of 0.69, 0.65, 0.65 and 0.55 were obtained for the anodic branch curves at 850 °C, 800 °C, 750 °C and 650 °C respectively. In section 3.3.2.4.2 a value of 0.62 was obtained for the Ni/YSZ fuel electrode from FZJ full cells in this work at 800 °C in a 50/50 H_2/H_2O fuel. In section 3.3.2.4.2 as well, a value of 0.63 was obtained for the same electrode from two DTU Energy cells investigated at 700 °C in a 80/20 H_2/H_2O fuel mixture in this work. Leonide et al.[3] obtained 0.59 for the Ni/YSZ electrode at 800 °C from impedance spectra under load from the FZJ full cell geometry. Meanwhile Utz *et al*.[82] however investigating patterned Ni/YSZ anodes but also from impedance spectra under load obtained comparable values with 0.69, 0.65 and 0.61 for the temperatures 800 °C, 750 °C and 700 °C respectively. Apart from being at most 6 % smaller at corresponding temperatures, the consistency of the results obtained in this work with Utz´s results consist of the fact that the apparent transfer coefficient increases with increasing temperature as well.

From the exchange current densities displayed in the Arrhenius plot in Figure 3.4-12 (b) an activation energy of 1.3 eV is obtained—a value comparable with the 1.25 eV obtained at + 50 mV overpotential from the Figure 3.4-11 (d) and lies in the same order of magnitude as the 1.13 eV obtained from impedance spectra at OCV in section 3.4.1.2.3.

A similar analysis was carried out for cathodic branch C/V-curves of Figure 3.4-11 (a) and the resulting transfer coefficients and exchange current densities are displayed in Figure 3.4-13 (a) and (b)[xi] respectively. From Figure 3.4-13 (a) it is evident that the fits are less accurate[xii] than those of the anodic branch. Also, much larger apparent charge transfer coefficients are obtained ranging from 0.82 at 850 °C, 0.83 at 800 °C and 0.84 at 750 °C to 0.85 at 650 °C. The trend of increasing transfer coefficient with decreasing temperature is opposite to that obtained from anodic branch curves, which increased with increasing temperature. From the FZJ cell investigated in section 3.3.2.4.2 a slightly lower value of 0.72 was determined from SOEC mode. This value was however also larger than the 0.62 obtained from the anodic branch.

From the Arrhenius plot of the exchange current densities in Figure 3.4-13 (b) an activation energy of 1.16 eV was obtained—the same value obtained from cathodic branch current densities at – 50 mV, - 100 mV and - 150 mV in Figure 3.4-11 (c). For comparison 1.3 eV was obtained from the exchange current densities determined from the anodic branches and the 1.13 eV obtained from OCV impedance data. However although all three values are in the same order of magnitude as the 1.09 eV obtained from impedance spectra at OCV for the Ni/YSZ electrode of s.t.a. FZJ cells by Leonide et al[3] the slightly higher values obtained in this work consistently depict the smaller performance of the investigated electrodes as compared to the Ni/YSZ electrode of FZJ cells.

[xi] For comparison the exchange current densities from anodic branch fits have also been displayed
[xiixii] Residuals in found in ref. [185]

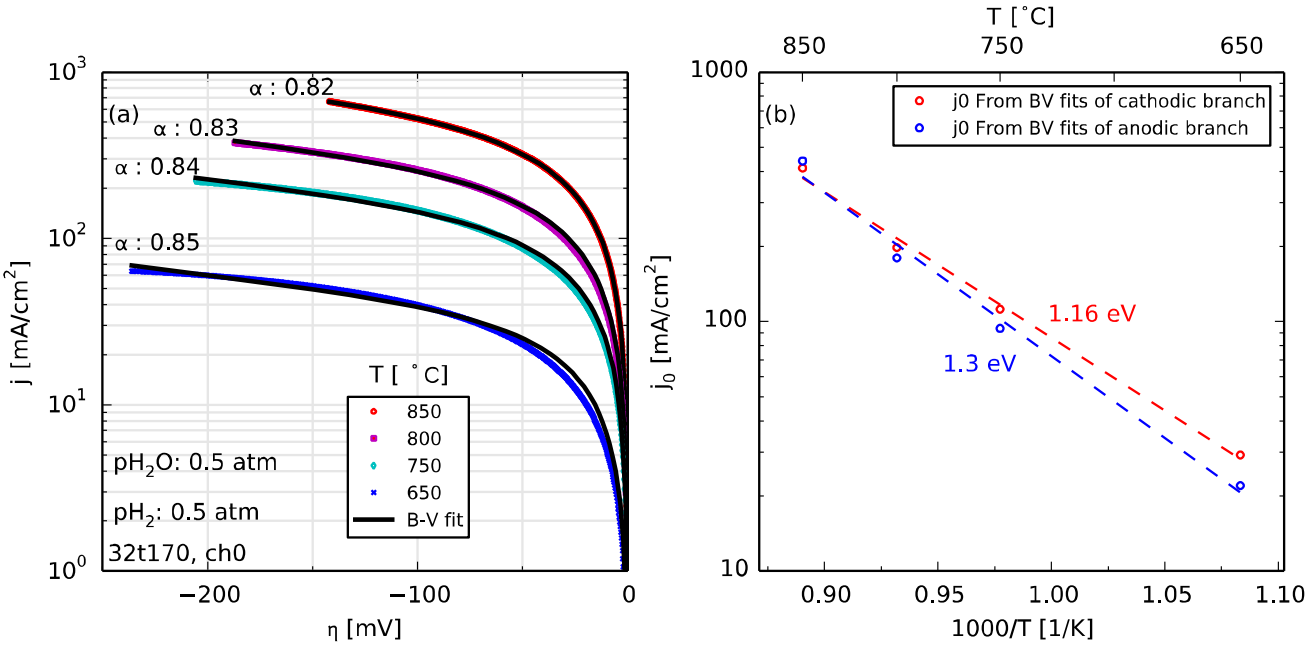

Figure 3.4-13: (a) Cathodic current density – overpotential curves in a 50/50 H_2/H_2O atmosphere recorded between 650 - 800°C and corresponding BV fits. (b) Arrhenius plot of exchange current density from the BV fit from cathodic branch[xiii]

The residuals[xiv] of the discussed BV fits (difference between measured and BV -fitted curves) have been displayed in Figure 3.4-14 (a) and the corresponding relative equivalents in Figure 3.4-14 (b). From the plot of absolute residuals it is evident that the anodic branch values lie within a $\pm$ 5 mA/cm^2 while the cathodic branch residuals lie within a $\pm$ 10 mA/cm^2 window. Furthermore, unlike the anodic branch residuals that are almost randomly distributed around the y = 0 line the cathodic branch residuals are displaying a pronounced fluctuating trend suggesting a systematic error. Also, from the plot of the relative residuals in Figure 3.4-14 (b) the anodic branch displays values well within $\pm$ 5 % window, whereas the cathodic branch reveals overestimation of the current density for cathodic overpotentials < 50 mV.

The inaccuracy of the fits of the cathodic branch and thus corresponding higher transfer coefficient and exchange current density values weaken the credibility of the results from the cathodic branch fits. This greater difficulty to reliably obtain charge transfer coefficients for the cathodic branch has been observed previously in literature [79] and suggests that a simple BV model of the measured electrode kinetics is insufficient and/or different reaction mechanisms might be occurring in anodic vs cathodic polarization. This is true especially for cathodic branch overpotentials smaller than 50 mV in Figure 3.4-14 (b).

[xiii] Anodic branch included for comparison
[xiv] From Origin software employed for the fits

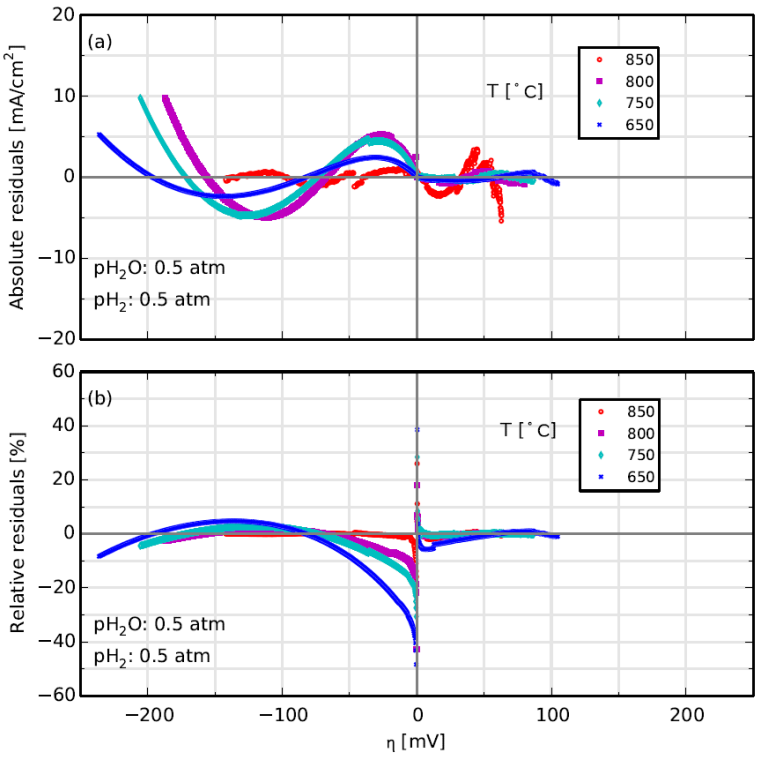

Figure 3.4-14: (a) Absolute residuals of the BV-fits of the cathodic and anodic branches of the C/V curves at in the temperature range 850 – 650 °C in a 50/50 H_2/H_2O fuel. (b) Corresponding relative residuals obtained by normalizing the absolute values with the corresponding recorded current density

The temperature trend around 0 mV suggests that the BV-type equation applied to the cathodic branch curves underestimates or does not account for a thermally activated mechanism predominant at lower cathodic overpotentials. As will be seen in section 5.3 this could be a result of impurities that poison SOEC mode operation more with decreasing temperature.

3.4.1.3.3 Steam- and Hydrogen Partial Pressure Dependencies

After recording the impedance spectra during the steam and hydrogen partial pressure variations discussed in section 3.4.1.2.4, C/V curves were recorded, appropriately i-R-corrected and displayed in Figure 3.4-15 (a) and (b) for pH_2O and pH_2 variations respectively.

A qualitative comparison of the C/V curves reveals a negligible dependence of the kinetics on pH_2 variation against pH_2O variation where the curves of both branches display a more appreciable pH_2O dependence. Current

density values at 25 mV overpotential intervals were recorded for both branches of the C/V curves, displayed in a double logarithmic plot of $j(\eta)$ vs. $p\mathrm{H_2}$ (or $p\mathrm{H_2O}$) and a linear fit done (i.e. power law dependency assumed). From the slopes corresponding gas dependencies were determined at different overpotentials. These are displayed in Figure 3.4-15(c) and (d) for steam and hydrogen variations respectively.

The evolutions of gas dependencies with increasing overpotential in both anodic and cathodic branches reveal changes in reaction kinetics. For the $p\mathrm{H_2O}$ variation, this change occurs in both branches from an overpotential of 50 mV. The $p\mathrm{H_2O}$ dependency b determined from the cathodic branch curbs towards lower values at higher overpotentials while a trend in the opposite direction is observed for values obtained from the anodic branch curves. In the $p\mathrm{H_2}$ variation the $p\mathrm{H_2}$ dependency a from the cathodic branch displays an increasing trend with overpotentials up 100 mV and then curbs towards decreasing values for $\eta > 100$ mV. On the other hand this decreasing trend is more pronounced for values from the anodic branch already at 25 mV.

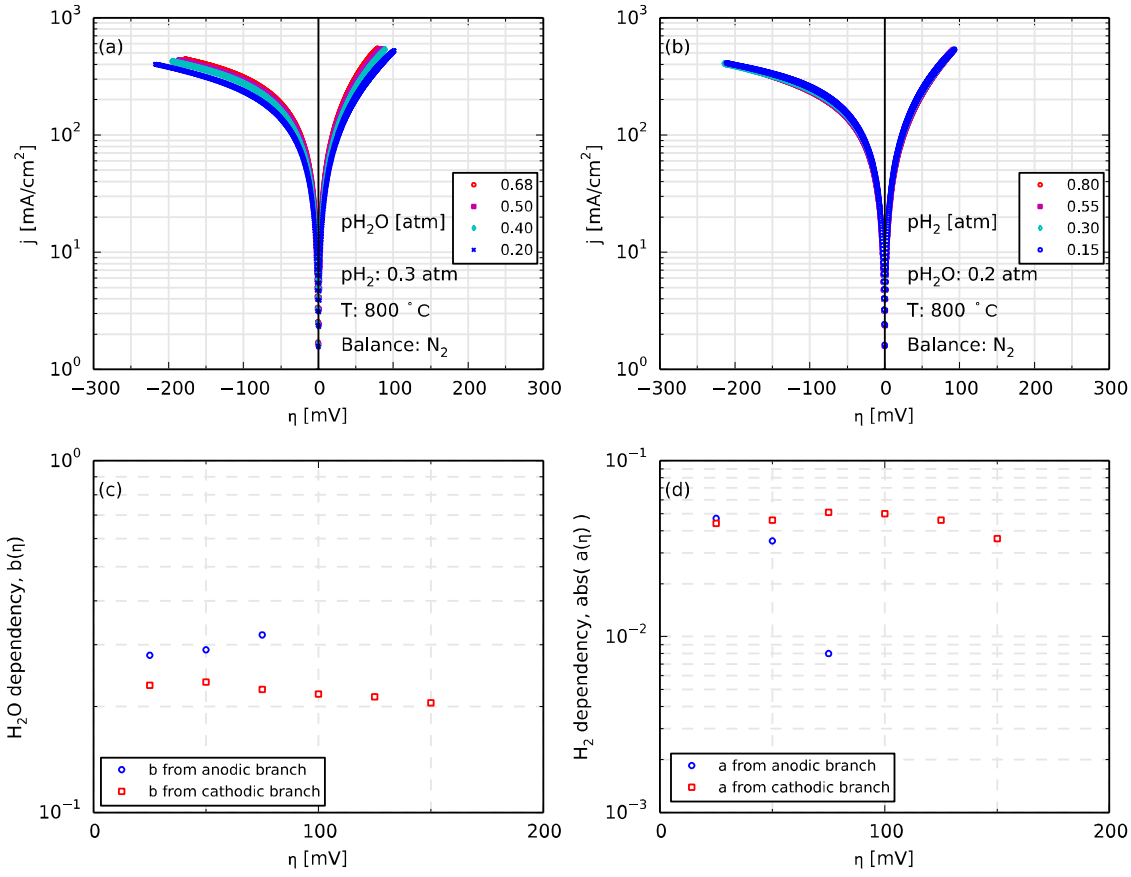

Figure 3.4-15: (a) Current density – overpotential curves in a $p\mathrm{H_2O}$ variation at constant $p\mathrm{H_2}$ of 0.3 atm with $\mathrm{N_2}$ balance. (b) Current density – overpotential curves in a $p\mathrm{H_2}$ variation at constant $p\mathrm{H_2O}$ of 0.2 atm with $\mathrm{N_2}$ balance. (c) $p\mathrm{H_2O}$ dependency as a function of overpotential (d) $p\mathrm{H_2}$ dependency as a function of overpotential.

A thorough analysis of the observed trends requires a detail analysis of available modeling approaches describing the elementary kinetic steps involved in hydrogen oxidation and/or steam reduction reactions[83–86] whereby the overpotential dependence of the individual kinetic steps are considered at different pH_2 or pH_2O partial pressures. These analyses are outside the scope of this work and the results are available for validation of such models. Although the impact of microstructure cannot be underestimated so that the here presented results may also be microstructure specific, the possible impact of impurities especially during cathodic polarization although not critical at temperatures around 800 °C may not be overlooked.

3.4.1.4 Summary of Determined Kinetic Parameters

A summary of some of the kinetic parameters determined here is displayed in Table 3.4-3 alongside corresponding values from literature. Furthermore, the exchange current densities obtained from AC measurements at OCV, anodic and cathodic C/V curves (DC measurements) as well as those calculated through the analytical expression in equation (37) and parameters from Table 3.4-3 are compared in Figure 3.4-16.

Assuming that j_0 values determined from EIS spectra at OCV and equation (33) are the ideal values, it can be seen from Figure 3.4-16 that except at 850°C the analytical expression using the herein determined parameters predicts j_0 with very good accuracy. The values from the anodic branch BV fit come closest at all temperatures, whereas the values from the cathodic branch fits approximate j_0 better with increasing temperature.

Table 3.4-3: Kinetic parameters of the Ni/YSZ electrode determined through electrochemical impedance spectroscopy under OCV as well as from C/V curves

Parameter	Equation	Value	Literature value[3]
E_a [kJ/mol]	(36)	109.2 (1.13 eV)	105.04 (1.09 eV)
B [Ωcm²]	(36)	$1.28 \cdot 10^{-6}$	$3.83 \cdot 10^{-7}$
γ_{an} [A/m²]	(37)	$3.7 \cdot 10^{5} \cdot T$	$1.83 \cdot 10^{6} \cdot T$
a	(37)	-0.07	-0.1
b	(37)	0.22	0.33
α	(32)	0.55 – 0.69	0.59
			0.61 – 0.69 Ref. [82]

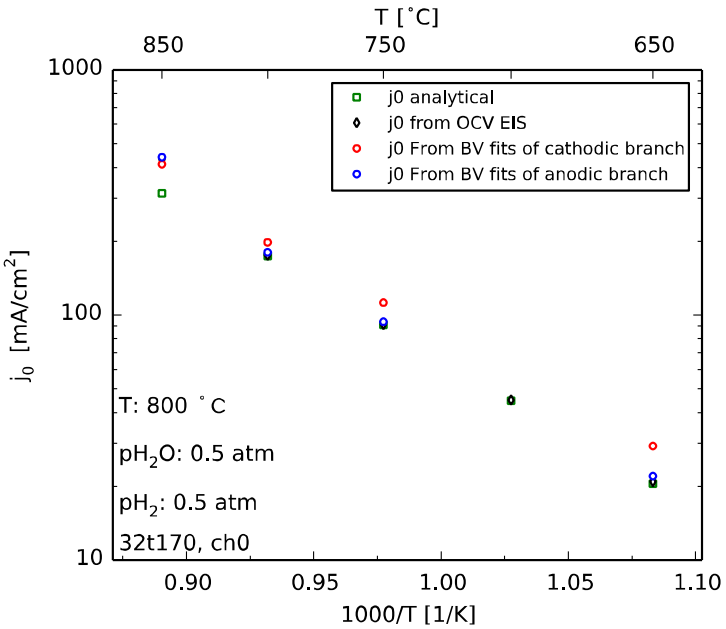

Figure 3.4-16: Exchange current densities of the Ni/YSZ calculated in a 50/50 H_2/H_2O gas composition in the temperature range 650 °C to 850 °C from equations (37), OCV (equation (33)) and from the cathodic and anodic branch BV-fits.

3.5 Oxygen Electrodes

The DTU Energy and FZJ single cells investigated within the framework of this thesis had LSC/CGO and LSCF oxygen electrodes respectively as described in Table 3.2-1. This served as motivation to aim to obtain the kinetics of these electrodes with the *SmallWE* geometry and its advantages (cf. section 3.4.1.3). Furthermore, it was shown in section 3.3.2.2 that the ASR of the LSC/CGO electrode was very small and difficult to deconvolute from full-cell impedance data due to the proximity of its characteristic frequency to that of the substrate diffusion process. This difficulty as will be seen in section 5.2.2.3 is even more severe for the LSCF oxygen electrode whose relaxation frequency is lower in the frequency domain and in H_2/H_2O fuels completely overlaps the substrate diffusion peak[87]. This means that the corresponding current density vs. overpotential curves of these electrodes in H_2/H_2O fuels determined from full cell analysis could be more prone to error than those of processes whose relaxation frequencies do not overlap.

The *SmallWE* cells of the oxygen electrodes LSC/CGO and LSCF were fabricated and sintered as described in section 3.2.1.3 and electrochemical characterization was done as described in section 3.2.3. Thereby the test-set up displayed in Figure 3.2-7 in section 3.2.2 was employed. Both electrodes were mounted on separate channels and thus were operated under the exact same conditions of temperature and oxidant gas.

3.5.1 Temperature Dependency

3.5.1.1 AC Analysis

A variation of temperature was carried out from 850 °C down to 650 °C in 50 K intervals and with air as oxidant flowing at 6 l/h. Thereby the spectra of both electrodes were recorded in succession and then repeated before setting the next target temperature. To avoid eventual destruction of electrodes upon polarization no C/V curves were recorded during this first variation.

The resulting spectra are displayed in Figure 3.5-1 (x_i, x = a – e) for the LSC/CGO electrode for temperatures 850 °C - 650 °C respectively and the corresponding DRTs in subplot f_i. Corresponding equivalent plots for the LSCF electrode are displayed in subplots x_ii, x = a – f.

3.5.1.1.1 Data Quality, CNLS Fits and Fit Residuals.

The Nyquist plots in Figure 3.5-1 display a kink at high frequencies. This kink results from the measurement equipment auto ranging. As can be seen from the KK-residuals in Figure 3.5-2 (b) for a spectrum of the LSCF electrode at 850 °C (cf. also Figure 3.5-1 (a_ii)) the kink occurs at 100 kHz and does not significantly affect the otherwise excellent data quality.

The CNLS fit of the data was carried out with an ECM model comprising a series resistance R_S for the electrolyte resistance, an RQ-element for the high frequency process, a Gerischer Element for the oxygen electrode and an RQ-element for the low frequency process. Exemplarily, a simulation of the so fitted processes of an LSCF electrode spectrum recorded at 850 °C and the corresponding residuals are displayed in Figure 3.5-2 (c) and (d) respectively. For the relaxation frequencies of the process, the corresponding imaginary part representations and DRTs are displayed in subplots (e) and (f) respectively.

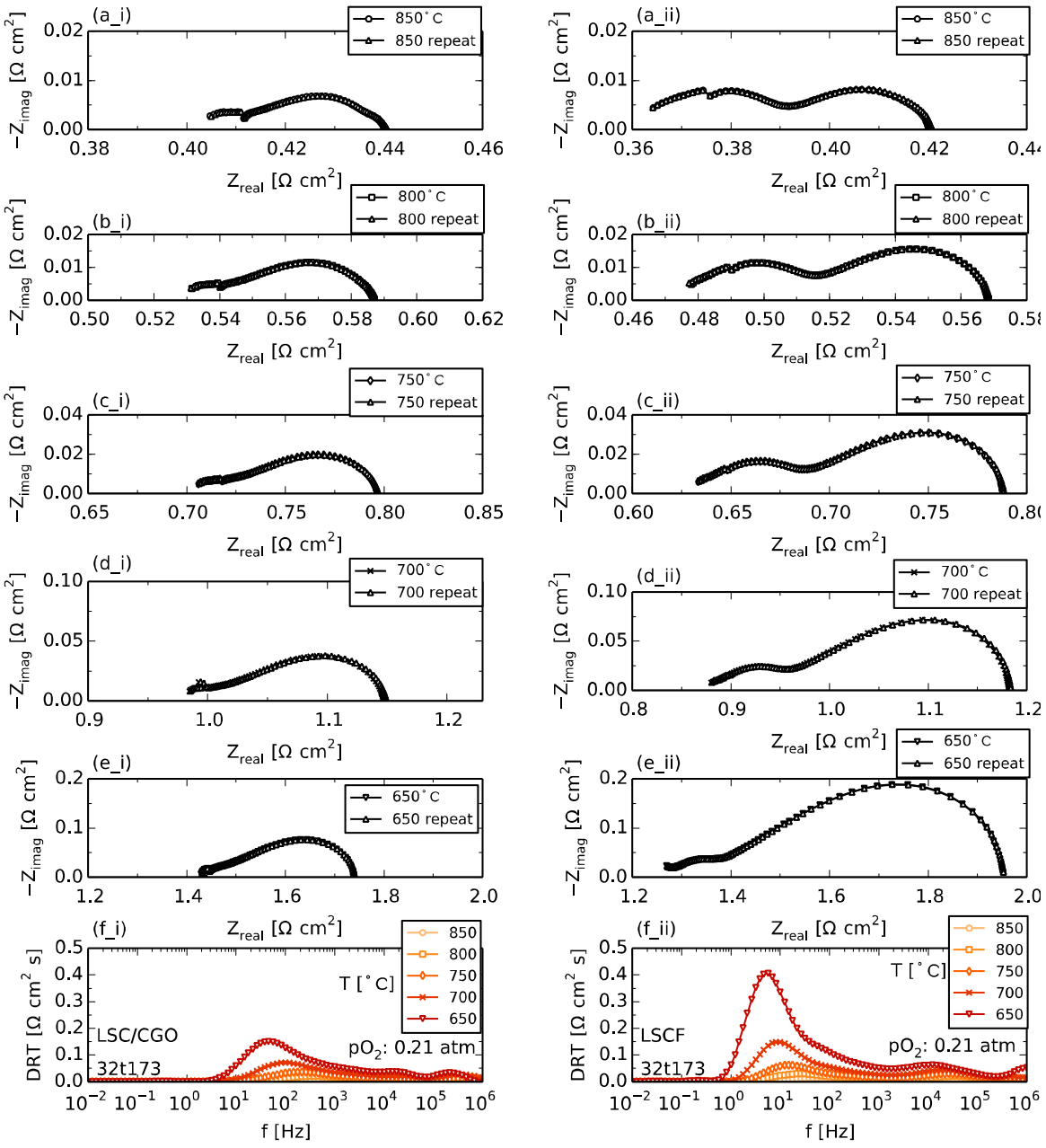

Figure 3.5-1: (a_i – e_i) Evolution of Impedance spectra of LSC/CGO *SmallWE* cells recorded during a temperature variation from 850 °C down to 650 °C. Corresponding spectra for the LSCF electrode are displayed in figures (a_ii – e_ii). The DRTs (of the first spectra) of the electrodes are displayed in subplot f_i and f_ii for LSC/CGO and LSCF respectively.

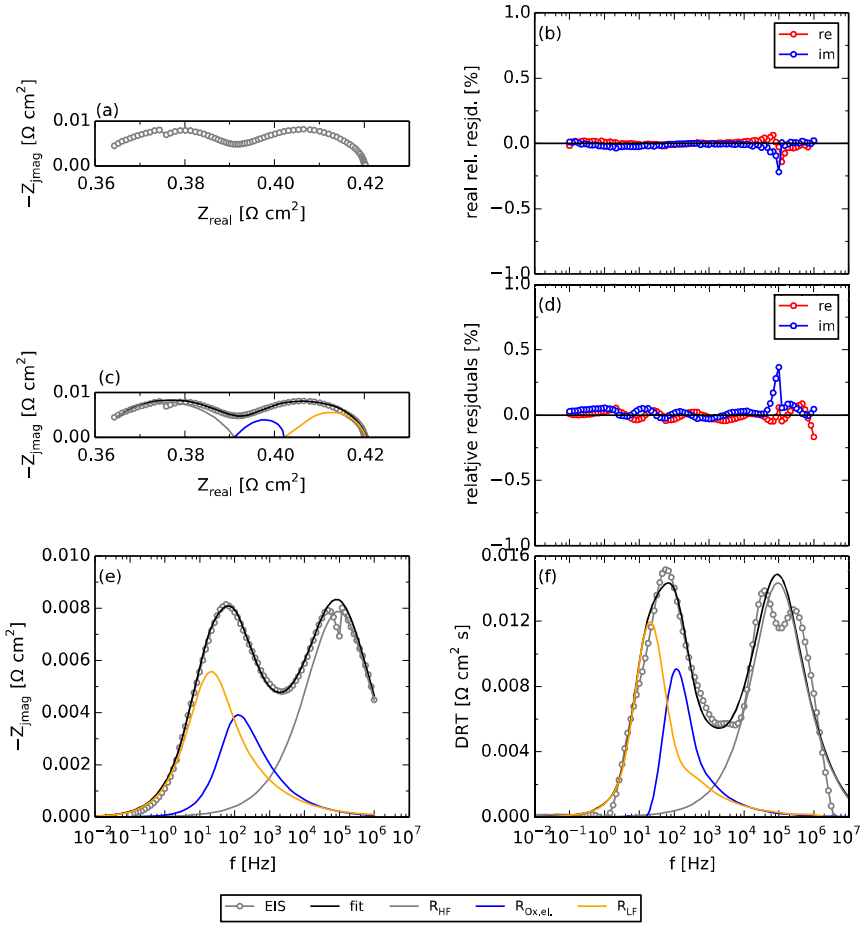

Figure 3.5-2: (a) Impedance spectrum of an LSCF *SmallWE* cell recorded at 850 °C (b) the corresponding KK-test residuals, (c) the CNLS fit, with Boukamp goodness of fit χ^2 = 1.69·10^{-5}, (d) corresponding CNLS fit residuals, (e) imaginary part of spectrum, overall fit and fit results of individual processes (f) DRT of spectrum, overall fit and individual fit results

3.5.1.1.1 Results and Discussion

To obtain the activation energies from the ASR contributions obtained through CNLS fits of the electrode spectra the series resistances of both cells were evaluated with equation (35) and the rest from the linear fits in the Arrhenius plots shown in Figure 3.5-3[xv]. Thereby the LSC/CGO and LSCF values are displayed in subplots (a) and (b) respectively.

[xv] The annotated series resistance values have only been included for completion as they were determined differently through equation (35)

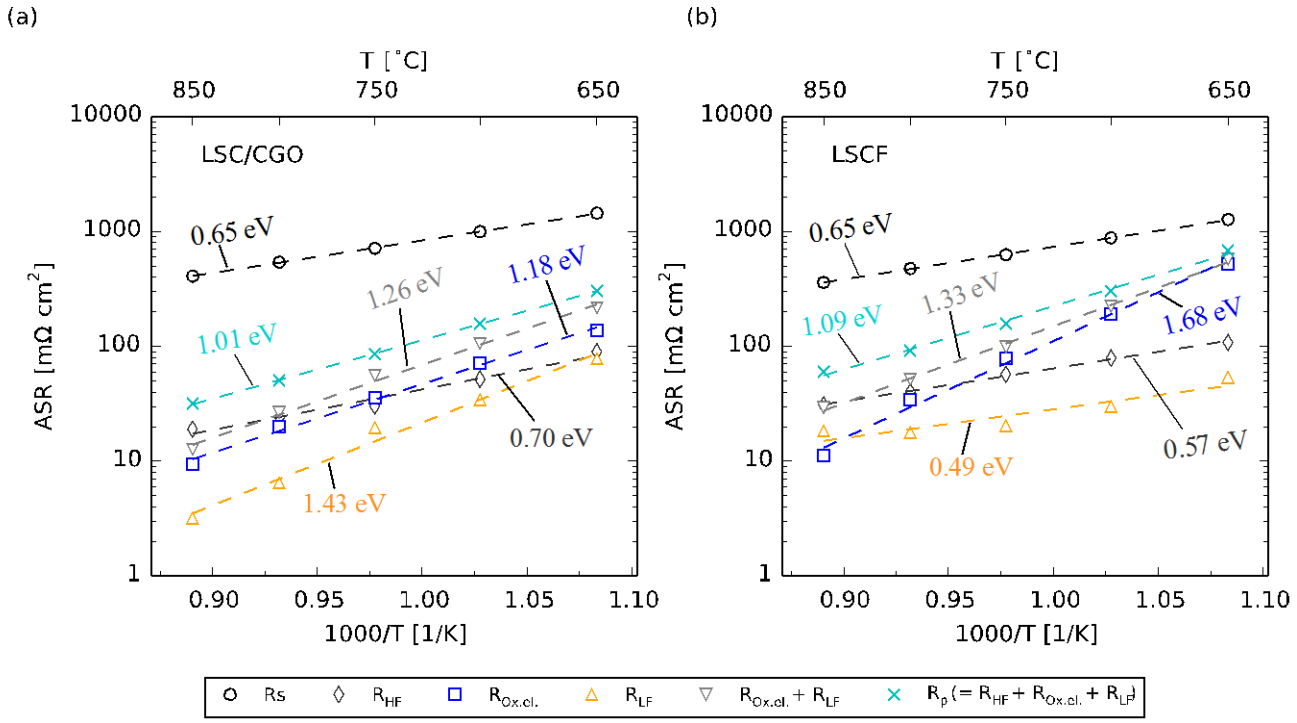

Figure 3.5-3: Evolution of individual ASRs of oxygen electrode *SmallWE* cells in the temperature range 850 °C – 650 °C (a) LSC/CGO and (b) LSCF. Spectra are recorded in air flowing at 6 l/h air.

For the CGO electrolytes 0.65 eV (62.6 kJ/mol) was obtained from both electrode cells—values consistent with the 65.18 kJ/mol (0.68 eV) reported[88] for ionic transport in CGO10.

For the LSC/CGO electrode an activation energy of 1.18 eV (113.93 kJ/mol) was obtained from the Gerischer element. Hjelm *et al.* [69] reported 1.2 eV (120 kJ/mol) for electrodes sintered at 1080 °C and Samson *et al.* [49] reported 123 kJ/mol (1.27 eV) for cells sintered at 1050 °C and a smaller value of 99 kJ/mol (1.03 eV) for cells with LSC infiltrated into a CGO backbone.

For the LSCF electrode 1.68 eV (161.95 kJ/mol) was obtained for the Gerischer element in this work. For LSCF cathodes of FZJ cells 1.45 eV has been reported[3] suggesting a lower performance of the screen-printed electrodes investigated herein.

The high frequency arc of the LSC/CGO electrode displayed an activation energy of 0.7 eV (67.25 kJ/mol) against 0.57 eV (54.87 kJ/mol) for that of the LSCF electrode. Like similar high frequency arcs observed in the *SmallWEs* of the Ni/YSZ fuel electrodes (cf. Figure 3.4-8), it is not clear how much of these high frequency arcs are artefacts related to the cell geometry since similar arcs in LSC/CGO and especially LSCF have been suggested[48] to be related to adhesion at the electrode / electrolyte interface[48]. In fact Tietz *et al.* [89] do not only report decrease in performance due to electrode / electrolyte adhesion but also adhesion between oxygen electrode particles.

Nielsen et al. [48] observed that the process could only be fit with an RQ-element with exponents as low as 0.45. In this work the exponents 0.45 and 0.6 were employed for the fits of the results displayed in Figure 3.5-3 for the LSC/CGO and LSCF electrodes. However according to Adler et al. [64] the contributions of the electronic and ionic conduction across the interfaces with the current collector and electrolyte respectively to the ASR would be located here, with the electronic contributions higher up in frequency.

The low frequency process in both electrodes displayed activation energies of 1.43 eV (138 kJ/mol) and 0.49 eV (47 kJ/mol) respectively for LSC/CGO and LSCF electrodes. These activation energies suggest the presence of a thermally activated process overlapping the negligibly small (cf. section 3.4.1.2.1) stagnant layer diffusion contribution since this does not display a temperature dependency (cf. Figure 3.4-2). The process distorts the 45 ° slope of the Gerischer shape of the electrodes as observed in literature[48]. It is believed to be related to contributions from the grain boundaries of the oxygen electrodes[48].

Finally, for consistency, activation energies have been determined for the sum of the Gerischer ASR and the low frequency process as well as the activation energy of the whole polarization ASR comprising the depressed high frequency arc, Gerischer element and low frequency process. The values are annotated in the figure for comparison.

3.5.1.2 DC Analysis

A second variation of temperature was carried out under the same conditions of oxidant gas, flow rate and temperature range as in section 3.5.1.1 above, with the sole difference that current density vs. overpotential (j/η) curves were recorded between the EIS spectra at each temperature interval.

The spectra recorded prior to the C/V curves were evaluated as described in section 3.5.1.1.1 to obtain the series resistance used to i - R-correct the C/V curves. These are displayed for temperatures 850 °C – 650 °C in Figure 3.5-4 (a_i) and (b_i) for the LSC/CGO and LSCF electrodes respectively. The corresponding linear representations are displayed in subplots (a_ii) and (b_ii) respectively.

For a quantitative appreciation of the similarities and differences between the polarization curves of both electrodes, the current densities at 50 mV have been read out from both anodic (positive η) and cathodic branches (negative η) and displayed in Figure 3.5-5. Based on this figure and the resulting activation energies, the following observations and comments can be made:

i. The LSC/CGO oxygen electrode displays current densities larger than those from the LSCF electrode under both anodic and cathodic polarization modes. This is consistent with the corresponding ASRs at OCV obtained from symmetric cells of the same materials.(cf. Figure 5.4-1 and Figure 5.4-2 in section 5.4)
ii. The LSC/CGO anodic branch current densities are larger than those from the cathodic branch, with the difference (asymmetry) decreasing with decreasing temperature.

iii. The LSCF electrode displays the exact opposite of (ii) above with the cathodic branch current densities larger than those of the anodic branch and the asymmetry increasing with decreasing current density.

iv. For both electrodes anodic branch activation energies $E_{a,an}$ are larger than those from the cathodic branch $E_{a,cat}$ current densities (cf. – 1.15 eV vs – 0.99 eV for the LSC/CGO electrode and – 1.32 eV vs. - 1.14 eV for the LSCF electrode)

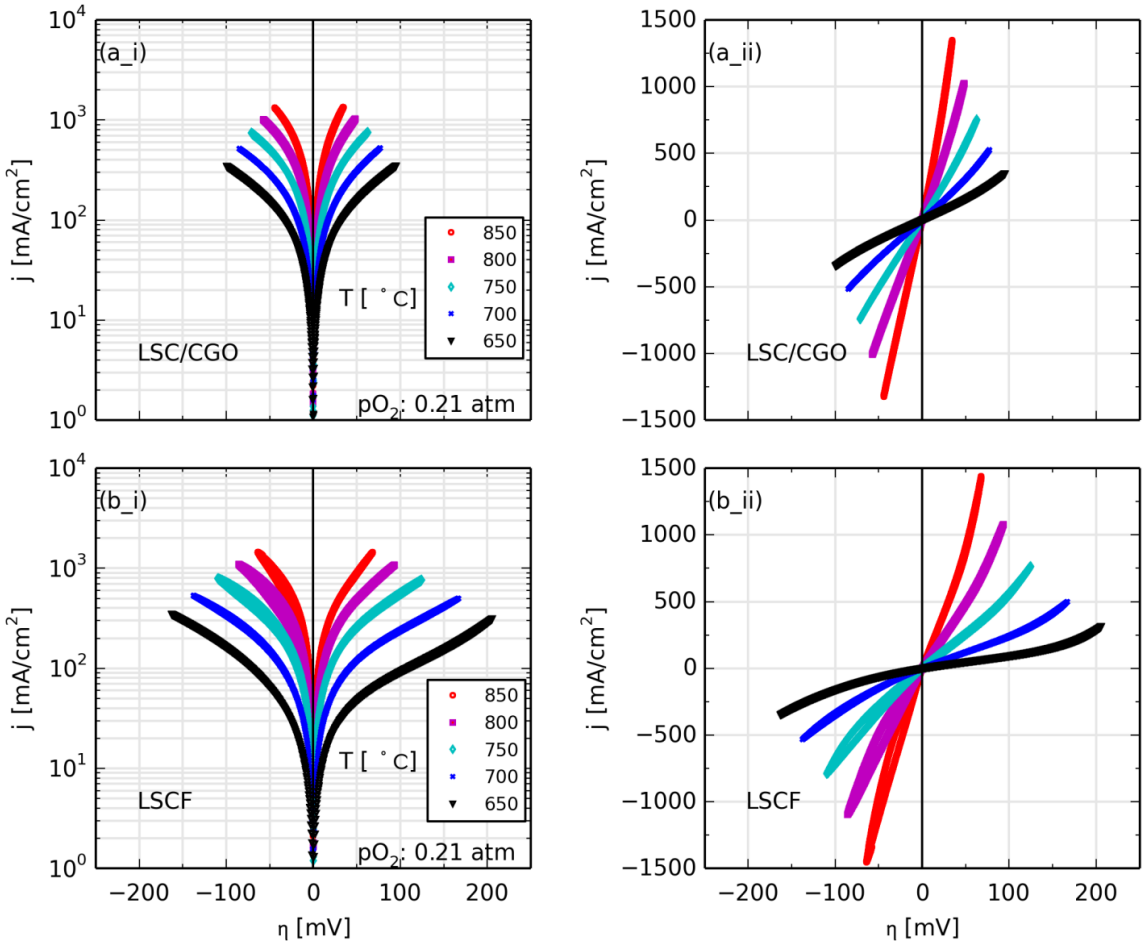

Figure 3.5-4: Current density vs. overpotential curves for oxygen electrodes LSC/CGO and LSCF recorded on *SmallWE* cells in the temperature range 850 – 650 °C. Linear displays of the same data are shown in subplots a_ii and b_ii respectively.

From points (ii) and (iii) above whereby the symmetry of the performance at 50 mV of the LSC/CGO electrode *decreases* with *increasing temperature* while that of the LSCF electrode *improves*, the activation energies from both branches listed in point (iv) can be employed to further understand what is happening;

For the LSC/CGO electrode, both branches are delivering the same current density at 650 °C. The higher activation energy obtained for current densities from the anodic branch means that at 50 mV the operation of the LSC/CGO in anodic mode is favored against operation in cathodic mode. Anodic mode operation means oxygen ion oxidation and oxygen evolution is taking place at the electrode whereas in cathodic mode oxygen molecules are being reduced and transported through the electrolyte towards the counter electrode. Thus for the LSC/CGO oxygen electrode, at 50 mV (and in air) increasing temperature favors the overall oxygen evolution reaction more than it does the oxygen incorporation reaction.

Furthermore, the results suggest that at 50 mV overpotential (and in air) the symmetry of the LSCF oxygen electrode improves with increasing temperature. This improvement is because the anodic branch performance improves more for the same temperature increase than the cathodic branch.

Thus at 50 mV overpotential, although (i) the symmetry of the LSC/CGO and LSCF electrodes displays opposing trends with increasing temperature and (ii) for LSC/CGO electrode the overall oxygen evolution is favored to the overall oxygen incorporation whereas the opposite holds for the LSCF electrode, both electrodes display a common characteristic; The overall oxygen evolution reaction is improving more with increasing temperature than the overall oxygen incorporation reaction is improving. An explanation of this characteristic (which is not necessarily the same at all overpotentials) requires an investigation of all involved steps and mechanisms in both reactions and their temperature dependencies. This is out of the scope of this thesis.

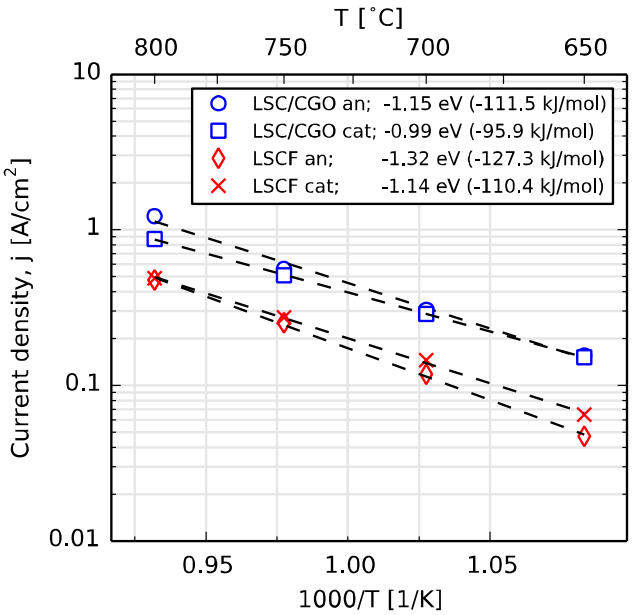

Figure 3.5-5: Current densities of LSC/CGO and LSCF *SmallWE* cells at 50 mV overvoltage from the anodic and cathodic branches in the temperature range 800 – 650 °C . The curves are recorded with air as oxidant flowing at 6 l/h.

Both branches of the C/V curves in Figure 3.5-4 were for both electrodes fit with to BV-type equation (32) in a bid to determine the charge transfer coefficients α_{el} and exchange current densities $j_{0,el}$ in the temperature

range 800 – 650 °C. These are displayed Figure 3.5-6 with the exchange current densities in subplot (a) and transfer coefficients in subplot (b).

Both anodic and cathodic branches of the LSC/CGO electrode display same exchange current densities at all temperatures suggesting an overall symmetry of C/V curves in both modes at all temperatures. The LSCF electrode does not display as much symmetry, with the exchange current densities from both branches diverging at lower temperatures—consistent with the trend observed at 50 mV for the current densities.

With the exception of 800 °C all transfer coefficients of both electrodes lie between 0.4 and 0.6. For the LSCF oxygen electrode Leonide *et al*. [3] reported 0.65 determined from EIS spectra under load, with the cell operating in fuel cell mode. For the FZJ cells investigated in section 3.3.2.4.2 the values 0.67 and 0.72 were determined for the LSCF electrode for SOFC and SOEC operation modes of the full cell i.e. for the oxygen electrode the anodic mode value was 0.72 and was larger than the 0.67 obtained when the oxygen electrode was operating in cathodic mode. This represents a qualitative consistency with the observations in Figure 3.5-6 (b) for the LSCF electrode at 800 °C whereby the anodic branch value of 0.56 is larger than the 0.3 obtained from the cathodic branch. Thus for the *SmallWE* LSCF electrode cells investigated herein and at 800 °C , it is the value from the anodic branch (0.56) that comes closest to those obtained from full cells while the value from the cathodic branch is with a value of 0.3 significantly smaller. Furthermore, the LSCF values from the cathodic branch are displaying a decreasing trend with increasing current density whereas all other values are increasing to different extents with increasing temperature.

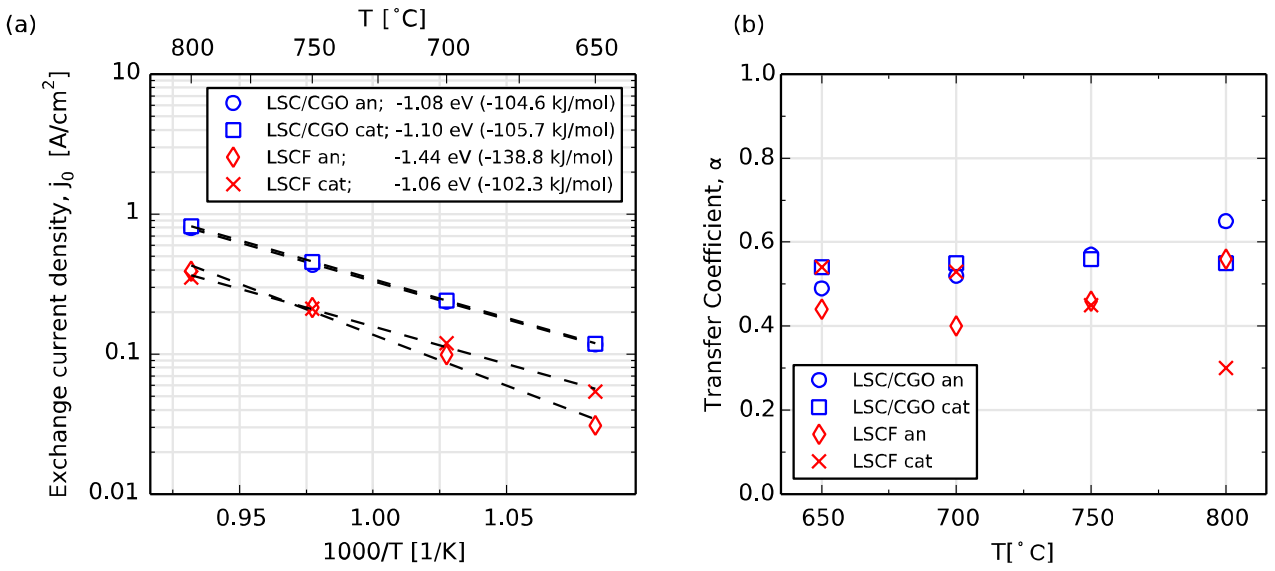

Figure 3.5-6: (a) Evolution of the exchange current densities of the LSC/CGO and LSCF oxygen electrodes with temperature determined through fitting of corresponding C/V curves to the BV-type equation (32) (b) the corresponding charge transfer coefficients.

3.5.2 Oxygen Partial Pressure Dependency

3.5.2.1 DC Analysis

The oxygen partial pressure was varied at 800 °C from 0.21 atm (air) to 0.02 atm by diluting the air with appropriate amounts of N_2 and maintaining the total flow rate of 6 l/h. At each oxygen partial pressure, an impedance spectrum was recorded, then a C/V curve and finally another EIS spectrum. The C/V curves were i – R – corrected with the spectra recorded before the C/V curves. The results for LSC/CGO and LSCF electrodes are displayed in Figure 3.5-7 (a_i) and (b_i) respectively with corresponding linear plots in corresponding subplots (x_ii, x = a, b).

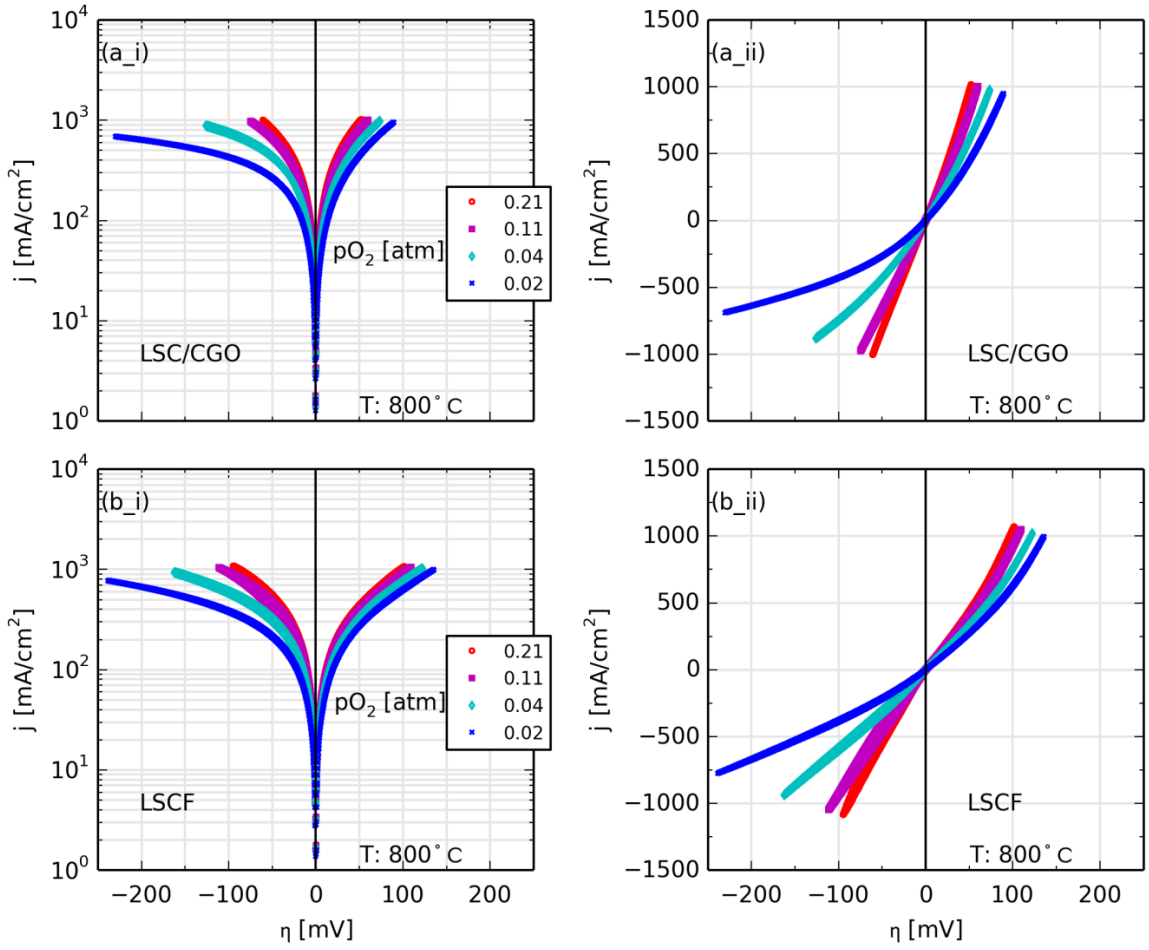

Figure 3.5-7: Current density vs. overpotential curves for oxygen electrodes LSC/CGO and LSCF recorded on SmallWE cells at 800 °C in a pO_2 variation from 0.21 – 0.02 atm. Linear displays of the same data are shown in subplots a_ii and b_ii respectively.

A qualitative appreciation of Figure 3.5-7 reveals that with decreasing pO_2 the cathodic branch requires more overvoltage to deliver the same amount of current as the anodic branch—anodic and cathodic branches are

increasingly asymmetric at lower pO_2. To quantitatively compare the pO_2 dependency of both electrodes and both operation modes, the current densities at 50 mV were extracted and plotted in Figure 3.5-8.

At 0.21 atm, the higher performance of the LSC/CGO electrode against the LSCF electrode is visible. Furthermore, for the LSC/CGO oxygen electrode, the current density from the anodic branch is with 960 mA/cm^2 larger than the 820 mA/cm^2 from the anodic branch. Meanwhile for the LSCF electrode the cathodic branch current density at 50 mV and at 0.21 atm is 30 mA/cm^2 larger than that from the anodic branch (cf. with 450 mA/cm^2 vs 420 mA/cm^2) These findings are consistent with observations for 800 °C in Figure 3.5-5.

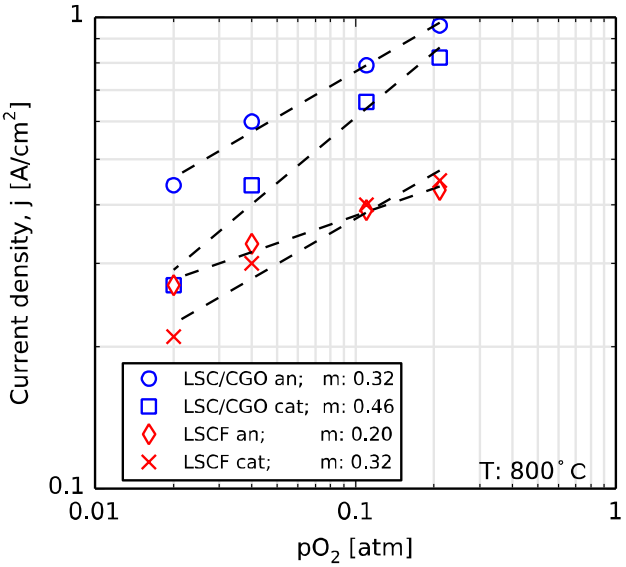

Figure 3.5-8: Current densities of LSC/CGO and LSCF *SmallWE* cells at 50 mV overvoltage from the anodic and cathodic branches at 800 °C in a pO_2 variation from 0.21 – 0.02 atm.

With decreasing pO_2 Figure 3.5-8 further reveals that at 50 mV the asymmetry between anodic and cathodic branches increases for both electrodes. The slopes of the linear fits (annotated in Figure 3.5-8) represent the pO_2 dependency of the current densities at 50 mV overvoltage. For either electrode, the cathodic branch dependency is larger than the corresponding anodic branch dependency. This suggests a higher sensitivity of the cathodic branch reactions to pO_2 change at 50 mV and 800 °C.

Furthermore the LSC/CGO electrode displays higher pO_2 dependencies than the corresponding LSCF branches (cf. 0.32 vs. 0.20 for the anodic branch and 0.46 vs. 0.32 for the cathodic branch). This also suggests a higher sensitivity of the LSC/CGO electrode at 50 mV overvoltage to pO_2 change than the LSCF electrode.

Further comments on the above observations will be made in section 3.5.2.1 based on AC analysis of EIS spectra recorded during the pO_2 variation.

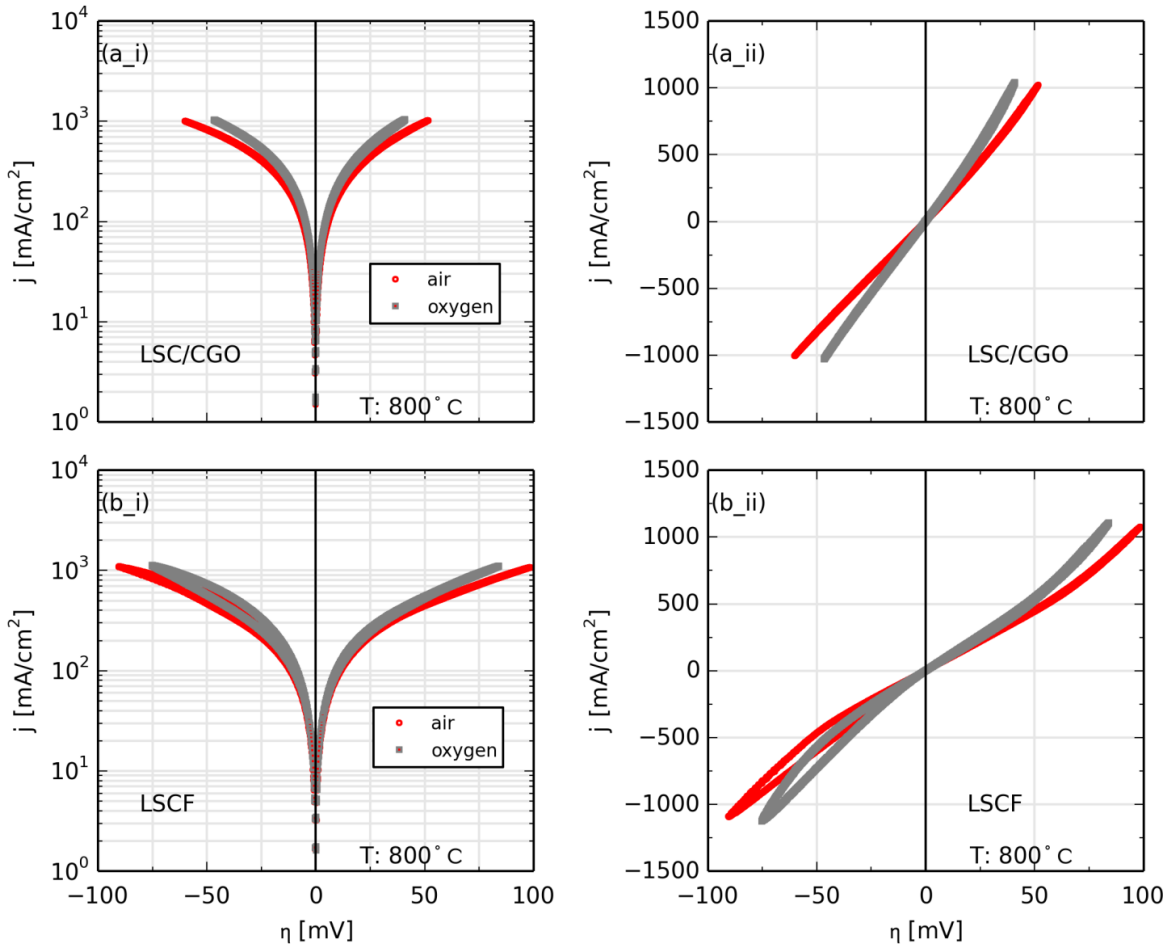

Figure 3.5-9: Operation in air vs. in pure oxygen at 800 °C for (a_i) LSC/CGO (b_i) LSCF; Linear representations of the curves are displayed in subplots (a_ii) and (b_ii) for LSC/CGO and LSCF electrodes respectively. The oxidant flow rate is 3 l/h in each case.

A comparison between operation in air and in pure oxygen was carried out for both electrodes at 800 °C with oxidant gas flowing at 3 l/h. The results are displayed in Figure 3.5-9 (a_i) and (a_ii) for the LSC/CGO electrode and in subplots (b_i) and (b_ii) for the LSCF electrode.

It is evident from Figure 3.5-9 that for both investigated electrodes the electrochemical performance is higher in pure oxygen than in air for all overpotentials in the investigated range. Although it would not be irrational to expect that in pure oxygen i.e. pO_2 = 1 atm, oxygen incorporation would be electrochemically easier than oxygen evolution Figure 3.5-9 clearly suggests that both processes are accelerated at higher pO_2. Again, the pO_2 dependency of all processes and elementary kinetic steps involved in both oxygen incorporation and oxygen evolution reactions *under polarization* is needed to explain these observations. These investigations are outside the scope and timeframe of this work.

3.5.2.2 AC Analysis

To complement the DC analysis in section 3.5.2.1 above the evolution of LSC/CGO and LSCF oxygen electrode ASR under varying pO_2 was evaluated for the *SmallWE* cells in the pO_2 range 0.21 atm – 0.01 atm at 800 °C. The Nyquist plots of the impedance spectra are displayed in Figure 3.5-10 (a_i) and (b_i) for the LSC/CGO and LSCF electrodes respectively. Corresponding DRTs are displayed in the corresponding Figure 3.5-10 (a_ii) and (b_ii).

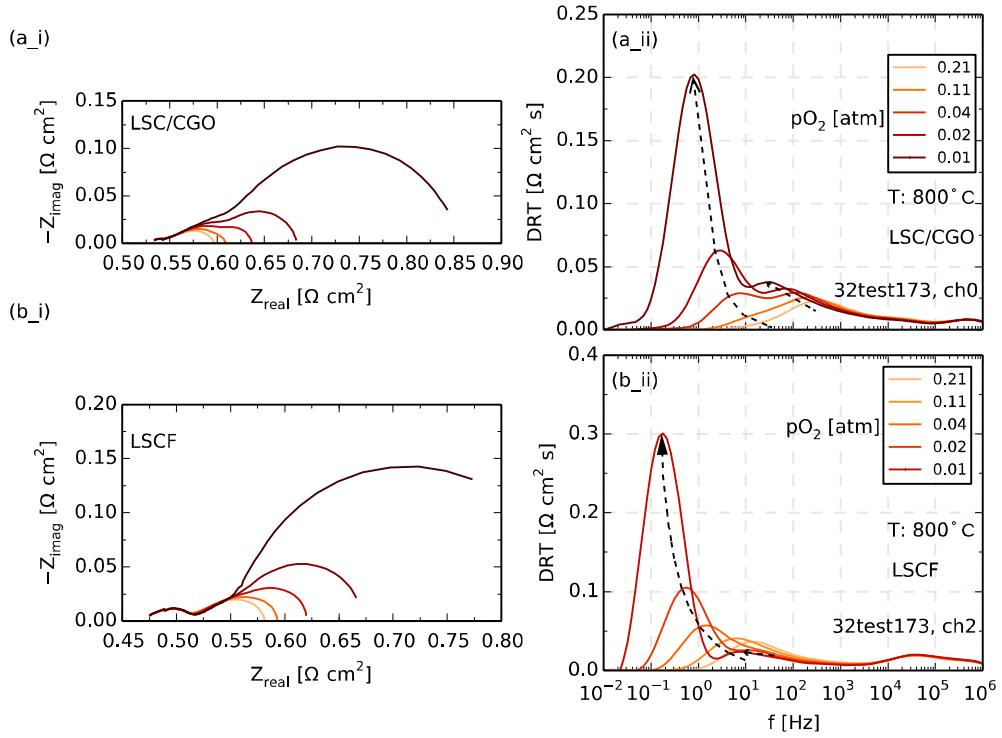

Figure 3.5-10: Evolution of ASRS of the LSC/CGO (a_i) and LSCF, (b_i) oxygen electrodes during a variation of oxygen partial pressure at 800 °C. The corresponding DRTs are displayed in subplots (a_ii) and (b_ii) respectively.

It is evident that the ASRs of both electrodes qualitatively display the same increasing trend with decreasing pO_2. As such further quantitative analysis will be focused on the LSCF oxygen electrode. Furthermore, it has to be pointed out that unlike in pO_2 variations in full-cells[3] or symmetric cells[64], the dominant low frequency peak that is increasing the most with decreasing pO_2 is not a diffusion process as this has been successfully minimized through the employed cell geometry (cf. Figure 3.4-6). The process is part of the oxygen electrode ASR i.e. surface exchange and ionic transport within the electrode material. This has further been verified by checking for

negligible temperature dependence of the process by comparing the spectra at low pO_2 of 0.02 atm for 800 °C and 700 °C (cf. Figure in Appendix A). The process is equally large at 700 °C. Furthermore, the stagnant layer diffusion would be expected to be comparable at least in peak frequency for both electrodes since they are in the same gas mixture and the temperature dependence is negligible.

A CNLS fit of the LSCF spectra in Figure 3.5-10 was carried out with the EEC model described in section 3.5.1.1.1 whereby the Gerischer impedance[64,90] in equation (38) was employed to quantify the coupled processes of surface exchange and solid state diffusion in the LSCF electrode.

$$\underline{Z}_G(\omega) = \frac{R_{chem}}{\sqrt{1 + j\omega t_{chem}}} \tag{38}$$

In the equation above R_{chem} and t_{chem} are characteristic resistance and time constants respectively related. With these values from the CNLS fits and equations (39) and (40) the chemical surface exchange coefficient K^{δ} and chemical oxygen ion diffusion coefficient D^{δ} can be calculated[91,92].

$$K^{\delta} = \frac{c_0(1-\varepsilon)}{a c_{mc} t_{chem}} \tag{39}$$

$$D^{\delta} = \left(\frac{RT}{4F^2}\right)^2 \frac{\tau \gamma^2 t_{chem}}{(1-\varepsilon)^2 c_{mc} c_0 R_{chem}^2} \tag{40}$$

In equations (39) and (40) c_0, c_{mc}, a, ε, τ and γ represent the O^{2-} ion concentration in mol/m^3, concentration of oxygen lattice sites in mol/m^3, surface area density in µm^{-1}, porosity in %, solid phase tortuosity and thermodynamic factor.

These parameters were obtained from literature[2,87,92] and although the corresponding parameters for the herein investigated LSCF oxygen electrode may vary, they are all constants and will quantitatively influence the obtained K^{δ} and D^{δ} values but not their trend or evolution with pO_2—which is targeted with the analysis.

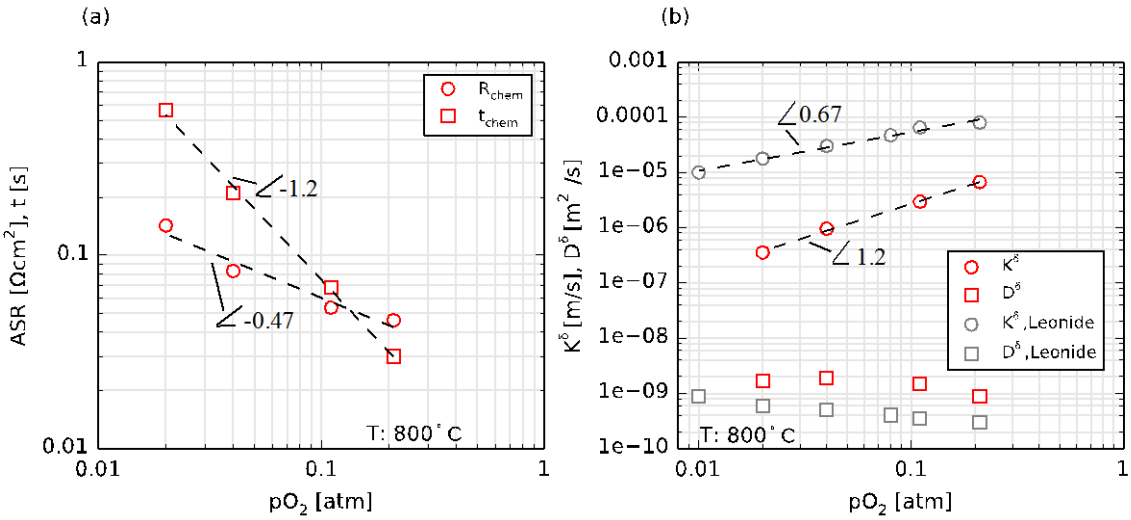

Figure 3.5-11: (a) Evolution of the characteristic resistance R_{chem} and time constant t_{chem} of the LSCF electrode under pO_2 variation at 800 °C . (b) Corresponding chemical surface exchange coefficient and chemical diffusion coefficients. For comparison L68SCF K^{δ} and D^{δ} values from reference [91] labeled K^{δ},Leonide and D^{δ},Leonide respectively

R_{chem} and t_{chem} obtained from CNLS fits are displayed in Figure 3.5-11 (a). The calculated corresponding chemical surface exchange coefficient K^{δ} and chemical diffusion coefficient D^{δ} are displayed in subplot (b). To check the consistency of their trends under pO_2 variation literature values from reference [91] have been included for comparison. Corresponding values differ in magnitude[xvi] but the evolution under pO_2 variation is similar with the chemical surface exchange coefficients K^{δ} decreasing with decreasing pO_2 meanwhile the diffusion coefficients D^{δ} display a weak increase with decreasing pO_2.

Although the above analysis was aimed at obtaining the evolution of K^{δ} and D^{δ} with varying pO_2, the comparison with literature values[91] in Figure 3.5-11 (b) suggests that the cell investigated herein has a K^{δ} value that is at least an order of magnitude smaller and decreases almost twice as much (cf slopes 1.2 vs. 0.67) with decreasing pO_2. On the other hand the herein investigated cell displays a slightly higher oxygen ion diffusion coefficient D^{δ} (at least twice as much). This is consistent since the herein investigated $La_{0.58}Sr_{0.4}Co_{0.2}Fe_{0.8}O_3$ is expected to have a high oxygen ion diffusion coefficient than the $La_{0.68}Sr_{0.3}Co_{0.2}Fe_{0.8}O_3$ compared in Figure 3.5-11 (b)[2]

Based on the differences in magnitude and evolution with decreasing oxygen partial pressure of K^{δ} and D^{δ} in Figure 3.5-11 (b) it can be speculated that observed difference between cathodic and anodic branch polarization curves of both LSC / CGO and LSCF oxygen electrodes in Figure 3.5-7 is related more to surface exchange reaction steps than ionic transport. This means that if comparable impact of polarization is assumed for both anodic and

[xvi] This is expected as the microstructural and geometric parameters employed herein have been taken from literature and not cell specific

cathode operation modes with decreasing pO_2 the surface exchange related processes of the cathodic mode are being more challenged than anodic mode exchange steps.

To circumvent speculating on the impact of polarization, electrically driven surface exchange and diffusion coefficients K^Q and D^Q [93,94] need to be determined. However since the effective surface rate constant $\bar{k}^\delta$ determined from chemical diffusion experiments is larger than that from electrical conductance experiments $\bar{k}^Q$ [93] it can be assumed that under polarization as in Figure 3.5-7 the chemical surface exchange coefficient K^δ is still more determining than the electrically driven surface exchange coefficient K^Q.

3.6 Conclusion

In this chapter the kinetics of single solid oxide cells from DTU Energy and from FZJ were explored in different fuel gas compositions and at different temperatures. The Ni/YSZ fuel electrode and oxygen electrodes LSC / CGO and LSCF were further investigated in a pseudo-symmetric cell geometry that enabled the current density vs. overpotential curves of the electrodes to be determined with negligible heating and concentration related influences present in full cell investigations.

From the full cell investigations at 700 °C it was found that the Ni/YSZ displayed comparable kinetic performance in CO/CO_2 and CH_4 based model reformates against a slightly better performance in H_2/H_2O fuel at same OCV voltage and fuel utilization at 0.5 A/cm^2.

It could be shown that the Ni/YSZ fuel electrode in a 50/50 H_2/H_2O fuel was kinetically less performing when operating under cathodic than under anodic polarization. The same observation was made for the more performing of the two investigated oxygen electrodes i.e. the LSC/CGO oxygen electrodes was kinetically more challenged under cathodic mode operation at 50 mV than in anodic mode. However under decreasing oxygen partial pressure the performance decrease in cathodic operation was similar for both oxygen electrodes and more than the decrease in anodic mode performance. By determining the chemical surface exchange coefficient K^δ and oxygen ion diffusion coefficient D^δ it could be shown that decrease in performance under decreasing pO_2 was related to surface exchange kinetic steps.

Chapter 4 Performance Prediction of SOCs in SOFC and SOEC Operation

4.1 Introduction

The performance of the solid oxide cell (SOC) at a given operation point of temperature, fuel and oxidant gas compositions can be evaluated from the current / voltage (C/V) characteristic. Under open circuit conditions (OCV), the cell voltage is defined through the Nernst equation by the operation temperature and electrode gas compositions—of course under assumption of ideal gas tightness and negligible electronic conductivity of the electrolyte or ideal tightness of the fuel compartment towards the external atmosphere. Under load e.g. during recording of a C/V characteristic the cell voltage deviates from the OCV in accordance with the ASR contributions of the different loss processes or mechanisms.

To thus predict or simulate the C/V characteristic requires a thorough understanding of the involved loss mechanisms as well as a quantitative description of their ASR contributions under any given operation condition. Thus, dependent on the dynamic process, operation point features such as component gas partial pressure, temperature and pressure dependencies as well as microstructural features such as porosity, pore radii, particle size, particle size distribution etc. need to be quantifiable. Such knowledge can aid a cell or stack operator in choosing an adequate operation point or a cell manufacturer in engineering the cell for defined operation conditions. The latter point has increasingly gained importance due the increasing operation of the solid oxide fuel cell (SOFC) in reverse mode as solid oxide electrolysis cells (SOEC) for energy storage. As such a process that under a given operation condition and mode is not power limiting could suddenly become critical for cell life time when operation mode is changed. This means that a SOC that will be operated exclusively in fuel cell (FC) mode may be engineered to have different microstructural features than a SOC that will be operated in electrolysis cell (EC) or cyclic modes.

Although the operation of the SOFC as an SOEC didn´t commence with this thesis, research on SOEC operation of SOCs at the *Institut für Angewandte Materialien - Werkstoffe der Elektrotechnik* (*IAM-WET*) formerly *Institut für Werkstoffe der Elektrotechnik (IWE)* started with this work.[42,53,61,95] The immediate tasks included:

i. Updating the existing test set-ups for EC mode operation of the SOCs—and by virtue of the then extremely high-tech state of the rigs a redesign of the measurement board[xvii] was enough to enable the tests.
ii. With SOEC measurements possible, the next task entailed checking for the applicability of and further developing the existing in house developed 0-D stationary model predicting the current / voltage characteristic of the SOFC[3,4] for SOEC operation.
iii. Finally, the long-term stability of the SOCs in SOEC and cyclic operation modes were to be investigated.

[xvii] Details are outside the scope of this work

In this section the 0-D stationary model predicting the current / voltage (C/V) characteristic of a SOC in both SOFC and SOEC modes will be discussed. The first and second sections will handle operation in the binary fuels H_2/H_2O and CO/CO_2 respectively. Section three will address the case in which the fuels H_2, H_2O, CO and CO_2 are present in the fuel under equilibrium conditions. Whereas point (i) above is out of the scope of this work, point (iii) will be treated in a separate chapter.

4.2 Model Presentation

The 0-D model implemented on a *Matlab* platform is based on fundamental electrochemical and physical relationships, such as the Butler-Volmer (BV) equation, Fick's law and Ohm's law. With the exception of the charge transfer coefficients α_{an} and α_{cat} that were determined from impedance measurements under load all model parameters were determined from open-circuit impedance measurements. The model accounts for all processes non-negligibly contributing to the internal resistance of the investigated cells such as:

- ohmic losses in the electrolyte and the electrodes
- gas diffusion (or concentration) overpotential in the substrate and the fuel electrode and the air electrode
- activation polarization at the fuel electrode and the air electrode.

The model equations, assumptions, concepts and approaches have been fully discussed in literature[2–4,42]. However, for a better overview of the results a brief overview of the equations will be given.

4.2.1 Cell Voltage

The cell voltage (U_{cell}) is calculated by subtracting the overvoltage contributions η_i of the individual loss mechanisms from the open-circuit voltage U_{OCV} (sticking to SOFC operation mode nomenclature, fuel electrode quantities are subscripted with "an" while those referring to the air electrode subscripted with "cat")[xviii].

$$U_{Cell} = U_{OCV} - (\eta_{ohm} + \eta_{act,an} + \eta_{act,cat} + \eta_{conc,an} + \eta_{conc,cat}) \qquad (41)$$

In equation (41) η_{ohm} denotes the overpotential owing to ohmic losses in the cell, $\eta_{act,an}$, $\eta_{act,cat}$, $\eta_{conc,an}$, and $\eta_{conc,cat}$ denote the activation and concentration overpotentials at the fuel and air electrodes respectively.

[xviii] In SOEC mode, the cell voltage is obtained by *adding* the overvoltages to the open circuit voltage.

4.2.2 Open-circuit voltage

The open-circuit voltage U_{OCV} is described by the Nernst equation adapted for H_2/H_2O operation (cf. equation (4) also).

$$U_{\mathrm{OCV}}(T) = U_0(T) - \frac{RT}{2F}\ln\left(\frac{pH_2O_{\mathrm{an}}}{pH_{2,\mathrm{an}} \cdot \sqrt{pO_{2,\mathrm{cat}}}}\right) \tag{42}$$

In equation (42) $U_0(T)$ is the temperature dependent theoretical standard voltage[96], $p\mathrm{X}_{\mathrm{an/cat}}$ the partial pressure of gas X at fuel and air electrodes respectively in atm normed to the absolute pressure of 1 atm. Meanwhile R, F and T represent universal gas constant, Faraday constant and absolute temperature, respectively.

4.2.3 Ohmic Losses

The overpotential contribution resulting from Ohmic losses is given by equation (43) whereby R_k represents the area-specific ohmic resistance contribution of cell layer k.

$$\eta_{\mathrm{ohm}} = j \cdot \sum_k R_{\mathrm{k}} = j \cdot R_{\mathrm{ohm}} \tag{43}$$

As the conductivity of the substrate, the fuel electrode and the air electrode is orders of magnitude higher, R_{ohm} is dominated by the ohmic resistance of the YSZ electrolyte, the GDC interlayer and the interdiffusion zone[97] between them. This has been proven thorough microstructural and electrical analysis of the tested fuel electrode supported cell[34,98] and can thus be modelled through thermally activated charge transport mechanisms with equation (35) derived from the Arrhenius equation[99,100]. Thereby $E_{\mathrm{act,ohm}}$ represents the activation energy in kJ/mol, whereas B_{ohm} is a material-specific constant. They do not represent physically meaningful material parameters of the individual layers. The model uses averaged values representing the thermally activated ionic conduction of the electrolyte, GDC and the interdiffusion zone in between. This approach enables a precise simulation of the ohmic losses in any C/V-characteristic for the given cell but is unsuitable to predict the performance for a variation in layer thicknesses or microstructural features like porosity.

4.2.4 Diffusion Overpotential

The gas diffusion (or concentration) polarization is caused by the partial pressure difference between the gas channel atmosphere and the triple-phase boundary (TPB), acting as the driving force for the diffusion of reactants and reaction products in the porous electrodes and the substrate. It has to be noted that for the fuel electrode although the *TPB* is implied here, it actually denotes the end of the substrate or start of the fuel electrode functional layer as has been shown that gas diffusion in the 7 – 10 µm functional layer is quite small with a characteristic frequency of ca. 45 kHz[40] not only overlaps[40,73,76] but is strongly coupled to the electrochemical processes of charge transfer and ionic conduction in the matrix[64,73,101]. As such for the fuel electrode, the diffusion overpotential considered here is that of the substrate.

The diffusion overpotential ($\eta_{conc,el}$) for the fuel and air electrodes is given by equations (44) and (45) respectively derived from the Nernst equation[40].

$$\eta_{\mathrm{conc,an}} = \frac{RT}{2F}\ln\left(\frac{pH_2O_{\mathrm{an}}^{TPB}\cdot pH_{2,\mathrm{an}}}{pH_2O_{\mathrm{an}}\cdot pH_{2,\mathrm{an}}^{TPB}}\right) \tag{44}$$

$$\eta_{\mathrm{conc,cat}} = \frac{RT}{4F}\ln\left(\frac{pO_{2,\mathrm{cat}}}{pO_{2,\mathrm{cat}}^{TPB}}\right) \tag{45}$$

$p\mathrm{H}_{2,an}$, $p\mathrm{H}_2\mathrm{O}_{an}$, and $p\mathrm{O}_{2,cat}$ are the known partial pressures of hydrogen, water and oxygen, respectively, in the gas channel meanwhile unknown partial pressures $p\mathrm{H}_{2,\mathrm{an}}^{\mathrm{TPB}}$, $p\mathrm{H}_2\mathrm{O}_{\mathrm{an}}^{\mathrm{TPB}}$, and $p\mathrm{O}_{\mathrm{cat}}^{\mathrm{TPB}}$ are determined by applying Fick's first law, assuming a linear concentration gradient as a function of the current density *j* [102].

$$pH_{2,\mathrm{an}}^{TPB} = pH_{2,\mathrm{an}} - \frac{RTL_{\mathrm{an}}}{2FD_{\mathrm{H_2}}^{eff}}\,j\cdot\left(1.0133\cdot10^5\,\frac{\mathrm{Pa}}{\mathrm{atm}}\right)^{-1} \tag{46}$$

$$pH_2O_{\mathrm{an}}^{TPB} = pH_2O_{\mathrm{an}} + \frac{RTL_{\mathrm{an}}}{2FD_{\mathrm{H_2O}}^{eff}}\,j\cdot\left(1.0133\cdot10^5\,\frac{\mathrm{Pa}}{\mathrm{atm}}\right)^{-1} \tag{47}$$

and

$$pO_{2,\mathrm{cat}}^{TPB} = pO_{2,\mathrm{cat}} - \left(\frac{p_{\mathrm{tot}} - pO_{2,\mathrm{cat}}}{p_{\mathrm{tot}}}\right)\frac{RTL_{\mathrm{cat}}}{4FD_{\mathrm{O_2}}^{eff}}\, j \cdot \left(1.0133\cdot 10^5\,\frac{\mathrm{Pa}}{\mathrm{atm}}\right)^{-1} \tag{48}$$

p_{tot} denotes the absolute atmospheric pressure (1 atm). By inserting equations (46), (47) and (48) into equations (44) and (45) the expressions in equations (49) and (50) relating the diffusion-related overpotential $\eta_{conc,el}$ of the fuel and air electrodes respectively to the current density[102] are obtained.

$$\eta_{\mathrm{conc,an}} = \frac{RT}{2F}\ln\left(\frac{1+\dfrac{RTL_{\mathrm{an}}}{2FD_{H_2O}^{eff}\,pH_2O_{\mathrm{an}}}\cdot j}{1-\dfrac{RTL_{an}}{2FD_{H_2}^{eff}\,pH_{2,\mathrm{an}}}\cdot j}\right) \tag{49}$$

$$\eta_{\mathrm{conc,cat}} = \frac{RT}{4F}\ln\left(1\Big/\left(1-\frac{RTL_{\mathrm{cat}}}{4FD_{O_2}^{eff}\,pO_{2,\mathrm{cat}}}\cdot j\right)\right) \tag{50}$$

L_{an} and L_{cat} denote the thickness of the fuel electrode substrate and the thickness of the air electrode. The effective molecular diffusion coefficient D_i^{eff} can be expressed according to equation (51)[102]

$$D_i^{eff} = \psi_{el}\cdot D_{\mathrm{mol},i} \tag{51}$$

whereby the structural parameter ψ_{el} describes the relationship between volumetric porosity ε_{el} and tortuosity τ_{el} of the corresponding electrode as given by equation (52)

$$\psi_{el} = \frac{\varepsilon_{el}}{\tau_{el}}\,, \tag{52}$$

and the molecular diffusion coefficient $D_{mol,i}$ of gas component i is given by equation (53) taking into account bulk and Knudsen components $D_{bulk,i}$ and $D_{Knudsen,i}$ respectively[56,102–104].

$$\frac{1}{D_{\text{mol},i}} = \frac{1}{D_{\text{bulk},i}} + \frac{1}{D_{\text{Knudsen},i}} \cdot \tag{53}$$

The Knudsen diffusion $D_{Knudsen,i}$ has to be considered when the pore radii are comparable with the mean free path length of the diffusing particles and is calculated based on equation (54) meanwhile the binary diffusion coefficient $D_{bulk,ij}$ is estimated for binary gas mixtures according to the Chapman-Enskog theory[102,105] according to equation (55)

$$D_{\text{Knudsen},i} = \frac{2}{3} \cdot r_{\text{Por},el} \sqrt{\frac{8RT}{\pi M_i}} \tag{54}$$

$$D_{\text{bulk},ij} = \frac{1.86 \cdot 10^{-3} \cdot T^{1.5} \sqrt{M_i^{-1} + M_j^{-1}}}{p_{tot} \cdot \sigma_{ij}^{\ 2} \cdot \Omega_D} \tag{55}$$

with the collision integral Ω_D given by

$$\Omega_D = \frac{A}{\tau_{ij}^B} + \frac{C}{\exp(D \cdot \tau_{ij})} + \frac{E}{\exp(F \cdot \tau_{ij})} + \frac{G}{\exp(H \cdot \tau_{ij})} \tag{56}$$

whereby

$$\tau_{ij} = \frac{k \cdot T}{\sqrt{\varepsilon_i \cdot \varepsilon_j}} \tag{57}$$

and the average collision diameter given by equation (58).

$$\sigma_{ij} = \frac{\sigma_i + \sigma_j}{2} \tag{58}$$

The molar mass M_i, characteristic length σ_i, characteristic Lennard-Jones energy ε_i of gas species i (given as ratio with Boltzmann constant k, i.e. ε_i/k) as well as the constants A – H that appear in equations (54) - (58) are obtained from literature[106] and summarized in Table 4.2-1. The mean pore radius of each electrode, $r_{Por,el}$, was extracted from semi-quantitative image analysis of SEM micrographs of the according electrode structures. For the substrate $r_{Por,an}$ was estimated to be 600 nm and for the air electrode $r_{Por,cat}$ was also estimated[3] at 600 nm.

Table 4.2-1: General physical modeling parameters and constants from literature[106] used in this work

Parameter	Value/Expression	Unit
R	8.3145	J/molK
F	96485.34	C/mol
$M_{\mathrm{H_2}}$	0.002016	kg/mol
$M_{\mathrm{H_2O}}$	0.018015	kg/mol
$M_{\mathrm{N_2}}$	0.028013	kg/mol
$\sigma_{\mathrm{H_2O}}$	2.641	Å
$\sigma_{\mathrm{H_2}}$	2.827	Å
$\sigma_{\mathrm{N_2}}$	3.798	Å
$\sigma_{\mathrm{O_2}}$	3.467	Å
$\varepsilon_{\mathrm{H_2}}/k$	59.7	K
$\varepsilon_{\mathrm{H_2O}}/k$	809.1	K
$\varepsilon_{\mathrm{N_2}}/k$	71.4	K
$\varepsilon_{\mathrm{O_2}}/k$	106.7	K
A	1.06036	-
B	0.15610	-
C	0.19300	-
D	0.47635	-
E	1.03587	-
F	1.52996	-
G	1.76474	-
H	3.89411	-

4.2.5 Activation Overvoltage

Activation polarization describes the electrochemical loss mechanisms taking place mainly at the three-phase boundary (TPB) where ionic-conducting, electronic-conducting and gas phases meet. The corresponding overpotential contributions have been modelled with the Butler-Volmer-type equation (32) whereby the exchange current densities $j_{0,el}$ obey the semi-empirical equations (59) (cf. equation (37) also) for the fuel electrode and equation (60) for the oxygen electrode.

$$j_{0,\mathrm{an}} = \gamma_{\mathrm{an}} \left(pH_{2,\mathrm{an}}^{TPB} \right)^{a} \left(pH_2O_{\mathrm{an}}^{TPB} \right)^{b} \exp\left(-\frac{E_{\mathrm{act,an}}}{RT} \right) \tag{59}$$

$$j_{0,\mathrm{cat}} = \gamma_{\mathrm{cat}} \left(pO_{2,\mathrm{cat}}^{TPB} \right)^{m} \exp\left(-\frac{E_{\mathrm{act,cat}}}{RT} \right) \tag{60}$$

Alongside the rests of the model parameters for the different overpotential contributions, the charge transfer coefficient α_{el}, the prefactors γ_{an} and γ_{cat}, the exponents a, b, and m as well as the activation energies $E_{\mathrm{act,an}}$ and $E_{\mathrm{act,cat}}$ as well as the procedures to determine them are given in reference [3].

4.3 Experimental

4.3.1 Cell System

The investigations were performed on the very stable and widely investigated s.t.a. fuel electrode supported cells manufactured by Forschungszentrum Jülich[24–26]. Cell details have been described in section 3.2.1.1.

4.3.2 Operation and Characterization

The cells were mounted into an Al_2O_3 housing located at the high temperature region of the measuring setup. Electrical contacting and sealing were carried out as described elsewhere[30]. Gas flow rates and compositions were realized with the use of computer controlled digital mass flow controllers (MFC). Fuel was supplied to the fuel electrode at 250 sccm and air to the oxygen electrode at the same flow rate. In H_2/H_2O mixtures, the fuel composition was achieved by allowing appropriate amounts of O_2 to react with 250 sccm of H_2 in a burning chamber[107] preceding the cell housing.

The C/V curves for validating the model predictions were recorded with an Agilent 6612C DC power supply with current density incremented by 0.02 A/cm² every 10 s. The C/V curves were first measured in SOFC operation mode from 0 to 2.5 A/cm² or to a minimum cell voltage of 0.6 V. The voltage limit of 0.6 V was chosen to prevent alteration of the cell, i.e., oxidation of Ni to NiO and other irreversible reactions. After this measurement a waiting time of two hours at OCV was inserted so that the cell temperature could relax back to the set temperature. The C/V curve in SOEC mode was then recorded, from 0 to -2.5 A/cm² or until cell voltage exceeded 1.6 V. In both cases, no return sweeps were recorded to check for hysteresis.

4.4 Model Validation

4.4.1 Operation in Hydrogen/Steam Fuel Mixture

With the above described model equations, the general physical parameters in Table 4.2-1 as well as the cell system specific parameters determined through electrochemical impedance spectroscopy[3] and displayed in Table 4.4-1 the C/V characteristics of the investigated cell could be predicted for different operation conditions.

Table 4.4-1: System specific modeling parameters used in this work determined[3] via EIS for the same type of fuel electrode supported single cells as investigated herein

Parameter	Value/Expression	Unit
B_{ohm}	$4.1879 \cdot 10^{12}$	S·K/m²
$E_{act,ohm}$	90.31	kJ/mol
a	-0.10	-
b	0.33	-
m	0.22	-
γ_{an}	$1.82527 \cdot 10^{6} \cdot T$	A/m²
γ_{cat}	$1.51556 \cdot 10^{8} \cdot T$	A/m²
$E_{\mathrm{act,an}}$	105.04	kJ/mol
$E_{\mathrm{act,cat}}$	139.86	kJ/mol
α_{an}	0.59	-
α_{cat}	0.65	-
ψ_{an}	0.13	-
ψ_{cat}	0.09	-

4.4.1.1 Model Validation for Different Fuel Mixtures and Temperatures

In Figure 4.4-1a C/V curve model predictions for H_2O/H_2-ratios 70/30, 50/50 and 30/70 at 800 °C are compared with measured curves for both SOFC and SOEC modes. In Figure 4.4-1b a comparison between model and measurement for the operation temperatures 850 °C and 800 °C in a 50/50 H_2O/H_2 ratio. As can be seen from both figures, there is excellent agreement between model and simulation.

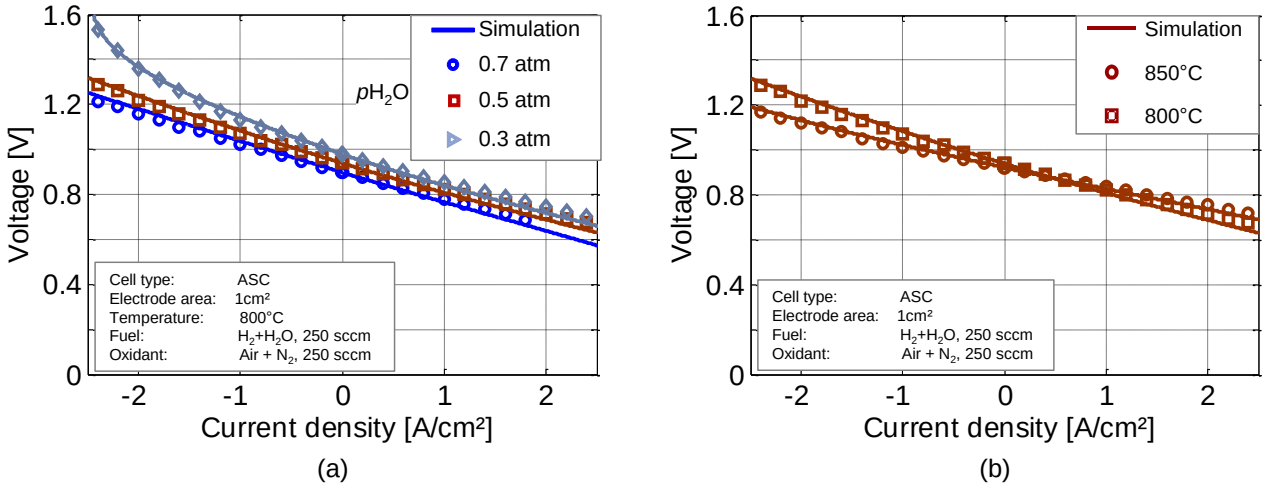

Figure 4.4-1: Validation of model predictions in SOFC and SOEC modes for (a) different steam partial pressures *p*H_2O at 800 °C and (b) different temperatures, T in a 50/50 H_2/H_2O fuel mixture

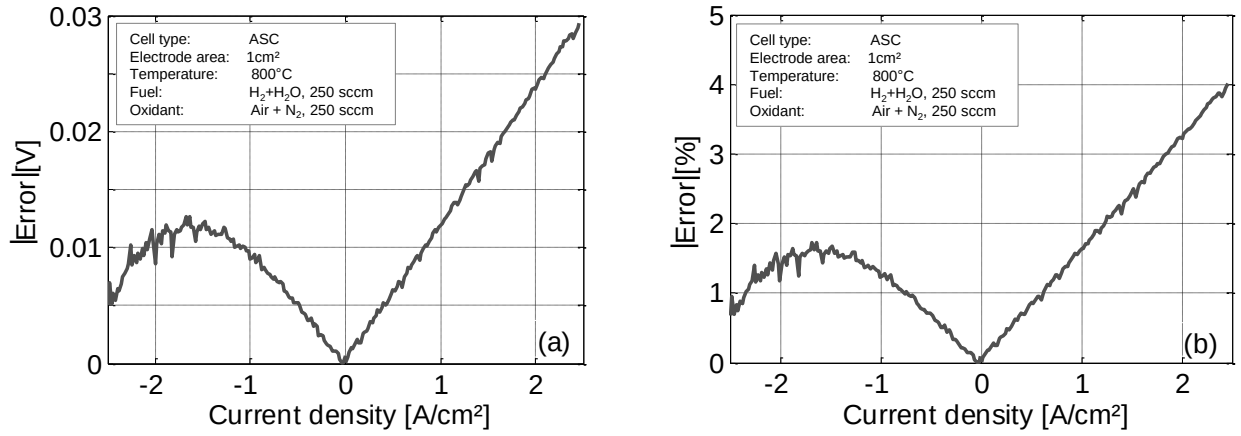

Figure 4.4-2: Error between model prediction of the C/V curve at 800 °C and 50/50 H_2/H_2O (a) Absolute values and (b) relative values normalized with the dynamic range (maximum measured voltage in SOEC mode minus minimum measured voltage in SOFC mode)

For a quantitative estimate of the model accuracy, the deviation between measurement and simulation was calculated, and the resulting absolute and relative[xix] error curves for the 50/50 H_2O/H_2 gas compositions at 800 °C are displayed in Figure 4.4-2a and b respectively. First of all, the evolution of the error shows a characteristic difference between SOFC and SOEC mode. Whereas the error increases linearly in SOFC mode to 28 mV or 4.5 % at 2.5 A/cm², the error follows a semicircular trend in SOEC mode, with a maximum of 15 mV or 1.5 % at -1.5

[xix] Difference between measurement and simulation normalized with the dynamic range (maximum measured voltage in SOEC mode minus minimum measured voltage in SOFC mode)

A/cm². The error seems to be caused by specific temperature effects originating from hydrogen generation consuming electrical (ΔG) and thermal (TΔS) energy in SOEC mode and by the generation of heat in SOFC mode.

4.4.1.2 Model Extension to include Temperature Change during C/V Recording

During C/V curve recording, the losses in the cell cause joule heating raising the cell temperature from the OCV temperature. As would be expected, the joule heating is independent of current flow direction. In fuel cell mode, the exothermic nature of the hydrogen oxidation reaction raises the cell temperature further; meanwhile the endothermic nature of steam reduction in electrolysis mode decreases the cell temperature.

In a bid to increase the accuracy of the model, it is necessary to include the *real* temperature of the cell at any given point along the C/V characteristic i.e. to have a current density dependent expression for the temperature at a given operation point of temperature and electrode gas compositions. To this end the single frequency electrochemical impedance spectroscopy (SFEIS) technique[61,108] was applied. The concept involves determining the actual temperature of the electrolyte through two major steps after careful[xx] selection of the adequate single frequency f_T (here 120 kHz):

i. Recording a ***reference curve***: Under electrode gas compositions of interest and under open circuit conditions, the operation temperature is varied stepwise and real part of the impedance Re{$\underline{Z}(f_T)$} is recorded after enough time has been allowed for steady state conditions
ii. Recording the ***load curve***: Under electrode gas compositions and operation temperature of interest, the current density j is varied firstly in one mode (e.g. FC mode) in a stepwise manner from OCV to at least the maximum current density j_{max} attainable during C/V curve recording, allowing for steady state conditions and then recording Re{$\underline{Z}(f_T)$}. The cell is then brought back to OCV and allowed long enough for the temperature to relax to the set temperature and then the procedure is repeated in the other mode e.g. EC mode.

From step (ii) above, Re{$\underline{Z}(f_T)$} is obtained for every current density in the given mode and from the reference curve the corresponding actual or *real* temperature of the cell can be deduced or extrapolated. For a more detailed explanation of the concepts, assumptions and procedure involved in the SFEIS technique references [61,108] are recommended.

In Figure 4.4-3 the temperature evolution during a C/V curve recording in FC and EC modes at 800 °C and 50/50 H_2O/H_2 fuel has been displayed, wherein the cell temperature as recorded by a thermocouple 1.5 mm away from the cell in an Al_2O_3 block is compared with the *real* cell temperature calculated through SFEIS. From Figure 4.4-3,

[xx] The chosen frequency has to be high enough to be free of polarization effects and low enough to enable consistent measurement results[108]

it is evident that in both modes the SFEIS technique reveals a greater change in cell temperature under load than recorded by the thermocouple. At + 2.2 A/cm^2 the *real* cell temperature has changed by + 8 °C relative to the OCV value. The large change certainly stresses the need to make the model non-isothermal. In EC mode the real cell temperature decreases to a minimum and then gradual increases back to the OCV temperature of 800 °C at a current density of - 2.2 A/cm^2. At this characteristic point called *thermo-neutral point* the cooling effect of the endothermic steam reduction reaction is balanced by the heating effect of joule heating across the electrolyte. From the 50/50 H_2O/H_2O curve in Figure 4.4-1a the cell voltage at this point is 1.27 V—a value consistent with the theoretical expectation according to equation (61) for 800 °C. At 850 °C 1.29 V has been calculated[109].

$$E_{tn} = \frac{1}{nF}\Delta H_f(\mathrm{T}) \tag{61}$$

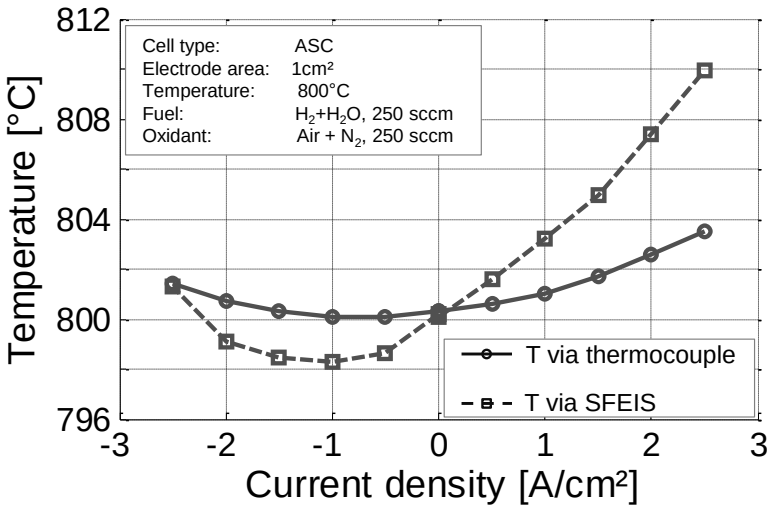

Figure 4.4-3: Comparison of measured cell temperature and real cell temperature determined through SFEIS as a function of current density during SOFC and SOEC operation modes at 800°C in an H_2/H_2O ratio of 50/50.

With the revised temperature-dependent model, which includes the actual cell temperature, the accuracy of simulation is improved particularly for SOFC mode. At a current density of +2.4 A/cm² the error decreases from 28 mV (4.5 %) in Figure 4.4-2a,b to 18 mV (2.5 %) in Figure 4.4-4a,b. The SOEC curve which witnessed a maximum temperature change of only 2°C (at j = -1 A/cm²) seems to be insensitive to the temperature correction function. With a maximum attained accuracy of 2.5 % in SOFC mode, these results suggest that the temperature correction functions improve accuracy to around 2.5 % and that the SOEC does not require any temperature correction in the investigated current density range.

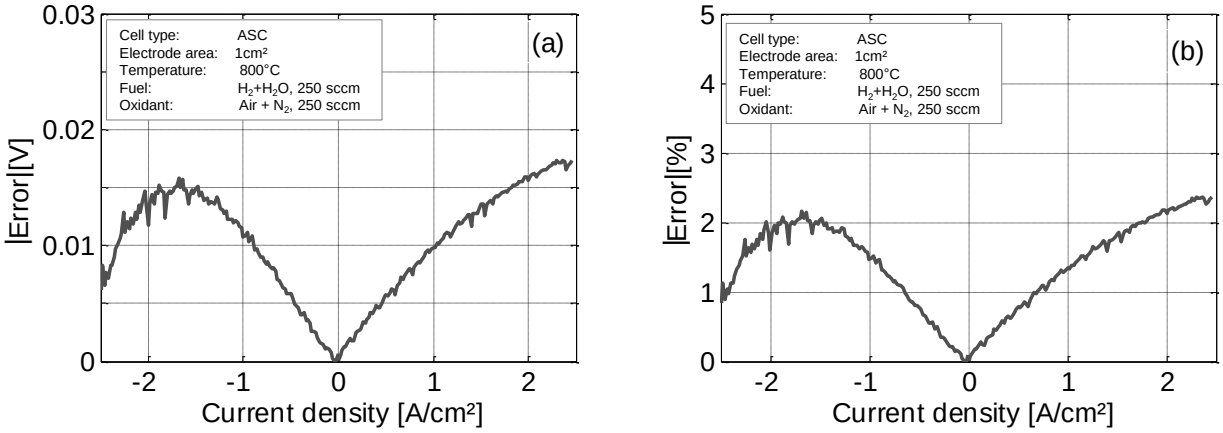

Figure 4.4-4:Error between model prediction of the C/V curve at 800 °C and 50/50 H2/H2O with real cell temperature determined through SFEIS technique (a) Absolute values and (b) relative values normalized with the dynamic range (maximum measured voltage in SOEC mode minus minimum measured voltage in SOFC mode)

From Figure 4.4-4 a or b it is interesting to realize that the trends of the error curves are now similar to the temperature trends in the respective operation modes. As such, it can be hypothesized that the still remaining uncorrected error (or the model inaccuracy) is either related (1) to an intrinsic temperature dependent characteristic not described by our model, or (2) to a summation of residual temperature dependent inaccuracies in already described characteristics.

4.4.1.3 Asymmetry of the C/V Characteristic

Alongside validating this zero-dimensional stationary model for SOEC mode (cf. section 4.4.1.1 above) as well as extending the model to include the temperature evolution during C/V curve recording (cf. section 4.4.1.2) another concern was to propose an explanation for the asymmetry between fuel cell and electrolysis cell mode branches of the C/V characteristic. This asymmetry is best observable for the C/V characteristics at pH_2O = 0.7 atm (SOFC-mode) and pH_2O = 0.3 atm (SOEC-mode) in Figure 4.4-1. These operating conditions describe a scenario, in which the fraction of the fuel gas, which is consumed in the electrochemical reaction, is 30 % at zero current conditions and therefore subject to depletion at current densities increasing to 2.5 A/cm² in SOFC mode and to -3 A/cm² in SOEC mode (gas conversion of 7 % and 8.4 % respectively). To better understand the phenomena, a closer look at the calculated individual overvoltages for these gas compositions as displayed in Figure 4.4-5a and b needs to taken.

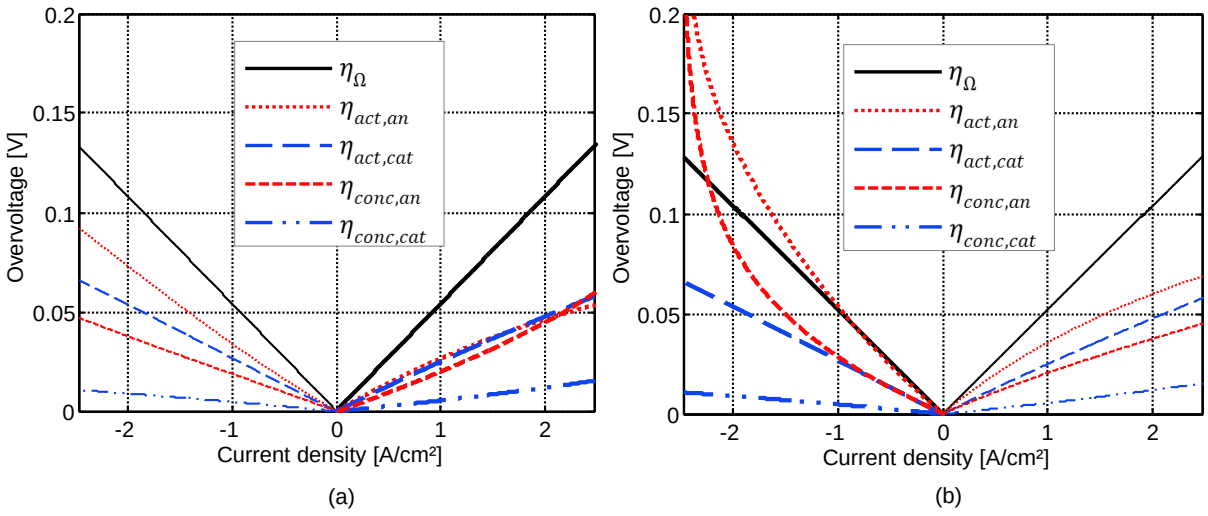

Figure 4.4-5: Overvoltages of curves simulated at 800°C for (a): 70/30 and (b) 30/70 fuel electrode H_2O/H_2 gas composition

In these figures a depletion of gas occurs at each half of the corresponding figure. Naturally, the overvoltage originating from the ohmic resistance, η_{ohm}, is symmetrical in both modes. For SOFC mode, all overpotentials displayed in Figure 4.4-5 a increase rather linearly and gas diffusion of the air electrode, $\eta_{conc,cat}$, contributes the least. At + 2.4 A/cm², the contributions of gas diffusion and activation overpotential of the fuel electrode, $\eta_{conc,an}$ and $\eta_{act,an}$ and activation overpotential of the air electrode, $\eta_{act,cat}$, are of similar size. After this point the magnitude of $\eta_{conc,an}$ starts to dominate the other two polarization losses.

For SOEC mode, and from all overpotentials displayed in Figure 4.4-5 b, only gas diffusion and activation overpotential of the air electrode, $\eta_{conc,cat}$ and $\eta_{act,cat}$, increase rather linearly up to -2.4 A/cm² and contribute least to the total polarization loss. In contrast to this, gas diffusion and activation overpotential of the fuel electrode, $\eta_{conc,an}$ and $\eta_{act,an}$, drastically increase at high current densities in SOEC mode, pointing out that the depletion of H_2O at the TPB becomes substantial around -1 A/cm². Here, the model indicates clearly, that the fuel electrode functional layer is the weakest part of the fuel electrode supported cell and has to be improved in its microstructure characteristics. Furthermore, the same conclusion can be made for the fuel electrode substrate. The nonlinear contributions of $\eta_{conc,an}$ and $\eta_{act,an}$ to the total polarization loss are deemed responsible for the observed asymmetry. Corresponding results were reported by Knibbe et al.[110] using a 5 × 5 cm² fuel electrode supported cell with YSZ/LSM oxygen electrode, identifying gas diffusion as a major source of asymmetry. Knibbe showed that gas conversion overvoltage, taking place in the gas channel above the fuel electrode substrate, was significant at high current densities. However, as this source of polarization loss is not considered in our model, it is not responsible for the observed asymmetry. This is bound to the fact that gas conversion losses are negligibly small (cf. only 7- and 8 % gas conversion at 2.5- and 3 A/cm² respectively) for cells with an active area of 1 cm² operated at high gas flow rates as done in this work.

A short analysis of the two major overpotential contributions $\eta_{conc,an}$ and $\eta_{act,an}$ responsible for the observed asymmetry of the C/V curves is given in the following points:

i. **Gas diffusion overpotential at the fuel electrode ($\eta_{conc,an}$)**: Considering the above described scenario, in which the fraction of the gas, which is consumed in the electrochemical reaction is fixed, in equation (49) the effective diffusion coefficients of H_2O, $D_{H_2O}^{eff}$, and H_2, $D_{H_2}^{eff}$, are the only values that differ, with $D_{H_2}^{eff}$ ≈ 6.5·10^{-5} m²/s almost double $D_{H_2O}^{eff}$ ≈ 3.8·10^{-5} m²/s. This causes the gas diffusion overvoltage at the fuel electrode, $\eta_{conc,an}$, to be much larger in SOEC mode than in SOFC mode. As the binary diffusion coefficient for bulk diffusion is the same for H_2 diffusion in H_2O as for H_2O diffusion in H_2, bulk diffusion alone is symmetrical for both operation modes. Hence, the asymmetry in the diffusion overpotential for SOFC at current densities ≥ 2.4 A/cm² and SOEC mode at ≤ -1 A/cm² in turn proves that the Knudsen diffusion has to be taken into account for determining the diffusion overpotential of the fuel electrode of an electrode supported cell.

   This has been further elucidated in Figure 4.4-6 whereby the diffusion overpotential has been calculated for a fuel mixture of 50/50 H_2/H_2O at 800 °C with and without the Knudsen contribution. As can be seen, the diffusion overpotential is symmetrical in fuel cell and electrolysis modes without the Knudsen contribution. When this is considered in the calculation, the overvoltage is (i) higher in both modes, (ii) asymmetrical whereby (iii) the overvoltage is higher in SOEC mode than SOFC mode. (cf. 57 mV at – 2.5 A/cm^2 against 42 mV at + 2.5 A/cm^2 when Knudsen diffusion and 21 mV at ± 2.5 mV without Knudsen diffusion contribution, i.e. 170.6 % increase in diffusion overvoltage in SOEC mode at 2.5 A/cm^2 against 99.2 % increase in SOFC mode at 2.5 A/cm^2 or an asymmetry of 71.4 % at ± 2.5 A/cm^2)

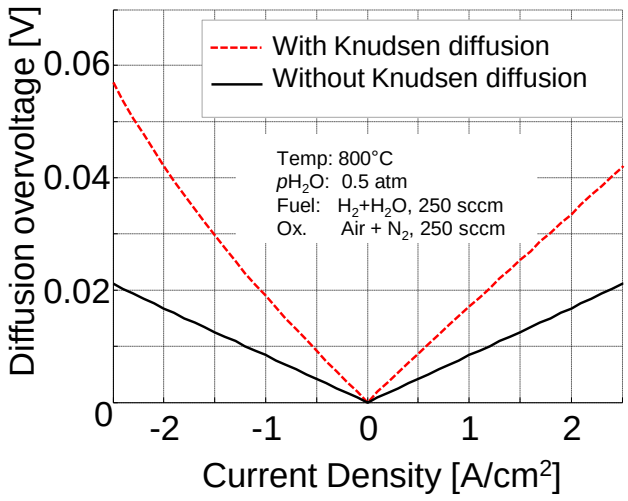

Figure 4.4-6: Simulated diffusion overvoltage with and without Knudsen diffusion contribution for a 50/50 H_2/H_2O fuel mixture at 800 °C

ii. **Activation overpotential at the fuel electrode ($\eta_{act,an}$):** To explain the influence of fuel electrode activation overvoltage, a closer look at equation (59) describing the exchange current density is necessary. It is a measure of the reaction rate and depends on the partial pressures of H_2 and H_2O. The exponents a = -0.1 (for pH_2) and b = 0.33 (for pH_2O) reveal that the smaller the pH_2O at the fuel electrode the lower the reaction rate of the electrochemical fuel oxidation. Hence, the highest reaction rate is found for SOFC operation at high current densities and the lowest for SOEC operation at high current densities, respectively.

In a similar manner to (i) above, the model has been used to calculate the activation overpotential for a fuel mixture of 50/50 H_2/H_2O at 800 °C using inlet values against a calculation taking into account the depletion at the TPB due to diffusion in the substrate (cf. Figure 4.4-7). As can be seen from Figure 4.4-7, non-consideration of the diffusion-related depletion at TPB leads to an underestimation of the activation losses in SOEC mode and the opposite in SOFC mode.

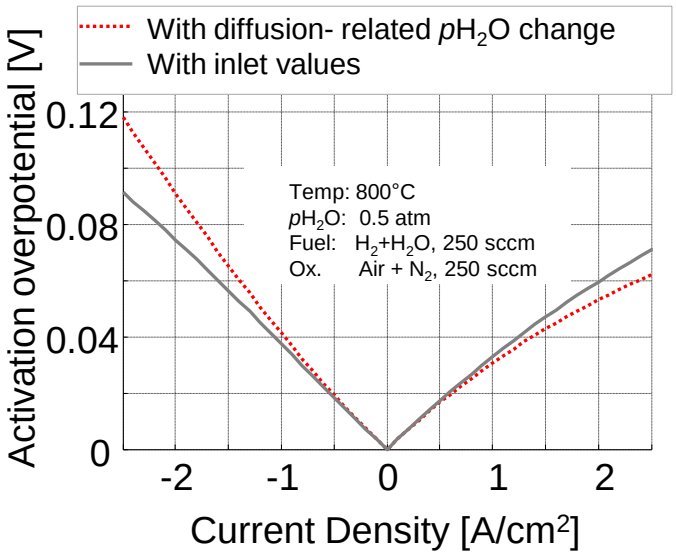

Figure 4.4-7: Simulated activation overpotential for inlet H_2/H_2O of 50/50 for inlet values compared against that considering pH_2O depletion at TPB due to Substrate diffusion.

Therefore alongside an H_2O depletion for current densities ≥ |1 A/cm²| in SOEC mode causing a large diffusion overvoltage at the fuel electrode – also the reaction rate decreases significantly, thereby causing an increase in activation polarization at the fuel electrode. Both processes have been nicely described by the model.

4.4.1.4 Applicability of the Butler Volmer (BV) – type Approach for SOCs

To discuss the adequacy of using the full BV-type equation in this work, C/V curves were recorded at 600-, 650-, 700- and750 °C in a fuel with 62 % H_2O content as displayed in Figure 4.4-8. For comparison, the plot also contains linear C/V predictions, which are extrapolated on the basis of the ASR at OCV for each measurement (dotted lines). For all temperatures, it is obvious that the measured C/V curves are nonlinear. Theoretically, both concentration polarization and activation polarization can be responsible for the observed nonlinear behavior. The former loss process shows minor temperature dependence and for the applied humidification of the fuel gas (62 % H_2O), becomes nonlinear only for high current densities. The deviation of the measured C/V curves from the linear approximation however increases significantly for decreasing operating temperatures, where only small current densities are achieved. It is hence obvious that the thermally activated activation polarization has a significant contribution to the observed non-linearity of the measured C/V curves. The prediction based on the physically meaningful model hence shows excellent agreement with the measured data at low temperatures. At high temperatures, the model predictions are slightly lower than the measured

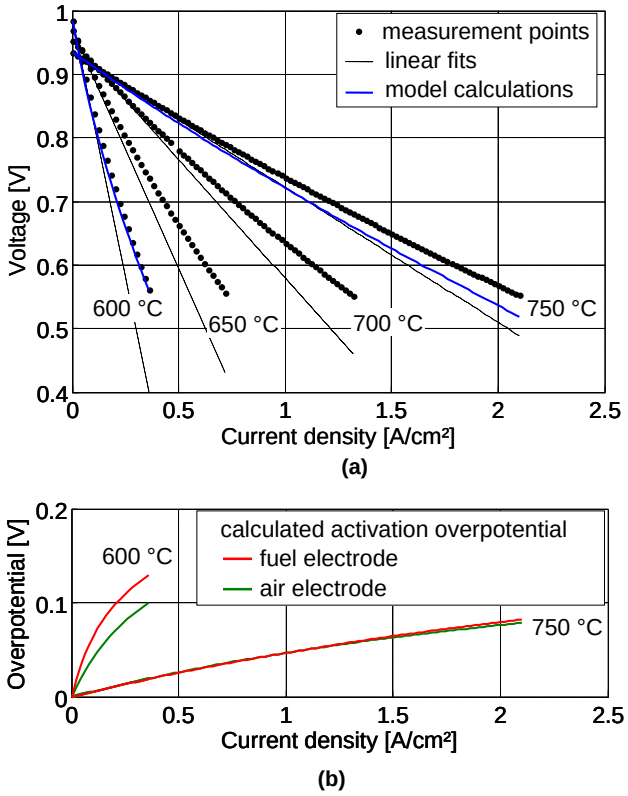

Figure 4.4-8: (a) Measured C/V curves at temperatures between 600 °C and 750 °C plus linear predictions and (b) the activation overpotentials calculated by the proposed model for a H_2O/H_2 fuel mixture of 62:38

C/V curves, however even here, the error is still smaller than for a linear prediction. Illustrating their non-linear contribution to the overall C/V curve, the model calculation of the activation overpotential for the fuel and air electrodes respectively, are depicted in Figure 4.4-8 b. These are small and show almost linear shape for the C/V curve at 750 °C. For 600 °C however, the activation overpotentials are much greater and their nonlinear C/V characteristic becomes obvious. In this light, it is proven that the fuel electrode supported cell type investigated herein, would be insufficiently described by a linear approach for the activation polarization overvoltages, when a wide range of operation conditions shall be predicted with a model.

4.4.1.5 Model Predictions for Selected Conditions

As mentioned earlier on, a good model would assist a system developer in the choice of optimal operation point (i.e., temperature, electrode gas composition) and/or of operation mode, or to guide the cell manufacturer in further improving the cells for the desired operation mode. In Figure 4.4-9 a are model predictions of overvoltages resulting from individual loss mechanisms for operation at 850°C, fuel electrode steam partial pressures of 80-, 50- and 20 % for both SOFC and SOEC operation at 1.5 A/cm². Figure 4.4-9 b displays predictions for the same conditions for 750 °C.

Figure 4.4-9 a reveals that at 850 °C, at most gas compositions, and for both modes, the major performance limiting mechanism is the ionic conductivity of the electrolyte (including GDC and interdiffusion layer) as depicted by the large ohmic losses (η_{ohm}). It can further be seen that only for operation with 80 % H_2O are the losses in SOEC mode smaller than those in SOFC mode. With decreasing fuel humidification, the fuel electrode side losses in SOEC mode increase, becoming greater than the losses for SOFC mode. Hereby, the increasing overall overvoltages have to be attributed to an increase of both fuel electrode concentration and activation polarizations for the above mentioned reasons. It is further interesting to see the coupling of both loss mechanisms. In any case, non-ideal gas diffusion leads to an accumulation of H_2O at the TPB in SOFC mode and to an H_2O depletion in SOEC mode. Therefore the fuel electrode activation overvoltage, which increases significantly with decreasing pH_2O_{an} (cf. equations (32) and (59), is always greater in SOEC mode. Particularly for 20 % H_2O, this effect becomes notable. Due to the non-ideal gas diffusion, the pH_2O at the TPB is reduced to 0.019 atm at the TPB, resulting in a dramatically increased $\eta_{act,an}$. In the last columns of the diagram, the gas diffusion polarization in the substrate was not considered (i.e., the substrate thickness L_{an} was set to 10^{-15} m). Consequently, the predicted pH_2O at the TPB is constant at 0.2 atm and as a result, fuel electrode activation polarization in SOEC mode is decreased from 101 mV (with gas diffusion polarization) to 48 mV (without gas diffusion polarization). For SOFC operation, the constant pH_2O_{an} has a negative impact on the activation overvoltage. Accordingly, the model without gas diffusion polarization reveals an increased fuel electrode activation polarization of 41 mV compared to 34 mV with gas diffusion polarization.

From Figure 4.4-9 b in which the 750 °C case is predicted, similar trends to those at 850 °C can be observed. Except for SOEC mode with pH_2O = 0.2 atm, the concentration overpotentials do not represent a major

contribution to the overall overvoltages of the cell. Gas diffusion still plays an important role at 750 °C, where the thermally activated activation overvoltages are more pronounced and hence the impact of gas diffusion on the activation polarization becomes more significant. The latter implicates in greater differences in $\eta_{act,an}$ for SOFC and SOEC mode and, as a result, the overall overvoltages in SOEC mode are always higher than in SOFC mode.

These results show that there is a strong coupling of gas diffusion and activation polarization. For the loss mechanisms of the cells analyzed herein, this coupling plays an important role, particularly in SOEC operation. It is thus important for SOEC mode operation to improve or optimize gas transport properties at the fuel electrode. As discussed above, fuel-side gas transport is represented by gas diffusion of H_2/H_2O, mainly through the porous fuel electrode support. From equations (49) and (51), it is obvious that fuel-side gas transport properties can be improved by either thinner thickness of the electrode support (L_{an}) or improved microstructure represented by the parameter ψ_{an} depicting the ratio between porosity and tortuosity of the substrate. For further predictive strengths and gains of the model references [2,3,42] are recommended.

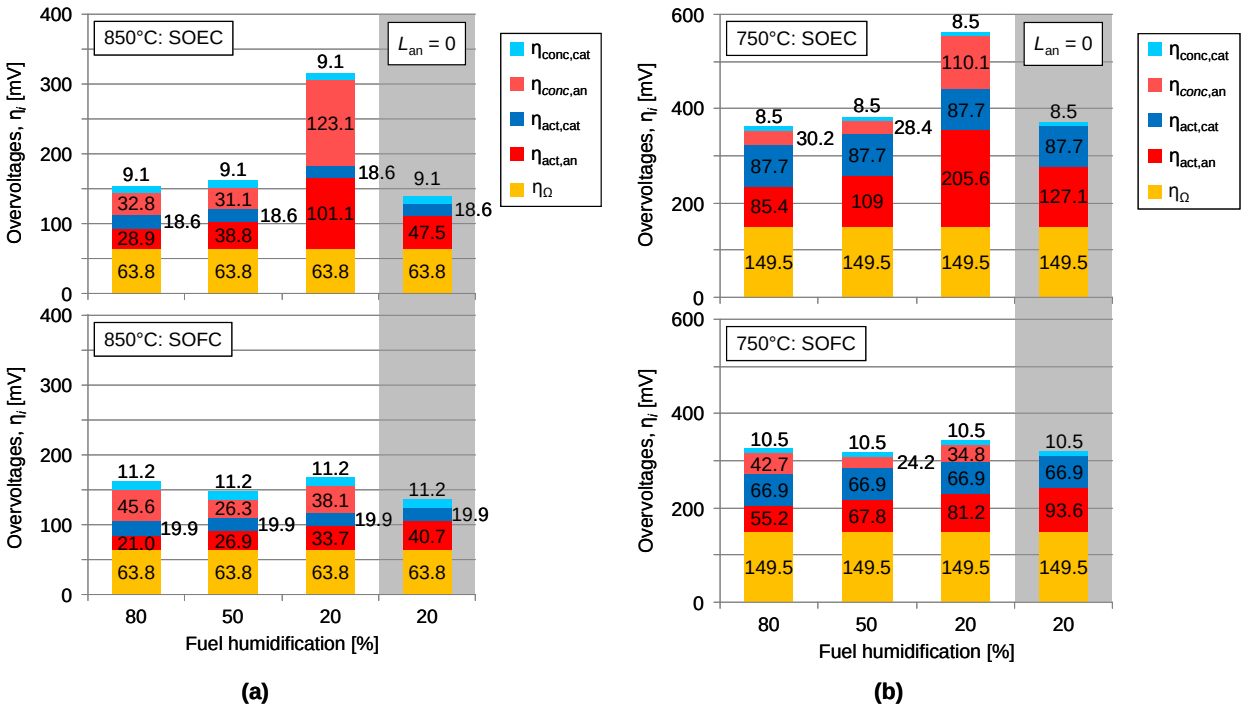

Figure 4.4-9: Simulation/predicted overvoltages for SOFC and SOEC modes for fuel electrode pH2O of 0.8-, 0.5- and 0.2 atm, air (0.21atm pO2) at air electrode pO2 at 1.5A/cm² for: (a) 850°C and (b) 750°C

4.4.2 Operation in Carbon monoxide/Carbon Dioxide Fuel Mixture

In a similar manner to the H_2/H_2O operation described in section 4.4.1 above modeling results in CO/CO_2 will be discussed in this section—though with much less degree of detail. After validating the 0-D model in H_2/H_2O fuel mixtures, Leonide et al.[4] extended the model to cover fuel cell mode operation in CO/CO_2 fuels by determining appropriate model parameters in the according gas and temperature variations. There as well electrochemical impedance spectroscopy, DRT and CNLS fit analysis with the help of the physically meaningful model[3] were employed. This was possible and rather straight forward[xxi] as operation in CO/CO_2 fuel meant the exact same loss mechanisms contributed to the overall overpotential albeit with different magnitudes and the processes had different characteristic frequencies. Again, with electrolysis mode measurement capability in place, it was interesting to validate the existing model[4] for the reduction of CO_2 as well.

4.4.2.1 Model Parameterization

As mentioned above, through careful variations of adequate operation conditions, DRT analysis and CNLS fits, model parameters were determined and are summarized in Table 4.4-2 whereby some of the parameters didn´t have to be determined anew and thus adopted from Ref. [3]. The model equations were same as those in the H_2/H_2O fuels albeit replacing H_2 with CO and H_2O with CO_2. The corresponding gas dependencies in the exchange current density expression (equation (59)) a and b were also relabeled to c and d for CO and CO_2 respectively. Furthermore, the CO/CO_2 model has not been calibrated to include temperature evolution under load. As will be seen from the small maximum recorded current densities—and thus expected small changes in temperature in both modes, the need for such correction is less severe than for H_2/H_2O operation.

Table 4.4-2: Cell and model parameters for CO/CO_2 operation[4]

Parameter	Value
B_{ohm}	$5.8 \cdot 10^{12}$ S·K/m^2
$E_{act,ohm}$	91.66 kJ/mol 0.95eV
c	-0.058
d	0.253
m	0.22

[xxi] Contrary to reformate involving H_2, H_2O, CO and CO2 whereby an extra low frequency process appears due to existence of water gas shift and revers water shift reactions[38]

γ_{An}	$4.5629 \cdot 10^6 \cdot T$ A/m^2	
γ_{cat}	$1.51556 \cdot 10^8 \cdot T$ A/m^2	
$E_{act,An}$	118.64 kJ/mol	1.229 eV
$E_{act,Kat}$	139.86 kJ/mol	1.45 eV
α_{An}	0.6219	
α_{cat}	0.65	
ψ_{an}	0.13	
Ψ_{cat}	0.022	

4.4.2.2 Model Validation

In Figure 4.4-10a model results for C/V curves at 800 °C and CO/CO_2 ratios 30/70, 50/50 and 70/30 are compared with measurements in fuel cell and electrolysis modes. In Figure 4.4-10b C/V curves have been simulated for the temperatures 700 °C, 800 °C and 850 °C in a CO/CO_2 ratio of 50/50. It can be seen from both figures that the model reproduces the measured curves in both modes with acceptable accuracy.

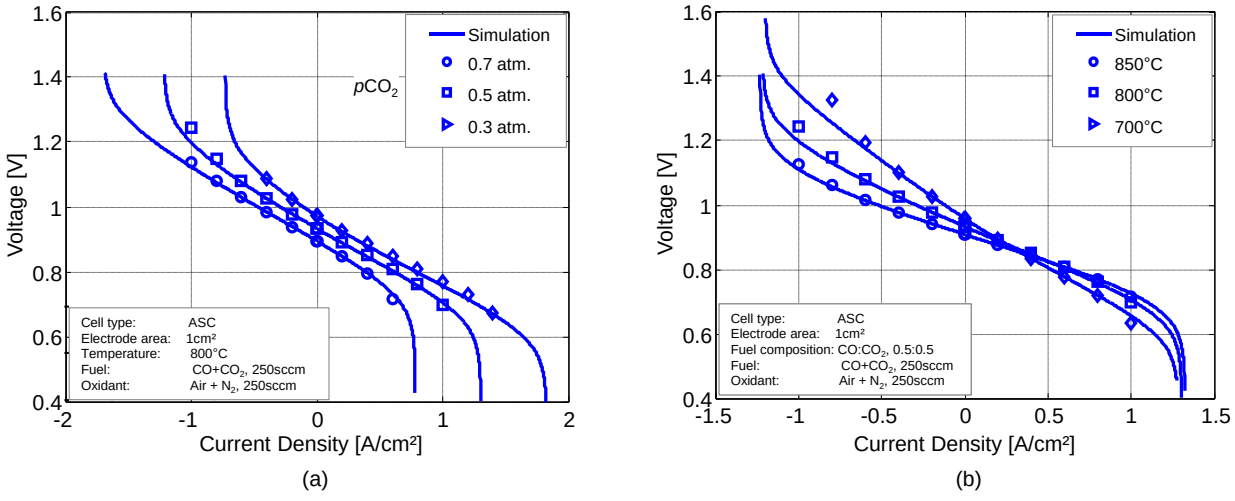

Figure 4.4-10: Simulation results of C/V curves (a) for the three different fuel electrode gas mixtures CO/CO_2 of 30/70, 50/50 and 70/30 at 800°C and (b) for three different operation temperatures with a constant 50/50 fuel electrode CO/CO_2 gas composition

However, from Figure 4.4-10b it can be noticed from the 700 °C and 800 °C SOEC mode curves that despite the low maximum measured current densities, the discrepancy between model and measurement starts increasing at ca. - 0.6 A/cm^2 and - 0.8 A/cm^2 respectively—points at which the model curves are still more or less linear. This abnormal deviation suggests the possible presence of an ageing phenomenon present only in or predominant in SOEC mode in the investigated current density window under the considered fuel mixtures.

At this juncture it is hypothesized that in SOEC mode and current densities beyond - 0.7A/cm² (cf. the 800 °C curve) carbon dioxide is not being replenished fast enough at the TPB, so that the product carbon monoxide is reduced so long to solid carbon. This blocks the TPB thereby reducing the available reaction surface, raising the ASR to values greater than those predicted in the model. In fuel cell or SOFC mode, this phenomenon is non-existent and the simulations correctly reproduce measurements right up to limiting current densities with acceptable degree of accuracy.

To investigate this hypothesis, the SOEC mode C/V curve recorded at 800 °C in a fuel electrode gas composition of 50/50 CO/CO_2 was considered (cf. Figure 4.4-11a). The same conditions were set and the current density in electrolysis mode was increased at 0.2 A/cm² steps with waiting time of 30 minutes after which an impedance spectrum was recorded. The voltage evolution with time during the process is shown in Figure 4.4-11b. As can be seen the cell voltage and current density show a linear relationship up to - 0.6 A/cm². After this point (at 0.8 A/cm²) the cell voltage is no longer constant despite the constant current density. This current density in the C/V-curve in Figure 4.4-11 a corresponds to the first point at which model and measurement no longer match.

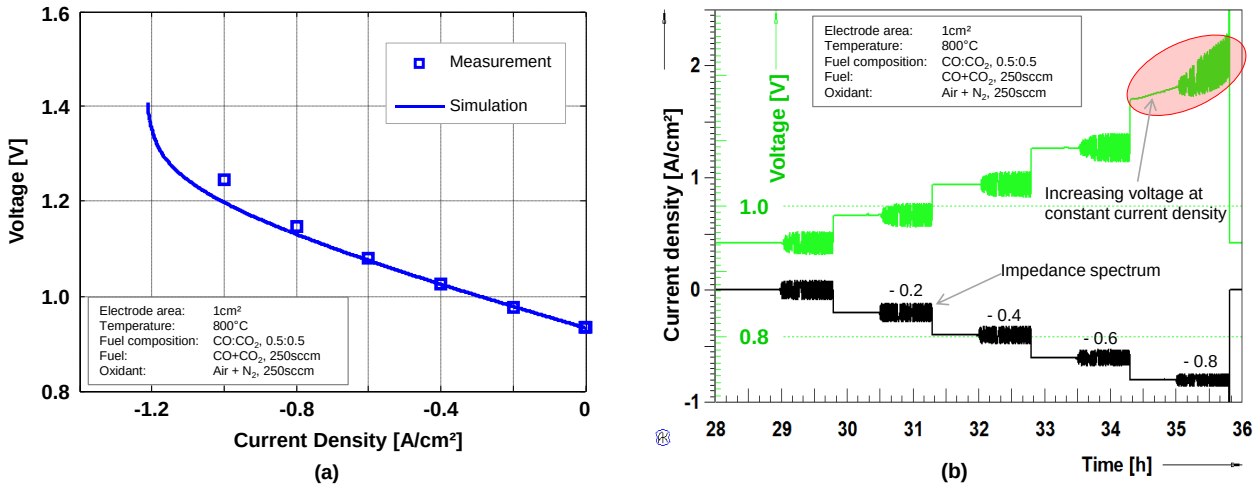

Figure 4.4-11: (a) Simulated and measured SOEC mode C/V curve at 800 °C and 50/50 CO/CO_2 fuel (b) Cell voltage evolution over time in a stepwise variation of electrolysis mode current density at 800°C in a 50/50 CO/CO_2 fuel.

Using the commercially available software MALT[111] thermodynamic calculations were carried out to determine the concentrations and overvoltage for the onset of carbon deposition at 800 °C. These are shown in Figure 4.4-12 from which can be seen that at 800°C carbon deposition begins at a carbon monoxide content of around 88% with a corresponding electrode potential vs. air of ca. 1.041 V.

At 800°C in a 50/50 CO/CO_2 fuel electrode gas composition, the open circuit voltage is 0.945 V. From the model the sum of fuel electrode overvoltages (i.e. diffusion and activation) at - 0.8 A/m² amounts to 0.134 V. Addition of this value to the OCV results in a fuel electrode potential vs. air of ca. 1.0754 V—a value greater than the 1.041 V fuel electrode overvoltage necessary for carbon deposition. This implies that at - 0.8 A/cm² the governing fuel electrode potential is already greater than that required for carbon deposition, proving that the increasing cell voltage is indeed a result of reduction of carbon monoxide at the TPB to solid carbon. Since the cell voltage is stable at - 0.6 A/cm² and unstable at - 0.8 A/cm² it can be assumed, that the window for carbon deposition free operation at 800°C and 50/50 CO/CO_2 fuel electrode gas composition is - 0.7 A/cm². This type of analysis can be done for other temperatures and gas compositions to determine the corresponding maximum possible electrolysis current densities—an important gain of the presented model.

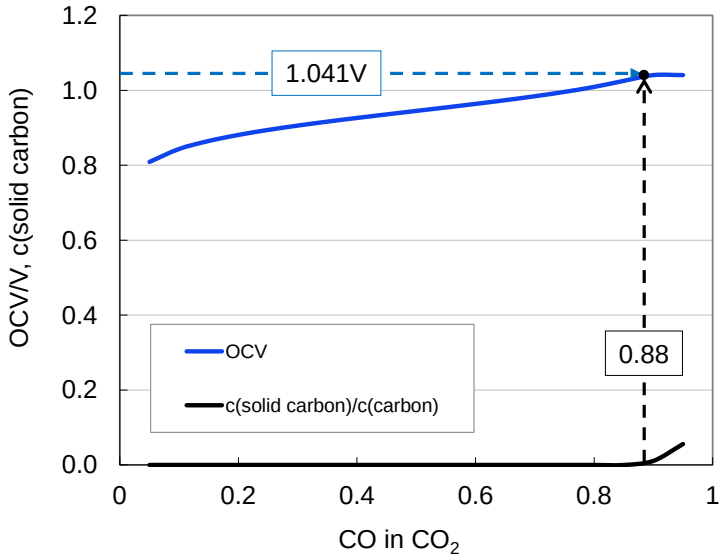

Figure 4.4-12: Open Circuit Voltage and onset of carbon deposition at 800°C from thermodynamic calculations using the software *Malt*.

4.4.3 Operation in Reformate Fuel Mixtures and Co-Electrolysis Mode

This section probably involves the most significant extension of the 0-D model since the original model[3,4] was not designed for multicomponent gas mixtures ($H_2/H_2O/CO/CO_2$) as reformate fuels and gas compositions in the co-electrolysis mode. In this section the model has been extended to cover the situation where the four gas components are present in the inlet fuel. Furthermore the model presented in this chapter is validated with measurements on a newer generation of FZJ cells with 0.5 mm thick substrate instead of the cells with 1 mm thick substrate used in the H_2/H_2O and CO/CO_2 model validations. This means, appropriate model parameters were determined anew, through electrochemical impedance spectroscopy, DRT and CNLS fit analysis as proposed by Leonide[3].

4.4.3.1 Model Concepts and Equations

Operation of the SOC in a fuel containing the four components H_2, H_2O, CO and CO_2 (henceforth called reformate fuel) is intrinsically accompanied by the presence of the water gas shift reaction (WGSR) as shown in reaction (4-1). Under OCV conditions interplay between the WGSR and the reverse water gas shift reaction (RWGSR) results in an equilibrium fuel composition defined by the temperature and inlet fuel composition.

$$CO + H_2O \xleftrightarrow{WGSR/RWGSR} CO_2 + H_2 \qquad \Delta_R H^0 = -41\ kJ/mol \qquad (4\text{-}1)$$

When the cell is polarized current will flow. At this juncture, it is pertinent to decide which fuel components are electrochemically converted to what extent. Although no group contests the presence of the WGSR or RWGSR there is no general consensus in literature as to whether solely H_2 is directly electrochemically converted in FC mode and CO over the WGSR or both H_2 and CO are directly electrochemically converted. The same holds for H_2O and CO_2 when the cell is polarized in EC mode. The model concept presented in this chapter will be based on the assumption that solely H_2 (or H_2O in EC mode) is directly electrochemically converted as demonstrated by Kromp *et al.*[38]. Thereby CO (and CO_2) conversion occurs indirectly over the WGSR (and RWGSR).

It has been shown[38,112] that in reformate fuels there is an extra low frequency process contributing to the cell ASR which is believed to be coupling between diffusive gas transport and shift[38] or reforming[113] reactions. The overpotential contribution of this reformate process $\eta_{conc,Ref}$ will be in a first approximation assumed to be diffusive in nature involving solely the diffusion of CO and CO_2 molecules from the surface of the substrate adjacent to the gas channel towards the fuel electrode functional layer. $\eta_{conc,Ref}$ is derived following the same concepts as Primdahl et al.[40]—CO/CO_2 flux given by Fick´s first law, assumption of linear concentration gradient, corresponding overvoltage given by difference of Nernst equation expressions for inlet and TPB concentrations,

assumption of ideal gas law to obtain molar fractions from concentrations etc. However contrary to the diffusion flux of H_2/H_2O molecules being controlled by the faraday current density j the here derived diffusion flux of CO/CO_2 will be controlled by the reaction rate R_{WGSR} [molm^{-3}s^{-1}] of the shift (revers shift) as done literature[114,115]. The resulting expression is displayed in equation (62) which looks very similar to equation (49) for the pure CO/CO_2 case. However, by virtue of the number of involved reactant molecules (2 in equation (49) and 4 in equation (62)) the difference between both equations does not lie solely on the physical meanings of j in equation (49) and j^* in equation (62) but also in the values of the effective diffusion coefficients D_{eff}^{j} of CO and CO_2 in both equations.

$$\eta_{conc,Ref} = \frac{RT}{2F} ln\left(\frac{1 + \frac{RTl}{D_{eff}^{CO_2} P_0 pCO_2} j^*}{1 - \frac{RTl}{D_{eff}^{CO} P_0 pCO} j^*}\right) \tag{62}$$

In equation (62) R, T and F have the usual meanings meanwhile l represents the thickness of the substrate, P_0 the atmospheric pressure, *p*CO and *p*CO_2 the carbon monoxide and carbon dioxide partial pressures respectively, D_{eff}^{j} the effective diffusion coefficient of gas j calculated based on equation (51) and j^* the CO/CO_2 flux based on the WGSR rate and distance l from cell surface to TPB and defined by equation (63).

$$j^* = l \cdot R_{WGSR} \tag{63}$$

R_{WGSR} [molm^{-3}s^{-1}] is the widely used WGSR (or RWGSR) rate[114,115] or mass rate production per unit volume as defined by Habermann *et al*.[116] as shown in equation (64)

$$R_{WGSR} = k_{sf}\left(pH_2OpCO - \frac{pH_2pCO_2}{K_{PS}}\right) \tag{64}$$

whereby the equilibrium constant K_{PS} is given by equation (65) also containing an empirical exponential expression.

$$K_{PS} = \frac{pH_2pCO_2}{pCOpH_2O} = \frac{k_{sf}}{k_{sb}} \cong exp(-0.2935Z^3 + 0.6351Z^2 + 4.1788Z + 0.3169) \tag{65}$$

In equations (64) and (65) k_{sf} and k_{sb} are the forward and backward rate constants and the Z in the empirical expression is given by equation (66)

$$Z = \frac{1000}{T(K)} - 1 \tag{66}$$

and the forward reaction rate constant k_{sf} in [molm^{-3}Pa^{-2}s^{-1}] is given by equation (67).

$$k_{sf} = 0.0171 exp\left(-\frac{103191}{RT}\right) \tag{67}$$

In electrolysis mode and under assumption that only H_2O is directly electrochemically converted, the RWGSR will replenish the H_2O according to reaction (4-1), with the backward reaction rate of the k_{sb} calculated from the rate constant K_{PS} in equations (65) and the forward rate constant k_{sf} in (67). As such the corresponding mass production rate R_{WGSR} as well as the correct CO/CO_2 flux j^* for electrolysis mode can be calculated.

4.4.3.2 Model Parameters

As mentioned earlier on the C/V measurements used to validate the version of the model described in this section were recorded on a newer generation of the FZJ cells. This meant that some cell and model parameters had to be determined anew. The new parameters are given in Table 4.4-3. Although the new parameters can be used to evaluate similarities and differences between the two cell generations with respect to performance or other indices such a comparison falls outside the scope of this thesis. Thus the parameters will solely serve to evaluate how well the overall model matches the measured C/V curves.

Table 4.4-3: Cell and model parameters of the fuel electrode determined anew for the newer FZJ cell generation with 0.5 mm substrate thickness

Parameter	New Cell value	Old Cell values[3,42,53]
B_{ohm}	$6.9 \cdot 10^{12}$ S·K/m^2	$4.19 \cdot 10^{12}$ S·K/m^2
$E_{act,ohm}$	93.7 kJ/mol (0.97 eV)	90.31 kJ/mol
a	-0.04	-0.10
b	0.26	0.33
γ_{An}	$1.48 \cdot 10^{6} \cdot T$ A/m^2	$1.83 \cdot 10^{6} \cdot T$ A/m^2

$E_{act,An}$	103.04 kJ/mol	(1.068 eV)	105.04 kJ/mol
α_{An}	0.67		0.59
ψ_{an}	0.078		0.13
l	0.5 mm		1 mm

4.4.3.3 Model Validation

The model is validated in a similar manner as done with the H_2/H_2O and CO/CO_2 models by comparing simulated C/V curves with measured curves. An important difference between the measurements in this section to the two binary fuel cases is that the fuel mixtures are equilibrium mixtures carefully adjusted in a two-step process as done elsewhere[38]. In the first step, the according H_2 and H_2O ratios are set with N_2 balance until the theoretically correct cell voltage is attained and then the N_2 is replaced with CO/CO_2 mixtures that are adjusted again until the cell voltage is attained. This enables accurate setting of the required equilibrium mixtures.

In Figure 4.4-13 a C/V curves measured at 800 °C in three different fuel mixtures with $H_2/H_2O/CO/CO_2$ ratios (i) 15/15/35/35 (ii) 25/25/25/25 and (iii) 35/35/15/15 are compared with model predictions. The fuel mixtures are chosen to evaluate the different cases of fuel composition symmetry (ii) and asymmetries in H_2/H_2O and CO/CO_2 components (i and iii). In Figure 4.4-13b the measurements are recorded in the symmetrical fuel composition 25/25/25/25 $H_2/H_2O/CO/CO_2$ at the temperatures 775 °C, 800 °C and 825 °C.

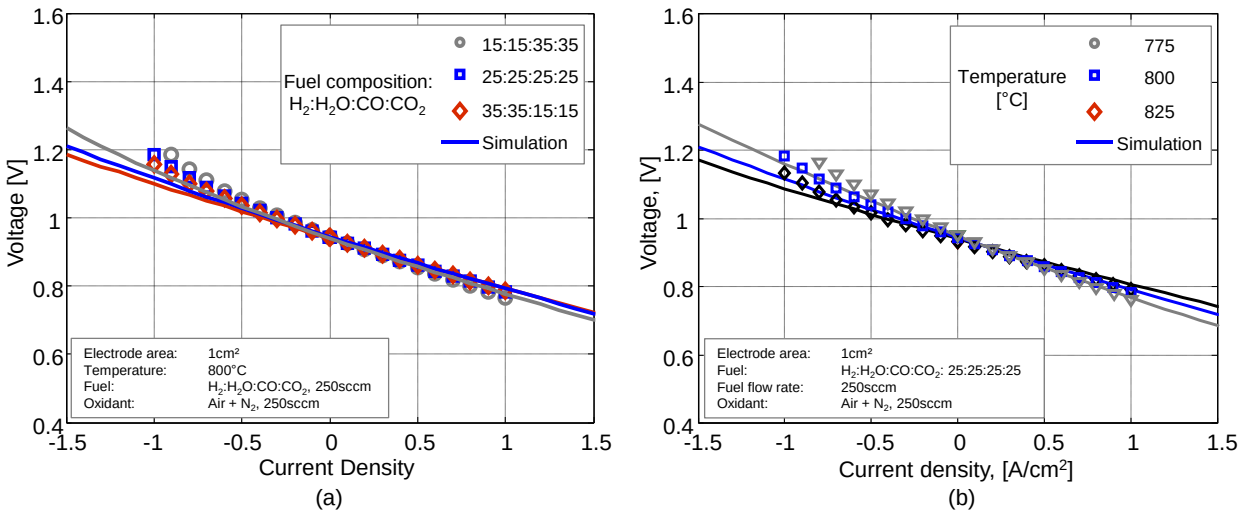

Figure 4.4-13: Validation of model predictions in SOFC and SOEC modes for (a) different $H_2/H_2O/CO/CO_2$ ratios at 800 °C and (b) for different temperatures, T in a 25/25/25/25 ratio inlet fuel mixture.

To evaluate the model accuracy, error curves have been calculated as difference between simulated and measured curves for the temperature variation in Figure 4.4-13 b. These are displayed in Figure 4.4-14 a and the corresponding relative values in % are displayed in Figure 4.4-14 b. It can be seen that in the investigated current density range of j = -1 to 1 A/cm^2 the measurements are predicted with less than 2 % error in FC mode and less than 6 % error in EC mode. With the assumption that CO/CO_2 is not directly electrochemically converted, the larger error in EC mode can be attributed to the fact that with solely 25 % H_2O in the fuel, H_2O starvation under load leads to (i) CO_2 reduction after all and which is not accounted for by the model or (ii) a much slower replenishing of H_2O through the RWGSR as predicted by the empirical expressions from literature.

Furthermore the temperature evolution under load due to joule heating, electrochemical oxidation of hydrogen and the prevailing WGSR as well as the electrochemical reduction of H_2O and prevailing RWGSR has not been considered. Coupled to the errors associated with the made assumptions the errors less than 6- and 2 % in EC and FC modes respectively can be considered acceptable. If it is further considered that the relevant operation window for SOCs in stack would be in the range $j \leq \pm 0.5$ A/cm^2 then the error range becomes less than 2 % for both modes—a fairly acceptable accuracy. In literature, in a 1 D space resolved model to predict SOEC operation in reformate fuels, Ni[114] evaluates his model accuracy by comparing the calculated current density at given voltages and comparing with measured values. For an inlet composition of 50/25/25 $H_2O/H_2/CO_2$ at 800 °C he reports a difference between model and measurement of 25 % at a cell voltage of only 1 V (at ca. 0.4 A/cm^2). A 2 D (thermal model) extension is reported[115] but not validated with measurement. Kazempoor et *al*.[117] have obtained better agreement between model and measurement, however calibrating their model activation and ohmic overvoltage parameters from experimental data.

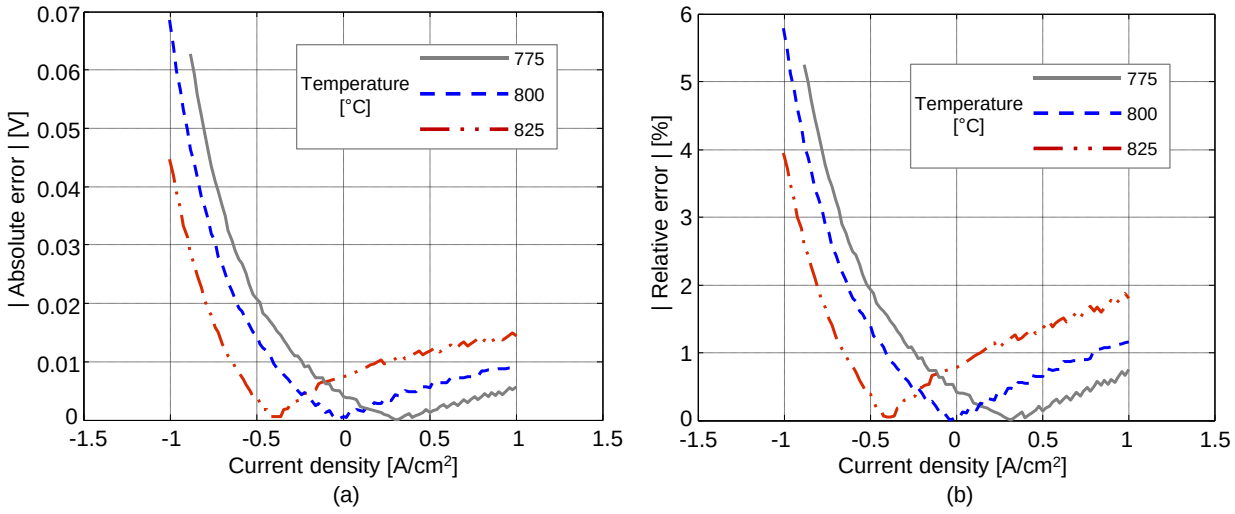

Figure 4.4-14:Error between model prediction of the C/V curves at 775 °C , 800 °C and 825 °C and 25/25/25/25 $H_2/H_2O/CO/CO_2$ ratios (a) Absolute values and (b) relative values NOT normalized with the dynamic range

The evolution of the calculated overpotentials η_i for the different loss processes for the 800 °C and 25/25/25/25 $H_2/H_2O/CO/CO_2$ fuel mixture is displayed in Figure 4.4-15. The figure includes the overvoltage contribution $\eta_{conc,Ref}$ of the concentration related reformate process. Two major observations can be made:

i. In EC mode the activation overpotential is making a much larger contribution than in FC mode: This would be expected based on the asymmetry considerations discussed in section 4.4.1.3. However, contrary to Figure 4.4-5b the activation overpotential is not accompanied by an equivalent increase in diffusion overpotential since this is now split into the two pathways—the H_2/H_2O path governed by the faraday current and the CO/CO_2 pathway governed by the shift and reverse shift reactions.

ii. The reformate diffusion contribution $\eta_{conc,Ref}$ in EC mode is larger than its equivalent in FC mode for all current densities. This observation is consistent given that in EC mode the depletion of H_2O at the TPB favors the RWGSR whereby CO_2 is consumed. Consequently more CO_2 has to diffuse to the reaction sites to replenish that consumed by the RWGSR. A similar process happens in FC mode where CO diffuses to replenish that consumed in the WGSR. However, the CO_2 molecule is larger than the CO molecule and should have a smaller effective diffusion coefficient. The model calculated effective diffusion coefficients of $D_{CO_2}^{eff} = 2.22e^{-5}$ m²/s for CO_2 and $D_{CO}^{eff} = 2.78e^{-5}$ m²/s for CO consistently confirm the hypothesis.

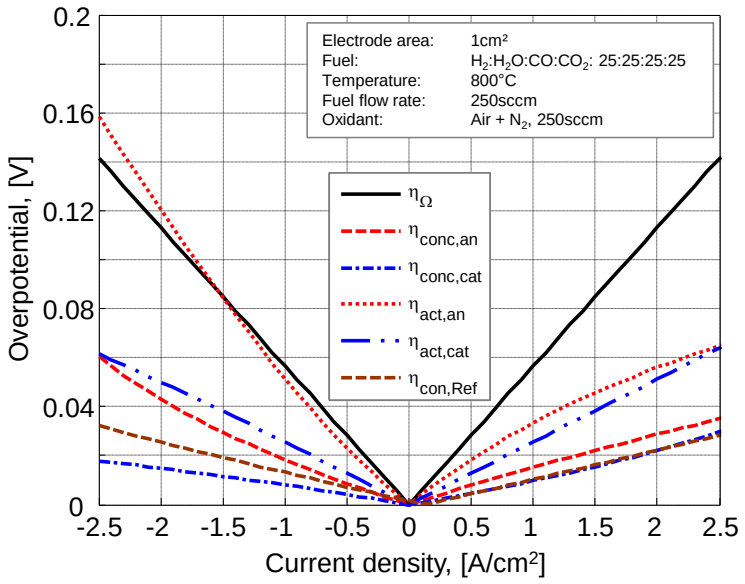

Figure 4.4-15: Overvoltages of the 800°C and 25/25/25/25 $H_2/H_2O/CO/CO_2$ fuel simulated C/V curve including the contribution of the water gas and reverse water gas shift reaction-related concentration loss.

4.5 Conclusion

In this chapter, the 0-D isothermal model developed to predict the C/V characteristic of a SOC in fuel cell mode was verified for electrolysis operation in both H_2/H_2O and CO/CO_2 binary fuels. The H_2/H_2O model was extended to consider temperature change under load. The model was further extended to cover operation in reformate fuels $H_2/H_2O/CO/CO_2$ whereby a new concentration-related overpotential contribution was included in the model, to account for the CO/CO_2 diffusion to the reaction sites as a results of the water gas shift and reverse water gas shift reactions. To that end, new model parameters were determined for the fuel electrode as measurements were done on a different generation of cells as those used for the H_2/H_2O and CO/CO_2 models. The new model was validated by predicting C/V characteristics under different operation points of temperature and fuel electrode composition and comparing with experiments.

Chapter 5 Long-term Stability of SOCs in SOEC, Cyclic and Dynamic Operation modes

5.1 Introduction

The commercialization of SOCs operated in fuel cell-, electrolysis or reversible modes depend on the long-term stability of the cells under operation. As such while it is essential to understand the involved mechanisms[14,118–122] (cf. Chapter 3) or predict cell performance[42,54,114,115,123–128] (cf. Chapter 4) it is equally important to understand the contributions to the overall ageing of the individual cell compartments or mechanisms during long-term operation[110,129,130]. The ageing rates and ageing mechanisms depend on operating conditions like temperature, fuel composition, pressure, overpotential distribution and fuel conversion rate. The ageing mechanisms and rates also depend on whether a single cell[110,131–138] or stack[139–147] is being investigated. In stacks for instance, the impacts of interconnects such as chromium poisoning[147], impurities from glass sealings[140,148] or fuel starvation are important, and they are either absent or very minimal in single cell tests. Also, impurities[148] such as sulfur[149] definitely impact the long-term stability of SOCs. With respect to cell type, cells with Sr-doped $LaMnO_3$ (LSM)/YSZ oxygen electrodes have a much larger oxygen electrode ASR than those with LSC/CGO under same conditions. As such under similar conditions of temperature and current density cells with LSM/YSZ oxygen electrodes will be subjected to a much larger overpotential at the oxygen electrode[110] than at the fuel electrode. This of course will lead to different ageing mechanisms and rates for both electrodes in both cells[150]. Then of course the nature of the load—constant[8,110,129,134,136,137], cyclic[151–153] or dynamic[133,151]—and the associated overpotentials and thermal stresses will influence the ageing mechanisms and rates.

In this chapter the long-term stability of SOCs under different load dynamics will be addressed. This will be done in tests ranging between 1000- and 2500 hours. A 1000 h test at 800°C (Cell A) will be reported in which the SOC undergoes constant electrolysis mode operation. This test will be compared with a second 1000 h test (Cell B) carried under same conditions whereby the SOC undergoes rapid cycling between fuel cell and electrolysis modes with no duration at OCV. In a third test (Cell C) a 2500 h test at 800°C will be reported in which the SOC is operated in cyclic modes in five 500 h phases with differing cycle lengths—dynamic cycling. A further dynamic cycling test (Cell D) will be reported with the SOC operated at 700°C for comparison with Cell C. Finally, a further 1000 h test will be reported wherein two oxygen electrodes in a symmetric cell geometry are operated at 800 °C and OCV.

The evaluation of the ageing will be done with respect to the overall cell voltage ageing but more importantly the ageing of the individual compartments—oxygen electrode, electrolyte, fuel electrode and substrate will be deconvoluted through EIS, equivalent circuit modeling and DRT.

5.2 Constant Electrolysis vs Cyclic Mode Operation

5.2.1 Experimental

5.2.1.1 Cell System and Experimental Set-up

The cells employed in these durability investigations—Cells A and B—are single SOCs from FZJ described in section 4.3.1 with a fuel electrode substrate thickness of 500 µm—similar to those used to validate the model in section 4.4.3. Also, the same experimental set-up as in section 4.3.2 was used.

5.2.1.2 Operation and Characterization

Operation temperature was 800 °C, with air supplied to the oxygen electrode at 250 sccm and a 50/50 H_2/H_2O gas mixture supplied to the fuel electrode at 250 sccm. As usual the H_2/H_2O gas composition was achieved by allowing appropriate amounts of O_2 to react with 250 sccm of H_2 in a burning chamber preceding the cell housing.

While Cell A was operated solely in electrolysis mode under constant current density of - 1.5 A/cm², Cell B was cycled between SOFC and SOEC modes with the same current density of ± 1.5 A/cm² (ca. 4.2 % fuel utilization), with no delay at OCV. The holding time was 3 h per operation mode resulting in a cycle length of 6 hours. Figure 5.2-1 displays two cycles of a randomly picked section of the measurement course of cell B. It can be seen that cycling at ± 1.5 A/cm² is accompanied by a measured thermal cycle of 2 °C (at least 4 °C based on the real temperature from EIS in Section 4.4.1.2 and Figure 4.4-3). Under these conditions, the cells in SOEC mode were operated close to thermoneutral[41,54,61,109,117–119,133,138,152] conditions. There-by the heat requirements for the endothermic electrolysis reaction are balanced by joule heat from irreversible losses. At the thermoneutral point, the cell voltage—the thermoneutral voltage, E_{tn} is defined as the minimum thermodynamic voltage at which a perfectly insulated electrolyzer would operate, if there were no net inflow or outflow of heat[41,109] and is given by[xxii]:

$$E_{tn} = \frac{1}{nF}\Delta H_f \tag{68}$$

[xxii] Cf. Equation (61)

whereby ΔH_f represents the molar enthalpy of formation of H_2O, F the faraday constant (96485 Coulomb/mol) and n the number of electrons involved in the formation of 1 mol of H_2O. For pure steam electrolysis at 800 °C, E_{tn} values between 1.27 – 1.3 V[117,133,138,152] are cited in literature. For the cells investigated herein and under the employed operation conditions the initial cell voltage was 1219 mV.

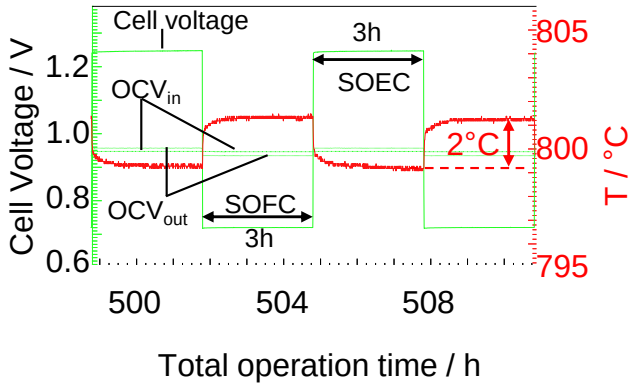

Figure 5.2-1: Two cycles of cell B cycled at ±1.5A/cm² at 800 °C and 0.5 atm fuel electrode steam partial pressure

Electrochemical characterization was carried out every 100 h for both cells. Figure 5.2-2 displays a typical characterization step wherein the numbered steps (i) to (v) represent EIS under current load in SOEC mode (- 1.5 A/cm²)[xxiii], C/V-curve in SOEC mode, EIS at OCV in 50/50 H_2/H_2O fuel electrode gas composition, C/V-curve in SOFC mode and EIS at OCV in a 50/50 CO/CO_2 fuel electrode gas composition respectively. It can be seen from Figure 5.2-2 as well that the temperatures at OCV and under SOEC mode are equal as expected for thermoneutral operation. To avoid damaging the cells during C/V-curve recording, the lower voltage limit in SOFC mode was set at 0.6 V and in SOEC mode the upper voltage limit has been set at 1.6 V. The current density was abruptly cut upon attaining the limiting voltages immediately returning the cell voltage to OCV. Also shown in Figure 5.2-2 are voltage courses from the OCV probes with outlet voltage OCV_{out} greater than the inlet voltage (OCV_{in}) in SOEC mode and the other way around during SOFC operation periods. This is consistent since in SOEC mode the outlet gas is *dryer* due to the "consumed" H_2O but contains more H_2O due to the "produced" H_2O in SOFC mode. At OCV all three voltages overlap as expected. Also, the characterization step contains an EIS spectrum at OCV in a 50/50 CO/CO_2 fuel electrode gas composition. Due to the larger binary diffusion coefficient of the H_2/H_2O gas mixture as compared to that of CO/CO_2 the EIS spectrum in a CO/CO_2 atmosphere enables the fuel electrode process "gas diffusion" to be "pushed down" to lower frequencies. This enables better deconvolution and

[xxiii] For cell B there are also EIS in SOFC mode (+1.5 A/cm²) at the beginning and end of every 100h interval

quantification of the oxygen electrode ASR contribution as well as the ASR contribution of the fuel electrode substrate diffusion process that would otherwise overlap[154].

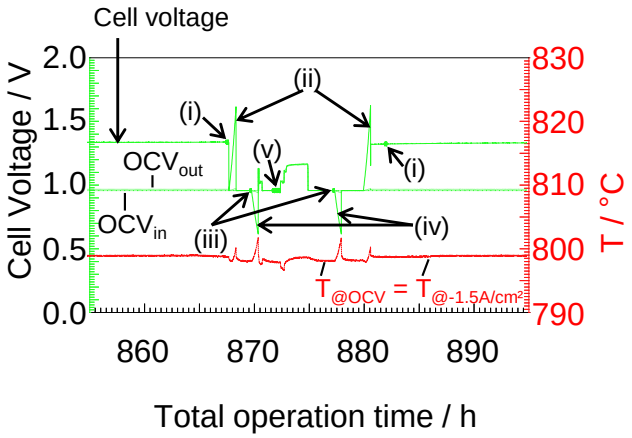

Figure 5.2-2: Typical characterization step applied during characterization intervals of cells A and B

Post-test scanning electron microscopy analysis was performed with a Zeiss 1540XB on cross sections of the tested cells, prepared by fracturing. Transmission electron microscopy (TEM) analyses were performed with a FEI Titan^3 80-300 FEG on a focused ion beam prepared TEM lamella at the Laboratory for Electron Microscopy of the Karlsruhe Institute of Technology (KIT). The local chemical composition of the samples was analyzed by EDX using an EDAX Si-Li detector.

5.2.1.3 Impedance Spectroscopy and Data Analysis

The EIS measurements were carried out with a Solartron 1260 FRA in the frequency range from 1 MHz down to 100 mHz for the H_2/H_2O fuel electrode gas composition and 30 mHz for CO/CO_2 atmosphere. Quantitative analysis of recorded spectra was realized through CNLS fit with the proven equivalent circuit model[2,34,98] displayed in Figure 5.2-3 describing the impedance response of the investigated cell type. Thereby, the element R_0 quantifies the series resistance and the two RQ-elements (R_{2A}, Q_{2A}) and (R_{3A}, Q_{3A}) quantify the coupled charge transfer reaction and ionic transport in the Ni/YSZ fuel electrode structure. The Gerischer element R_{2C} quantifies the ASR of the oxygen electrode, i.e. the oxygen surface exchange kinetics and O^{2-} ion diffusivity in bulk of LSCF and the Warburg element R_{1A} quantifies the gas diffusion in fuel electrode substrate. The dependencies and frequency ranges of these processes can be found in literature[2,3].

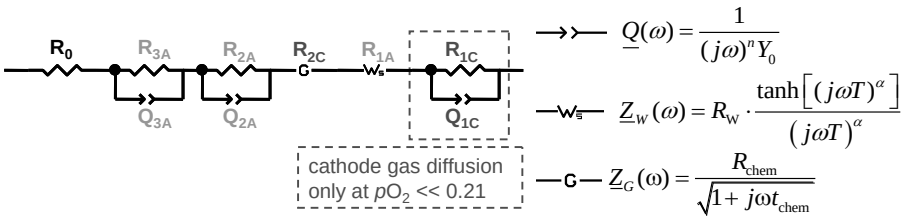

Figure 5.2-3: Equivalent circuit model[2,34] used in CNLS fit of impedance spectra

Preliminary investigations in which the partial pressure of oxygen at the oxygen electrode was varied at constant fuel electrode conditions, revealed that "gas diffusion" at the oxygen electrode (~ 5 mΩcm^2 and generally significant only for low oxygen partial pressures, $pO_2 << 0.21$)[2] had to be included in the analysis to obtain a better match between the DRTs of recorded and fit spectra. As such the model as used by Endler et al.[98] was extended with this process to obtain a finer and even more accurate deconvolution of electrode polarization contributions of the CO/CO_2 spectra. From these first CNLS fits in CO/CO_2 fuel electrode atmosphere the obtained air electrode polarization ASR is then used (held constant) in the fit of corresponding spectra in H_2/H_2O atmosphere.

5.2.2 Results and Discussion

5.2.2.1 Voltage Ageing

Figure 5.2-4a and b shows the evolution of the cell voltage for Cells A and B respectively. The voltage courses of both cells can be split into two sections: (I) an activation or pre-conditioning phase after cell reduction and (II) the actual ageing phase that begins with an initial characterization step as described in section 5.2.1.2. The custom characterizations in phase I are conventionally carried out on all single cells tests at IAM-WET and enable reproducibility checks of all tested cells. This phase will not be further elucidated—solely phase II will be discussed.

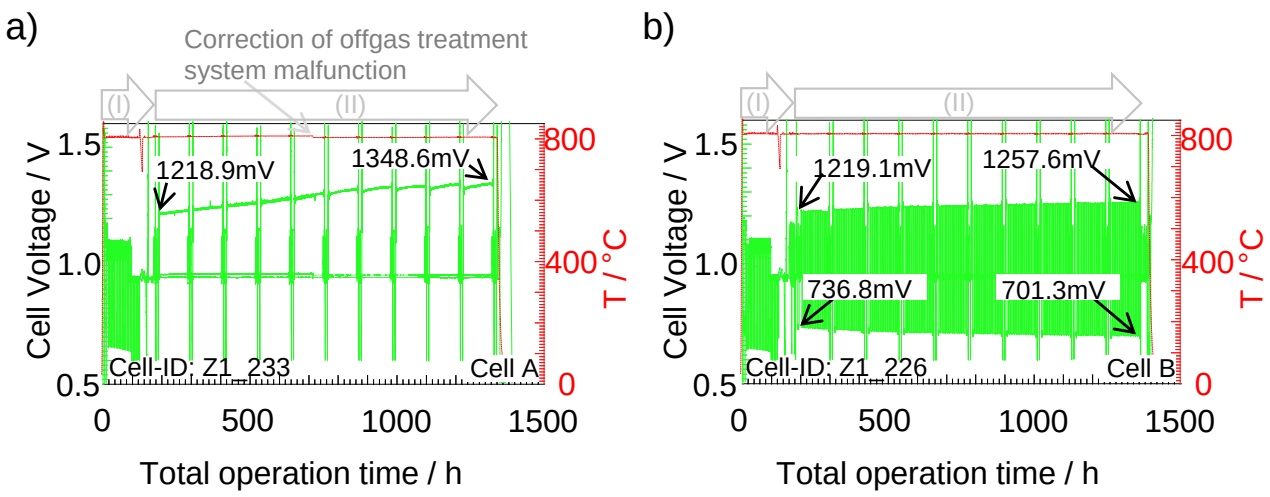

Figure 5.2-4: Cell voltage ageing under operation at 1.5A/cm², 800°C, 50/50 H_2/H_2O fuel electrode gas composition and air at the fuel electrode under a) constant electrolysis (cell A) and b) cyclic (cell B) modes

From cell voltage values at start and end of the ageing phases (i.e. phase II) in Figure 5.2-4, and the total duration of this phase, overall ageing rates can be determined. SOEC operation of cell A under a high constant current density of - 1.5 A/cm² results in an overall ageing of + 114.2 mV/kh. Cell B cycled at ± 1.5 A/cm² shows a much lower ageing rate of + 32.8 mV/kh from the cell voltages in SOEC mode and - 30.4 mV/kh from those in SOFC modes.

A zoom-in[xxiv] of the voltage courses reveals that all cells are ageing in two stages—a high initial ageing rate followed by a relaxation to a much lower ageing rate. Cell A for instance ages at + 153 mV/kh in the first 500 hours of phase II and relaxes to + 75.5 mV/kh for the remaining 500 hours. In a similar manner Cell B initially ageing at + 49.6-(SOEC mode) and – 56.8 mV/kh (SOFC mode) in the first 348 hours relaxes to its final ageing rates of + 25.7- (SOEC mode) and – 19.5 mV (SOFC mode) for the rest of the test. The ageing rates are summarized in Table 5.2-1 and based on the investigated time window the following observations can be made:

i. SOEC operation of Cell A at – 1.5 A/cm² leads to three times as much overall voltage ageing as that of Cell B cycled between SOFC and SOEC at the same current density under similar conditions
ii. Irrespective of operation mode, the final ageing rates are at most half of the initial ageing rates
iii. In cyclic operation, the initial voltage ageing in SOFC mode is at least equal to that in SOEC mode. The situation is however reversed on the long-term whereby the final ageing and overall SOEC mode ageing becomes greater than SOFC mode ageing.

[xxiv] Not shown

Table 5.2-1: Voltage ageing of cells A and B with t = 0 representing start of phase II

Cell	Rate of Voltage Change [mV/kh]					
	Initial		Final		Overall	
A	+ 153 (t = 0 – 562 h)		+ 75.5 (t = 562 – 1136 h)		+ 114.2 (t = 0 – 1136 h)	
B	SOEC	SOFC	SOEC	SOFC	SOEC	SOFC
	+ 49.6	- 56.8	+ 25.7	- 19.5	+ 32.8	- 30.4
	(t = 0 – 348 h)		(t = 348 – 1176 h)		(t = 0 – 1176 h)	

The initial and final voltage ageing rates of + 153 mV/kh and + 75 mV/kh for cell A are however very low if compared with the values obtained at 850°C under similar conditions of fuel and current density by Knibbe *et al*.[110] whereby their cell aged with + 1140 mV/kh and + 330 mV/kh in the initial and later phases respectively. Using a similar cell as Knibbe[110], however investigated at 800 °C and – 1 A/cm^2 in a 10/90 H_2/H_2O fuel Graves *et al*.[152] reported a cell voltage change from 1.33 V to 1.74 V in 420 h (corresponding to 976 mV/kh). Sun et al.[155] operated a similar 4 x 4 cell like Knibbe and Graves, however with an LSCF oxygen electrode, at 800 °C and - 1 A/cm^2 and also reported a high initial ageing of 700 mV/kh relaxing to 25 mV/kh from 1100 h onward. The overall ageing after 4500 h of operation was 53 mV/kh. Sun *et al*.[134] in H_2O/CO_2 co-electrolysis at 800°C obtained + 820 mV/kh for - 1.5 A/cm² and + 240 mV/kh for operation at -1 A/cm². Since both authors used cells with LSM/YSZ air electrode the difference in both cases can on the one hand be attributed to the higher performance of LSCF compared to LSM/YSZ air electrode[156] as well as operating temperature and fuel electrode gas composition and reactant utilization. The final ageing of + 75 mV/kh of cell A emphasizes the impact of current density[157] when compared with the + 40 mV/kh reported by Schefold *et al*.[8,132] investigating a cell with similar component materials at – 1 A/cm², 800°C and 80 % absolute humidity for 9 kh. Schefold et al.[9,158] have reported an even smaller ageing rate of 8 mV/kh for a 6Sc1CeSZ electrolyte supported cell with NiO/GDC fuel electrode and LSCF oxygen electrode operated with – 0.9 A/cm^2 at 847 °C in an 11 kh test.

In their reversible operation test, Graves et *al*.[152] demonstrated that cycling not only prevented the degradation observed during constant electrolysis operation, but have reversed or repaired the deterioration. They reported negligible degradation during reversible cycling. The cycles comprised -1 A/cm^2 for 1 h in a 10/90 H_2/H_2O fuel and + 0.5 A/cm^2 for 5 h in a 50/50 H_2/H_2O fuel in SOEC and SOFC modes respectively[xxv]. A similar *in-situ cell repair* technique[153] has been termed *reverse current treatment* (RCT) and used to improve the performance by creating a nano-scaled layer of the fuel electrode close to the electrolyte[159]. It has to be pointed out that in the RCT, the cathodic polarizations were done at 700 °C in an H_2 fuel with 5.5 % H_2O and - 2 A/cm^2 pulses of 10 seconds. For

[xxv] The length of the electrolysis mode period was increased in further testing

cells with LSM/YSZ oxygen electrode the cycling has gone to improve the performance by improving the microstructure at the oxygen electrode / electrolyte interface[152,153]

Tang et al.[151] reported reversible operation of SOCs at 750 °C with – 0.5 A/cm² SOEC and + 0.25 A/cm² SOFC mode cycles. Their cycles were much longer with daily cycles of 10.5 h of SOEC and 12.5 h of SOFC. The fuel in SOEC mode was 50/50 H_2/H_2O and in SOFC mode the fuel was composed of nearly dry H_2. They reported a small voltage ageing in SOFC mode of – 94 mV in 14,500 h corresponding to – 6.5 mV/kh and in another test of less than 4000 h they reported – 8.5 mV/kh of SOFC mode ageing. SOEC mode ageing was not reported. For a two cell stack operated in a 50 % humidified H_2 under constant electrolysis operation at – 0.5 A/cm² and 50 % steam conversion rate Fang *et al.*[130] reported a voltage ageing of 0.7 %/kh after 2300 h of operation at 800 °C and a higher ageing rate of 1.9 %/kh in the following 1800 h of operation at 700 °C. Using a similar two-cell stack operated under different conditions of current density and fuel during different segments of a 4000 h test Nguyen et al.[139] reported an increase in voltage ageing at higher electrolysis current densities as well as a higher ageing in co-electrolysis operation against steam electrolysis.

5.2.2.2 Cell Performance and Power Density

A commonly used parameter to assess the performance of SOCs is the power density at a given operating point. This information can be obtained from current / voltage (C/V) characteristics recorded under according operation conditions. In Figure 5.2-5 a and b, C/V-curves recorded during the characterization intervals of cells A and B respectively are displayed.

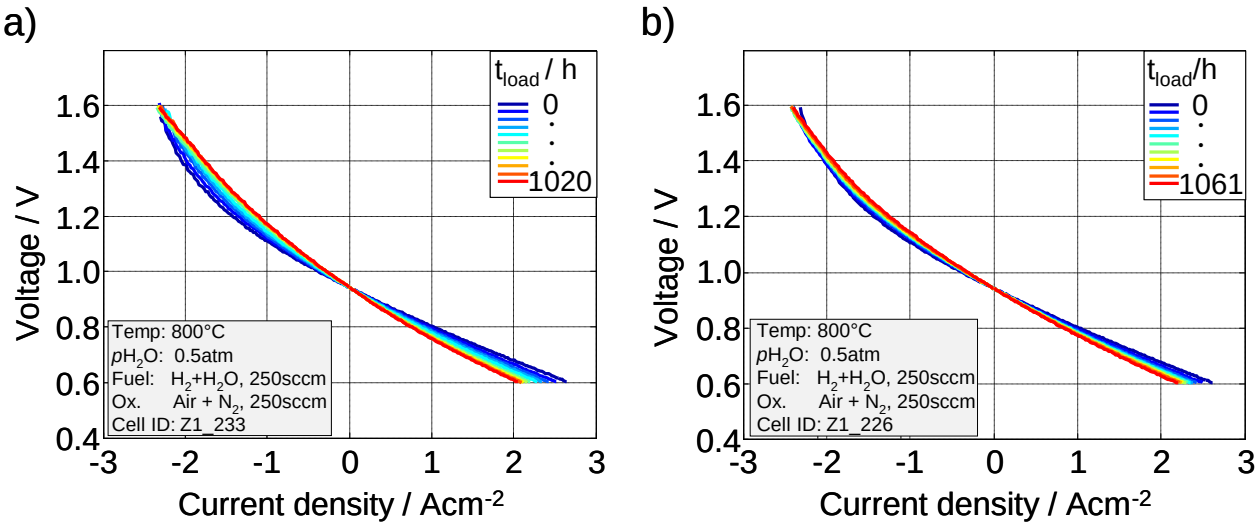

Figure 5.2-5: Current – voltage characteristics recorded in the characterization intervals for cell A operated in SOEC mode (b): Corresponding C/V curves for cell B operated in cyclic mode

The power density at a conventional comparison cell voltage of 0.7 V was determined from C/V curves in Figure 5.2-5 and plotted against time in Figure 5.2-6a for cells A and B. The figure reveals a high performance of the investigated cells with initial power densities of 1.28 W/cm² for cell A and 1.26 W/cm² for cell B. From Figure 5.2-6a the two-step ageing trend of both cells can be seen. After 1000 hours of operation, the power densities of the cells have dropped by 25- and 17.5 mW/cm² for cells A and B respectively.

The power densities at the operating point of + 1.5 A/cm² for cells A and B have been accessed from the C/V-curves as well and displayed in Figure 5.2-6b. These values and their evolution with operation time provide the more relevant degradation rates for the investigated operation point. Again both cells show a high initial power density of approximately 1.11 W/cm² at + 1.5A/cm² for cell A and B. In this representation, the cells show slightly better durabilities with 1.02 Wcm^{-2} and 1.05 W/cm² for cells A and B respectively after 1000 h. This comparison shows that the operating point in the C/V-characteristic employed to quantify degradation has a significant impact on the obtained ageing rate[160]. An extreme case of this would be to determine the ageing in SOEC mode based on the power supplied to drive a current density of ca. - 2.2 A/cm². From the corresponding voltage values in the C/V curves in Figure 5.2-5a and b no ageing or even improvement over time would be demonstrated in the investigated time. This is because the analysis would be at an operation point on the C/V-curve where-in the dominant loss mechanism (gas diffusion in the substrate in this case) is actually improving with time. It can equally be speculated that the ageing of the electrolyte with time results in effective more joule heating at – 2.2 A/cm² with time. Electrolysis at – 2.2 A/cm² is occurring at increasingly higher temperature over time and it has been shown that the electrolysis voltage is lower at higher temperatures[42].

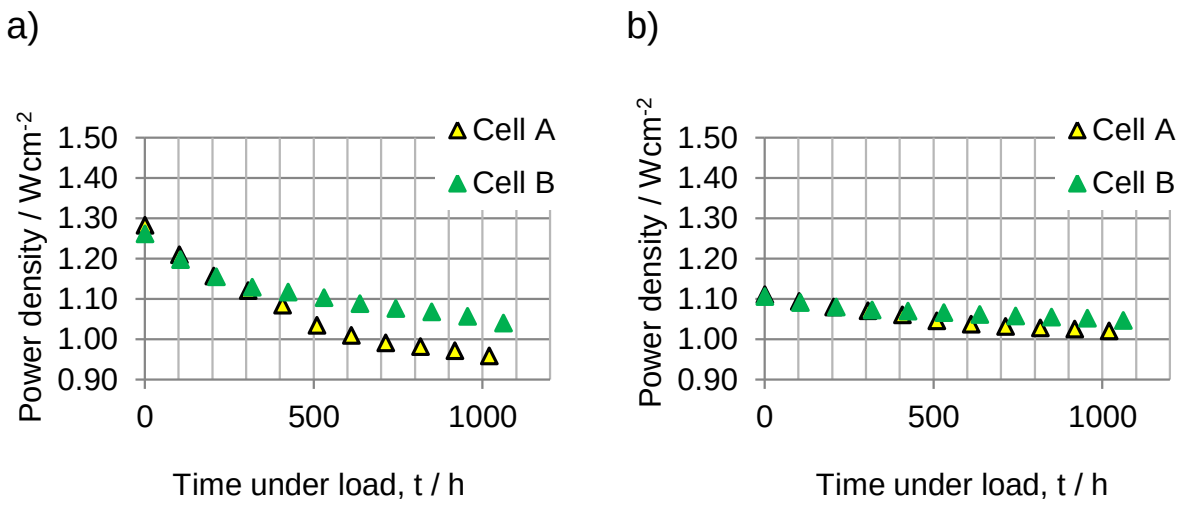

Figure 5.2-6: Power densities of cells A and B from C/V- curves recorded during characterization intervals at 800°C, 50/50 H_2/H_2O fuel electrode gas composition and air at air electrode at (a) at 0.7 V and (b) +1.5A cm^{-2}

5.2.2.3 Qualitative analysis of Impedance Spectra

Whereas the cell voltage or power evolution give information about the overall cell ageing, impedance spectra and the thereof calculated DRTs can offer more information about the ageing trends of specific regions of the cell such as electrolyte, electrodes or substrate.

The impedance spectra recorded every 100 h during the characterization intervals in H_2/H_2O fuel electrode gas mixture are shown in Figure 5.2-7a (i) and (ii) for cells A and B respectively. The corresponding DRTs are displayed in Figure 5.2-7b (i) and (ii) respectively.

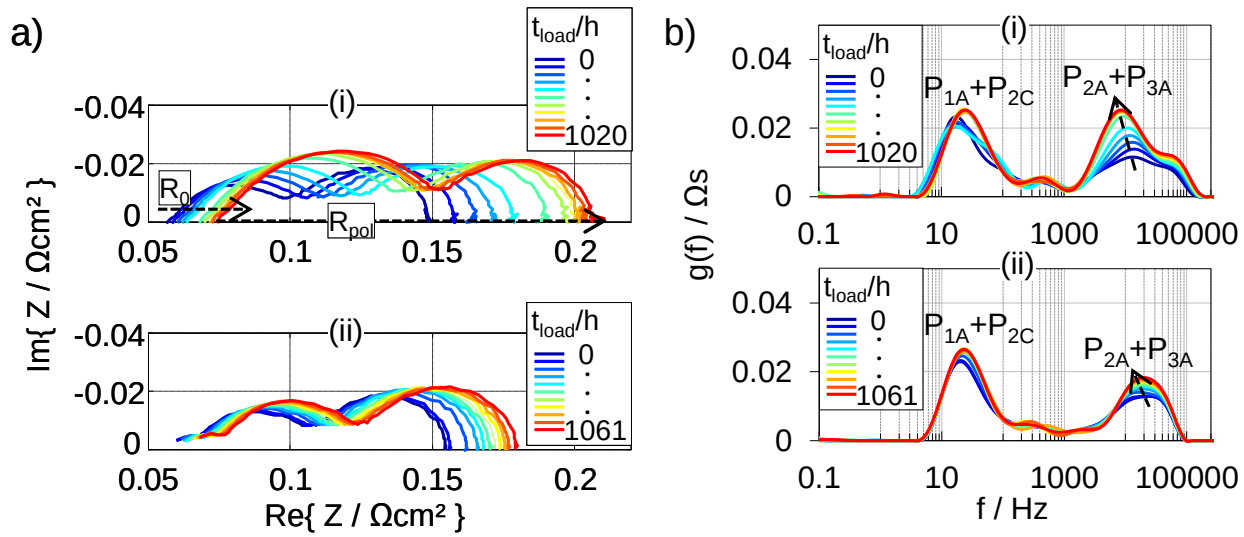

Figure 5.2-7: (a-i) Electrochemical impedance spectra (EIS) recorded at 800 °C in a 50/50 H_2/H_2O fuel in the characterization intervals for cell A operated in SOEC mode and (ii) cell B operated in cyclic mode. (b) Corresponding DRTs calculated from the EIS spectra of both cells

Qualitative analysis of the spectra in Figure 5.2-7a reveal greater ageing of the ohmic resistance R_0 as well as total polarization resistance R_{pol} of cell A. Analysis of the DRTs in Figure 5.2-7b reveal severe ageing of the fuel electrode electrochemistry ($P_{2A}+P_{3A}$) for cell A that underwent constant electrolysis when compared to cell B that was operated in cyclic mode. A minor ageing of either fuel electrode gas diffusion process P_{1A} and or air electrode electrochemistry P_{2C} can also be observed at ca. 50 Hz for both cells.

To resolve the ageing contributions of the two processes P_{1A} and P_{2C} that overlap at ca. 50 Hz impedance spectra recorded in a 50/50 CO/CO_2 fuel electrode gas mixture are analyzed in Figure 5.2-8 for both cells[87,98]. Whereas the impedance spectra in Figure 5.2-8a display comparable trends to those in Figure 5.2-7a the DRTs in Figure

5.2-8b (i) and (ii) reveal *ageing* of the air electrode electrochemistry P_{2C} for both cells and an *improving* gas diffusion in the substrate P_{1A} for both cells as well. This observation stresses the gains of recording spectra in CO/CO_2 fuel for cells whose diffusion peaks overlap with the oxygen electrode ASR peak.

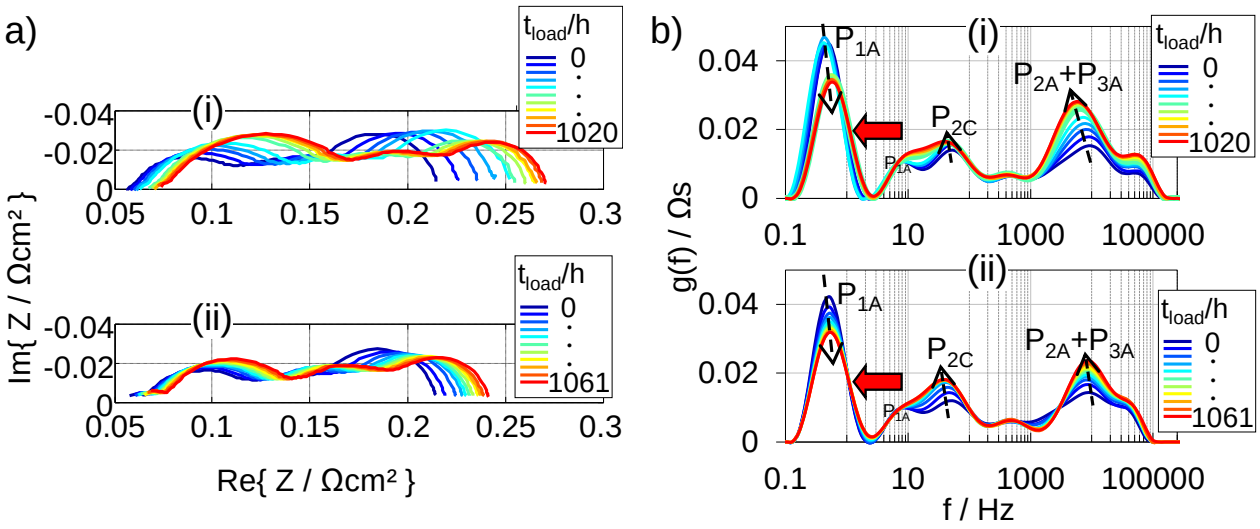

Figure 5.2-8: (a-i) Electrochemical impedance spectra (EIS) recorded at 800°C in a 50/50 CO/CO_2 fuel in the characterization intervals for cell A operated in SOEC mode and (ii) cell B operated in cyclic mode. (b) Corresponding DRTs calculated from the EIS spectra of both cells

5.2.2.4 Data Quality and KK-Residuals

Before proceeding with CNLS fit of the recorded impedance spectra, the quality of the data has to be checked. A widely accepted check is to verify the compliance of the data with Kramers Kronig transformation. This was done for cells A and B with the "KK test for Windows" software[19,20] and displayed in Figure 5.2-9a and b respectively.

The greater part of the real and imaginary part residuals of all spectra lie well below 1 % error margin for both cells. These are residuals of spectra in H_2/H_2O fuel electrode gas atmosphere for first (t = 0 h) and last characterizations (t > 1000 h) of phase II. The higher imaginary part error of cell B (cf. Figure 5.2-9b) at ca. 3.5 kHz is a measuring equipment artifact which does not considerably affect the CNLS fits.

With such low error values, the recorded spectra could further be analyzed through CNLS fit with the ECM presented in Figure 5.2-3 to obtain the area specific resistances and the corresponding ageing trends of the individual polarization mechanisms or cell components. These fits were done using the commercially available software ZView®

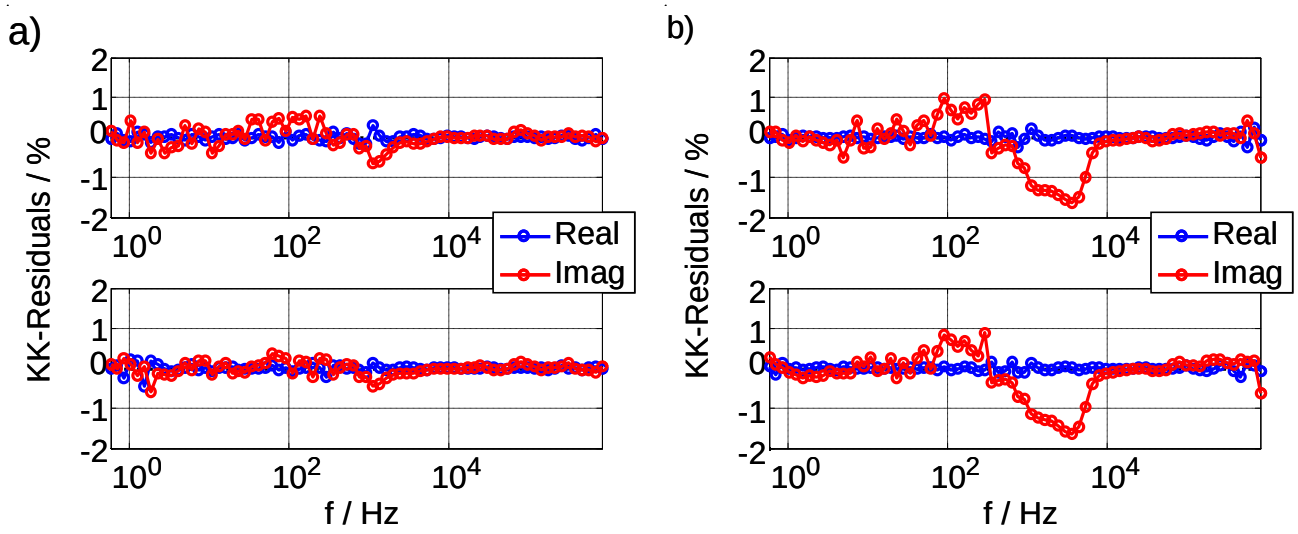

Figure 5.2-9: Kramers Kronig residuals of impedance spectra recorded in a 50/50 H_2/H_2O fuel electrode gas composition for the first and last characterizations for cell A (a) and cell B (b).

5.2.2.5 Quantitative Analysis and Ageing Trends of Individual Cell Compartments

In Figure 5.2-10 the evolution of the area specific resistances of cells A and B are displayed[xxvi] for (i) ohmic (electrolyte) resistance R_0 (ii) fuel electrode electrochemistry $R_{2A}+R_{3A}$ (iii) fuel electrode substrate gas diffusion R_{1A} and (iv) air electrode electrochemistry R_{2C}.

From Figure 5.2-10 and based on values from ca. 200 h (phase II, cf. Figure 5.2-4) the individual ASR ageing rates were determined and summarized in Table 5.2-2.

[xxvi] An error in the off-gas treatment system of the test rig during test of cell A led to a gradual temperature (and pressure) increase in the first 400 h hours attaining a maximum temperature increase of 5 °C (cf. Figure 5.2-4a). A sudden drop in temperature after ca. 400 h is seen in Figure 5.2-4a after problem is solved The impact of this temperature deviation on the ASR values was taken into account. The ASR values of Cell A displayed in Figure 5.2-10 (i) – (iii) were corrected using the temperature dependencies of the individual loss mechanisms[3] and conductivities[186]. This correction works quite well for the thermally activated processes. However in the case of R_{1A}, which shows no significant temperature dependency[40] but a strong pressure dependency a step can still be seen in Figure 5.2-10 (iii). The detection of this step in the diffusion process further stresses the high degree of accuracy of the CNLS fits when the rather small absolute value of the diffusion ASR is considered.

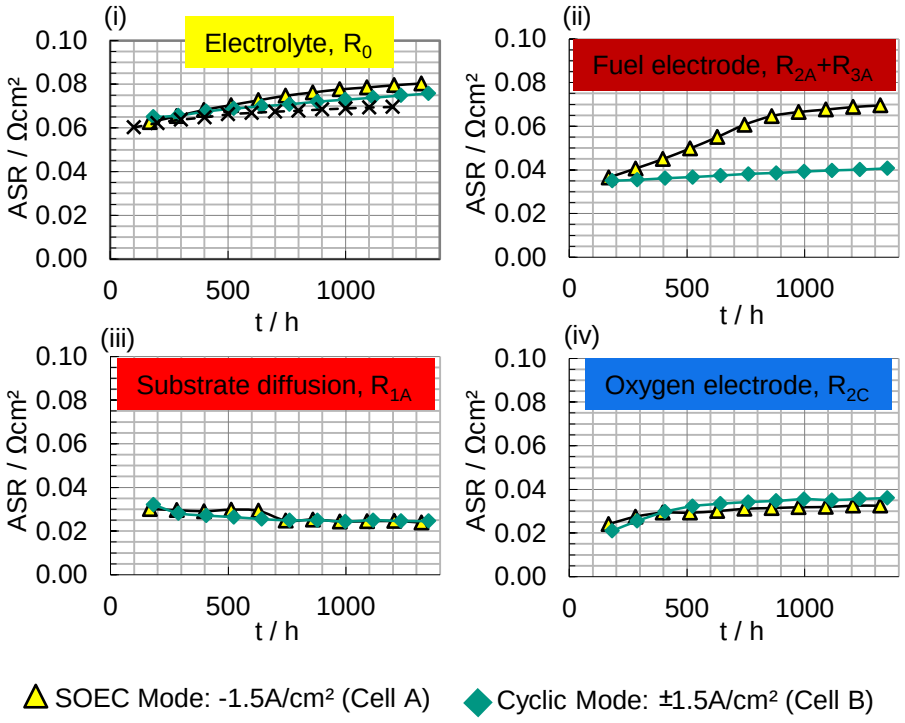

Figure 5.2-10: Evolution of the area specific resistances of cells A and B for (i) Ohmic (electrolyte) resistance R_0, (ii) fuel electrode electrochemistry R_{2A}+R_{3A}, (iii) Fuel electrode substrate gas diffusion R_{1A} and (iv) air electrode electrochemistry R_{2C}. For comparison the "x" data in subplot (i) from references [160,161] has been included.

Table 5.2-2: Ageing rates of individual ASRs for cells A and B in mΩ/kh. For cell A the time intervals corresponding to *Initial* and *Final* are t = 0 – 562 h and t = 562 – 1336 h respectively. For Cell B *Initial* and *Final* correspond to time intervals t = 0 – 348 h and t = 348 – 1176 h respectively

Process→ / Cell↓	R_0 (Electrolyte) [mΩ/kh]		R_{2A}+ R_{3A} (Fuel electrode) [mΩ/kh]		R_{2C} (Oxygen electrode) [mΩ/kh]		R_{1A} (Substrate diffusion) [mΩ/kh]	
	Initial	Final	Initial	Final	Initial	Final	Initial	Final
A (- 1.5 A/cm²)	23.7	10.9	43.7	11.7	25.5	4.4	-1.5	-1.8
B (± 1.5 A/cm²)	10.2	10.2	5.6	5.6	35.9	4.5	-14.2	-0.5

For Cell A operated under constant electrolysis mode at – 1.5 A/cm^2 Table 5.2-2 reveals that the fuel electrode dominates cell ageing within the initial phase of operation with 43.7 mΩ/kh. This is followed by the oxygen electrode and the electrolyte with 25.5- and 23.7 mΩ/kh respectively. For Cell B operated in cyclic mode with $\pm$ 1.5 A/cm^2 the oxygen electrode ages the most in the initial phase with 35.9 mΩ/kh. This is followed by the electrolyte, ageing half as much with 10.2 mΩ/kh. The air electrodes of both cells show a characteristic nonlinear ageing trend, with higher initial rates 25.5- and 35.9 mΩ/kh followed by a relaxation to much lower values of 4.48 and 4.5 mΩ/kh for Cell A and B respectively. This nonlinear ageing trend was also observed at 750 °C under OCV operation[154] and shown to be reversible and decreasing with increasing temperature. The authors[89,161] acknowledged an impact of strontium depletion from the LSCF but attributed the major course of ageing to the ageing of the solid state oxygen ion diffusion (bulk diffusion coefficient D^{δ})—a finding further confirmed by Endler et al.[92]. As such they postulated a phase change from the rhomboidal structure at room temperature[87]. Endler-Schuck et al.[154] reported initial and final ageing rates of 0.72 %/h and 0.033 %/h respectively at OCV and 750 °C. For comparison, cells A and B had initial ageing rates of 0.11- and 0.17 %/h respectively and both relaxed to the same final ageing rate of 0.015 %/h at 800 °C respectively, —the lower ageing rates are consistent with Endler-Schuck´s finding that the ageing decreases with increasing temperature. The slightly greater initial ageing of this electrode in cyclic mode at ± 1.5 A/cm² suggests that electrical and thermal stresses accompanying cycling may enhance strontium depletion or that the effective greater SOFC operation of cell B causes more ageing of the air electrode. However the comparable final ageing rate suggest a saturation[154] of the ageing process after the initial phase or an independence of the oxygen ageing on load type (constant SOEC or cyclic) after the initial phase.

Gas diffusion in the fuel electrode substrate is improving with operation time for all cells. The activation rates show no clear operation mode dependency and lie below – 2 mΩ/kh. The improving gas diffusion ASR, R1A is attributed to decreasing tortuosity resulting from the agglomeration of the Ni particles[110,154,162] at high temperatures and high pH_2O as well as Ni loss in volatile form as $Ni(OH)_2(g)$[14,163–165].

The electrolyte ASR R_0, of both cells portrays a nonlinear ageing trend with higher initial values and lower final rates. Although both cells end up with almost the same final ageing rates of 10 mΩ/kh, the initial ageing rate of Cell A operated under constant electrolysis is with 23.7 mΩ/kh double that of Cell B operated in cyclic mode and ageing at 10.2 mΩ/kh. According to Knibbe et al.[110] the large ohmic resistance ageing observed in long-term SOEC mode operation, which is not present when the cell is operated in SOFC mode under similar conditions[166], could be a result of one or more of the following mechanisms:

i. Delamination at the electrode/electrolyte interface
ii. Degradation of electrical conductivity in the electrode (or electrode structure near the electrolyte)
iii. Reduced contact between current collector and electrode structures
iv. Kinetic demixing[xxvii]
v. Internal fracture or porosity formation

[xxvii] electric field-induced diffusion of the cation sublattice leading to appreciable inhomogeneities[110]

For their Ni/YSZ-YSZ-LSM/YSZ cell system, operated at 850 °C and current densities between - 1 A/cm^2 and - 2 A/cm^2 in a 50/50 H_2/H_2O fuel, with *oxygen* supplied to the oxygen electrode Knibbe et al[110] attributed the large ageing of the ohmic resistance to porosity formation at the electrolyte/oxygen electrode interface. The porosity being a result of oxygen release in the YSZ grain boundaries close to the oxygen electrode—this in turn a consequence of the large polarization drop across the oxygen electrode. Two major differences of the here reported tests to Knibbe´s tests are:

i. The LSCF oxygen electrode of cells A and B has a much lower ASR compared to the LSM/YSZ oxygen electrode employed by Knibbe. The implications are that in cells A and B the voltage drop across the Ni/YSZ fuel electrode is much larger than at the oxygen electrode—a situation opposite to that in Knibbe´s tests.
ii. Also, the oxygen electrodes in this work are supplied with air instead of pure oxygen. This means that in the herein reported tests and especially for Cell A the oxygen partial pressure at the oxygen electrode is just 0.21 atm against 1 atm in Knibbe´s tests.

Based on the above two points and the fact that the LSCF electrode has a much smaller ASR than the Ni/YSZ fuel electrode[xxviii] it can be expected that in the herein investigated cells the larger voltage drop would be at the fuel electrodes and not the oxygen electrodes. As such it can be expected that the ageing mechanism in the tests reported herein would be different to that in reference [[110]]. Brisse *et al*.[9,158] investigating electrolysis on an electrolyte supported cell at 847 °C and – 0.9 A/cm^2 observed that the 130 µm thick scandia/ceria doped zirconia (6Sc1CeSZ) electrolyte with a larger ASR (and thus larger voltage drop) than the nickel oxide/gadolina doped ceria (NiO/GDC) fuel and LSCF oxygen electrodes accounted for the overall cell ageing whilst recording no indications for electrode ageing. Investigating electrolysis at a high current density of - 1 A/cm^2 at 800 °C, however on a cell with LSC/CGO oxygen electrode (with an even smaller ASR than LSCF, cf. section 3.5.2.2), Hjalmarsson *et al*.[129] also reported negligible ageing of the oxygen electrode and showed depletion of Sr and Co of the oxygen electrode as a result of electrolysis.

The fuel electrode electrochemistry, R_{2A}+R_{3A} ages severely with 47.3 mΩ/kh in the first 600 h of constant electrolysis operation at - 1.5 A/cm² before relaxing to a much lower value final value of 11.7 mΩ/kh. In cyclic mode the fuel electrode displays a small ageing rate of 5.6 mΩ/kh in both initial and final phases.

In this work the higher ageing of the fuel electrode as well as the electrolyte (closest to the fuel electrode) in SOEC operation is attributed to breakdown or reduction of ionic conductivity of the 8YSZ matrix. As reported in literature[70,167,168] it is believed that the enhanced reducing conditions during constant SOEC operation[xxix] lead to the reduction of Ni cations that diffused into the 8YSZ matrix during sintering of electrolyte and fuel electrode under oxidizing conditions at high temperatures (> 1400 °C). The reduced Ni precipitates would on the one hand

[xxviii] Cf. Initial ASR values of both electrodes in Figure 5.2-10

[xxix] These very reducing conditions at the fuel electrode during SOEC mode operation at high current densities in co-electrolysis of CO_2 and H_2O have led to formation of carbon fibers at the fuel electrode [157,187]

cause larger lattice distances enhancing Y and Zr cation mobilities as well as precipitation of the less oxygen ion (O^{2-})- conducting tetragonal YSZ[169]. On the other hand, the Ni precipitates are squeezed out at the grain boundaries. All these lead to decreased ionic conductivity. SOEC operation-enhanced cation mobilities at the electrolyte/CGO boundary could also lead to growth of the less conducting[xxx] $SrZrO_3$-containing interdiffusion layer[132,160,161,170] with relaxation frequency at ca. 10 kHz increasing R_0. Voids in the electrolyte around the electrolyte / air electrode region due to high pO_2 have also been reported to increase R_0 ageing in long-term SOEC operation at high current density[8,14,110,120,122,152]. Meanwhile The et al.[170] comparing the microstructural changes in two cells operated under constant electrolysis at – 0.75 A/cm^2 for 6100 h and - 1 A/cm^2 for 9000 h have accounted for the greater ageing of the cell operated under - 1 A/cm^2 for 9000 h suggesting that Ni is lost from the fuel electrode functional layer and subsequently deposited at the fuel electrode further away from the electrolyte, thereby effectively increasing the thickness of the electrolyte and decreasing TPB. An "increasing" electrolyte will be subject to "increasing" voltage drop across it and enhance any electrolyte-related loss mechanism. Pore formation in the fuel electrode was attributed to kinetic demixing of the electrolyte followed by yttrium migration to the fuel electrode due to electric potential[170].

A similar cell operated in SOFC mode at a current density of + 0.3 A/cm² [160,161] (cf. Figure 5.2-10(i)) also shows a similar ageing trend with a final ageing of 3.1 mΩ/kh from 500 h onwards. This suggest that R_0 ageing is in the order SOFC < cyclic < SOEC. Also the final ageing rates of the R_0 of cells A and B are a factor three greater than the R_0 ageing of 3.4 mΩ/kh at 750°C under OCV conditions in the period after the first 200 h of operation in literature[154].

5.2.3 SEM Analysis

Post-test scanning electron microscopy (SEM) analyses were carried out on the investigated cells. In addition, TEM analysis was performed on cell A, operated under a high electrolyzer current density of – 1.5 A/cm².

5.2.3.1 Fracture Behavior

Figure 5.2-11 shows SEM micrographs of cross sections of cells A and B, revealing a significantly different fracture behavior of the electrolyte. Whereas cell A displays chunky fractures along grain boundaries (intergranular) as well as through grains (intragranular), cell B predominantly shows intragranular fractures. Though no further mechanical stability investigations were carried out, these results undoubtedly suggest that SOEC operation at high current densities may lead to decreased mechanical stability of the electrolyte, specifically along the grain boundaries. Furthermore, the SOEC operated by Schefold *et al*.[8] and Tietz *et al*.[132] at – 1 A/cm^2 exhibited after

[xxx] Oxide ion conductivity of ca. $2 \cdot 10^{-6}$ S/cm at 800 °C which is ca. four times less than that of YSZ[170]

9000 h of operation a predominately intergranular fracture behavior of the electrolyte, whereby an impact of operation under steam or feed gas failure cannot be ruled out. However, this cell also exhibited heavy morphological changes of the grain boundaries within the electrolyte, presumably due to the aforementioned critical testing conditions.

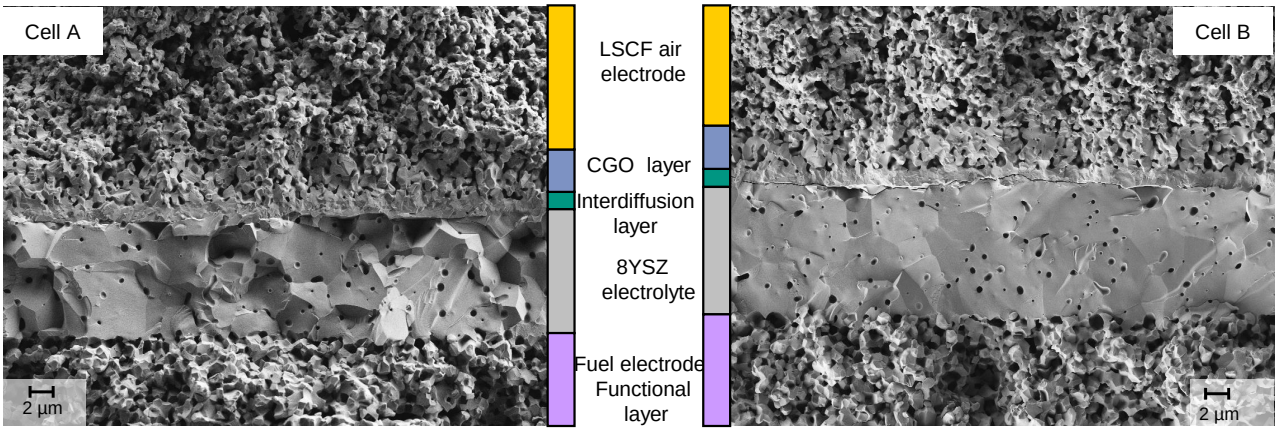

Figure 5.2-11: SEM images of cross sections of both cells revealing different fracture behavior of their electrolytes. Cell A exhibits both an intergranular and an intragranular fracture behavior, whereas cell B predominantly shows an intergranular fracture behavior.

The delamination of the electrolyte of Cell B at the interface with the interdiffusion layer Figure 5.2-11 most likely results from sample preparation. However the breakage at that interface suggests that the electrical and temperature stresses accompanying cyclic operation reduce the mechanical stability of the interface between the electrolyte and the interdiffusion zone. Contrary to literature[8,110,120,132] no porosity was observed in this region in either of the cells despite the high current densities.

5.2.3.1 Nano-scaled Precipitates at the 8YSZ Electrolyte Grain Boundaries

At the interface between the electrolyte and the fuel electrode functional layer, Cell A displayed nano-scaled precipitates at the 8YSZ electrolyte grain boundaries. The nano-scaled particles marked by arrows in Figure 5.2-12 (I) are presumably Ni particles that precipitate at the grain boundaries of the 8YSZ electrolyte near the fuel electrode functional layer, which result from the reduction of NiO that originally interdiffused into the 8YSZ during co-firing of the NiO/8YSZ fuel electrode and the 8YSZ electrolyte under oxidizing atmosphere[70,167].

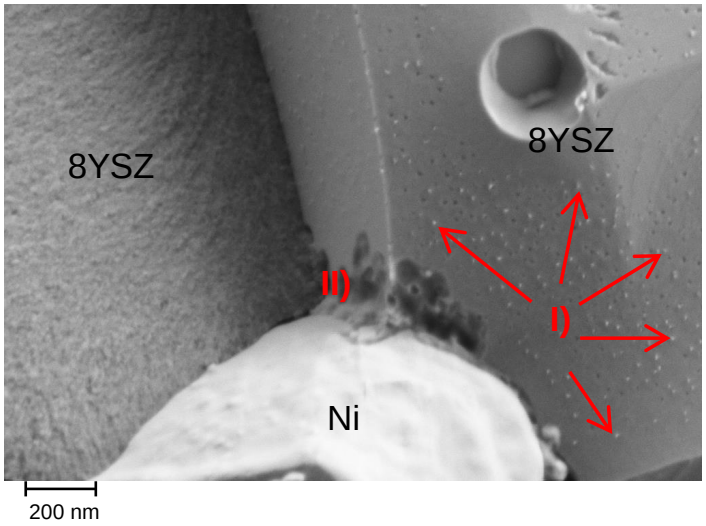

Figure 5.2-12: SEM image of cell A displaying Ni precipitates at the grain boundaries of the 8YSZ electrolyte close to the fuel electrode

These Ni precipitates can also be seen in Figure 5.2-13 next to nanoscaled voids at the grain boundary, which are assumed to be the negative imprint of the Ni precipitates. Therefore, they have to be distinguished from the pores at electrolyte grain boundaries reported in literature[8,110,120,132].

5.2.3.1 Nano-scaled Structural Changes at the Ni/YSZ-interface

At the fuel electrode in the electrode/electrolyte vicinity, another peculiarity of however rare occurrence is a bubble structure at the Ni/YSZ interface, as shown in Figure 5.2-13 and denoted (II). The negative or imprint is also labeled with (II) in Figure 5.2-12. It presumably consists of a secondary phase; however detailed TEM investigations will be necessary to clarify its origin. Due to the rare occurrence of the phase and the location underneath a nickel grain, the influence on the fuel electrode electrochemistry can be assumed to be negligible.

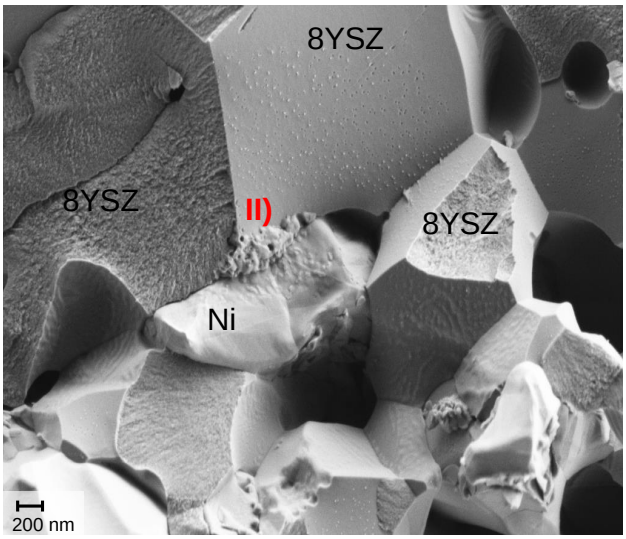

Figure 5.2-13: SEM image of Cell A displaying nano-scaled structural change at the Ni/YSZ-electrolyte interface.

5.2.3.2 Secondary Phase Formation on the Ni Surface at the Three Phase Boundary

The major peculiarity at the fuel electrode close to the electrolyte is the occurrence of a secondary phase on the surface of the Ni grains at the three phase boundary with the electrolyte (cf. Figure 5.2-14) labeled (III). Not every grain is affected, but it can be found frequently throughout the electrode. As it is difficult to obtain detailed information on the chemical composition of such small particles by means of energy dispersive spectroscopy (EDX)-analysis in a SEM, TEM investigations were performed on a focused ion beam prepared TEM-lamella (cf. Figure 5.2-15a). EDX analysis was carried out on two spots of the lamella, marked by red arrows in Figure 5.2-15a. The EDX spectrum displayed in Figure 5.2-15b (i) suggests that the phase contains the elements Ni, Zr, Y and O. In the nickel grain however (cf. Figure 5.2-15b (ii)) no other elements (e.g. Zr) were detected.

This clearly shows that the phase contains no foreign elements (e.g. Si)[171] and it seems to be a result of the operation of the cell in electrolyzer mode. (The copper peaks in both spectra in Figure 5.2-15b result from the TEM sample holder and are therefore not related to the secondary phase.) The detailed composition and the crystalline structure of the secondary phase had not been identified at the time of documenting this thesis. However, based on the fuel electrode electrochemistry trends from EIS analysis their impact on the observed ageing can at this juncture only be assumed to be negative.

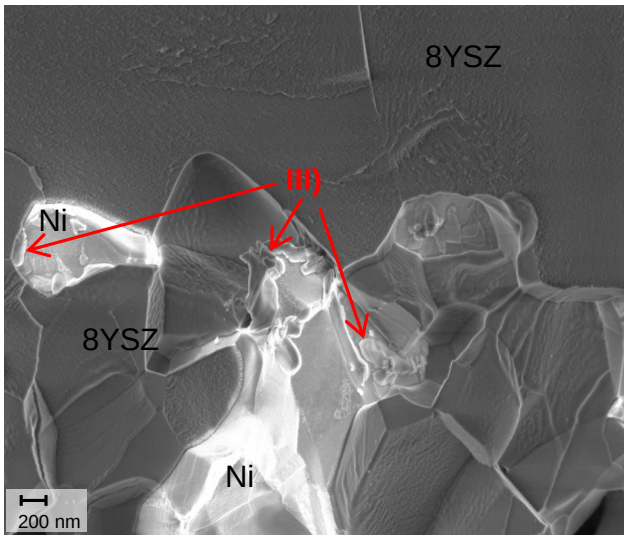

Figure 5.2-14: SEM image of Cell A displaying secondary phase formation on the Ni surface at the tripple phase boundary of the fuel electrode functional layer

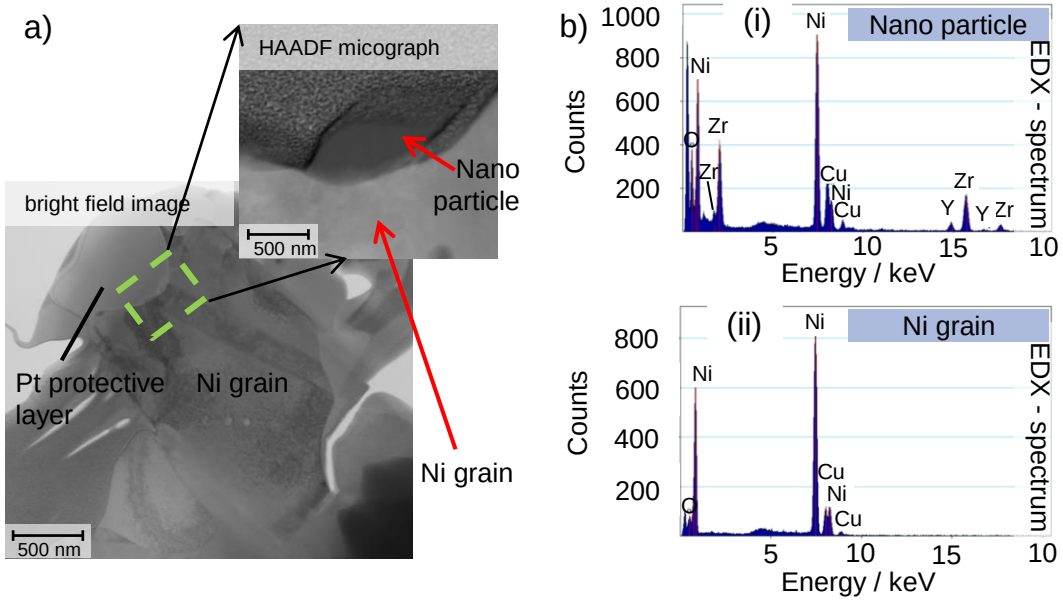

Figure 5.2-15:(a) TEM bright field and HAADF[xxxi] images of a FIB lamella of the fuel electrode functional layer of cell A including a secondary phase covered nickel grain. (b) EDX spectra of (i) the secondary phase on the Ni surface and (ii) of the Ni grain underneath

Chen et al[157] in their durability tests < 1300 h investigating co-electrolysis of CO_2 and H_2O at high current densities of -1.5 A/cm^2 at 800 °C and - 1 A/cm^2 at 850°C identified the formation of similar nanoparticles covering most of

[xxxi] high-angle annular dark field

the Ni grains closest to the electrolyte as an ageing mechanism. The coverage was more for the test at 850 °C and also decreased from cell inlet through cell center towards cell outlet. The Ni particles further away from the interface or in the substrate did not contain the nanoparticles. Through SEM and TEM as well as thermodynamic calculations, they could show that the nanoparticles were ZrO_2 nanoparticles that compromised the percolation of Ni-Ni, Ni-YSZ interfaces and presumably reduced active TPB sites. These nanoparticles were also present in the fuel electrode of the 9000 h SOEC test reported by Tietz *et al*.[8,132]

5.2.4 Overpotential Considerations

Although there are no doubts that constant electrolysis at higher current densities leads to greater overall cell ageing[110,134,157] it is not always readily resolvable if the observed rates are a consequence of high associated overpotential or the high current density itself. Further, the overpotential at the oxygen or fuel electrodes is hardly experimentally resolved during evaluation of SOEC ageing in literature. It has been shown for instance, that high overpotentials and not necessarily high current densities cause irreversible long-term sulfur poisoning-related ageing of the fuel electrode in SOFC mode operation[172]. Further, the formation of ZrO_2 nanoparticles during SOEC mode operation of SOCs in co-electrolysis of CO_2 and H_2O has been shown to be related to the high overpotentials at the interface fuel electrode/electrolyte[142]. In fact Knibbe et al.[110] discarded the major influence of current density on the ageing of the fuel electrode during high current density constant SOEC operation but rather attributed the ageing to impurities[110].

It is trivial to read off the initial cell voltage under load in either SOEC modes (e.g. 1219 mV for Cells A and B cf. Figure 5.2-4) or SOFC mode (e.g. 736.8 mV for Cell B, cf. Figure 5.2-4). The OCV can then be deducted from the SOEC voltage or the SOFC voltage deducted from the OCV to obtain the total overpotential under load. However, the distribution of this overpotential across the cell is hardly resolved in literature. Of course models have been proposed explaining the theoretically expected distribution of electrical, chemical and electrochemical potentials across the electrolyte and electrodes for both modes[173,174] or distribution of oxygen activity gradients during SOFC, OCV or SOEC operation modes[14,175]. Through thermodynamic calculations, the different local potentials can be calculated and ageing mechanisms theorized.

The overpotential distribution of the total electrical overpotential would however give an idea of the overpotential *stress* to which the different components are subjected during constant galvanostatic operation or the overpotential *stress* window in which compartments switch during cyclic mode operation. In Figure 5.2-16a and b, the evolution and distribution of the overpotentials under current load has been resolved for the same cell type as Cell A and Cell B for SOEC and SOFC modes respectively. Thereby electrochemical impedance spectra were recorded under load from OCV to ± 1.2 A/cm^2. The curves have been determined through integration of ASRs obtained from CNLS fits under load operation in the according operation modes[112] (cf. section 3.3.1.4).

If it is assumed that the galvanostatic SOEC mode operation of Cell A was carried out at – 1.2 A/cm^2 instead of - 1.5 A/cm^2 and that the cyclic operation of Cell B took at $\pm$ 1.2 A/cm^2 then the following observations can be made[xxxii] based on Figure 5.2-16:

i. At 1.2 A/cm^2 the total overpotential under SOEC mode (of 211 mV) is greater than that in SOFC mode (of 172 mV) by 39 mV. This means, an extra overvoltage of 39 mV is required to drive a current density of 1.2 A/cm^2 through these cells in electrolysis mode under the investigated conditions than in fuel cell mode. The difference at 1.5 A/cm^2 can be extrapolated from Figure 5.2-16a and b to ca. 80 mV. From the voltage evolutions in Figure 5.2-4a and an OCV of 941 mV, initial SOEC voltage of 1219 mV and initial SOFC mode voltage of 736.8 total overvoltages of 278- and 204.2 mV for SOEC and SOFC mode can be calculated. These result in a consistent difference of 74 mV required to drive the same current density of 1.5 A/cm^2 in SOEC mode across the cell as compared to SOFC mode.

ii. From Figure 5.2-16a, the voltage drop across the fuel electrode calculated as sum of the diffusion-related overvoltage and the activation overvoltage[163] (also, cf. section 4.4.2) is in SOEC mode with 90 mV at 1.2 A/cm^2 twice as much as the voltage drop across the oxygen electrode (44 mV)—a difference of 46 mV. At 1.5 A/cm^2 this difference can be extrapolated to ca. 60 mV—approximately 50 % more voltage drop across the fuel electrode than the oxygen electrode. Thus during SOEC operation of these cells at 800 °C with a mixture of 50/50 H_2/H_2O and air supplied to the fuel electrode, the fuel electrode is subject to 50 % more overvoltage *stress* than the oxygen electrode. If larger overpotential leads to larger ageing, the observed greater ageing of the fuel electrode in Cell A against the oxygen electrode is expected. If the cells were operated in SOFC mode (cf. Figure 5.2-16b) the voltage drop across the fuel electrode at 1.2 A/cm^2 (66 mV) would still be greater than that across the oxygen electrode (31 mV) by more than double. However, the greater share of the overall voltage drop is across the electrolyte with 77 mV. As such if the cells were operated at 1.2 A/cm^2 in SOFC mode, it could be speculated that the electrolyte would age the most, followed by the fuel electrode.

iii. Finally, in $\pm$ 1.5 A/cm^2 cyclic mode, the cell is being switched between 1219 mV in SOEC mode and 737 mV in SOFC mode (cf. Figure 5.2-4) at the start of the test—an overpotential window of 482 mV. From Figure 5.2-16a and b, at 1.2 A/cm^2 the overpotential across the fuel electrode is 90 mV and 66 mV in SOEC and SOFC modes respectively. This means that the fuel electrode is switched between – 66 mV and + 90 mV—a potential window of 156 mV. In a similar manner, the oxygen electrode is cycled between 30- and 44 mV in SOFC and SOEC modes—a potential window of 74 mV. This means that in cyclic mode, the fuel electrode is cycled in an overpotential window that is more than double that at which the oxygen electrode is being cycled. At $\pm$ 1.5 A/cm^2 the difference extrapolating from Figure 5.2-16 would be greater. Based on the final[xxxiii] ageing rates of the fuel and oxygen electrodes in cyclic

[xxxii] From the previous sections, it is clear that for these cells under the operation conditions of 800 °C and 50/50 H_2/H_2O - 1.2 A/cm^2 represents a point below the thermoneutral point, i.e. in the endothermic regime and long-term operation could lead to different ageing trends.

[xxxiii] It is not recommended to evaluate the initial ageing, since the LSCF oxygen electrode has been shown to display a rapid initial ageing even at OCV conditions[87,92,154].

mode (cf. Table 5.2-2) of 5.6- and 4.5 mΩ/kh respectively, the cyclic stability of the fuel electrode can be stressed, since this ages with less than 25 % more than the oxygen electrode, despite being cycled in a potential window that is more than 50 % larger. This finding definitely is mildly consistent with the reparative impact of cycling SOCs to improve performance[152,159].

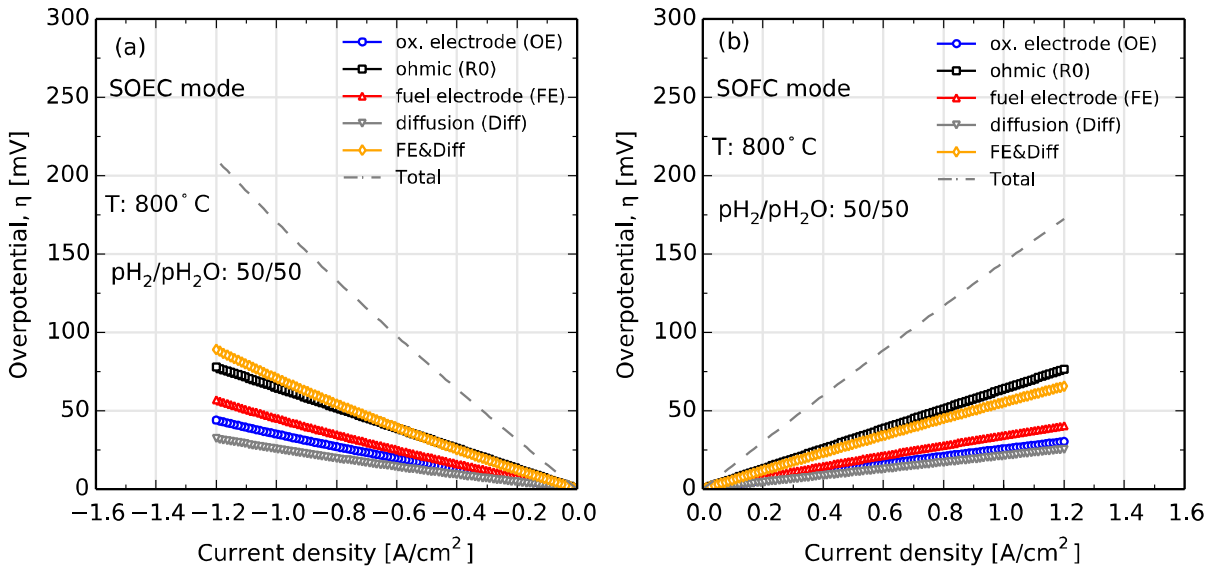

Figure 5.2-16: Evolution of overpotentials under current load at 800 °C in a 50/50 H_2/H_2O fuel for the different loss mechanisms of the cell type investigated in the constant SOEC and cyclic operation modes in (a).SOEC mode and (b) SOFC mode

5.3 Dynamic Operation

In principle *dynamic operation* of SOCs could mean anything from operating at different current densities at different segments of the tests, to different temperatures or simply different operation conditions along the time axis. In this work, *dynamic operation* refers to the cyclic operation of the SOC with the cycles having a different length at different phases along the time axis. This will enable investigation of the cyclic stability of the SOCs for different load durations.

A particular motivation for these investigations was to evaluate the cyclic and dynamic stability of the herein investigated SOC chemistries at 700 °C. This is important as the current trend in SOFC research is aimed at reducing operation temperature towards 700 °C in a bid to reduce material costs. This trend favors cyclic, reversible or dynamic operation, since a major aim of reversible operation is to convert “excess” electrical energy into chemical energy for storage. As such, at reduced temperatures the share of the required thermal enthalpy $T\Delta S$, can be compensated by raising the share of required electrical energy ΔG which is available in “excess” e.g. from wind and solar plants.

5.3.1 Experimental

The tests reported here were planned to run in five 500 h segments or phases (I - V). In phase I, the cell was operated at OCV. In the subsequent phases, the cell was cycled between fuel cell and electrolysis modes with abrupt switching without residing at OCV. The cycles had equal durations x in each mode (FC and EC modes) and were such that in phases II, III, IV and V x was 0.05-, 0.5-, 5- and 50 h long respectively. The increasing cycle length is expected to inevitably lead to dominance of the ageing of one mode over the other. Investigations were carried out at 700 °C and current densities 1-, 0.5- and 0.25 A/cm^2 were investigated. Another test was done at 800 °C and 0.5 A/cm^2 for comparison. All investigations were done in a fuel mixture of 50/50 H_2/H_2O supplied at 24 l/h and air supplied to the oxygen electrode at 140 l/h.

The investigated cells were DTU Energy of type II in Figure 3.2-1 (cf. Table 3.2-1) with an electrode area of 0.5 x 4 = 2 cm^2. With the FZJ cells investigated in section 5.2 labeled cells A and B, the herein operated cell at 800 °C and 0.5 A/cm^2 is labeled Cell C, while that investigated at 700 °C is labeled Cell D[xxxiv].

The cells underwent a custom initial in-house characterization prior to the tests and at the target operation temperature an initial characterization was carried out at t_0 = 0 h. At t_0 and at the end of every 500 h segment i.e. in between phases, a characterization was carried out whereby two impedance spectra were recorded in succession followed by a C/V-curve in fuel cell mode, a waiting period of 60 minutes for relaxation and another C/V-curve in EC mode. The voltage limits were 650 mV in SOFC mode and 1600 mV in SOEC mode. Within the 500 h phases, a minor characterization was done every 100 h at OCV whereby two impedance spectra were recorded in quick succession. No C/V curves were recorded to avoid interfering with ageing phenomena.

The impedance spectra were recorded in the frequency range 96.850 kHz to 30 mHz using a Solartron 1260 FRA. The excitation signal amplitude was 3 V root mean square value (rms) leading to an output current signal of ca. 60 mA rms (shunt resistance of 50 Ω). To exclude contributions from the test set-up, the recorded spectra were corrected with a short-circuit measurement and lead inductance was removed through a procedure utilizing the Kramers-Kronig relations[19,20].

[xxxiv] Because the cells investigated at 700°C aged too fast upon cycling begin, and are not further analyzed, only the successful test operated with gas cleaning is considered and called Cell D

5.3.2 Results and Discussion

5.3.2.1 Voltage Ageing

The evolution of the cell voltage for all investigated cells is displayed in Figure 5.3-1. The tests reported in Figure 5.3-1a, b and c were carried out at 700 °C in successive attempts. In Figure 5.3-1a the current density was 1 A/cm^2 and this would be stepped down successively to 0.5- and 0.25 A/cm^2 respectively in the next tests after the cells aged beyond the set voltage limits in less than 200 h of cycling in phase II. This displayed current density independence of the ageing mechanism under the investigated conditions.

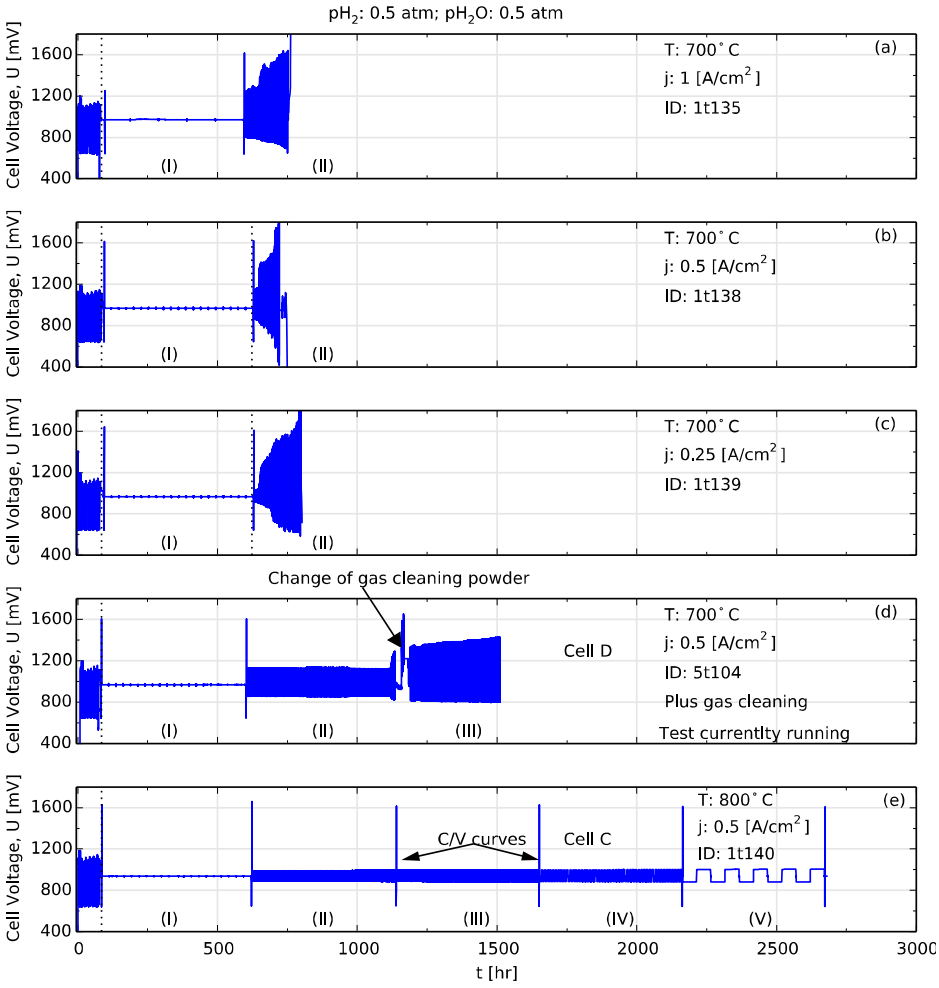

Figure 5.3-1: Overview of the voltage evolution with time for all dynamic cycling tests in a 50/50 H_2/H_2O fuel. (a) – (c) are tests at 700 °C that broke down in Phase II after the cycling started with 1-, 0.5- and 0.25 A/cm^2 respectively (and will not be quantitatively analyzed in this manuscript). (d) Dynamic cycling of Cell D at 700 °C with H_2 being passed through crushed NiO-YSZ powder heated at 700 °C as a gas cleaning measure. The test was ongoing at the time of documenting this manuscript. (e) Dynamic cycling of Cell C at 800 °C with 0.5 A/cm^2 and no gas cleaning (test also running at time of manuscript writing)

A further test (cf. Figure 5.3-1d) was started at 700 °C with a gas cleaning unit operated at 700 °C through which the H_2 fuel was passed before entering the combustion chamber where it reacted with adequate amounts of oxygen to produce the required H_2/H_2O fuel ratio. The cycling was done at 0.5 A/cm^2. Based on the rather short cyclic stability of the preceding three tests, an impedance spectrum was recorded every 25 h for Cell D. As can be seen, unlike the previous cells, the tested cell, Cell D did not age in phase II and as shall be seen later the cell even activated. After 447 h of cycling the cell started ageing rapidly with a cell voltage increase of 152 mV in 13 h in SOEC mode and was interrupted and gas cleaning powder replaced[176]. Since 530 h (447 h of cycling plus 38 h of OCV characterizations) of phase II had been completed, phase III was started after changing the gas cleaning powder. Thereafter the cell didn´t activate further but started ageing.

The test reported in Figure 5.3-1e was operated at 800 °C and 0.5 A/cm^2. As can be seen, the cell—Cell C was operated smoothly through all five segments with no incidents.

5.3.2.1.1 Dynamic and Cyclic Stability at 700 °C

The voltage evolution of Cell D, operated at 700 °C has been displayed in Figure 5.3-2a and the corresponding zoom-ins for SOEC mode and SOFC mode voltage evolutions are displayed in subplots b and c respectively. The subplots reveal asymmetrical *activation* in phase II with the SOEC mode voltage activating more than SOFC mode. From the cell voltages at start of phase II and those immediately before the rapid ageing, the cell is seen to be activating with 21 mV/kh in SOEC mode and seven fold less in SOFC mode with only 3 mV/kh. With ca. 50 h of cycling left for completion of phase II, the cell voltage aged rapidly with 13 h with the SOEC voltage increasing from 1130.2- to 1281.8 mV and the SOFC voltage decreasing from 850.7- to 824 mV. These correspond to ageing rates of + 11300- and – 2000 mV/h in SOEC and SOFC modes respectively. The test was brought to OCV, the gas cleaning powder changed and cell allowed in pure H_2 for 16 h followed by 6 h in the operation fuel mixture of 50/50 H_2/H_2O. Phase III was then started, cycling the cell at $\pm$ 0.5 A/cm^2 with 0.5 h duration in SOEC mode and 0.5 h in SOFC mode and no duration at OCV. In phase III, Cell D with 320 h of cyclic operation at time of thesis documentation is ageing at reduced[xxxv] rates of + 320 mV/kh in SOEC mode and - 61 mV/kh in SOFC mode. After 1500 h of operation with ca. 850 h of dynamic cycling the Cell D is displaying an overall voltage ageing rate of + 325.8 mV/kh in SOEC mode and - 60.5 mV/kh in SOFC mode respectively in the cyclic phases. The *disturbance* in Figure 5.3-2 is due to a low frequency AC voltage from the impedance measuring equipment as a result of system malfunction towards the end of an impedance spectrum recording and does not affect the cell and the ageing trend.

[xxxv] compared to the rapid ageing of 11300 and 2000 mV/kh in SOEC and SOFC modes respectively within 13 h prior to phase III

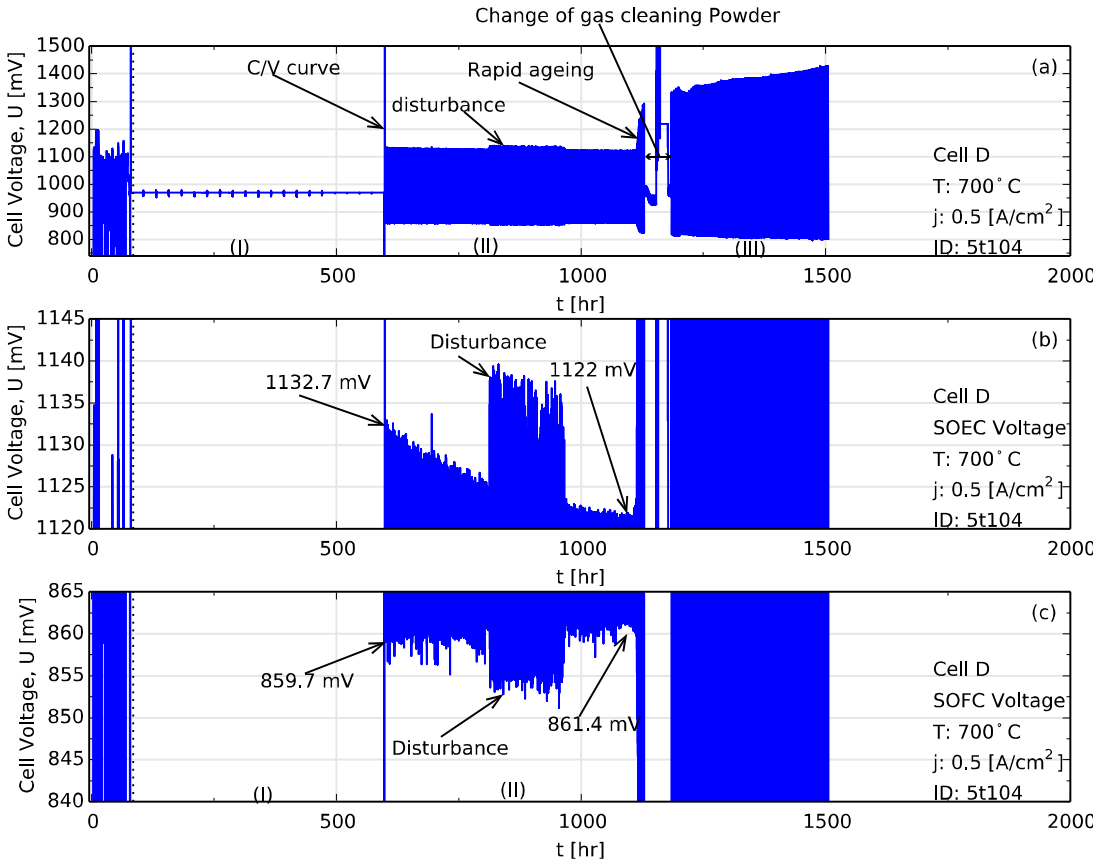

Figure 5.3-2: Voltage evolution of Cell D operated at 700°C in a fuel mixture of 50/50 H_2/H_2O supplied at 24 l/h and air at the oxygen electrode supplied at 140 l/h. The H_2 is passed through crushed NiO as a fuel cleansing strategy[176]. Similar to Cell C the cell is planned to be operated in five phases—I – V whereby phase I is OCV. Phases II – V are to be cycled between fuel cell and electrolysis cell modes with 0.05-, 0.5-, 5- and 50 h duration at each mode. The cell is running and in Phase II at the time of manuscript writing (a) Overview (b) SOEC mode voltage zoom-in (c) SOFC mode voltage zoom-in

Table 5.3-1: Voltage ageing rates of Cell D operated at 700 °C and cycled with ± 0.5 A/cm² in a 50/50 H_2/H_2O fuel supplied to the fuel electrode with 24 l/h and air supplied to the oxygen electrode at 140 l/h

Phase	II		Rapid ageing		III		Overall	
Mode	SOEC	SOFC	SOEC	SOFC	SOEC	SOFC	SOEC	SOFC
Rate [mV/kh]	- 21	+ 3	+ 11300	- 2000	+ 320	- 61	+ 325.8	- 60.5
Interval [h]	599.2 - 1113		1114.8 – 1128.6		1185.1 – 1504.6-		599.2 – 1504.6	

From the voltage evolutions in Figure 5.3-2 and the rates in Table 5.3-1 the following observations could be made about the cyclic and dynamic stability of SOCs operated at 700 °C and $\pm$ 0.5 A/cm^2:

i. The investigated cell, Cell D activated for close to 500 h of cyclic operation with 0.05 h (3 minutes) per mode with the cell activating 7 times as much in SOEC than SOFC mode.
ii. The cell aged rapidly after 447 h of cycling within a 13 h window with the SOEC voltage ageing 5 times as much as SOFC mode voltage
iii. In the second cyclic phase with 0.5 h duration at each mode, the cell aged with SOEC voltage ageing 5 times as much as the SOFC mode voltage.
iv. After 850 h of dynamic cycling, the cell has an average ageing rate in SOEC mode that is 5 times greater than that in SOFC mode
v. After replacing the gas cleaning powder, the SOEC cell voltage ageing dropped from + 11300 mV/kh to + 320 mV/kh despite the 10 times longer cycle length. The corresponding drop in SOFC mode voltage was from - 2000 mV/kh to - 61 mV/kh.

5.3.2.1.2 Dynamic and Cyclic Stability at 800 °C

As a result of the rather low cyclic stability of the SOCs at 700 °C when the fuel gas was not cleaned, Cell C was tested at 800 °C under similar conditions of current density and gas composition as Cell D, i.e. at $\pm$ 0.5 A/cm^2 with a fuel composition 50/50 H_2/H_2O mixture supplied at 24 l/h and air supplied to the oxygen electrode at 140 l/h. The cell voltage evolution with time has been displayed in Figure 5.3-3a and zoom-ins of the SOEC and SOFC voltages have been displayed in the subplots b and c respectively. In a similar manner to Cell D, the ageing rates during the different cyclic phases have been calculated as difference between values at start and end of phase divided by the corresponding time span. These have been displayed in Table 5.3-2.

From Figure 5.3-3 and Table 5.3-2 the following observations can be made about the dynamic cyclic stability of the investigated SOC at 800 °C and cyclic current density of $\pm$ 0.5 A/cm^2:

i. In phase II with a cycle length of 2 x 0.05 h the cell voltage is ageing at almost equal rates of + 15- and - 14 mV/kh for SOEC and SOFC modes respectively.
ii. In the next 500 h window, i.e. phase III the cell voltage is ageing half as much as in phase II and again almost equally for both SOEC and SOFC modes with + 7- and - 6 mV/kh despite the 10 times longer cycle length.
iii. In phase IV, with again 10 times longer cycle length than phase III, the SOEC mode voltage is again ageing at a higher rate of + 12 mV/kh. However, the SOFC mode voltage continues to age almost as much as in phase III with - 5 mV/kh.
iv. In the final phase (phase V), the SOC is ageing with slightly lower rates of + 11 and - 4 mV/kh in SOEC and SOFC modes respectively and again despite the 10 fold longer cycle lengths.

v. At the end of test and based on the total duration of the cyclic phases, the SOC displays and overall ageing rate of + 9.8 mV/kh in SOEC mode and – 6.6 mV/kh in SOFC mode.

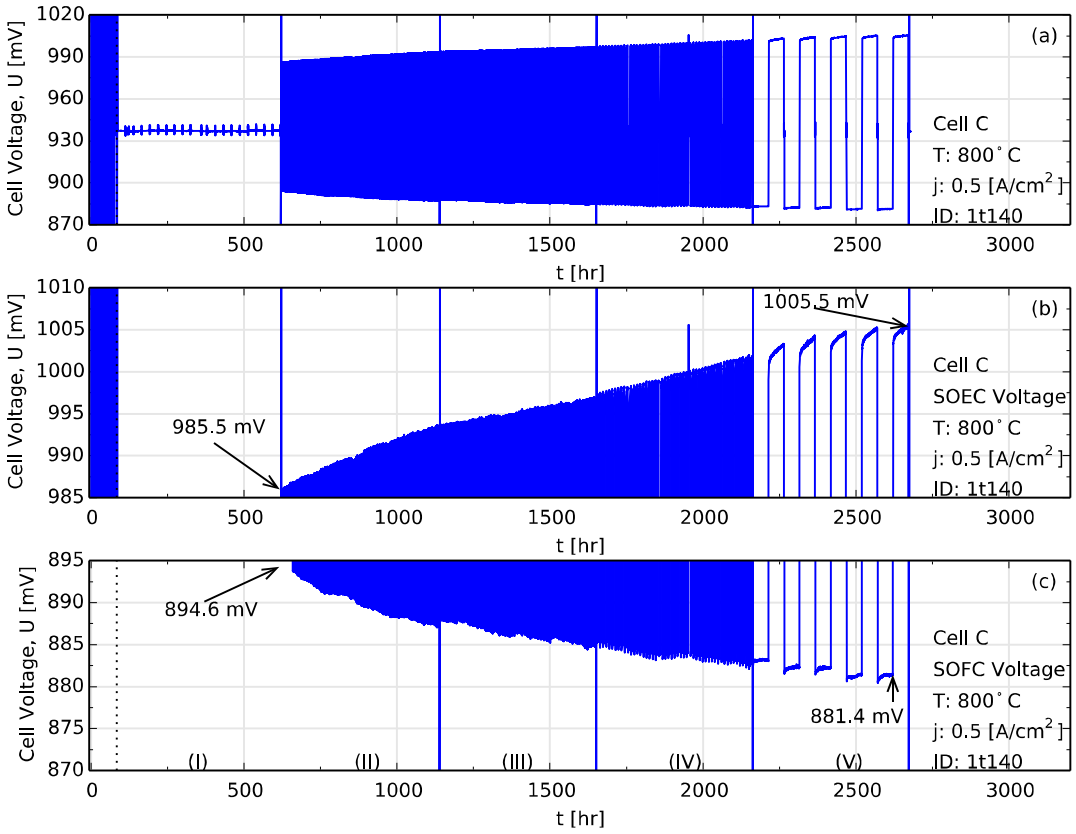

Figure 5.3-3: Voltage evolution of Cell C operated at 800°C in a fuel mixture of 50/50 H_2/H_2O supplied at 24 l/h and air at the oxygen electrode supplied at 140 l/h. The cell is operated in five phases—I – V whereby phase I is OCV. Phases II – V are cycled between fuel cell and electrolysis cell modes with 0.05-, 0.5-, 5- and 50 h duration at each mode. (a) Overview (b) SOEC mode voltage zoom-in (c) SOFC mode voltage zoom-in

Table 5.3-2: Voltage ageing rates of Cell C operated at 800 °C and cycled with ± 0.5 A/cm² in a 50/50 H_2/H_2O fuel supplied to the fuel electrode with 24 l/h and air supplied to the oxygen electrode at 140 l/h

Phase	II		III		IV		V		Overall	
Mode	SOEC	SOFC	SOEC	SOFC	SOEC	SOFC	SOEC	SOFC	SOEC	SOFC
Rate [mV/kh]	+ 15	- 14	+ 7	- 6	+ 12	- 5	+ 11	- 4	+ 9.8	- 6.6
Interval [h]	622.4 - 1137.3		1141.2 – 1648.5		1653.7 – 2160.4		2163.8 – 2620.4		622.4 – 2620.4	

5.3.2.1.3 Discussion and Conclusions based on the Voltage Ageing Trends

Based on the findings from the investigated cells in sections 5.3.2.1.1 and 5.3.2.1.2 it can be concluded that at 700 °C without gas cleaning, the SOCs can only withstand cyclic operation for ca. 200 h at current densities between 0.25- and 1 A/cm^2 and the ageing is independent of current density. The longer cyclic stability observed at 700 °C upon cleaning[176] the gases suggests the ageing mechanism is related to the adsorption of impurities from the fuel at the reaction sites as suggested in literature[148,177]. In SOFC mode the impurities are desorbed releasing more reaction sites. This will lead to a larger passivation of the SOEC mode electrochemistry than SOFC mode electrochemistry as consistently depicted by the voltage evolutions of both modes. Fu *et al*.[178] did however demonstrate 2000 h of electrolysis operation of a 5-cell stack at 700 °C with a current density of – 0.6 A/cm^2 without observing the herein impurity-related ageing. Unlike the tests reported herein, whereby steam is generated by allowing H_2 to react with appropriate amounts of O_2 , they generated the reduced steam by direct injection water vapor.

Furthermore, at the reaction sites, the endothermic SOEC operation has a cooling effect at least locally against the exothermic hydrogen oxidation that raises the temperature at the reaction sites. This effect is definitely more impacting at 700- than at 800 °C —and although the contaminants in the fuel were not investigated in this work, sulfur is a common contaminant in SOCs and its poisoning effect is well known to be more sever at lower temperatures[179,180]. This again would poison SOEC mode electrochemistry more than SOFC mode one giving the higher SOEC mode ageing rates compared to SOFC mode ageing rates. This hypothesis is further enhanced by the fact that at 800 °C the SOC displays ageing rates in both SOEC and SOFC modes that are an order of magnitude smaller than those registered at 700 °C. The same reasoning also justifies the rather symmetrical ageing rates of both SOEC and SOFC modes in phase II of the test at 800 °C.

The halving of the ageing rates of Cell C in phase III will be addressed after further analysis of the recorded spectra in the next sections.

5.3.2.2 Cell Performance and Power Density

The performance of the cell (Cell C) was evaluated by recording C/V-curves during the characterizations between segments. These have been displayed in Figure 5.3-4 from which (i) the asymmetric ageing of C/V curves in SOFC and SOEC modes can be appreciated.(cf. ca. $\pm$ 2/cm^2) (ii) the rapid ageing in the first 1000 h corresponding to phases I and II can be observed for both modes.

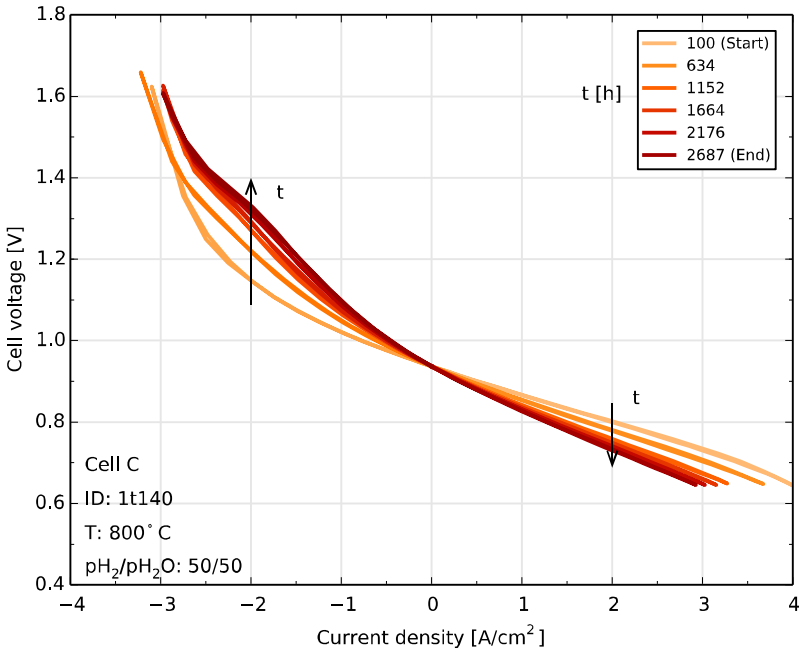

Figure 5.3-4: C/V curves of Cell C recorded at OCV at 800 °C in a 50/50 H_2/H_2O fuel mixture supplied at 24 l/h with air supplied at the oxygen electrode at 140 l/h.

From the C/V curves the power densities at the conventional voltage of 0.7 V have been calculated and displayed in Figure 5.3-5(a_i). Further, the power densities at the operation current density of $\pm$ 0.5 A/cm^2 have also been calculated for both SOEC and SOFC modes and displayed in Figure 5.3-5(b_i). To further illustrate the asymmetrical operation and ageing of both modes the power densities have also been calculated for $\pm$ 2 A/cm^2 and displayed in Figure 5.3-5(c_i). The corresponding relative changes with respect to the C/V curve at t = 100 h have been displayed in the corresponding Figure 5.3-5(*x*_ii), with *x* = a, b and c.

From Figure 5.3-5(a_i) the cell at 0.7 V is having a power density of 2.4 W/cm^2 and at the end of the test still can deliver 1.6 W/cm^2 corresponding to a ca. 35 % drop in power density (cf. Figure 5.3-5(a_ii)). On the other hand, at the operation point of $\pm$ 0.5 A/cm^2 the power density in SOFC mode initially at 0.45 W/cm^2 (cf. Figure 5.3-5(b_i)) has only dropped by 2.4 % (Figure 5.3-5(b_ii)) at the end of the test to 0.44 W/cm^2. In SOEC mode, the cell initially requiring 0.49 W/cm^2 to drive the current density of 0.5 A/cm^2 has aged such that at the end of the test 3 % more power density is required to drive the same current through the cell—again an asymmetric ageing when compared to the 2.4 % drop in SOFC power density. By comparing the power densities at $\pm$ 2 A/cm^2, it can be seen from Figure 5.3-5(c_i) that initially, the cell is delivering 1.6 W/cm^2 at + 2 A/cm^2 against requiring 2.3 W/cm^2 for SOEC mode at - 2 A/cm^2. At the end of the test, the power density in SOFC mode has dropped by 9 % (cf. Figure 5.3-5(c_ii)) meanwhile in SOEC mode, 16 % more power is required to drive the same amount of current. Thus at the end of the test, and at $\pm$ 2 A/cm^2 SOEC and SOFC modes have aged asymmetrically by almost a factor of 2.

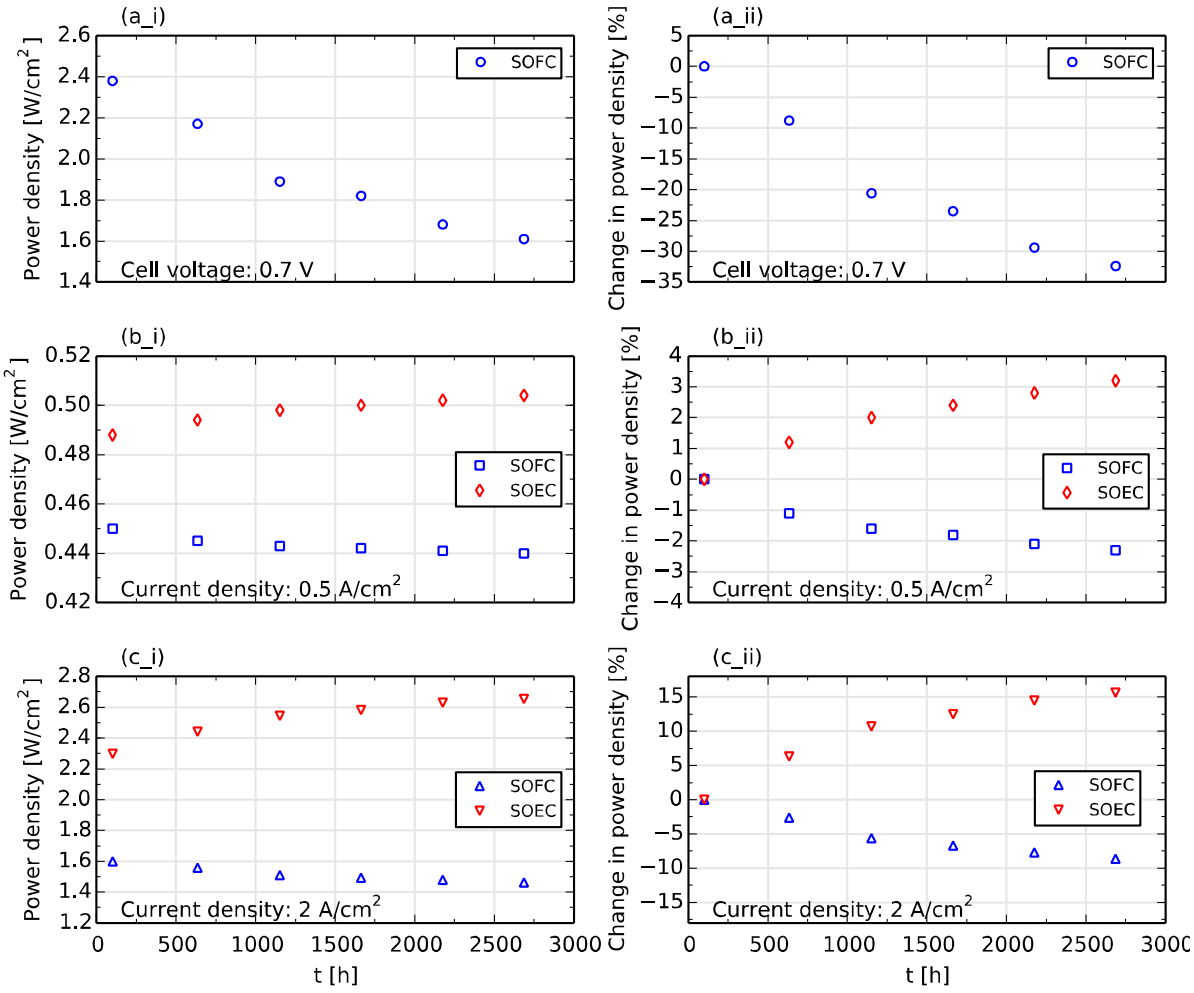

Figure 5.3-5: Power densities and corresponding changes relative to initial values of Cell C recorded at 800 °C in a 50/50 H_2/H_2O fuel mixture supplied at 24 l/h with air supplied at the oxygen electrode at 140 l/h. (a_i) Power density at a conventional comparison point of 0.7 V (a_ii) Corresponding relative change of power density at 0.7 V (b_i) Power density at operation point current densities of ± 0.5 A/cm² (b_ii) Corresponding relative power density change at ± 0.5 A/cm² (c_i) Power density at 2 A/cm² (c_ii) Corresponding relative power density change at 2 A/cm².

5.3.2.3 Qualitative Analysis of Impedance Spectra

The evolution of impedance spectra of Cell C with time has been displayed in Figure 5.3-6a and the corresponding DRTs are displayed in Figure 5.3-6b. From the Nyquist plots, it can be seen that both the series resistance and polarization resistances are ageing with time. The DRTs reveal further, that all frequency regions of the cell are ageing albeit to different degrees.

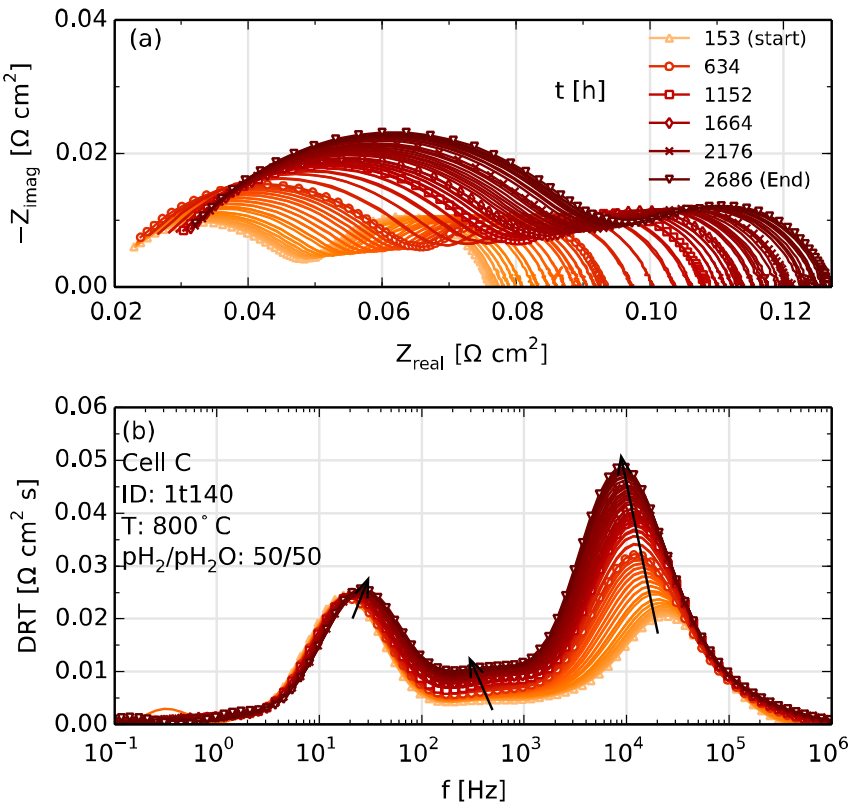

Figure 5.3-6: Electrochemical impedance spectra (a) and corresponding DRTs (b) of Cell C recorded at OCV at 800 °C in a 50/50 H_2/H_2O fuel mixture supplied at 24 l/h with air supplied at the oxygen electrode at 140 l/h.

5.3.2.4 Data Quality and KK-Residuals

Prior to quantifying the individual ASRs and their corresponding ageing rates through CNLS fit of the spectra displayed in Figure 5.3-6, the spectra were controlled for compliance with KK-transforms. The relative residuals for the spectra at the beginning and end of test are displayed in Figure 5.3-7a and b respectively. As can be seen, the recorded spectra are of excellent quality with residuals well in a $\pm$ 0.5 % window.

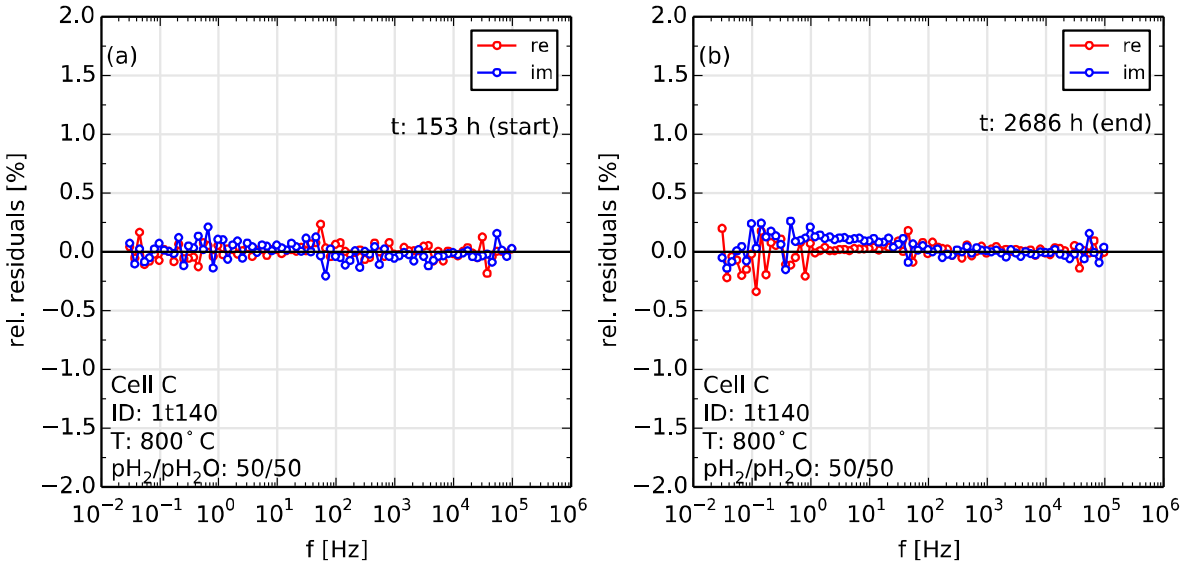

Figure 5.3-7: KK-Residuals of electrochemical impedance spectra of Cell C recorded at OCV during characterization intervals at the start (a) and end (b) of the tests in a 50/50 H_2/H_2O fuel mixture.

5.3.2.5 Quantitative Analysis and Ageing Trends of Individual Cell Components

The equivalent circuit model shown in Figure 5.2-3 was used to fit the spectra recorded in the characterization intervals. In the ECM, however, the RQ-element for the oxygen electrode diffusion was used for gas conversion losses at the fuel electrode because the diffusion losses in the 40 µm oxygen electrode were assumed negligible. The CNLS fits were done with the software RAVDAV[21] and excellent goodness of fits were obtained with the Boukamp goodness of fit χ^2 in the rage 1.01 - $3.6 \cdot 10^{-4}$.

The evolution of the different ASR contributions has been displayed in Figure 5.3-8 from which the following observations and comments can be made for the different phases of the dynamic operation:

a) **Series Resistance**: The series resistance displayed in Figure 5.3-8a displays a distinct ageing trend wherein in the first 500 h of operation at OCV conditions, it does not age. In Phase II, under dynamic cycling at ± 0.5 A/cm^2 the series resistance ages from 10.1 mΩcm^2 to 13.1 mΩcm^2 corresponding to 5.7 mΩcm^2/kh and then relaxes to a factor 10 less ageing rate in which the ASR only changes from 13.1 mΩcm^2 at start of phase III to 13.8 mΩcm^2 at end of phase V. The rapid increase in series resistance in Phase II is an indication of microstructural changes within the cell, possibly formation of microstructural porosity at the grain boundaries of the electrolyte during electrolysis mode cycles[132,170] but also a result of impurities at the fuel electrode[136].

b) **Substrate diffusion**: The substrate diffusion displayed in Figure 5.3-8b improves in phase I displaying an ASR of 10.5 $m\Omega cm^2$ at the end of phase I against 13.6 $m\Omega cm^2$ at the start of the phase. This improvement in substrate diffusion ASR has been attributed to improving tortuosity as a result of agglomerating Ni particles as well as loss of Ni as $Ni(OH)_2(g)$ in section 5.2.2.5 for cells A and B.

c) **Fuel electrode ASR**: The fuel electrode ASR displayed in Figure 5.3-8c is increasing in phase I (OCV) with values of 11.8- and 19.6 $m\Omega cm^2$ at start and end of phase I respectively. This corresponds to an ageing rate of 16.2 $m\Omega cm^2/kh$, which is 3 times as much as the electrolyte is ageing in the same period. The ageing can be attributed to a loss of TPB due to agglomeration of Ni particles. Upon cycling start in phase II, the fuel electrode ASR only ages half as much as in the preceding OCV phase with 7.2 $m\Omega cm^2/kh$. In phase III, the ASR relaxes to an even slower ageing rate of 2.7 $m\Omega cm^2/kh$. With the longer cycles in phases IV and V (cycle lengths of 2 x 5- and 2 x 50 h respectively), the fuel electrode ages with a greater rate of 5.1 $m\Omega cm^2/kh$. The same ageing rate for phases IV and V suggests a cycle length independence of the ageing for cycles longer than 5 h for both modes. Although gold sealing was used in all tests reported so that impurities from the sealing can be excluded impurities have been reported[136] to segregate from YSZ bulk phase (e.g. Si, Al and Na) or from the Ni phase[181,182] at the grain boundaries or TPB. During high temperature electrolysis at high pH_2O and current density, the corrosive SiO_2 in form of $Si(OH)_4(g)$ increases.

d) **Gas Conversion:** The gas conversion ASR displayed Figure 5.3-8d displays a two-stage ageing profile with a high ageing rate of 6.8 $m\Omega cm^2/kh$ in the OCV followed by a relaxation to a lower and constant ageing rate of 1.04 $m\Omega cm^2/kh$ for all cycling phases. The ageing of the gas conversion seems to be coupled with the two-step ageing of the substrate diffusion ASR (cf. Figure 5.3-8 b vs d). It has been shown that the gas conversion ASR depends on the active electrode area[112,183] and also on the porosity of the substrate[184]. The agglomeration of Ni particles in the substrate does not affect the porosity of the substrate but the tortuosity, however if the loss of Ni as $Ni(OH)_2(g)$ is significant the porosity will improve and the gas conversion ASR is expected to decrease[184]. This is opposite to the trend observed in phase I where the substrate diffusion is improving the most and gas conversion ASR is increasing the most.
By virtue of the rather finer microstructure[xxxvi] agglomeration of the Ni particles in the fuel electrode functional layer is expected with time especially in the first 500 h of phase I. If this loss of TPB, or "deactivation" varies locally then consequently the *constant* excitation current density will no longer be homogeneously distributed. This can be interpreted as decreasing effective active electrode area and might have an impact on the shape of the gas conversion peak in the DRT and eventually the fit values obtained, since the DRT has been employed for pre-identification but also control of CNLS fits. Furthermore, as shown in section 5.3.1, the current excitation signal is generated by employing a voltage of 3 V with a 50 Ω resistor in series. Because the changes in ASR of the cell are in mΩ range (<< 50 Ω),

[xxxvi] Finer microstructure than that of the standard DTU cell

these are not expected to affect the current density excitation and consequently the voltage response to the excitation—consequently since flow rate, inlet gas composition and excitation signal are constant and not affected by the insignificant change in cell ASR gas conversion ASR is expected to not change with time. As such it is not excluded, that the observed "ageing" is a mere consequence of greater overlap between the gas conversion and diffusion peaks (in the DRT).

In co-electrolysis of CO_2 and H_2O under constant load of – 1 A/cm^2 at 800 °C with the same cell type, however with a 4 x 4 cm^2 active electrode area Hjalmarrson et al.[135] reported a coupling between gas conversion ASR and fuel electrode ASR; The gas conversion ASR was observed to increase during phases when the fuel electrode was degrading—They could not explain the observation. Assuming the above discussed inhomogeneous current distribution as a result of the inhomogeneous local "deactivation" of active sites with the consequent loss of active electrode area, the shape of the gas conversion peak may have been influenced.

e) **<u>Oxygen Electrode</u>**: The ageing trend of the oxygen electrode ASR is displayed in Figure 5.3-8e. Despite the very small ASRs of less than 3 mΩcm^2 the ageing trend of the oxygen electrode can be seen to also be a two-step trend. An initial ageing trend in the first ca. 1600 h of operation with the electrode ageing at solely 0.6 mΩcm^2/kh is followed by a relaxation whereby the ASR activates in the last two phases at a rate of - 0.2 mΩcm^2/kh. The ageing of the LSC/CGO oxygen electrode is independent of cyclic load including OCV operation.

The evolution of the overall polarization ASR is displayed in Figure 5.3-8f and the strong similarity to the ASR evolution of the fuel electrode suggests that it is fuel electrode ASR that dictates the ageing of the investigated cell. However, the electrolyte ageing plays a major role in phase II as can be seen from the overall voltage evolution in Figure 5.3-3 where the rapid voltage ageing in phase II relaxes to a lower value in phase III just like the electrolyte. However, with the beginning of phase IV the fuel electrode ASR is the only contribution that ages at an increased rate similar to the voltage trend. This suggests that the ageing caused by longer phases of SOEC operation is not reversed by SOFC mode operation phase of equal lengths. This observation speaks in favor of the cation demixing ageing mechanism whereby the Ni ions that in-diffused into the YSZ matrix during sintering are reduced to metallic Ni during high current density SOEC, enhancing precipitation of tetragonal YSZ from the cubic matrix as well as enhancing mobilities of Y and Zr cations[167]. This however does not exclude other known ageing mechanisms of the fuel electrode during long-term SOEC operation such as formation of ZrO_2 nano-particles[132,157], porosity formation at the fuel electrode [170], loss of Ni as $Ni(OH)_2(g)$[14,163–165] whose mechanisms are interrupted during SOFC mode operation. The mechanism involved in the herein presented work might be elucidated through microscopy.

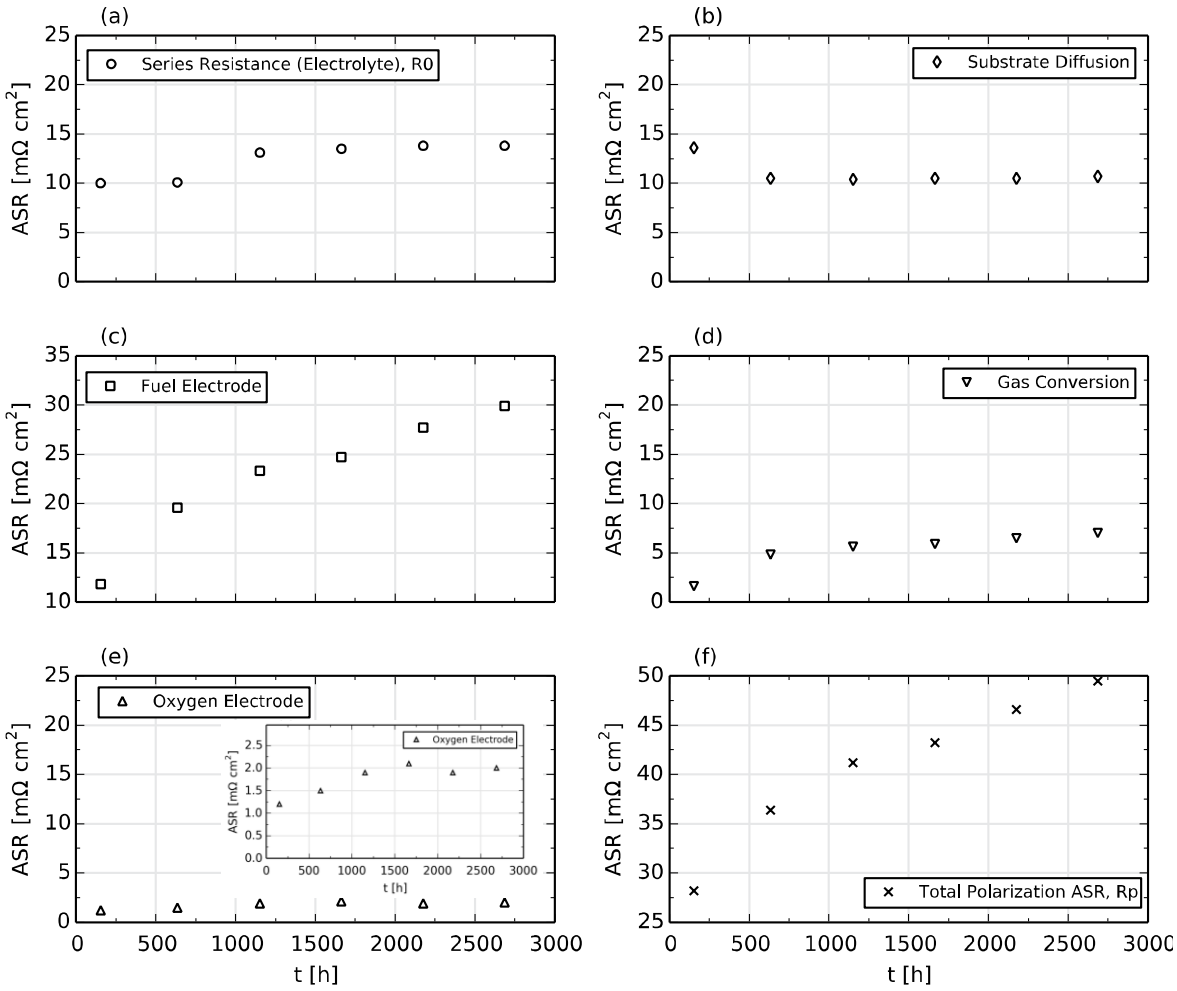

Figure 5.3-8: Evolution of Individual ASRs of Cell C operated at 800 °C in a 50/50 H_2/H_2O fuel mixture supplied at 24 l/h and 140 L/H of air supplied to the oxygen electrode. The ASRs are determined from impedance spectra recorded at OCV during characterization intervals. (a) Series/Electrolyte ASR (b) Substrate diffusion (c) Fuel electrode (d) Gas conversion (e) Oxygen electrode and (f) Total polarization resistance (no series resistance)

5.4 OCV Operation of Oxygen Electrodes

The oxygen electrodes LSC/CGO and LSCF were investigated using symmetric cells at 800 °C in a single gas atmosphere with air supplied at 6 l/h for 1200 h under OCV conditions. The electrodes were screen-printed on both sides of a 200 µm CGO electrolyte and sintered in oxidizing atmosphere at 1200 °C. The electrodes had a thickness of ca 15 µm after sintering. The cells are of Type IV in Table 3.2-1.

The test set-up[31] used offered the possibility of investigating four cells in four separate channels (serial characterization) however only three channels were occupied, for which one was a reproduction of the LSC/CGO cell. Only results of two cells and channels will be discussed here.

Electrochemical characterization was done by recording electrochemical impedance spectra with a Solartron 1260 FRA in the frequency range 96.850 kHz to 30 mHz. Characterization was done every 50 h and the Nyquist plots of the spectra are displayed in Figure 5.4-1(a_i) and (b_i) for the LSC/CGO and LSCF electrodes respectively.

From the corresponding DRTs in subplots Figure 5.4-1(a_ii) and (b_ii) it is evident that both electrodes display two major peaks at 800 °C. A low frequency peak at f = 8 Hz corresponding to diffusion in the stagnant gas layer above the electrode[40,68] and a high frequency peak at f = 80 Hz for LSCF and f = 2 kHz for LSC/CGO corresponding to the ASR related to the bulk diffusion and surface exchange kinetics of the oxygen ions[2,87,154]. Furthermore, knowing that the area beneath the DRT peak corresponds to the ASR of the dynamic process[5,39] it can be seen that the high frequency peak for LSC/CGO is much smaller than that of LSCF. This results in very low overall polarization resistance or very high performance SOCs with LSC/CGO cells[112,135]. Further the DRTs display rapid ageing within the first 500 h followed by a relaxation to lower ageing rates for both cells. On the other hand, the low frequency concentration process is constant for both cells.

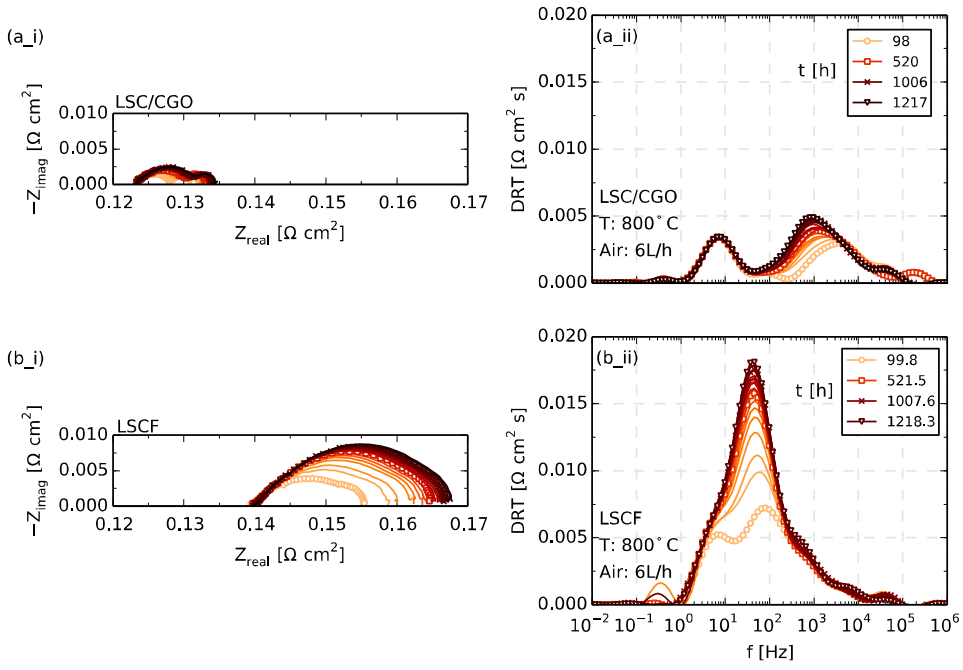

Figure 5.4-1: (a_i) electrochemical impedance spectra of LSC/CGO at 800 °C under OCV operation with 6 l/h of air. (a_ii) Corresponding DRTs calculated from the impedance spectra of LSC/CGO. (b_i) EIS spectra of LSCF recorded under same conditions in same test on a second channel in the same set-up and (b_ii) corresponding DRTs of LSCF spectra.

A CNLS fit of the spectra displayed in Figure 5.4-1(a_i) and (b_i) was carried out with an ECM consisting of a series resistance for the electrolyte ASR, a Gerischer element for the oxygen electrode ASR and a Warburg element for the diffusion process. Thereby the inductive components had been subtracted through the KK-transforms based routine. The results are displayed in Figure 5.4-2a, b and c for the oxygen electrode, diffusion and series resistance respectively. In subplot (a) both electrodes display a relaxation to much slower ageing rates after ca. 400 h as reported by Endler-Schuck *et al*.[87,154] for cells at 750 °C and OCV operation. The series resistance and stagnant layer diffusion resistances do not age significantly with time.

Comparing the LSC/CGO and LSCF ageing rates at 800 °C in air flowing at 6 l/h and under OCV operation the following observations can be made:

i. In the first 400 h of operation the LSCF oxygen electrode with 37.1 $m\Omega cm^2$/kh (0.42 %/h) is ageing 6 times as fast as the LSC/CGO electrode that is ageing at 5.9 $m\Omega cm^2$/kh (0.15 %/h).
ii. In the second ageing step from 500 h onwards, both electrodes relax to lower ageing rates whereby the LSCF electrode ages with 4.2 $m\Omega cm^2$/kh (0.02 %/h) against the LSC/CGO electrode ageing at a smaller rate of 1.7 $m\Omega cm^2$/kh (0.03 %/h). Thus, relative to the ASRs at t = 521 h of 18.2- and 5.8 $m\Omega cm^2$ for the LSCF and LSC/CGO electrodes respectively, the LSC/CGO is ageing with a relative rate of 0.03 %/h against 0.02 %/h for the LSCF electrode—factor 1.5 times faster than the LSCF electrode.

At 750 °C Endler-Schuck et al.[154] reported a higher initial ageing rate of 0.72 %/h in the interval 11 – 304 h and 0.033 %/h for 304h – 1012 h for the LSCF oxygen electrode of the investigated FZJ full cells. Thus the final ageing rate of 0.02 %/h obtained in this work for the LSCF symmetric cell compares with the 0.033 %/h in literature[154]. However, the initial ageing rate of 0.15 %/h is factor 4.8 less than that of Endler-Schuck et al.[154]. The differences can be explained based on two points:

a. Endler-Schuck investigated high performing FZJ full cells in a two-atmosphere set-up with 250 sccm flow rate (ca. 15 l/h/cm^2) where as in this work in-house and screen printed symmetrical cells were characterized in a single atmosphere with a flow rate of 6 l/h flowing in an alumina tube of 1.7 L—gas is replaced every 17 minutes. The ageing mechanism is believed to be related to Sr (and Co) depletion[154]. This means that in a rather stagnant layer of gas, this mechanism would be slowed down against a set-up where the electrode is swept clean of depleted Sr thus increasing the gradient and enhancing the ageing.
b. The tests reported here are carried out at 800 °C and it has been demonstrated that the ageing rate of the LSCF oxygen electrode increases with decreasing temperature[87,154]. As such the recorded initial ageing rate of 0.42 %/h recorded at 800 °C in this work is consistently smaller than the 0.72 %/h recorded at 750 °C by Endler-Schuck.

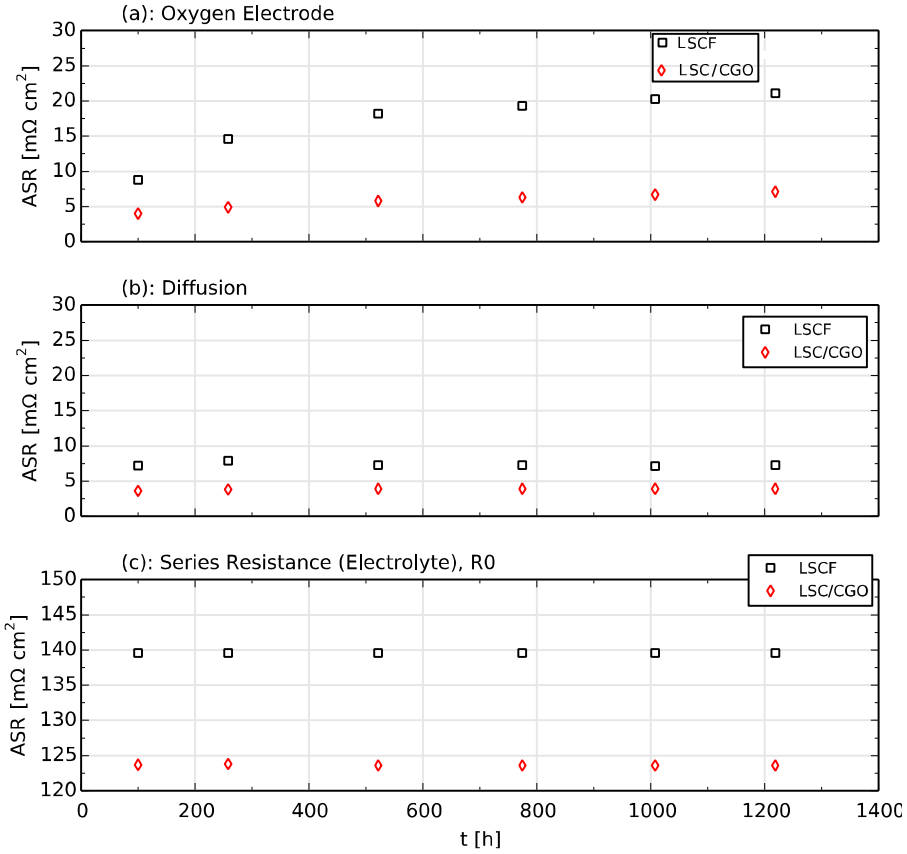

Figure 5.4-2: Evolution of individual ASRs of oxygen electrode symmetric cells at 800 °C under OCV conditions. Oxidant air is supplied at 6 l/h. Each figure displays values for LSCF and LSC/CGO electrodes. Both cells are mounted in the same rig and operated under exact same conditions, with impedance spectra recorded serially—LSC/CGO channel first follow by LSCF channel. (a) The oxygen electrode (b) the diffusion (stagnant layer)-related ASR (c) the series resistance of the 8YSZ electrolyte

5.5 Conclusion

In this chapter, the long-term stability of s.t.a. Ni-YSZ supported FZJ and DTU solid oxide cells were investigated in different constant and cyclic operating profiles. The FZJ cell was investigated for constant electrolysis operation at a high current density of - 1.5 A/cm^2 in a 1000 h test. The cell displayed the smallest ageing rates when compared to literature values. The fuel electrode dominated the ageing, followed by the electrolyte and then the oxygen electrode. The long-term stability of a sister cell in cyclic operation was investigated under similar conditions of temperature, fuel and oxidant gases for $\pm$ 1.5 A/cm^2. The cell displayed much smaller overall voltage ageing rates of + 32.8 mV/kh in SOEC mode and – 30.4 mV/kh in fuel cell mode against + 114.2 mV/kh

of the cell operated under constant SOEC operation. In cyclic mode, the oxygen electrode aged the most in the first 500 h, however its small absolute ASR values meant the contribution to the overall ageing was negligible.

The dynamic stability of SOCs was investigated in two 2500 h tests at 700 °C and 800 °C in a 50/50 H_2/H_2O fuel. The tests were carried out on DTU Energy SOCs with a similar fuel electrode and electrolyte materials like the FZJ cells, however with LSC/CGO oxygen electrodes against LSCF oxygen electrodes for the FZJ cells. A severe influence of impurities was demonstrated for operation at 700 °C whereby cyclic operation without gas cleaning could not last for more than 250 h independent of current density. With gas cleaning however, the cells had been operated beyond 900 h of cyclic operation at $\pm$ 0.5 A/cm^2 at the time of documenting the thesis. Thereby (and including the rapid ageing) phase, SOEC mode ageing with + 325.8 mV/kh was much more than the fuel cell mode ageing of - 60 mV/kh. At 800 °C and $\pm$ 0.5 A/cm^2 a sister cell to the one operated at 700°C successfully completed all five 500 h phases—OCV and cyclic phases with cycle lengths of 2 x 0.05 h, 2 x 0.5 h, 2 x 5 h and 2 x 50 h respectively. Although no gas cleaning was employed, the severe impact of impurities recorded at 700 °C was not present. The ageing was also asymmetric at 800 °C with SOEC mode ageing more than SOFC mode operation in all cyclic phases. Extremely small overall ageing rates of + 9.8- and – 6.6 mV/kh were recorded for the entire cyclic phases in SOEC and SOFC modes respectively. The greatest ageing took place within the first 500 h of cycling i.e. phase II, with rather symmetrical ageing rates of + 15 mV/kh and – 14 mV/kh in SOEC and SOFC modes respectively. The ageing relaxed in phase III, however with longer cycle lengths in phases IV and V, the SOEC mode ageing increased while the SOFC mode voltage aged at half the SOEC ageing rate.

A major conclusion from the cyclic and dynamic operations is that, for cycles with equal durations in SOEC and SOFC modes whereby the cycle length is less than or equal to 2 x 5 h, the ageing is almost symmetric in either mode with slightly higher ageing in SOEC mode. For longer cycle lengths SOEC mode ageing is at least double SOFC mode ageing.

The OCV ageing of LSCF and LSC/CGO oxygen electrodes was investigated at 800 °C in a 1000 h test. Both electrodes displayed a two-step ageing trend. However the LSC/CGO electrode did not only have a much smaller ASR but aged less than the LSCF electrode. From 600 h onwards, the LSC/CGO electrode despite the smaller ASR and smaller ageing rate had with 0.03 %/kh a 1.5 times higher relative ageing rate than LSCF electrode in the same time range.

Chapter 6 Summary and Conclusion

This thesis was aimed at investigating major aspects of the solid oxide cell (SOC) technology such as electrode kinetics, performance prediction and durability under practically feasible operation conditions in the operation mode: (i) constant electrolysis (ii) reversible and (iii) dynamic operation modes.

Electrochemical reaction kinetics at the electrodes of SOCs were investigated at 700 °C for two cells with different fuel electrode microstructures as well as on a third cell with a reduced active electrode area. Three fuel mixtures were investigated – hydrogen/steam and reformate fuels hydrogen/carbon-dioxide and hydrogen/methane/steam.

It was found that the kinetics at the fuel electrode were exactly the same in both reformates. The hydrogen/steam fuel displayed slightly faster kinetics than the reformate fuels. The measured gas conversion impedance was compared with models in literature for both the 16- and the 2 cm^2 cells. The continuously stirred tank reactor (CSTR) AC model approximated the overpotential of the smaller cells (2 cm^2) with greater accuracy in the current density range 0 – 0.5 A/cm^2 while the plug flow reactor (PFR) model although derived for the case of zero DC bias predicted the 16 cm^2 cell ASR better than the zero bias CSTR model. Furthermore the gas conversion impedance in the hydrogen/steam fuel split into two processes with opposing temperature behavior in the reformate fuels. By using a 87.5 % smaller active electrode area the gas conversion impedance was diminished in the hydrogen/steam fuel at (the same absolute) high fuel flow rates. In both reformates, the second and third lowest frequency processes merged into a single process as the gas conversion was reduced. The SOC with finer electrode microstructure displayed improved kinetics

In a 50/50 H_2/H_2O fuel mixture, the Ni/YSZ fuel electrode showed slower reaction kinetics operating under cathodic polarization than anodic. The same observation was made for the higher performing of the two investigated oxygen electrodes i.e. the LSC/CGO oxygen electrode showed slower reaction kinetics under cathodic mode operation at 50 mV than in anodic mode. However under decreasing oxygen partial pressure the performance decrease in cathodic operation was similar for both oxygen electrodes and more than the decrease in anodic mode performance. By determining the chemical surface exchange coefficient K^{δ} and oxygen ion diffusion coefficient D^{δ} it could be shown that the decreasing performance with decreasing pO_2 was related to surface exchange kinetic steps.

The 0-D isothermal model developed at IAM-WET (formerly IWE), Germany to predict the current / voltage (C/V) characteristic of a SOC in fuel cell mode was verified for electrolysis operation in both H_2/H_2O and CO/CO_2 binary fuels. The H_2/H_2O model was extended to consider temperature change under load. The model was further extended to cover operation in reformate fuels $H_2/H_2O/CO/CO_2$ whereby a new concentration-related overpotential contribution was included in the model, to account for the CO/CO_2 diffusion to the reaction sites as a results of the water gas shift equilibrium reactions. New model parameters were determined for the fuel electrode since measurements were done on a different generation of cells as those used for the H_2/H_2O and

CO/CO_2 models. The new model was validated by predicting C/V characteristics under different operation conditions of temperature and fuel gas composition. For the temperature 825 °C, 800 °C and 775 °C a relative error of less than 6 % was achieved in the current density window $\pm$ 1 A/cm^2 in the fuel $H_2/H_2O/CO/CO_2$ of 25/25/25/25.

The long-term stability of a SOC under constant electrolysis operation at a high current density of - 1.5 A/cm^2 was investigated in a 1000 h test with a cell from Forschungszentrum Jülich (FZJ). The cell displayed the lowest ageing rates when compared to literature values of cells operated under similar conditions. The fuel electrode dominated the ageing, followed by the electrolyte and then the oxygen electrode. The long-term stability of a sister cell in cyclic operation was investigated under similar conditions of temperature, fuel and oxidant gases for $\pm$ 1.5 A/cm^2. The cell displayed much smaller overall voltage ageing rates of + 32.8 mV/kh in SOEC mode and – 30.4 mV/kh in fuel cell mode against + 114.2 mV/kh of the cell operated under constant SOEC operation. In cyclic mode, the oxygen electrode aged the most in the first 500 h, however its small absolute ASR values meant the contribution to the overall ageing was negligible.

To investigate the long-term durability of SOCs under cyclic and dynamic operation, SOCS manufactured at DTU Energy were investigated at 700 °C in a symmetrical binary fuel of 50/50 H_2/H2O. It was found that, for cycles with equal durations in SOEC and SOFC modes whereby the cycle length was less than or equal to 2 x 5 h, the ageing was almost symmetrical with slightly higher ageing in SOEC mode. For longer cycle lengths SOEC mode ageing was at least double SOFC mode ageing.

The OCV ageing of LSCF and LSC/CGO oxygen electrodes was investigated at 800 °C in a 1000 h test. Both electrodes displayed a two-step ageing trend. However, the LSC/CGO electrode did not only have a much smaller ASR but aged less than the LSCF electrode. From 600 h onwards, the LSC/CGO electrode despite the smaller ASR and smaller ageing rate had with 0.03 %/kh a 1.5 times higher relative ageing rate than LSCF electrode in the same time range.

References

1. E. Bauer and H. Preis, *Zeitschrift für Elektrochemie und Angew. Phys. Chemie*, 727 – 732 (1937).

2. A. Leonide, *SOFC Modelling and Parameter Identification by means of Impedance Spectroscopy- PhD Thesis, Karlsruhe Institute of Technology*, KIT Scientific Publishing, Karlsruhe, (2010).

3. A. Leonide, Y. Apel, and E. Ivers-Tiffee, in *ECS Transactions*,, vol. 19, p. 81–109, ECS (2009).

4. A. Leonide, S. Hansmann, A. Weber, and E. Ivers-Tiffée, *J. Power Sources*, **196**, 7343–7346 (2011).

5. H. Schichlein, *J. Appl. Electrochem.*, **32**, 875 – 882 (2002).

6. J. Weese, *Comput. Phys. Commun.*, **69**, 99–111 (1992).

7. J. Schefold, *J. Electrochem. Soc.*, **156**, 897 – 904 (2009).

8. J. Schefold, A. Brisse, and F. Tietz, *J. Electrochem. Soc.*, **159**, A137 (2012).

9. A. Brisse, J. Schefold, and A. Glauche, *Proc. 11th Eur. Solid Oxide Fuel Cell Forum*, B1302 (2014).

10. S. P. S. Badwal, F. T. Ciacchi, and D. Milosevic, *Solid State Ionics*, **136-137**, 91–99 (2000).

11. C. Graves, C. Chatzichristodoulou, and M. B. Mogensen, *Faraday Discuss.*, **182**, 75–95 (2015).

12. E. Ivers-Tiffée, *Batterien & Brennstoffzelle, Course Material Karlsruhe Institute of Technology*.

13. R. Green, C. Liu, and S. Adler, *Solid State Ionics*, **179**, 647–660 (2008).

14. R. Knibbe, A. Hauch, J. Hjelm, S. D. Ebbesen, and M. Mogensen, *Green*, **1**, 141 – 169 (2011).

15. R. R. Mosbæk, *Solid Oxide Fuel Cell Stack Diagnostics, Ph.D. Thesis, Technical University of Denmark*, Roskilde, (2014).

16. D. Klotz, *Characterization and Modeling of Electrochemical Energy Conversion Systems by Impedance Techniques-Ph.D. Thesis Karlsruhe Institute of Technology*, KIT Scientific Publishing, Karlsruhe, (2012), p. 189.

17. C. R. Graves, *Recycling CO2 into Sustainable Hydrocarbon Fuels: Electrolysis of CO2 and H2O - PhD Thesis Columbia University*, (2010).

18. A. Lasia, *Electrochemical Impedance Spectroscopy and its Applications*, Springer, (2014).

19. B. Boukamp, *SOLID STATE IONICS*, **74**, 85 – 101 (1994).

20. B. Boukamp, *J. Electrochem. Soc.*, **142**, 1885 – 1894 (1995).

21. C. Graves, *RAVDAV Data Anal. Software, Version 0.9.8* (2014).

22. T. H. Wan, M. Saccoccio, C. . Chen, and F. Ciucci, *Electrochim. Acta*, **184**, 483–499. (2015).

23. J.-C. Njodzefon, A. Leonide, V. Sonn, A. Weber, and E. Ivers-Tiffée, *Electrochemical Impedance Spectroscopy, Case study: SOFC, 2nd Joint European Summer School on Fuel Cells and Hydrogen Technology*, Heraklion, Crete, Greece, (2012).

24. N. H. Menzler et al., *Mater. Sci. Forum*, **654-656**, 2875–2878 (2010).

25. D. Stöver, H. P. Buchkremer, and J.P. Huijsmans, *Handbook of Fuel Cells* W. Vielstich, A. Lamm, and H. A. Gasteiger, Editors, John Wiley & Sons Ltd., Chichester, (2003), p. 1015.

26. F. Tietz, H.-P. Buchkremer, and D. Stöver, *J. Electroceramics*, **17**, 701–707 (2006).

27. W. Schafbauer, N. H. Menzler, and H. P. Buchkremer, *Int. J. Appl. Ceram. Technol.*, **11**, 125–135 (2014).

28. N. H. Menzler, J. Malzbender, P. Schoderböck, R. Kauert, and H. P. Buchkremer, *Fuel Cells*, **14**, 96–106 (2014).

29. P. H. Lasen and K. Brodersen, US Patent 20080124602 (2007).

30. A. Weber, Müller, A.C., D. Herbstritt, and E. Ivers-Tiffée, in *in Proceedings of the Seventh International Symposium on Solid Oxide Fuel Cells (SOFC-VII)*, H. Yokokawa and S. C. Singhal, Editors, p. 952 (2001).

31. T. Ramos, K. Thydén, M. Mogensen, E. C. S. Transactions, and T. E. Society, *ECS Trans.*, **28**, 123–139 (2010).

32. D. Johnson, *ZPlot, ZView Electrochem. Impedance Software, Version 2.3b, Scribner Assoc. Inc.* (2000).

33. A. Hauch, *Proc. 10th Eur. SOFC Forum* (2012).

34. A. Leonide, V. Sonn, A. Weber, and E. Ivers-Tiffée, *J. Electrochem. Soc.*, **155**, B36 (2008).

35. S. Primdahl and M. Mogensen, *J. Electrochem. Soc.*, **145**, 2431 – 2438 (1998).

36. A. A. Leonide, A. Weber, E. Ivers-Tiffée, and E. Ivers-Tiffée, *ECS Trans.*, **35**, 2961–2968 (2011).

37. A. Hagen, G. B. Johnson, and P. Hjalmarsson, *J. Power Sources*, **272**, 776–785 (2014).

38. A. Kromp, A. Leonide, A. Weber, and E. Ivers-Tiffée, *J. Electrochem. Soc.*, **158**, B980 (2011).

39. V. Sonn, A. Leonide, and E. Ivers-Tiffée, *J. Electrochem. Soc.*, **155**, B675 (2008).

40. S. Primdahl and M. Mogensen, *J. Electrochem. Soc.*, **146**, 2827 (1999).

41. S. D. Ebbesen and M. Mogensen, *ECS Trans.*, **50**, 167–182 (2013).

42. J.-C. Njodzefon, D. Klotz, A. Kromp, A. Weber, and E. Ivers-Tiffée, *J. Electrochem. Soc.*, **160** (2013).

43. Verein Deutscher Ingenieure VDI-Gesellschaft Verfahrenstechnik und Chemieingenieurwesen (GVC), Ed., *VDI Wärmeatlas*, Springer, Düsseldorf, (2006).

44. S. D. Ebbesen, R. Knibbe, and M. Mogensen, *J. Electrochem. Soc.*, **159**, F482–F489 (2012).

45. A. Weber and E. Ivers-tiffée, *Proc. 11th Eur. SOFC SOE Forum 2014*, **A1307** (2014).

46. S. H. Jensen, A. Hauch, P. V. Hendriksen, and M. Mogensen, *J. Electrochem. Soc.*, **156**, B757 (2009).

47. T. Jacobsen, P. V. Hendriksen, and S. Koch, *Electrochim. Acta*, **53**, 7500–7508 (2008).

48. J. Nielsen, P. Hjalmarsson, M. H. Hansen, and P. Blennow, *J. Power Sources*, **245**, 418–428 (2014).

49. A. J. Samson, P. Hjalmarsson, M. Søgaard, J. Hjelm, and N. Bonanos, *J. Power Sources*, **216**, 124–130 (2012).

50. M. Brown, S. Primdahl, and M. Mogensen, *J. Electrochem. Soc.*, **147**, 475 (2000).

51. S. Primdahl and M. Mogensen, *J. Electrochem. Soc.*, **144**, 3409 (1997).

52. C. Ratnasamy and J. P. Wagner, *Catal. Rev.*, **51**, 325–440 (2009).

53. J.-C. Njodzefon et al., *ECS Trans.*, **41**, 113–122 (2012).

54. J. Udagawa, P. Aguiar, and N. P. Brandon, *J. Power Sources*, **166**, 127–136 (2007).

55. M. NI, M. LEUNG, and D. LEUNG, *Int. J. Hydrogen Energy*, **32**, 2305–2313 (2007).

56. A. Virkar, J. Chen, C. Tanner W, and J.-W. Kim, *Solid State Ionics*, **131**, 189–198 (2000).

57. A. V. Akkaya, *Int. J. Energy Res.*, **31**, 79–98 (2007).

58. P. Aguiar, C. S. Adjiman, and N. P. Brandon, *J. Power Sources*, **138**, 120–136 (2004).

59. Y. Wang, F. Yoshiba, T. Watanabe, and S. Weng, *J. Power Sources*, **170**, 101–110 (2007).

60. J. Fleig, *Annu. Rev. Mater. Res.*, **33**, 361–382 (2003).

61. D. Klotz, J.-C.-C. Njodzefon, A. Weber, and E. Ivers-Tiffée, *ECS Trans.* , **45** , 523–530 (2012).

62. J. O. Bockris and Z. Nagy, *J. Chem. Educ.*, **50**, 839 (1973).

63. W. G. Bessler et al., *Phys. Chem. Chem. Phys.*, **12**, 13888–13903 (2010).

64. S. B. Adler, J. A. Lane, and B. C. H. Steele, *J. Electrochem. Soc.*, **143**, 3554–3564 (1996).

65. R. J. Gorte and J. M. Vohs, *Annu. Rev. Chem. Biomol. Eng.*, **2**, 9–30 (2011).

66. A. Utz, H. Störmer, A. Leonide, A. Weber, and E. Ivers-Tiffée, *J. Electrochem. Soc.* , **157** , B920–B930 (2010).

67. D. A. Noren and M. A. Hoffman, *J. Power Sources*, **152**, 175–181 (2005).

68. T. Ramos, M. Sogaard, and M. B. Mogensen, *J. Electrochem. Soc.*, **161**, F434–F444 (2014).

69. J. Hjelm, M. Soegaard, R. Knibbe, A. Hagen, and M. Mogensen, *ECS Trans.*, **13**, 285–299 (2008).

70. V. Sonn and E. Ivers-tiffée, *Proc. 8th Eur. SOFC Forum*, B1005 (2008).

71. G. Paasch, K. Micka, and P. Gersdorf, *Electrochim. Acta*, **38**, 2653–2662 (1993).

72. G. Paasch, *Electrochem. commun.*, **2**, 371–375 (2000).

73. A. Leonide, S. N. Dinh, A. Weber, and E. Ivers-Tiffée, in *In Proceedings of the 8th European Solid Oxide Fuel Cell Forum*, R. Steinberger-Wilckens and U. Bossel, Editor, p. A0501 (2008).

74. P. Ried et al., *J. Eur. Ceram. Soc.*, **28**, 1801–1808 (2008).

75. I. R. Gibson and J. T. S. Irvine, *J. Mater. Chem.*, **6**, 895–898 (1996).

76. A. Bertei, G. Arcolini, C. Nicolella, and P. Piccardo, *ECS Trans.*, **68**, 2897–2905 (2015).

77. M. VERKERK, B. MIDDELHUIS, and A. BURGGRAAF, *Solid State Ionics*, **6**, 159–170 (1982).

78. A. Bieberle, L. P. Meier, and L. J. Gauckler, *J. Electrochem. Soc.*, **148**, A646–A656 (2001).

79. P. Holtappels, L. G. J. de Haart, and U. Stimming, *J. Electrochem. Soc.*, **146**, 1620–1625 (1999).

80. M. Mogensen, J. Høgh, K. V. Hansen, and T. Jacobsen, *ECS Trans.*, **7**, 1329–1338 (2007).

81. OriginLab, Northampton, MA.

82. A. Utz, H. Störmer, A. Leonide, A. Weber, and E. Ivers-Tiffée, *J. Electrochem. Soc.*, **157**, B920 (2010).

83. J. MIZUSAKI et al., *Solid State Ionics*, **70-71**, 52–58 (1994).

84. P. Holtappels, I. C. Vinke, L. G. J. de Haart, and U. Stimming, *J. Electrochem. Soc.*, **146**, 2976–2982 (1999).

85. M. B. Mogensen, *Solid Oxide Fuel Cells*, 484 – 493 (1993).

86. W. BESSLER, J. WARNATZ, and D. GOODWIN, *Solid State Ionics*, **177**, 3371–3383 (2007).

87. C. Endler-Schuck, *Alterungsverhalten mischleitender LSCF Kathoden für Hochtemperatur-Festoxid-Brennstoffzellen (SOFCs), Ph.D. Thesis, Karlsruhe Institute of Technology*, KIT Scientific Publishing, (2011).

88. B. Dalslet et al., *J. Solid State Electrochem.*, **10**, 547–561 (2006).

89. F. Tietz, A. Mai, and D. Stöver, *Solid State Ionics*, **179**, 1509–1515 (2008).

90. S. Adler, *Solid State Ionics*, **135**, 603–612 (2000).

91. A. Leonide, B. Rüger, A. Weber, W. A. Meulenberg, and E. Ivers-Tiffée, *J. Electrochem. Soc.*, **157**, B234–B239 (2010).

92. C. Endler-Schuck, J. Joos, C. Niedrig, A. Weber, and E. Ivers-Tiffée, *Solid State Ionics*, **269**, 67–79 (2015).

93. J. Maier, *Solid State Ionics*, **112**, 197–228 (1998).

94. J. Maier, *Solid State Ionics*, **135**, 575–588 (2000).

95. J.-C. Njodzefon, D. Klotz, N. . Menzler, A. Weber, and E. Ivers-Tiffée, in *In Proceedings of the 10th European Solid Oxide Fuel Cell Forum*, M. Spirit, O. Bucheli, and F. Lefebbvre-Joud, Editors, p. B0713 (2012).

96. C. H. Hamann, A. Hamnett, and W. Vielstich, *Electrochemistry*, 2nd ed., Wiley-VCH Verlag GmbH & Co. KGaA, Weinheim, Germany, (2007).

97. C. Endler-Schuck et al., *J. Fuel Cell Sci. Technol.*, **8**, 41001 (2011).

98. C. Endler, A. Leonide, A. Weber, F. Tietz, and E. Ivers-Tiffée, *J. Electrochem. Soc.* , **157** , B292–B298 (2010).

99. D. Sánchez, R. Chacartegui, A. Muñoz, and T. Sánchez, *J. Power Sources*, **160**, 1074–1087 (2006).

100. A. C. Müller, J. R. Opfermann, and E. Ivers-Tiffée, *Thermochim. Acta*, **414**, 11–17 (2004).

101. T. Carraro, J. Joos, B. Rüger, A. Weber, and E. Ivers-Tiffée, *Electrochim. Acta*, **77**, 315–323 (2012).

102. J.-W. Kim, *J. Electrochem. Soc.*, **146**, 69 (1999).

103. E. A. Mason and A. P. Malinauskas, *Gas Transport in Porous Media: The dusty gas model*, Elsevier Ltd, Amsterdam, (1983).

104. R. Jackson, *Transport in porous catalsysts*, Elsevier Ltd, Amsterdam, (1977).

105. E. L. Cussler, *Diffusion: Mass Transfer in fluid Systems*, Cambridge University Press, Cambridge, (1984).

106. B. Poling, J. M. Prausnitz, and J. P. O´Connel, *The properties of gases and liquids*, 5th ed., McGraw-Hill, New York, (2001).

107. A. C. . Müller, A. Weber, A. . Krügel, D. . Gertsen, and E. Ivers-Tiffée, in *In Proceedings of the 6th Interregional European Colloquium on Ceramics and Composites*, R. Gadow, Editor, Stuttgart (1998).

108. D. Klotz, A. Weber, and E. Ivers-Tiffée, in *In Proceedings of the 8th European Solid Oxide Fuel Cell Forum*, R. Steinberger-Wilckens and U. Bossel, Editors, p. B0909 (2008).

109. S. D. Ebbesen, S. H. Jensen, A. Hauch, and M. B. Mogensen, *Chem. Rev.* (2014).

110. R. Knibbe, M. L. Traulsen, A. Hauch, S. D. Ebbesen, and M. Mogensen, *J. Electrochem. Soc.* , **157** , B1209–B1217 (2010).

111. H. Yokokawa, S. . Yamauchi, and T. Matsumoto, *Calphad*, **26**, 155 – 166 (2002).

112. J.-C. Njodzefon, C. Graves, M. B. Mogensen, A. Weber, and J. Hjelm, *ECS Trans.*, **64**, 51–65 (2015).

113. H. Zhu and R. J. Kee, *J. Electrochem. Soc.* , **153** , A1765–A1772 (2006).

114. M. Ni, *J. Power Sources*, **202**, 209–216 (2012).

115. M. Ni, *Int. J. Hydrogen Energy*, **37**, 6389–6399 (2012).

116. B. A. Haberman and J. B. Young, *Int. J. Heat Mass Transf.*, **47**, 3617–3629 (2004).

117. P. Kazempoor and R. J. Braun, *Int. J. Hydrogen Energy*, **39**, 5955–5971 (2014).

118. A. Brisse, J. Schefold, and M. Zahid, *Int. J. Hydrogen Energy*, **33**, 5375–5382 (2008).

119. M. A. Laguna-Bercero, *J. Power Sources*, **203**, 4–16 (2012).

120. M. A. Laguna-Bercero, R. Campana, A. Larrea, J. A. Kilner, and V. M. Orera, *J. Power Sources*, **196**, 8942–8947 (2011).

121. P. Kim-Lohsoontorn and J. Bae, *J. Power Sources*, **196**, 7161–7168 (2011).

122. C. Graves, S. D. Ebbesen, and M. Mogensen, *Solid State Ionics*, **192**, 398–403 (2011).

123. M. Ni, *Int. J. Hydrogen Energy*, **34**, 7795–7806 (2009).

124. M. Ni, *Chem. Eng. J.*, **164**, 246–254 (2010).

125. J. Udagawa, P. Aguiar, and N. P. Brandon, *J. Power Sources*, **180**, 46–55 (2008).

126. J. Laurencin, D. Kane, G. Delette, J. Deseure, and F. Lefebvre-Joud, *J. Power Sources*, **196**, 2080–2093 (2011).

127. C. J. Moyer, N. P. Sullivan, H. Zhu, and R. J. Kee, *J. Electrochem. Soc.*, **158**, B117–B131 (2011).

128. C. H. Wendel, Z. Gao, S. A. Barnett, and R. J. Braun, *J. Power Sources*, **283**, 329–342 (2015).

129. P. Hjalmarsson, X. Sun, Y.-L. Liu, and M. Chen, *J. Power Sources*, **262**, 316–322 (2014).

130. Q. Fang, L. Blum, and N. H. Menzler, *J. Electrochem. Soc.*, **162**, F907–F912 (2015).

131. A. Brisse and J. Schefold, *Energy Procedia*, **29**, 53–63 (2012).

132. F. Tietz, D. Sebold, A. Brisse, and J. Schefold, *J. Power Sources*, **223**, 129–135 (2013).

133. F. Petipas, Q. Fu, A. Brisse, and C. Bouallou, *Int. J. Hydrogen Energy*, **38**, 2957–2964 (2013).

134. X. Sun et al., *ECS Trans.*, **41**, 77–85 (2012).

135. P. Hjalmarsson, X. Sun, Y.-L. Liu, and M. Chen, *J. Power Sources*, **262**, 316–322 (2014).

136. A. Hauch, S. D. Ebbesen, S. H. Jensen, and M. Mogensen, *J. Electrochem. Soc.*, **155**, B1184–B1193 (2008).

137. A. Hauch, S. H. Jensen, S. Ramousse, and M. Mogensen, *J. Electrochem. Soc.*, **153**, A1741–A1747 (2006).

138. J. Mougin et al., *Energy Procedia*, **29**, 445–454 (2012).

139. V. N. Nguyen, Q. Fang, U. Packbier, and L. Blum, *Int. J. Hydrogen Energy*, **38**, 4281–4290 (2013).

140. S. D. Ebbesen, J. Høgh, K. A. Nielsen, J. U. Nielsen, and M. Mogensen, *Int. J. Hydrogen Energy*, **36**, 7363–7373 (2011).

141. J. Mougin et al., *Fuel Cells*, **13**, 623–630 (2013).

142. M. Chen et al., *Fuel Cells*, **13**, 638–645 (2013).

143. C. Stoots, J. O'Brien, and J. Hartvigsen, *Int. J. Hydrogen Energy*, **34**, 4208–4215 (2009).

144. C. M. Stoots, J. E. O'Brien, K. G. Condie, and J. J. Hartvigsen, *Int. J. Hydrogen Energy*, **35**, 4861–4870 (2010).

145. J. Schefold, A. Brisse, and M. Zahid, *ECS Trans.*, **28**, 357–367 (2010).

146. J. Schefold, A. Brisse, M. Zahid, J. P. Ouweltjes, and J. U. Nielsen, *ECS Trans.*, **35**, 2915–2927 (2011).

147. J. R. Mawdsley, J. David Carter, A. Jeremy Kropf, B. Yildiz, and V. A. Maroni, *Int. J. Hydrogen Energy*, **34**, 4198–4207 (2009).

148. S. D. Ebbesen, C. Graves, A. Hauch, S. H. Jensen, and M. Mogensen, *J. Electrochem. Soc.*, **157**, B1419 (2010).

149. A. ISENBERG, *Solid State Ionics*, **3-4**, 431–437 (1981).

150. P. Hjalmarsson, X. Sun, Y.-L. Liu, and M. Chen, *J. Power Sources*, **223**, 349–357 (2013).

151. E. Tang et al., *Advanced Materials for RSOFC Dual Operation with Low Degradation*, (2012).

152. C. Graves, S. D. Ebbesen, S. H. Jensen, S. B. Simonsen, and M. B. Mogensen, *Nat Mater*, **14**, 239–244 (2015).

153. C. Graves, *ECS Trans.*, **57**, 3127–3136 (2013).

154. C. Endler-Schuck et al., *J. Power Sources*, **196**, 7257–7262 (2011).

155. X. Sun, *Proc. 11th Eur. Sofc Soe Forum 2014* (2014).

156. F. S. Baumann et al., *J. Electrochem. Soc.*, **154**, B931–B941 (2007).

157. M. Chen et al., *J. Electrochem. Soc.*, **160**, F883–F891 (2013).

158. J. Schefold, A. Brisse, and H. Poepke, *Electrochim. Acta*, **179**, 161–168 (2015).

159. D. Klotz et al., *J. Electrochem. Soc.*, **158**, B587–B595 (2011).

160. M. Becker, A. Mai, E. Ivers-Tiffée, and F. Tietz, in *Proceedings of the Ninth International Symposium on Solid Oxide Fuel Cells (SOFC IX)*, S. C. Singhal and J. Mizusaki, Editors, p. 5014 (2005).

161. A. MAI et al., *Solid State Ionics*, **177**, 1965–1968 (2006).

162. A. Utz, A. Weber, H. Störmer, and E. Ivers-Tiffée, in *Proceedings of the 8th European Solid Oxide Fuel Cell Forum*, R. Steinberger-Wilkens and U. Bossel, Editors, p. A0509 (2008).

163. P. Moçoteguy and A. Brisse, *Int. J. Hydrogen Energy*, **38**, 15887–15902 (2013).

164. R. J. Aaberg, R. Tunold, M. Mogensen, R. W. Berg, and R. Ødegaård, *J. Electrochem. Soc.*, **145**, 2244–2252 (1998).

165. A. Gubner, H. Landes, J. Metzger, H. Seeg, and R. Strübner, in *In Solid Oxide Fuel Cells V, The Electrochemical Society Proceedings Series*, M. Dokiya, O. Yamamoto, H. TAGAWA, and S. C. Singhal, Editors, p. 844, Pennington, NJ (1997).

166. A. Hagen, R. Barfod, P. V. Hendriksen, Y.-L. Liu, and S. Ramousse, *J. Electrochem. Soc.*, **153**, A1165–A1171 (2006).

167. B. Butz et al., *Solid State Ionics*, **214**, 37–44 (2012).

168. M. Mogensen, S. Primdahl, M. J. Jérgensen, and C. Bagger, *J. Electroceramics*, **5**, 141 – 152 (2000).

169. J. Chevalier, L. Gremillard, A. V. Virkar, and D. R. Clarke, *J. Am. Ceram. Soc.*, **92**, 1901–1920 (2009).

170. D. The et al., *J. Power Sources*, **275**, 901–911 (2015).

171. B. Butz, R. Schneider, D. Gerthsen, M. Schowalter, and A. Rosenauer, *Acta Mater.*, **57**, 5480–5490 (2009).

172. A. Hauch, A. Hagen, J. Hjelm, and T. Ramos, *J. Electrochem. Soc.*, **161**, F734–F743 (2014).

173. T. Jacobsen and M. Mogensen, *ECS Trans.*, **13**, 259–273 (2008).

174. A. V. Virkar, *Int. J. Hydrogen Energy*, **35**, 9527–9543 (2010).

175. Y. Zhang, K. Chen, C. Xia, S. P. Jiang, and M. Ni, *Int. J. Hydrogen Energy*, **37**, 13914–13920 (2012).

176. S. D. Ebbesen and M. B. Mogensen, *EP2362475* (2011).

177. S. D. Ebbesen and M. Mogensen, *J. Power Sources*, **193**, 349–358 (2009).

178. Q. Fu, J. Schefold, a. Brisse, and J. U. Nielsen, *Fuel Cells*, **14**, 395–402 (2014).

179. Y. Matsuzaki and I. Yasuda, *J. Electrochem. Soc.*, **147**, 1630–1635 (2000).

180. S. Zha, Z. Cheng, and M. Liu, *J. Electrochem. Soc.*, **154**, B201–B206 (2007).

181. K. Jensen, *Solid State Ionics*, **160**, 27–37 (2003).

182. M. Mogensen, K. V. Jensen, M. J. Jørgensen, and S. Primdahl, **150**, 123–129 (2002).

183. S. Primdahl, M. Mogensen, and L. J. Sham, *J. Electrochem. Soc.*, **145**, 2431–2438 (1998).

184. S. D. Ebbesen, X. Sun, and M. B. Mogensen, *Faraday Discuss.*, **00**, 1–30 (2015).

185. J.-C. Njodzefon, B. R. Sudireddy, J. Hjelm, and C. Graves, *ECS Trans.*, **68**, 1169–1184 (2015).

186. A. Tsoga, A. Naoumidis, and D. Stover, *Solid State Ionics*, **135**, 403–409 (2000).

187. Y. Tao, S. D. Ebbesen, and M. B. Mogensen, *J. Electrochem. Soc.*, **161**, F337–F343 (2014).

Appendix

Appendix A

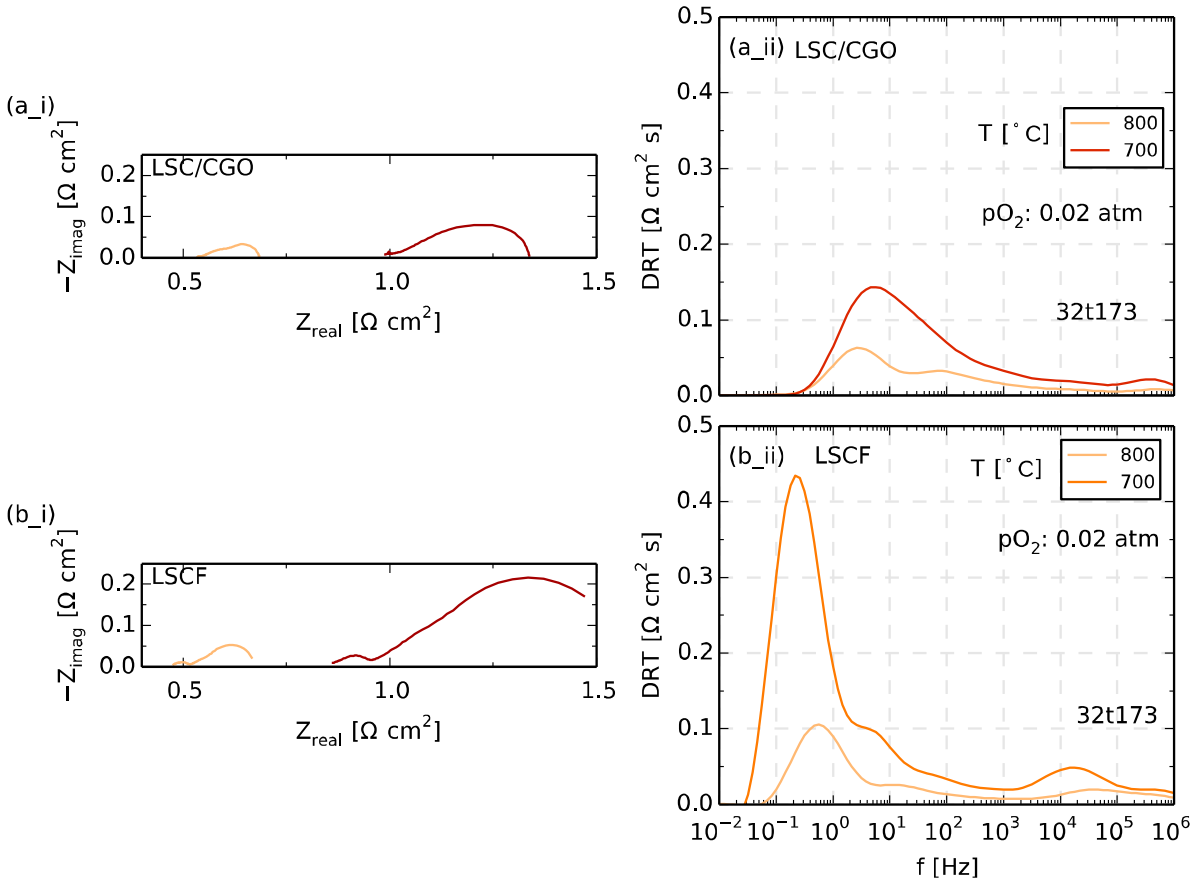

Appendix B

List of Figures

List of Tables

List of Abbreviations

AC	Alternating current
AFL	Anode functional layer
ASC	Anode supported cell
ASR	Area specific resistance
C	capacitor
CGO	Gadolinia-doped ceria
CH_4	Methane
CO	Carbon monoxide
CO_2	Carbon dioxide
C/V	Current/Voltage
CNLS	Complex nonlinear least squares
CPE	constant phase element
CSTR	Continuously stirred tank reactor
DC	Direct current
DRT	Distribution of relaxation times
DTU	Technical university of Denmark
ECM	Equivalent circuit model
EEC	Equivalent electric circuit
EDX	Energy dispersive X-ray spectroscopy
EIS	Electrochemical impedance spectroscopy
ESC	Electrolyte supported cell
FRA	Frequency response analyzer
FZJ	Forschungszentrum Jülich

H_2 Hydrogen

H_2O Water (or steam)

IAM-WET Institut für Angewandte Materialien - Werkstoffe der Elektrotechnik (IAM-WET)

KIT Karlsruhe institute of technology

KK Kramers-Kronig

LSC Lanthanum strontium cobaltite

LSCF Lanthanum strontium cobaltite ferrite

LSM Lanthanum strontium manganite

MFC Mass flow controller

MIEC Mixed ionic and electronic conducting

Ni/YSZ Nickel/yttria-stabilized zirconia

OCV Open circuit voltage

PFR Plug-flow reactor

Q constant phase element (also CPE)

R resistor

RQ parallel connection of a resistor and a CPE

RCT Reverse current treatment

RWGSR Reverse water gas shift reaction

SEM Scanning electron microscopy

SFEIS Single frequency impedance spectroscopy

SOC Solid oxide cell

SOEC Solid oxide electrolysis cell

SOFC Solid oxide fuel cell

s.t.a. state of the art

TEC Thermal expansion coefficient

TEM Transmission electron microscopy

TPB Triple phase boundary

Wgfl Finite length Warburg element

WGSR Water gas shift reaction

YSZ Yttria-stabilized zirconia

List of Symbols

Symbol	Description	Unit
A	Area	m^2
ASR	Area specific resistance	$\Omega \cdot m^2$
a	Hydrogen partial pressure dependency	–
a	Surface area density	μm^{-1}
α	Charge transfer coefficient	–
B_{ohm}	Material specific prefactor	$S \cdot K \cdot m^{-2}$
b	Steam partial pressure dependency	–
C	Capacitance	F
c	Carbon monoxide partial pressure dependency	–
c_{mc}	Concentration of oxygen lattice sites	$mol \cdot m^{-3}$
c_0	Concentration of oxygen ions	$mol \cdot m^{-3}$
$D_{bulk,i}$	Bulk diffusion coefficient of gas component i	$m^2 \cdot s^{-1}$
D_i^{eff}	Effective diffusion coefficient of gas component i	$m^2 \cdot s^{-1}$
$D_{Knudsen,i}$	Knudsen diffusion coefficient of gas component i	$m^2 \cdot s^{-1}$
$D_{mol,i}$	Molecular diffusion coefficient of gas component i	$m^2 \cdot s^{-1}$
D^{δ}	Chemical oxygen ion diffusion coefficient	$m^2 \cdot s^{-1}$
D^{Q}	Electrically driven oxygen ion diffusion coefficient	$m^2 \cdot s^{-1}$
d	Carbon dioxide partial pressure dependency	–
$E_{act,an}$	Activation energy of fuel electrode	$kJ \cdot mol^{-1}$
$E_{act,cat}$	Activation energy of oxygen electrode	$kJ \cdot mol^{-1}$
$E_{act,ohm}$	Activation energy for ohmic losses	$kJ \cdot mol^{-1}$
E_{tn}	Thermoneutral voltage	V
F	Raday constant	$C \cdot mol^{-1}$
f	Frequency	Hz
f_s	Peak frequency	Hz
f_u	Fuel utilization	%
G	Gibbs free energy	$kJ \cdot mol^{-1}$
ΔG	Change in Gibbs free energy	$kJ \cdot mol^{-1}$
H	Enthalpy	$kJ \cdot mol^{-1}$
ΔH	Enthalpy change	$kJ \cdot mol^{-1}$
h	Hour	s
I_{load}	Bias current	A
i	Current density	$A \cdot m^{-2}$
$i(t)$	AC excitation	A
j	Current density	$A \cdot m^{-2}$
j_0	Exchange current density	$A \cdot m^{-2}$
j	Imaginary unit	–
j^*	Flux of CO/CO_2	$molm^{-2}s^{-1}$

K^{δ}	Chemical surface exchange coefficient	$m \cdot s^{-1}$
K^{Q}	Electrically driven surface exchange coefficient	$m \cdot s^{-1}$
K_{PS}	Equilibrium constant	–
k_{sf}	Rate constant of the forward water gas shift reaction	$molm^{-3}Pa^{-2}s^{-1}$
k_{sb}	Rate constant of the backward water gas shift reaction	$molm^{-3}Pa^{-2}s^{-1}$
L	Inductance	H
L_{an}	Thickness of fuel electrode	m
L_{cat}	Thickness of oxygen	m
l	Length	m
M_i	Molar mass of gas component i	$Kg \cdot mol^{-1}$
m	Oxygen partial pressure dependency	–
n	Number of electrons	–
P	Pressure	Atm (Pa)
P_0	Conversion factor from *atm* to *Pa* (= 101330)	Pa/atm
pCO	Carbon monoxide partial pressure	atm
pCO_2	Carbon dioxide partial pressure	atm
pH_2	Hydrogen partial pressure	atm
pH_2O	Steam partial pressure	atm
$pX_{i,el}^{TPB}$	Partial pressure of gas component X_i at the TPB of electrode el	atm
ps	Particle size	m
R	Universal gas constant	$J \cdot mol^{-1} \cdot K^{-1}$
R_{chem}	Characteristic resistance of Gerischer element	Ω
R_{ohm}	Ohmic resistance	$\Omega \cdot m^2$
R_0	Ohmic resistance	$\Omega \cdot m^2$
R_s	Series Resistance	$\Omega \cdot m^2$
R_{WGSR}	Rate of the water gas shift reaction	$molm^{-3}s^{-1}$
$r_{Por,el}$	Mean pore radius of electrode el	m
S	Entropy	$J \cdot K^{-1}$
ΔS	Entropy change	$J \cdot K^{-1}$
T	Temperature	°C
ΔT	Temperature change	K
t_{chem}	Characteristic time of Gerischer element	s
U	Cell voltage	V
U_N	Nernst voltage	V
U_{OCV}	Open circuit voltage	V
u(t)	AC voltage signal	V
x_i	Mole fraction of gas component i	–
$\underline{Z}$	Impedance	Ω
α_{an}	Charge transfer coefficient of the fuel electrode	–
α_{cat}	Charge transfer coefficient of the oxygen electrode	–
β	Symmetry factor	–
γ	Thermodynamic factor	–
$\gamma(\tau)$	Distribution function of relaxation times	$\Omega \cdot s^{-1}$
γ_{an}	Fuel electrode exchange current density prefactor	$A \cdot m^{-2}$
γ_{cat}	Oxygen electrode exchange current density prefactor	$A \cdot m^{-2}$
δ	Fraction of oxygen vacancies	–

ε	Porosity	–
η	Overpotential	V
$\eta_{act,an}$	Activation overpotential of the fuel electrode	V
$\eta_{act,cat}$	Activation overpotential of the oxygen electrode	V
$\eta_{conc,an}$	Concentration overpotential of the fuel electrode	V
$\eta_{conc,cat}$	Concentration overpotential of the oxygen electrode	V
$\eta_{conc,Ref}$	Concentration overpotential associated with reformate process	V
η_{ohm}	Overpotential related to ohmic losses	V
σ_{ij}	Average collision diameter	Å
τ	Solid phase tortuosity	–
τ_s	Characteristic / Relaxation time	s
ψ_{el}	Structural parameter of electrode el	–
φ_{X_i}	Flow rate of gas component X_i	l/h
Ω_D	Collision integral	–
ω	Angular frequency	s^{-1}

List of Publications

[6] Jean-Claude Njodzefon, Bhaskar Reddy Sudireddy, Johan Hjelm, Christopher Graves, *Kinetic Studies on Ni-YSZ Composite Electrodes*, ECS Trans., **68**, 1169–1184 (2015).

[5] J.-C. Njodzefon, Christopher R. Graves, Mogens B. Mogensen, André Weber, Johan Hjelm, *Kinetic Studies on State of the Art Solid Oxide Cells – A Comparison between Hydrogen/Steam and Reformate Fuels*, ECS Trans. **64**, 51–65 (2015).

[4] J.-C. Njodzefon, D. Klotz, A. Kromp, A. Weber and E. Ivers-Tiffée, *Electrochemical Modeling of the Current-Voltage Characteristics of an SOFC in Fuel Cell and Electrolyzer Operation Modes*, J. Electrochem. Soc., **160** (4), p. F313 (2013).

[3] D. Klotz, J. C. Njodzefon, A. Weber and E. Ivers-Tiffée, *Current-Voltage and Temperature Characteristics of Anode Supported Solid Oxide Electrolyzer Cells (SOEC)*, ECS Trans., **45** (1), p. 523 (2012).

[2] J.-C. Njodzefon, D. Klotz, N. Menzler, A. Weber and E. Ivers-Tiffée, *Detailed Study of an Anode Supported Cell in Electrolyzer Mode under Thermo-Neutral Operation*, Proceedings of the 10th European Solid Oxide Fuel Cell Forum, M. Spirit, O. Bucheli, and F. Lefebbvre-Joud, Editors**,** p. B0713 (2012).

[1] J.-C. Njodzefon, D. Klotz, A. Leonide, A. Kromp, A. Weber and E. Ivers-Tiffée, *Electrochemical Studies on Anode Supported Solid Oxide Electrolyzer Cells (SOEC)*, ECS Trans., **41** (33), p. 113 (2012)

Conference Contributions

[11] J.-C. Njodzefon, Bhaskar Reddy Sudireddy, Johan Hjelm, Christopher Graves, *Kinetic Studies on Ni-YSZ Composite Electrodes,* Oral presentation at the ECS Conference on Electrochemical Energy Conversion & Storage with SOFC-XIV (**Glasgow, Scottland**), 26.07. – 01.08.2015

[10] J.-C. Njodzefon, C. Graves, M. B. Mogensen, A. Weber and J. Hjelm, *Kinetic Studies on State of the Art Solid Oxide Cells:Operation in H_2/H_2O, H_2/CO_2, $CH_4/H_2/H_2O$ Fuels,* Oral presentation at the 226th Meeting of The Electrochemical Society (**Cancun, Mexico**), 05.10. – 09.10.2014

[9] A. Weber, J.-C. Njodzefon, A. Leonide, E. Ivers-Tiffée, *Elektrochemie und Degradationsmechanismen – ein Vergleich zwischen SOFC- und SOEC-Betrieb anodengestützter Zellen*, Oral presentation at the SOFC Workshop "Technologieroadmapping" D A CH III (**Reutte, Austria**), 27. 06. 2013

[8] J.-C. Njodzefon, J. Hayd, A. Weber, E. Ivers-Tiffée, *Detailed Study of Anode Supported Solid Oxide Cells in Electrolyzer and Cyclic Operation Modes* , Oral presentation at the 5th International Conference on Fundamentals & Development of Fuel cells (**Karlsruhe, Germany**), 16. 04. – 18. 04. 2013

[7] J.-C. Njodzefon, A. Leonide, S. Hansmann, A. Weber, E. Ivers-Tiffée, *A 0-Dimensional Stationary Model for Anode-Supported Solid Oxide Fuel Cells (SOFC)*, Poster presentation at the workshop on Electrolysis and CO_2-Recycling for Production of Green Fuels (**Risø, Denmark**), 09.04 – 11.04. 2013

[6] J.-C. Njodzefon, A. Weber, E. Ivers-Tiffée, *Electrochemical Modeling of Cathode Supported Solid Oxide Electrolyzer Cells in Electrolysis of Carbon Dioxide*, Oral presentation at the 222nd Meeting of The Electrochemical Society (**Honolulu, USA**), 07.10. – 12.10.2012

[5] J.-C. Njodzefon, A. Leonide, V. Sonn, A. Weber, E. Ivers-Tiffée, *Electrochemical Impedance Spectroscopy, Case study: SOFC*, Oral presentation at the 2nd Joint European Summer School on Fuel Cells and Hydrogen Technology, (**Heraklion, Crete, Greece**), 17.09. – 28.09.2012

[4] J.-C. Njodzefon, A. Weber, and E. Ivers-Tiffée, *A 0-Dimensional Stationary Model for Anode-Supported Solid Oxide Fuel Cells (SOFC)*, Poster presentation at the 63rd Annual Meeting of the International Society of Electrochemistry (**Prague, Czech Republic**), 19.08. – 24.08.2012

[3] J.-C. Njodzefon, D. Klotz, N. Menzler, A. Weber, and E. Ivers-Tiffée, *Detailed Study of an Anode Supported Cell in Electrolyzer Mode under Thermo-Neutral Operation*, Poster presentation at the 10th European SOFC Forum (**Lucerne, Switzerland**), 06.26. - 06.29.2012

[2] D. Klotz, J.-C. Njodzefon, A. Weber, and E. Ivers-Tiffée, *Current-Voltage and Temperature Characteristics of Anode Supported Solid Oxide Electrolyzer Cells (SOEC)*, Oral presentation at the 221st Meeting of The Electrochemical Society (**Seattle, USA**), 06.05. - 11.05.2012

[1] J.-C. Njodzefon, D. Klotz, A. Leonide, A. Kromp, A. Weber, and E. Ivers-Tiffée, *Electrochemical Studies on Anode Supported Solid Oxide Electrolyzer Cells (SOEC)*, Oral presentation at the 220th Meeting of The Electrochemical Society (**Boston, USA**), 10.11. - 10.11.2011

Supervised Theses

[5] A. Lenis, *Electrochemical Investigation of a Solid Oxide Electrolyzer Cell under Current Load* , Student Research Project (Thesis)), 2013

[4] M. Krompic, *Modeling the Current-Voltage Characteristic of a Solid Oxide Fuel Cell in the co-electrolysis of Steam and Carbondioxide,* B. Sc., 2013

[3] B. Schwarz, *Stability Investigations of a Solid Oxide Fuel Cell in Electrolysis of Carbondioxide*, B. Sc., 2012

[2] C. Ksellmann, *Investigation of the Ageing Behavior of a Solid Oxide Electrolyzer Cell*, B. Sc., 2012

[1] J. Stahl, *Modeling the Stationary Behavior of a Solid Oxide Electrolyzer Cell*, Student Research Project (Thesis), 2011